UNIVERSITAT POLITÈCNICA
DE CATALUNYA

Escola Tècnica Superior d'Enginyers de Camins, Canals i Ports de Barcelona

THERMO-HYDRO-MECHANICAL ANALYSIS OF SOFT ROCK

APPLICATION TO A LARGE SCALE HEATING TEST AND LARGE SCALE VENTILATION TEST

PhD THESIS

Presented by:
Juan Jorge Muñoz

Supervised by:
Eduardo Alonso Pérez de Ágreda
Antonio Lloret Morancho

Barcelona, December of 2006

A mi esposa,
María Eugenia

A la memoria de mi padre,
Eduardo Federico Muñoz

ABSTRACT

This thesis deals with the theoretical and experimental analysis of the coupled Thermo-Hydro-Mechanical (THM) processes developed in geological formations suitable for the repository of radioactive waste of high activity. In the last decades, the argillaceous formations have been studied to be used as geological barriers, due to its reduced hydraulic conductivity. The degradation of clay shales induced by temperature and saturation effects is an important factor which is currently being investigated in large scale in situ tests as well as in laboratory studies.

In this thesis, the Opalinus clay rock has been widely characterized by means of laboratory tests. From a macro-structural point of view, the water retention curve, hydraulic conductivity, strength and deformability parameters have been determined. The micro-structural analysis is focused to the mineralogical characterization obtained by means of X ray diffraction, pore size distribution (PSD) determined by means of mercury intrusion porosimetry (MIP) and scanning electronic microscopy (SEM).

The thesis describes also a large scale heating in situ test designed to analyze the interaction between the engineer barrier (compacted bentonite blocks) and by the geological barrier, (Opalinus clay). This interaction has been analyzed by means of numerical simulations performed with the finite element code CODE_BRIGHT. A thermo hydraulic cell was specially designed to observe the coupled THM behaviour of the clay shale rock under drained and undrained conditions by means of heat pulses. Thermal and hydraulic parameters of rock were determined by means of back-analysis performed with the help of CODE_BRIGHT.

In order to reproduce the anisotropic and brittle behaviour of the clay shale, a 3D mechanical constitutive model has been formulated and implemented in CODE_BRIGHT. The constitutive model is formulated in a viscoplastic framework and it considers the strength and deformability of both matrix and discontinuities (joints). The failure criterion of the matrix and the joints is defined by means of hyperbolic yield surfaces in the p-J and τ-σ stress space, respectively. The brittle behaviour of clay shale is simulated by means of isotropic and kinematic softening defined in terms of a work-hardening criterion. The anisotropic constitutive model has been calibrated against triaxial laboratory tests performed on specimens with a main family of discontinuities having different dip angles. The constitutive model has been applied to a 3D numerical simulation of an “in-situ” heating test. A 3D numerical simulation of a ventilation test performed in an unlined micro tunnel was also performed in order to reproduce the changes of the rock permeability by drying effects. In this case, a hydraulic model able to consider the changes in joint thickness by drying effects has been developed to reproduce the changes of permeability in underground excavations.

RESUMEN

Esta Tesis está dirigida al análisis teórico y experimental de problemas acoplados Termo-Hidro-Mecánico (THM) que se desarrollan en formaciones geológicas profundas destinadas al almacenamiento de residuos radiactivos de alta actividad. En las últimas décadas, han sido estudiadas las formaciones arcillosas para ser utilizadas como barreras geológicas debido a su reducida conductividad hidráulica. La degradación de las rocas arcillosas producida por efectos de temperatura y por efectos de variación en el grado de saturación, es un factor de fundamental importancia, que es actualmente investigado en ensayos in situ a gran escala, como así también en ensayos de laboratorio.

En ésta tesis, la roca Opalinus Clay ha sido ampliamente caracterizada mediante ensayos de laboratorios. Desde un punto de vista macro-estructural se ha obtenido la curva de retención de agua, conductividad hidráulica, resistencia y deformación. El análisis micro-estructural está enfocado a la caracterización mineralógica obtenida por difracción de rayos X, la distribución del tamaño de los poros determinada por porosimetría de mercurio (MIP) y microscopía electrónica (SEM).

La tesis describe también un ensayo in situ de calentamiento diseñado para analizar la interacción entre la barrera de ingeniería (bloques de bentonita compactada) y la barrera geológica (Opalinus clay). Esta interacción ha sido analizada a través de simulaciones numéricas realizadas con el código de elementos finitos CODE_BRIGHT. Una célula termo-hidráulica fue especialmente diseñada para observar el comportamiento THM de la roca en condición drenada y no drenada, a través de pulsos de calor. Parámetros térmicos e hidráulicos de la roca fueron determinados por retro análisis a través de simulaciones numéricas realizadas con CODE_BRIGHT.

Desde el punto de vista mecánico, un modelo constitutivo ha sido formulado en 3D e implementado en CODE_BRIGHT con el objetivo de reproducir el comportamiento mecánico anisótropo y rotura frágil de las rocas arcillosas. El modelo es formulado en un marco viscoplástico y considera la resistencia y deformabilidad de la matriz y de las juntas. El criterio de falla de la matriz y de las juntas es definido por superficies de fluencias hiperbólicas en el espacio de tensiones p-J y $\tau-\sigma$, respectivamente. El comportamiento frágil de las rocas arcillosas es simulado por un reblandecimiento isótropo y cinemático definido en términos de trabajo de deformación plástico. El modelo constitutivo ha sido calibrado mediante ensayos triaxiales de laboratorio realizados en especimenes con diferentes ángulos de buzamiento. El modelo constitutivo anisótropo ha sido aplicado a la simulación numérica en 3D de un ensayo de calentamiento in-situ. Una simulación numérica en 3D de un ensayo de ventilación in-situ realizado en un micro-túnel sin recubrimiento ha sido realizada para reproducir el brusco cambio de permeabilidad por efectos de secado de la roca. En este caso, un modelo hidráulico que considera la apertura de las juntas por efectos de secado ha sido implementado para reproducir los cambios de permeabilidad en excavaciones subterráneas.

AGRADECIMIENTOS

En primer lugar quiero expresar mis agradecimientos a los profesores Eduardo Alonso y Antonio Lloret por la dirección de esta tesis. Haber trabajado con ellos ha sido para mí, una experiencia sumamente grata y enriquecedora.

Agradezco también a los profesores del Departamento de Ingeniería del Terreno que han contribuido en el desarrollo de esta tesis. A Sebastián Olivella y Jean Vaunat por la inestimable ayuda y paciencia en mis primeros pasos con CODE_BRIGHT. A Enrique Romero que me transmitió sus conocimientos y experiencias en técnicas experimentales de la mecánica de suelos y rocas.

A mi profesor y amigo Francisco Zabala, profesor del Instituto de Investigaciones Antisísmicas de la Universidad Nacional de San Juan, por la confianza en mí depositada para iniciarme en el ámbito científico y emprender mis estudios de doctorado.

Quiero agradecer la ayuda recibida por el personal del laboratorio, José y Fernando. Al Señor Tomás Pérez por su inestimable colaboración en el desarrollo y construcción de equipos de laboratorio utilizados en esta tesis. Aprovecho estas líneas para agradecer también al personal del departamento: Eva, Mari Carmen, Oscar, Maria del Mar, Albert y Mari Carmen (CIMNE); por realizar las diversas gestiones siempre con un trato cordial y amable.

Quiero agradecer el apoyo económico recibido durante estos años a ENRESA, que a través de CIMNE, permitieron la elaboración de esta tesis.

A mis compañeros y amigos de despacho que hicieron una convivencia tan agradable: Bety, Olga, Kanta, Fermín, Claudia, Alexandra, Carlos, Joseph María; y del laboratorio: Cristian, Ernesto, Rodrigo, Iván y Alejandro.

A mis amigos con quienes, mi esposa y yo, compartimos tantos buenos momentos y nos ayudaron a superar momentos difíciles: Marcelo, Lichi, Alejandro, Mabel, Carlos, Laura, Adolfo, Myriam, Sergio, Abel, Fátima y tantos otros…., mil gracias.

De manera muy especial, a mi esposa María Eugenia, por acompañarme en esta aventura, por su apoyo incondicional en todo momento, por tantas alegrías compartidas, por soportar con entereza momentos difíciles, por estar a mi lado.

Finalmente, quiero agradecer a mi familia que se quedó en Argentina. A mi madre, María Hortensia Yanzón, por sus dulces palabras de ánimo y su paciente espera. A mis hermanos, Eduardo y Federico, por el continuo apoyo moral. A mis suegros, Facundo y Norma, por el apoyo incondicional y por el afecto recibido.

TABLE OF CONTENTS

CHAPTER I 1

INTRODUCTION 1
1.1 BACKGROUND 1
1.2 OBJECTIVES 4
1.3 THESIS LAYOUT 5

CHAPTER II 7

T-H-M FORMULATION 7
2.1 INTRODUCTION 7
2.2 FORMULATION FEATURES 8
2.3 GOVERNING EQUATIONS 11
  2.3.1 Balance Equations 11
  2.3.2 Mass balance of solid 12
  2.3.3 Mass balance of water 13
  2.3.4 Mass balance of air 14
  2.3.5 Momentum balance for the medium 14
  2.3.6 Internal energy balance for the medium 15
  2.3.7 Constitutive equations 16
  2.3.8 Equilibrium restrictions 19
  2.3.9 Thermoelastoplastic constitutive model 20
  2.3.10 Damage-elastoplastic constitutive model 22

CHAPTER III 27

OPALINUS CLAY 27
ROCK LABORATORY CHARACTERIZATION 27
3.1 INTRODUCTION 27
3.2 OPALINUS CLAY MINERALOGY 27
3.3 INITIAL DETERMINATIONS 30
3.4 WATER RETENTION CURVE 31
  3.4.1 Water retention curve at constant volume 38
  3.4.2 Suction – swelling pressure relationship 42
3.5 HYDRAULIC CONDUCTIVITY 43
  3.5.1 Permeameters description 44
  3.5.2 Infiltration test 1 45
  3.5.3 Infiltration test 2 47
  3.5.4 Drying test 53
3.6 MERCURY INTRUSION POROSIMETRY AND ELECTRONIC MICROSCOPY 56
  3.6.1 Water retention curve 61
  3.6.2 Hydraulic conductivity 63
  3.6.3 Scanning electron microscopy 66
3.7 UNIAXIAL COMPRESSION TEST 66

CHAPTER IV 71

T-H-M FIELD AND SMALL SCALE EXPERIMENTS 71
HE EXPERIMENT AND PULSE HEATING TEST 71
4.1 INTRODUCTION 71
4.2 DESCRIPTION OF HEATING EXPERIMENT (HE) 71
4.3 THERMAL EXPANSION TEST 79
4.4 PULSE HEATING TEST 84
  4.4.1 Description of the equipment 84
  4.4.2 Experimental results 91

CHAPTER V 119

T-H-M AXISYMMETRIC ANALYSIS WITH ISOTROPIC CONSTITUTIVE MODELS 119
5.1 Introduction 119
5.2 Modeling of the HE experiment 119
5.2.1 Geometry of the HE experiment 120
5.2.2 Initial and boundaries conditions 122
5.2.3 Host rock parameters 124
5.2.4 Results of the analysis 127
5.3 Modeling of the laboratory pulse heating test 149
5.3.1 Geometry of the cell 149
5.3.2 Initial and Boundary conditions 150
5.3.3 Material parameters 151
5.3.4 Analysis of numerical simulations 153

CHAPTER VI 167

AN ANISOTROPIC CONSTITUTIVE MODEL FOR CLAY SHALES 167
6.1 Formulation of constitutive model 167
6.1.1 Elastic behaviour of transversely isotropic rocks 168
6.1.2 Viscoplastic flow rule 173
6.1.3 Yield function 174
6.1.4 Softening law 177
6.2 Programming in CODE_BRIGTH 181
6.3 Calibration of the constitutive model 183

CHAPTER VII 195

3D T-H-M MODELLING OF HE AND VE EXPERIMENTS INCLUDING ROCK ANISOTROPY 195
7.1 Introduction 195
7.2 3D modelling of HE experiment 195
7.2.1 Initial and boundary conditions 197
7.2.2 Opalinus Clay parameters 198
7.2.3 Analysis of results 199
7.3 3D Modelling of VE experiment 209
7.3.1 Drying and wetting influence in hydraulic permeability 209
7.3.2 Geometry of the VE experiment 210
7.3.3 Initial and boundary conditions 211
7.3.4 Analysis of results 212

CHAPTER VIII 221

SUMMARY, CONCLUSIONS AND FUTURE RESEARCH WORKS 221
8.1 Summary and Conclusions 221
8.1.1 Rock laboratory characterization 221
8.1.2 Coupled THM behaviour 222
8.1.3 Anisotropic constitutive modelling 225
8.1.4 Drying and wetting effects in argillaceous rock 226
8.2 Futures research 226

CHAPTER IX 229

REFERENCES 229

APPENDIX 239

A.1 Appendix A 239
A.2 Appendix B 243

INDEX OF FIGURES

FIGURE 2.1: COUPLED THERMO-HYDRAULIC PHENOMENA IN AN UNSATURATED POROUS MEDIUM SUBJECTED TO HEATING AND HYDRATION (GENS AND OLIVELLA, 2001) 8
FIGURE 2.2: SCHEMATIC REPRESENTATION OF AN UNSATURATED POROUS MEDIA 9
FIGURE 2.3: SCHEMATIC REPRESENTATION OF THE ARGILLACEOUS ROCK (VAUNAT & GENS, 2003) 23
FIGURE 2.4: REPRESENTATION OF OPALINUS CLAY MODEL IN A P-Q DIAGRAM (VAUNAT & GENS, 2003). 26
FIGURE 3.1: X-RAY DIFFRACTION OF OPALINUS CLAY POWDER. 29
FIGURE 3.2: TRANSISTOR PSYCHROMETER SENSOR (SOIL MECHANICS INSTRUMENTATION, SMI) USED TO MEASURE THE TOTAL SUCTION IN OPALINUS CLAY ROCK (DIMOS, (1991)) 31
FIGURE 3.3: UPPER VIEW OF THE HE NICHE. LOCATION OF DIFFERENT BOREHOLES 32
FIGURE 3.4: SPECIMENS AND CONTAINERS USED TO EVALUATE THE WATER RETENTION CURVE. 33
FIGURE 3.5: WATER RETENTION CURVE OF OPALINUS CLAY ROCK IN TERMS OF SUCTION-WATER CONTENT IN DRYING AND WETTING PATHS. 36
FIGURE 3.6: WATER RETENTION CURVE OF OPALINUS CLAY ROCK IN TERMS OF SUCTION-DEGREE OF SATURATION IN DRYING AND WETTING PATHS. 37
FIGURE 3.7: MEASURED FINAL VOID RATIO OF THE SPECIMENS 37
FIGURE 3.8: LEFT: ISOCHORIC CELL. RIGHT: DIFFERENT ISOCHORIC CELL COMPONENTS. A- STAINLESS STEEL RING OF 50 MM IN DIAMETER AND 20 MM IN HEIGHT, B- LOWER CAP WITH A POROUS DISC, C- UPPER HEAD WITH POROUS DISC, D- TOP CAP THAT IS THREADED TO THE LOWER CAP, E- STEEL RING TO TIGHTEN THE UPPER HEAD AGAINST THE SPECIMEN AND F- LOAD CELL TO MEASURE THE SWELLING PRESSURE 38
FIGURE 3.9: ISOCHORIC CELL USED TO PERFORM THE WATER RETENTION CURVE AT CONSTANT VOLUME. 39
FIGURE 3.10: WATER RETENTION CURVE IN TERMS OF SUCTION-WATER CONTENT RELATIONSHIP IN THE DRYING PATH FOR SPECIMENS 1 AND 2 MAINTAINED AT A CONSTANT POROSITY N = 0.178 AND N = 0.172, RESPECTIVELY. 41
FIGURE 3.11: WATER RETENTION CURVE IN TERMS OF SUCTION-DEGREE OF SATURATION RELATIONSHIP IN THE DRYING PATH FOR SPECIMENS 1 AND 2 MAINTAINED AT A CONSTANT POROSITY N = 0.178 AND N = 0.172, RESPECTIVELY. 41
FIGURE 3.12: WETTING AND DRAYING PATHS PERFORMED IN OPALINUS CLAY SAMPLE UNDER ISOCHORIC CONDITIONS. 42
FIGURE 3.13: TEMPORAL EVOLUTION OF SWELLING PRESSURE AND WATER CONTENT OF THE SAMPLE UNDERWENT WETTING AND DRAYING PATHS. 43
FIGURE 3.14: SCHEME OF PERMEAMETER BUILT TO PERFORM PERMEABILITY TEST. 44
FIGURE 3.15: SAMPLE PASTED TO THE RING BY MEANS OF EPOXI RESIN 45
FIGURE 3.16: VOLUME OF WATER INFILTRATED IN SAMPLES P1 TO P4 MEASURED IN LABORATORY TEST AND COMPUTED WITH CODE_BRIGHT. 46
FIGURE 3.17: MEASURED AND COMPUTED PROFILES OF DEGREE OF SATURATIONS IN THE SAMPLES P1 TO P3. 47
FIGURE 3.18: TIME EVOLUTION OF WEIGHT OF THE SALT SOLUTION DURING THE DRYING PROCESS OF THE SAMPLE. 48
FIGURE 3.19: VOLUME OF WATER INFILTRATED IN THE SAMPLE MEASURED IN LABORATORY TEST AND CALCULATED USING THREE DIFFERENT VALUES FOR PARAMETER λ. INTRINSIC PERMEABILITY IS THE SAME UNDER SATURATED OR UNSATURATED CONDITIONS. 50
FIGURE 3.20: RELATIVE PERMEABILITY LAWS AND THE ASSOCIATED VALUES OF λ USED IN THE NUMERICAL SIMULATIONS. 51
FIGURE 3.21: WATER VOLUME INFILTRATED IN THE SAMPLE MEASURED IN LABORATORY AND CALCULATED USING DIFFERENT INTRINSIC PERMEABILITY VALUES UNDER UNSATURATED CONDITIONS (T < 26 DAYS) AND UNDER SATURATED CONDITIONS. 51
FIGURE 3.22: DRYING TEST PERFORMED BY AITEMIN (FLORÍA ET AL. 2002) 54
FIGURE 3.23: VALUES MEASURED AND COMPUTED OF WATER MASS EXTRACTED IN THE DRYING TEST. 55
FIGURE 3.24: COMPUTED AND MEASURED WATER CONTENT PROFILES AT DIFFERENT TIMES DURING THE DRYING TEST. 55
FIGURE 3.25: PORES SIZE DISTRIBUTION OF THE OPALINUS CLAY SAMPLES 59
FIGURE 3.26: VOLUME OF MERCURY INTRUDED, NORMALIZED BY DRY WEIGHT OF THE SAMPLES. 59

FIGURE 3.27: CUMULATIVE TOTAL POROSITY OBTAINED IN THE MERCURY INTRUSION POROSIMETRY. 60
FIGURE 3.28: MERCURY DEGREE OF SATURATIONS. 60
FIGURE 3.29: WATER RETENTION CURVE OF OPALINUS CLAY ROCK, EXPRESSED IN TERMS OF WATER CONTENT, OBTAINED WITH MIP. 62
FIGURE 3.30: WATER RETENTION CURVE OF OPALINUS CLAY ROCK, EXPRESSED IN TERMS OF DEGREE OF SATURATION. MIP AND COMPARISON WITH EXPERIMENTAL DETERMINATION 62
FIGURE 3.31: RELATIVE FREQUENCY OF PORES DIAMETERS. 63
FIGURE 3.32: RELATIVE PERMEABILITY LAW OBTAINED BY MEANS OF MERCURY INTRUSION POROSIMETRY. 65
FIGURE 3.33: RELATIVE PERMEABILITY LAW OBTAINED BY BACK ANALYSIS OF INFILTRATION TESTS AND BY MEANS OF FITS WITH LEAST SQUARES METHOD OF MIP. 65
FIGURE 3.34: PHOTOMICROGRAPH OF THE OPALINUS CLAY FABRIC TAKEN WITH A ZOOM OF 500X. 66
FIGURE 3.35: PHOTOMICROGRAPH OF THE OPALINUS CLAY FABRIC TAKEN WITH A ZOOM OF 2000X. 66
FIGURE 3.36: INSTRUMENTATION OF SAMPLES WITH TWO DISPLACEMENT TRANSDUCERS (LVDT) AND TWO STRAIN GAGES IN ORDER TO MEASURE THE LONGITUDINAL STRAIN. RADIAL STRAIN WAS MEASURED USING TWO STRAIN GAGES PLACED HORIZONTALLY. 68
FIGURE 3.37: SAMPLE C3 AFTER THE FAILURE. SAMPLE C3 PRESENTS THE STRATIFICATION PLANES INCLINED BETWEEN 65º AND 70º WITH RESPECT TO THE LONGITUDINAL AXIS. FAILURE OCCURS IN A PLANE INCLINED BETWEEN 40º AND 43º WITH RESPECT TO THE LONGITUDINAL AXIS. 68
FIGURE 3.38: STRESS-STRAIN CURVES OF UNIAXIAL COMPRESSIVE TEST OF SAMPLE C1 69
FIGURE 3.39: STRESS-STRAIN CURVES OF UNIAXIAL COMPRESSIVE TEST OF SAMPLE C2 69
FIGURE 3.40: STRESS-STRAIN CURVES OF UNIAXIAL COMPRESSIVE TEST OF SAMPLE C3 70
FIGURE 4.1: 3D VIEW OF THE MONT TERRI UNDERGROUND ROCK LABORATORY AND THE LOCATION OF THE HEATING EXPERIMENT, HE NICHE (HTTP://WWW.MONT-TERRI.CH). 72
FIGURE 4.2: UPPER VIEW OF THE HE NICHE, (FUENTES-CASTILLANA J.L., ET AL., 2001) 73
FIGURE 4.3: VERTICAL SECTION OF THE BOREHOLE BHE-0. ALL TEST COMPONENTS ARE EMPLACED. 76
FIGURE 4.4: DETAIL OF THE TEST COMPONENTS. 76
FIGURE 4.5: TIME EVOLUTION OF TEMPERATURES MEASURED DURING THE HYDRATION, HEATING AND COOLING PHASES, IN POINTS LOCATED IN THE ROCK. 77
FIGURE 4.6: MEASURED DISTRIBUTION OF TEMPERATURE AS A FUNCTION OF DISTANCE FOR DIFFERENT TIMES DURING THE HEATING PHASE. 77
FIGURE 4.7: TIME EVOLUTION OF PORE WATER PRESSURE IN POINTS LOCATED IN ROCK DURING HYDRATION, HEATING AND COOLING PHASE 78
FIGURE 4.8: MEASURED DISTRIBUTION OF LIQUID PRESSURE AS A FUNCTION OF DISTANCE FOR DIFFERENT TIMES DURING THE HEATING PHASE. 78
FIGURE 4.9: PROFILE OF MEASURED RADIAL DISPLACEMENTS VERSUS DEPTH (GARCIA-SIÑERIZ & REY, 1999-2004). 79
FIGURE 4.10: EQUIPMENT BUILT TO CARRY OUT THE LINEAR THERMAL EXPANSION TEST 81
FIGURE 4.11: TIME EVOLUTION OF TEMPERATURE AND VERTICAL STRAIN DURING HEATING AND COOLING CYCLE. WATER CONTENT W = 5.67% 82
FIGURE 4.12: VERTICAL STRAIN VERSUS TEMPERATURE DURING HEATING AND COOLING CYCLES. WATER CONTENT W = 5.67% 82
FIGURE 4.13: TIME EVOLUTION OF TEMPERATURE AND VERTICAL STRAIN WITH THE TIME DURING HEATING AND COOLING CYCLES. WATER CONTENT W = 2.80%. 83
FIGURE 4.14: VERTICAL STRAIN VERSUS TEMPERATURE DURING HEATING AND COOLING CYCLES. WATER CONTENT W = 2.80% 83
FIGURE 4.15: CELL BUILT TO PERFORM LABORATORY PULSE HEATING TEST. 85
FIGURE 4.16: PORE WATER PRESSURE SENSOR INSTALLATION. 87
FIGURE 4.17: TEMPERATURE SENSOR INSTALLATION. 87
FIGURE 4.18: MINIATURE PORE WATER PRESSURE SENSORS (DRUC, MODEL PDCR 81). 89
FIGURE 4.19: TEMPERATURE SENSOR (THERMOCOUPLE TYPE K WITH WELD POINT). 89
FIGURE 4.20: STRAIN GAGES TO MEASURE THE VERTICAL STRAIN OF THE RING. 89
FIGURE 4.21: STRAIN GAGES TO MEASURE THE CIRCUMFERENTIAL STRAIN OF THE RING. 89
FIGURE 4.22: UPPER LID WITH STRAIN GAGES INSTALLED. 89
FIGURE 4.23: BOTTOM LID WITH THE HEATER ALREADY INSTALLED. 89
FIGURE 4.24: CELL BUILT TO PERFORM THE PULSE HEATING TEST. 90
FIGURE 4.25: CELL AND ITS COMPONENT, DATA ACQUISITION SYSTEM, SIGNALS CONDITIONER MODULES, POWER SUPPLY, WATER VOLUME MEASURE AND SOFTWARE 90
FIGURE 4.26: ROCK SAMPLE OF 68.5 MM IN DIAMETER AND 100 MM HEIGHT PREVIOUSLY TO BE PLACED INTO THE CELL RING. 91

Figure 4.27: Bottom view of the sample already placed into the cell ring. In the center of the sample 6.5 mm diameter hole was drilled to place the heater into the rock which was later filled with silicone oil to avoid occluded air in the heater-rock contact. The separation between vertical fissures is also indicated. 92
Figure 4.28: Time evolution of gas pressure in the inner of tank and both pressure sensor of the cell. 94
Figure 4.29: Gas pressure profile evolution into the sample. 94
Figure 4.30: Record data of gas pressure and time in the inner tank. 95
Figure 4.31: Identification and location of different sensors. 96
Figure 4.32: Time evolution of rock temperature. 97
Figure 4.33: Time evolution of rock pore water pressure. 97
Figure 4.34: Time evolution of swelling pressure developed by the rock. 97
Figure 4.35: Time evolution of temperature measured during the hydration phase (isothermal conditions). 99
Figure 4.36: Time evolution of pore water pressure measured during hydration phase. 99
Figure 4.37: Volume of water infiltrated during the hydration phase. 100
Figure 4.38: Time evolution of water inflow rate measured during hydration phase. 100
Figure 4.39: Water inflow rate as a function of pressure head. A average hydraulic permeability of K = 1.04E-12 m/s (area of sample 4.07E-03 m^2) is derived. 101
Figure 4.40: Time evolution of swelling pressure measured during the hydration phase. 101
Figure 4.41: Heater test (A) performed under drained condition. (Upper): Time evolution of temperature measured into the rock. (Middle): Time evolution of pore water pressure measured in the rock. (Lower): Time evolution of stresses induced by temperature strain measured during the heating phase. 105
Figure 4.42 (Upper): Rate of heating and temperature increments recorded by sensors (T2), (Bottom): Pore water pressure increments recorded by sensor (P_w1) and stress increments recorded by strain gages. 106
Figure 4.43: (Upper): Rate of cooling and temperature decrease recorded by sensor (T2), (Bottom): Pore water pressure increments recorded by sensor (Pw1) and stress decrease recorded by strain gages. 107
Figure 4.44: Water outflow measured during the heating (A). 108
Figure 4.45: Heater test (B) performed under undrained condition. (Upper): Time evolution of temperature measured in the rock. (Middle): Time evolution of pore water pressure measured in the rock. (Lower): Time evolution of stresses measured by strain gages during heating phase. 110
Figure 4.46: Time evolution of water inlet. 112
Figure 4.47: Heating test (C) performed under drained condition. (Upper): Time evolution of temperature measured in the rock. (Middle): Time evolution of pore water pressure measured in the rock. (Lower): Time evolution of stress measured by strain gages during heating phase. 113
Figure 4.48: Comparison of generated pore water pressure in Tests A and C performed at a power of 5.0 W under drained conditions. 114
Figure 4.49: Heating test (D) performed under drained condition. (Upper): Time evolution of temperature measured in the rock. (Middle): Time evolution of pore water pressure measured in the rock. (Lower)Time evolution of stresses measured during heating phase. 116
Figure 4.50: Gas permeability of the rock determined under saturated and unsaturated conditions. 118
Figure 5.1: Axisymmetric finite element mesh used in the model. 121
Figure 5.2: (Left): Geometry of HE niche and borehole BHE-0. (Right): Different components emplaced into the borehole BHE-0. 121
Figure 5.3: (Left): Boundary conditions applied on the niche perimeter at the niche excavation phase. (Right): Boundary conditions applied on the wall of the borehole at the borehole excavation phase. 123
Figure 5.4: (Left): Boundary conditions applied during hydration phase. (Right): Boundary conditions applied to the heater during heating phase. 124
Figure 5.5: Deformation of the HE niche calculated after 420 days of the niche excavation. 128
Figure 5.6: Minor principal stress (MPa) calculated after 420 days of niche excavation. 129
Figure 5.7: Major principal stress (MPa) calculated after 420 days of niche excavation. 129

FIGURE 5.8: HORIZONTAL STRESS (MPA) CALCULATED AFTER 420 DAYS OF NICHE EXCAVATION............130
FIGURE 5.9: VERTICAL STRESS (MPA) CALCULATED AFTER 420 DAYS OF NICHE EXCAVATION. 130
FIGURE 5.10: PLASTIC ZONE DEVELOPED AFTER 420 DAYS OF NICHE EXCAVATION. 131
FIGURE 5.11: DISTRIBUTION OF THE LIQUID PRESSURE (MPA) AROUND OF THE HE NICHE AFTER 420 DAYS. 131
FIGURE 5.12: DEGREE OF SATURATION (SR) AROUND OF THE HE NICHE AFTER 420 DAYS........................132
FIGURE 5.13: DISTRIBUTION OF THE TOTAL RADIAL STRESS (MPA) AROUND OF THE BOREHOLE BHE-0 AFTER 430 DAYS. 133
FIGURE 5.14: DISTRIBUTION OF THE TOTAL CIRCUMFERENTIAL STRESS (MPA) AROUND OF THE BOREHOLE BHE-0 AFTER 430 DAYS. 133
FIGURE 5.15: DISTRIBUTION OF THE LIQUID PRESSURE (MPA) AROUND OF THE BOREHOLE BHE-0 AFTER 430 DAYS. 134
FIGURE 5.16: DEGREE OF SATURATION (SR) AROUND OF THE BOREHOLE BHE-0 AFTER 430 DAYS. 134
FIGURE 5.17: TIME EVOLUTION OF TEMPERATURES COMPUTED AND MEASURED DURING THE HYDRATION, HEATING AND COOLING PHASES, IN POINTS LOCATED IN BENTONITE AND ROCK. 139
FIGURE 5.18: TIME EVOLUTION OF LIQUID PRESSURE IN POINTS LOCATED IN ROCK DURING HYDRATION, HEATING AND COOLING PHASE...139
FIGURE 5.19: TIME EVOLUTION OF THE RADIAL STRESS COMPUTED DURING THE HYDRATION, HEATING AND COOLING PHASES, IN POINTS LOCATED IN ROCK. 140
FIGURE 5.20: TIME EVOLUTION OF THE CIRCUMFERENTIAL STRESS IN POINTS LOCATED IN ROCK DURING HYDRATION, HEATING AND COOLING PHASE. 140
FIGURE 5.21: COMPUTED RADIAL DISPLACEMENTS OF ROCK DURING HYDRATION PHASE, HEATING PHASE AND COOLING PHASE. POINTS LOCATED AT 5.0 M DEPTH AND RADIAL DISTANCES OF 0.15M, 0.65M AND 1.65M. 141
FIGURE 5.22: (LEFT): LIQUID PRESSURE DISTRIBUTION (MPA) AFTER 45 DAYS OF HYDRATION. (RIGHT): DEGREE OF SATURATION ON THE SURROUNDING ROCK AFTER 45 DAYS OF HYDRATION. 141
FIGURE 5.23: TIME EVOLUTION OF THE DEGREE OF SATURATION OF THE BENTONITE DURING THE HYDRATION PHASE...142
FIGURE 5.24: TIME EVOLUTION OF THE DEGREE OF SATURATION IN THE SURROUNDING ROCK DURING THE HYDRATION PHASE...142
FIGURE 5.25: COMPUTED AND MEASURED WATER INLET DURING THE HYDRATION PHASE........................143
FIGURE 5.26: (LEFT): RADIAL STRESS (MPA) DEVELOPED AFTER 980 DAYS OF HYDRATIONS. (RIGHT): CIRCUMFERENTIAL STRESS (MPA) DEVELOPED AFTER 980 DAYS OF HYDRATIONS..........................144
FIGURE 5.27: (LEFT): RADIAL DISPLACEMENTS (M) DEVELOPED BY SWELLING PRESSURE OF BENTONITE DURING HYDRATION PHASE. (RIGHT): PLASTIC ZONE AROUND OF BOREHOLE BHE-0 144
FIGURE 5.28: COMPUTED AND MEASURED DISTRIBUTION OF TEMPERATURE AS A FUNCTION OF DISTANCE FOR DIFFERENT TIMES DURING THE HEATING PHASE. POINTS LOCATED AT 5.0 M DEPTH.................145
FIGURE 5.29: (LEFT): TEMPERATURE FIELD (ºC) DEVELOPED DURING THE HEATING PHASE (T =1050 DAYS). (RIGHT): LIQUID PRESSURE DISTRIBUTION (MPA) DURING THE HEATING PHASE (T = 1050 DAYS)...145
FIGURE 5.30: COMPUTED AND MEASURED DISTRIBUTION OF TEMPERATURE AS A FUNCTION OF DISTANCE FOR DIFFERENT TIMES DURING THE COOLING PHASE. POINTS LOCATED AT 5.0 M DEPTH. 146
FIGURE 5.31: EFFECTIVE STRESS PATH FOLLOWED BY A POINT OF THE ROCK CLOSE TO THE INTERFACE BENTONITE-ROCK (R = 0.18M). 146
FIGURE 5.32: (UPPER): TIME EVOLUTION OF PLASTIC MULTIPLIER COMPUTED AT RADIAL DISTANCES OF 0.16M AND 0.18M. (BOTTOM): TIME EVOLUTION OF THE TENSILE STRENGTH AT RADIAL DISTANCE OF 0.16M AND 0.18M. 147
FIGURE 5.33: PROFILE OF COMPUTED RADIAL DISPLACEMENTS VERSUS DEPTH. 148
FIGURE 5.34: PROFILE OF MEASURED RADIAL DISPLACEMENTS VERSUS DEPTH. 148
FIGURE 5.35: (LEFT): GEOMETRY AND MATERIALS CONSIDERED. (RIGHT): FINITE ELEMENT MESH OF THE CELL. 149
FIGURE 5.36: INITIAL AND BOUNDARY CONDITIONS APPLIED TO NUMERICAL SIMULATIONS OF THE PULSE HEATING TEST...151
FIGURE 5.37: TIME EVOLUTION OF WATER PRESSURE DURING THE HYDRATION PHASE. 153
FIGURE 5.38: TIME EVOLUTION OF WATER INLET MEASURED AND COMPUTED (K = 1.00E-19 M^2).............154
FIGURE 5.39: HEATING TEST (A) PERFORMED UNDER DRAINED CONDITIONS. (UPPER): TIME EVOLUTION OF TEMPERATURE COMPUTED AND MEASURED IN THERMOCOUPLES T2 AND T3. (BOTTOM): TIME EVOLUTION OF PORE WATER PRESSURE COMPUTED AND MEASURED IN WATER PRESSURE SENSOR P_w1. 156
FIGURE 5.40: TEMPERATURE DISTRIBUTION (ºC) AT THE BEGINNING OF HEATING (T =148.77 DAYS). (DEFORMATION X2000)..157

FIGURE 5.41: PORE WATER PRESSURE DISTRIBUTION (MPA) AT THE BEGINNING OF THE HEATING (T = 148.77 DAYS). (DEFORMATION X2000) 157

FIGURE 5.42: RADIAL STRESSES DISTRIBUTION (MPA) AT THE BEGINNING OF HEATING (T = 148.77 DAYS). (DEFORMATION X2000) 157

FIGURE 5.43: VERTICAL STRESSES DISTRIBUTION (MPA) AT THE BEGINNING OF THE HEATING (T = 148.77 DAYS). (DEFORMATION X2000)........ 157

FIGURE 5.44: CIRCUMFERENTIAL STRESS DISTRIBUTION (MPA) AT THE BEGINNING OF HEATING (T = 148.77 DAYS). (DEFORMATION X2000)........ 158

FIGURE 5.45: DAMAGE MULTIPLIER AT THE BEGINNING OF THE HEATING (T = 148.77 DAYS). (DEFORMATION X2000) 158

FIGURE 5.46: RADIAL STRAIN DISTRIBUTION AT THE BEGINNING OF THE HEATING (T = 148.77 DAYS). (DEFORMATION X2000) 158

FIGURE 5.47: VERTICAL STRAIN DISTRIBUTION AT THE BEGINNING OF THE HEATING (T = 148.77 DAYS). (DEFORMATION X2000) 158

FIGURE 5.48: HEATING TEST (B) PERFORMED UNDER UNDRAINED CONDITIONS. (UPPER): TIME EVOLUTION OF TEMPERATURE COMPUTED AND MEASURED IN THERMOCOUPLES T2 AND T3. (BOTTOM): TIME EVOLUTION PORE WATER PRESSURE COMPUTED AND MEASURED IN BOTH PRESSURE SENSORS P_w1 AND P_w2. INTRINSIC PERMEABILITY OF K=5.0E-20 M^2. 160

FIGURE 5.49: HEATING TEST (B) PERFORMED UNDER UNDRAINED CONDITIONS. TIME EVOLUTION OF PORE WATER PRESSURE COMPUTED AND MEASURED IN BOTH PRESSURE SENSORS P_w1 AND P_w2. INTRINSIC PERMEABILITY OF K=2.5E-20 M^2. 161

FIGURE 5.50: HEATING TEST (B) PERFORMED UNDER UNDRAINED CONDITIONS. TIME EVOLUTION OF PORE WATER PRESSURE COMPUTED AND MEASURED IN BOTH PRESSURE SENSORS P_w1 AND P_w2. INTRINSIC PERMEABILITY OF K=1.0E-20 M^2. 161

FIGURE 5.51: HEATING TEST PERFORMED UNDER DRAINED CONDITIONS. (UPPER): TIME EVOLUTION OF TEMPERATURE COMPUTED AND MEASURED IN THERMOCOUPLES T2 AND T3. (BOTTOM): TIME EVOLUTION PORE WATER PRESSURE COMPUTED AND MEASURED IN PRESSURE SENSORS P_w1 AND P_w2. INTRINSIC PERMEABILITY OF K=5.0E-20 M^2. 163

FIGURE 5.52: HEATING TEST (C) PERFORMED UNDER DRAINED CONDITIONS. TIME EVOLUTION OF PORE WATER PRESSURE COMPUTED AND MEASURED IN BOTH PRESSURE SENSORS P_w1 AND P_w2. INTRINSIC PERMEABILITY OF K = 2.5E-20 M^2........ 164

FIGURE 5.53: HEATING TEST (C) PERFORMED UNDER DRAINED CONDITIONS. TIME EVOLUTION OF PORE WATER PRESSURE COMPUTED AND MEASURED IN BOTH PRESSURE SENSORS P_w1 AND P_w2. INTRINSIC PERMEABILITY OF K = 1.0E-20 M^2........ 164

FIGURE 5.54: HEATING TEST (C) PERFORMED UNDER DRAINED CONDITIONS. ANALYSIS OF SENSITIVITY OF ROCK THERMAL CONDUCTIVITY. (UPPER): TIME EVOLUTION OF TEMPERATURE MEASURED AND COMPUTED IN TEMPERATURE SENSOR (T2) WITH ROCK THERMAL CONDUCTIVITY OF λ =1.25, 2.5 AND 5.0 [W M^{-1} K^{-1}]. (BOTTOM): TIME EVOLUTION OF PORE WATER PRESSURE MEASURED AND COMPUTED IN SENSOR (PW 1). INTRINSIC PERMEABILITY OF K = 2.5E-20 M^2 AND LINEAR THERMAL COEFFICIENT EXPANSION βS = 1.0E-05 $ºC^{-1}$. 165

FIGURE 5.55: HEATING TEST (C) PERFORMED UNDER DRAINED CONDITIONS. ANALYSIS OF SENSITIVITY OF ROCK LINEAR THERMAL COEFFICIENT EXPANSION. (UPPER): TIME EVOLUTION OF TEMPERATURE MEASURED AND COMPUTED IN TEMPERATURE SENSOR (T2) WITH ROCK THERMAL CONDUCTIVITY OF λ = 2.5 [W M^{-1} K^{-1}]. (BOTTOM): TIME EVOLUTION OF PORE WATER PRESSURE MEASURED AND COMPUTED IN SENSOR (PW 1) WITH LINEAR THERMAL COEFFICIENT EXPANSION OF β_S = 1.0E-06, 5.0E-06, 1.0E-05 AND 2.0E-05 $ºC^{-1}$ AND INTRINSIC PERMEABILITY OF K = 2.5E-20 M^2........ 166

FIGURE 6.1: CONCEPTUAL MODEL OF ELASTOVISCOPLASTIC MATERIAL. PERZYNA THEORY........ 168

FIGURE 6.2: DEFINITION OF ELASTIC CONSTANTS FOR A CASE OF CROSS-ANISOTROPIC ROCK IN A 3D ELEMENT (WITTKE W., (1990)). 170

FIGURE 6.3: RELATIONSHIP BETWEEN THE GLOBAL COORDINATE SYSTEM AND THE ORIENTATION OF THE ISOTROPIC PLANE........ 171

FIGURE 6.4: CROSS-ANISOTROPIC OPALINUS CLAY ROCK IN THE WALL OF THE EXCAVATION, DURING THE DISMANTLING OF THE HE EXPERIMENT. 171

FIGURE 6.5: HYPERBOLIC YIELD FUNCTION ROUNDED IN THE MERIDIONAL PLANE. 176

FIGURE 6.6: HYPERBOLIC YIELD FUNCTION ROUNDED IN THE OCTAHEDRAL PLANE........ 176

FIGURE 6.7: EVOLUTION OF THE PARAMETERS OF THE YIELD SURFACES AS A FUNCTION OF THE SCALE FUNCTION ¡ERROR! NO SE PUEDEN CREAR OBJETOS MODIFICANDO CÓDIGOS DE CAMPO. FOR DIFFERENT VALUES OF α........ 179

FIGURE 6.8: EVOLUTION OF HYPERBOLIC YIELD SURFACE ADOPTED FOR ROCK MATRIX IN A MERIDIONAL PLANE. (LODE ANGLE θ = -30º). 180

Figure 6.9: Evolution of hyperbolic yield surface adopted for rock matrix in the octahedral plane (mean stress p = 5.0 MPa). 180
Figure 6.10: Evolution of the hyperbolic yield surface adopted for the joints of rock. 181
Figure 6.11: Finite element mesh of the samples tested. (ϕ = 100 mm, h = 250mm) 184
Figure 6.12: Comparison between numerical simulations and triaxial laboratory test for a sample with angle of dip of 0º. (Upper): Stress-strain behaviour, (Bottom): Stress path. Number of iterations: 2650 186
Figure 6.13: Numerical simulations for a sample with angle of dip of 15º. (Upper): Stress-strain behaviour. (Bottom): Stress path. Number of iterations: 305 187
Figure 6.14: Numerical simulations for a sample with angle of dip of 30º. (Upper): Stress-strain behaviour. (Bottom): Stress path. Number of iterations: 520 188
Figure 6.15: Comparison between numerical simulations and triaxial laboratory test for a sample with angle of dip of 45º. (Upper): Stress-strain behaviour. (Bottom): Stress path. Number of iterations: 1490 189
Figure 6.16: Numerical simulations for a sample with angle of dip of 60º. (Upper): Stress-strain behaviour. (Bottom): Stress path. Number of iterations: 215 190
Figure 6.17: Numerical simulations for a sample with angle of dip of 75º. (Upper): Stress-strain behaviour. (Bottom): Stress path. Number of iterations: 310 191
Figure 6.18: Comparison between numerical simulations and triaxial laboratory test for a sample with angle of dip of 90º. (Upper): Stress-strain behaviour. (Bottom): Stress path. Number of iterations: 295 192
Figure 6.19: Stress-strain behaviour of the samples with different angles of dip. 193
Figure 6.20: Variation of strength with the angle of dip. 193
Figure 6.21: Shear strain for samples with different angles of dip. 194
Figure 7.1: 3D finite element mesh used in the model. 196
Figure 7.2: Upper view of the finite element mesh. 196
Figure 7.3: Vertical view of the borehole BHE-0 in 3D finite element mesh. 196
Figure 7.4: Upper view of the finite element mesh of the HE experiment. 202
Figure 7.5: Evolution of temperatures with time in points located in the rock during the excavation, hydration, heating and cooling phases. 203
Figure 7.6: Distribution of temperature field around of the borehole at time 1070 days. 203
Figure 7.7: Evolution of liquid pressure with time in points located in rock during the excavation, hydration, heating and cooling phase. 204
Figure 7.8: Distribution of the liquid pressure around of the borehole at time 1070 days. 204
Figure 7.9: Evolution of the stress state on borehole wall. (Upper): Radial stress. (Middle): Circumferential stress. (Bottom): Vertical stress. 205
Figure 7.10: Evolution of the calculated radial displacement on the borehole wall during the excavation, hydration, heating and cooling phases. 206
Figure 7.11: Evolution of the calculated radial displacement in points (2) and (5) during the excavation, hydration, heating and cooling phases. 206
Figure 7.12: Profile of calculated radial displacements versus depth at the end of heating phase (1535 days) in points (7) and (8). 207
Figure 7.13: Deformation of the borehole at the end of excavation. Isotropic model. 207
Figure 7.14: Deformation of the borehole at the end of excavation. Anisotropic model. 207
Figure 7.15: Deformation of the borehole after 982 days of hydrations. Isotropic model. 208
Figure 7.16: Deformation of the borehole after 982 days of hydrations. Anisotropic model. 208
Figure 7.17: Plastic zone developed in a horizontal section at 5.0 m depth. Isotropic model. 208
Figure 7.18: Plastic zone developed in a horizontal section at 5.0 m depth. Anisotropic model. 208
Figure 7.19: 3D mesh carried out for simulate the VE experiment. 211
Figure 7.20: Frontal view of the VE numerical simulation. 211
Figure 7.21: Pore water pressure distribution at end of forced ventilation phase, time t = 1775 days. 213
Figure 7.22: Distribution of the degree of saturations at end of the forced ventilation phase, time t = 1775 days. 214
Figure 7.23: Distribution of strain work computed end of forced ventilation phase, time t = 1775 days. 214

FIGURE 7.24: (UPPER): TIME EVOLUTION OF DEGREE OF SATURATION COMPUTED WITH β = 4 DURING ALL PHASES OF THE EXPERIMENT AT RADIAL DISTANCES OF R = 0.65 M (WALL OF THE TUNNEL), R = 1.30 M AND R = 1.80 M. (BOTTOM): TIME EVOLUTION OF INTRINSIC PERMEABILITY COMPUTED WITH β = 0 AND β = 4........215
FIGURE 7.25: TIME EVOLUTION OF PORE WATER PRESSURE COMPUTED DURING ALL PHASES OF THE EXPERIMENT AT 1.15 M, 2.05 M AND 2.60 M DEPTH. COMPUTED VALUES WITH β = 0 AND β = 4......216
FIGURE 7.26: PORE WATER PRESSURE SENSORS LOCATIONS IN THE SECTIONS SA1, SA2, SA3 AND SA4. 217
FIGURE 7.27: TIME EVOLUTION OF PORE WATER PRESSURE MEASURED AT 2.10 M DEPTH DURING THE DRYING PHASE. COMPUTED VALUES WITH β = 0 AND β = 4........218
FIGURE 7.28: (UPPER): PROFILE OF DEGREE OF SATURATION- DEPTH COMPUTED IN DRYING PHASE WITH β = 0 AND β = 4. (BOTTOM): PROFILE OF INTRINSIC PERMEABILITY-DEPTH COMPUTED IN DRYING PHASE. 219
FIGURE A.1: CALIBRATION CURVE OF LOAD CELL Nº 12 USED IN ISOCHORIC CELL. 242
FIGURE B.2: CALIBRATIONS CURVES OF THE PORE WATER PRESSURES SENSORS INSTALLED INTO THE HEATER CELL. 243
FIGURE B.3: CALIBRATIONS CURVES OF THE THERMOCOUPLES INSTALLED IN THE HEATER CELL. 244
FIGURE B.4: CALIBRATIONS CURVES OF THE STRAIN GAGES INSTALLED IN THE HEATER CELL........245
FIGURE B.5: CALIBRATIONS CURVES OF THE HEATER INSTALLED INTO THE HEATER CELL........246

INDEX OF TABLES

Table 2.1: Summary of Equations and Variables (Olivella et al., 1994) 10
Table 3.1: Mineralogy of Opalinus clay (Hohner and Bossart, (1998)) 28
Table 3.2: Phases of minerals observed in powder samples of Opalinus Clay by means of X-ray diffraction. 29
Table 3.3: Pore water chemistry of Opalinus Clay (squeezed) (Hohner and Bossart, (1998)) . 29
Table 3.4: Details of the samples from BVE-1 30
Table 3.5: Results of the determination of water content (w) bulk density (ρ), dry density (ρ_D), particle density (ρ_S) and initial suction (s) in samples at different depths. 31
Table 3.6: RH values and their consequent suction for solutions with different NaCl molality, sulphuric acid concentrations and saturated salts solutions. 34
Table 3.7: Parameters of the Van Genuchten model which fit the water retention curve of Opalinus clay in wetting and drying path. 36
Table 3.8: R.H. and suction value imposed in drying paths by means of axis translations and vapor equilibrium techniques. 40
Table 3.9: Hydraulic parameters used in the numerical modeling of test 52
Table 3.10: Hydraulic parameters used in the numerical modeling of infiltration test carried out with two intrinsic permeability values (unsaturated and saturated) and different relative permeability law. 52
Table 3.11: Hydraulic parameters used in the numerical modeling of the drying test. 56
Table 3.12: Total porosity distribution as a function of pore size of samples. 58
Table 3.13: Size, suctions, water contents and degrees of saturation values for test samples C1, C2 and C3. 67
Table 3.14: Determined parameters of deformation and strength of Opalinus clay rock in uniaxial compressive laboratory tests. 70
Table 4.1: Linear thermal expansion coefficient for heating and cooling cycle in samples with different water contents. 81
Table 5.1: Mechanical parameters of Opalinus Clay 125
Table 5.2: Hydraulic parameters of Opalinus Clay 125
Table 5.3: Thermal parameters of Opalinus Clay 126
Table 5.4: Mechanical parameters of FEBEX bentonite 126
Table 5.5: Hydraulic parameters of FEBEX bentonite 126
Table 5.6: Thermal parameters of FEBEX bentonite 127
Table 5.7: Measured injected water into the bentonite. 143
Table 5.8: Boundary conditions applied in the cell 150
Table 5.9: Mechanical parameters of Opalinus Clay 152
Table 5.10: Thermal parameters of Opalinus Clay 152
Table 5.11: Hydraulic parameters of Opalinus Clay 152
Table 6.1: Mechanical parameters of Opalinus Clay 185
Table 7.1: Mechanical parameters of Opalinus Clay 198
Table 7.2: Hydraulic parameters of Opalinus Clay 199
Table 7.3: Thermal parameters of Opalinus Clay 199
Table A.1: Initial state of specimens 239
Table A.2: Initial Wetting 240
Table A.3: Drying path 240
Table A.4: Initial Drying 241
Table A.5: Wetting path 241
Table A.6: Results of tests to determine the water retention curve along the drying path. 242

CHAPTER I

INTRODUCTION

1.1 Background

This thesis deals with the theoretical and experimental analysis of the coupled Thermo-Hydro-Mechanical (THM) behaviour of the argillaceous formations. In particular, the clay shale known as Opalinus Clay, located in Mont Terri (Switzerland) has been analyzed. This argillaceous formation is being considered as a reference host rock for deep geological repositories of high level radioactive waste. The work presented in this Thesis was, in part, developed under the research projects HE "*rock and bentonite thermo-hydro-mechanical (THM) process in the near field*" and VE "*Ventilations Experiment*". Both large scale experiments were performed in the Mont Terri Underground Rock Laboratory, located in the north western Switzerland.

During the last decade the response of the argillaceous formations against to Thermo-Hydro-Mechanical actions began to be analyzed. Some clay formations potentially interesting for deep geological repositories are Boom clay (Mol, Belgium), Callovo-Oxfordiense clay (Bure, France), Opalinus Clay (Mont Terri, Switzerland) *(Astudillo Pastor, 2001)*. The argillaceous formations have an extremely low hydraulic conductivity (1.0E-12 to 1.0E-14 m/sec), which makes them feasible as geologic barriers. The clay shale may experience volumetric changes when they undergo load-unload process, wetting-drying cycles or heating-cooling cycles. These processes produce important volumetric changes which generate degradations in their mechanical characteristics. The degradation process of clay shale is frequently observed in engineering works, such as excavations, foundations and tunneling constructions. The degradations process is often described in empirical form, being necessary to approach it in a scientific and quantitative form *(Alonso and Alcoverro, 2004)*.

The deep geological repository concept is considered as a realistic solution for a definitive repository of high level radioactive waste. The long term safety of this kind of repository is based on the existence of a series of superposed natural and artificial barriers. The natural barrier is constituted by the host rock (geological barriers), whereas the artificial barriers are constituted by the metallic container and the sealing materials, generally bentonite, located around the metallic container *(Horseman and McEwen, 1996)*. Each successive barrier represents an additional restraint to the movement of radionuclides from the waste towards the surface environment. The interaction between barriers need be completely identified and understood in order to predict the long term behaviour of the deep geological repository. Recent contributions in engineered clay barriers have been performed by *Alonso and Alcoverro, (2005); Fuentes-Cantillana, (2005); Villar et al., (2005) and Musso and Romero, (2005)*.

The artificial barrier is composed by a physical barrier (waste container) and the engineered barrier (bentonite). Bentonites are rocks composed of clay minerals of the group of the smectite, whose physical and chemical properties, such as low permeability, high swelling potential, high capacity of water retention, plasticity and mechanical strength makes them ideal to be used as sealing materials *(Astudillo-Pastor, 2001)*.

The geological formations proposed internationally as natural barriers are of three different types: crystalline rocks, argillaceous rocks and salt rocks. The underground laboratories of Stripa (Sweden), Äspö (Sweden), Grimsel (Switzerland), URL (Canada) and Okilouto (Finland) have been built in granite (crystalline rock). The underground laboratories of Mol (Belgium), Mont Terri (Switzerland) and Bure (France) have been built in argillaceous formations. The underground laboratory of Asse (Germany) was built in saline formations. The underground laboratory of Yucca Mountain (USA) was built in volcanic tuff *(Astudillo-Pastor, 2001)*.

When a heat source such as a canister of radioactive waste is buried in a saturated rock, the heat source will cause a temperature increment in the rock. The rock skeleton and the pore water will expand. However, the thermal dilatation coefficient of water is larger than the skeleton coefficient. As a result, pore water pressure will increase. The magnitude of the water pressure depends on the rate of temperature increase and also on a number of rock parameters (stiffness, permeability, porosity). The increase in water pressure may lead, under extreme conditions, to rock fracturing. The risk of fracture is controlled by the mentioned parameters, as well as the boundary conditions of the problem. *Booker & Savvidou, (1985); Ma & Hueckel, (1993)* have analyzed these phenomena regarding the response of saturated soil against temperature changes.

An analytical solution to solve the THM process was developed by *Booker and Savvidou, (1985)* for the fundamental problem of a point heat source buried in a saturated soil. Mixture theory of two interacting thermo-elastic constituents was proposed by *Ma and Hueckel, (1993)*. In this theory, mass transfer between the adsorbed water and bulk water is included to simulate the transformation of adsorbed water into bulk water occurring at elevated temperatures. An increase in permeability of one order of magnitude per 50 ºC of temperature increment, measured by *Pusch (1986),* provides an experimental evidence to support the assumption on the transformation of adsorbed water into bulk water at elevated temperatures. This permeability increment is larger than the permeability increment caused by water viscosity decrease with temperature.

Relevant contributions to coupled Thermo-Hydro-Mechanical process in clayed soils and rocks, have been published by *Baldi et al., (1991); Del Olmo et al., (1996) and Hueckel et al., (1998)*. Other theoretical contributions come from the works of the Universities of Duke and Trento and the Laboratory of Solid Mechanics of Grenoble *(Hueckel et al., 2001)*. Research on expansive clays and soft rocks performed in the Department of Geotechnical Engineering of the UPC have contributed with several works published from the beginning of 1990s. In these publications the concept of double structure was introduced to explain and to model phenomena associated with the mechanical behavior of these materials *(Alonso et al., (1991)*; *Gens & Alonso, (1992); Gens et al., (1993); Alonso et al., (1998); Gens et al., (1999)*; *Vaunat et al., (1999)*; *Alonso et al., (1999)*; *Alonso & Vaunat, (2001)* and *Sánchez, (2004))*. A pioneering development on constitutive models of cemented soils and soft rocks was presented by *Gens and Nova, (1993).* The behavior of some Spanish hard soils and soft rocks and its relation with phenomena of removal in mass has been studied by *Alonso, (2000)*.

The coupled THM formulations and the numerical codes have been widely used in design and analysis of nuclear waste repository *(Olivella et al., (1994)*; *Olivella et al., (1996) and Gatmiri and Delage, (1997))*. Formulations for coupled THM finite elements analysis involving unsaturated geomaterials were developed by *Gens et al., (1998)*. Inclusion of geochemical variables in the analysis, coupled THMG formulations have been applied in the numerical simulations of engineered barriers *(Guimaraes et al., (1999) and Gens et al., (2003))*.

1.2 Objectives

The general objective of this thesis is to advance in the knowledge of the soft rock response against thermo-hydro-mechanical actions. Special interest will be given to the coupling between the different types of phenomena. On the other hand, regarding the analysis of the "in situ" test, the interest is to improve the knowledge of the coupled Thermo-Hydro-Mechanic (THM) processes developed in the argillaceous rock "Opalinus Clay" and in the blocks of bentonite, when these materials are heated. Special emphasis was directed to study the interaction between the bentonite and the rock.

The specific objectives of this thesis are the following:

a- Formulation of a constitutive model for rock with transverse anisotropy and its implementation in CODE_BRIGHT.

b- Obtain thermal, hydraulic and mechanical parameters of the Opalinus Clay rock by means of laboratory tests. Laboratory tests are expected to:

- Evaluate the suction and temperature effects in the deformability and strength of the rock.
- Evaluate the behaviour of the rock against wetting and drying cycles
- Evaluate the behaviour of rock against heating and cooling cycles

c- Reproduce the “in-situ” heating test (HE) and laboratory heating test by means of numerical simulations performed with CODE_BRIGHT, using the constitutive model developed in order to explain the temperatures fields and pore water pressure distributions measured in the rock.

1.3 Thesis layout

The Thesis is organized in nine Chapters and two Appendices. A common list of the quoted references is presented in the Chapter IX. The contents of each Chapter are summarized as follows:

- Chapter I introduces the motivations and objectives of this Thesis.
- Chapter II describes the general formulation used to simulate the coupled THM process in porous media.
- Chapter III presents the results of laboratory tests carried out for the characterization of the Opalinus Clay rock.
- Chapter IV describes the THM behaviour of the Opalinus Clay rock measured in a large scale Heating Experiment (HE) and in a laboratory heating test.
- Chapter V presents the results of numerical simulations of the “in situ” Heating Experiment and laboratory heating experiment performed in an axisymmetric model with an isotropic constitutive model.
- Chapter VI introduces a new mechanical constitutive model formulated in order to reproduce the anisotropic behaviour of the argillaceous rocks.
- Chapter VII presents the 3D numerical simulation of the HE experiment and VE experiments in order to consider the anisotropic behaviour of rock and the drying effects in the argillaceous rock.
- Chapter VIII collects the main conclusions obtained in this thesis and suggests areas for further research.
- Chapter IX presents the list quoted references

CHAPTER II

T-H-M FORMULATION

2.1 Introduction

In this chapter, a fully coupled THM formulation in the context of continuum theory for porous media proposed by *Olivella et al., (1994)* and its implementation in finite element code CODE_BRIGHT *(Olivella et al., 1996)* will be introduced. The code is able to solve non-saturated multiphase flow under non-isothermal conditions.

The relevant coupled phenomena which occur in porous multiphase materials will be briefly described. It can be stated that in most cases the main mechanism for heat transport is heat conduction. Heat conduction responds to gradients of temperature *(**T**)*. Additional heat transfer will be performed by advection due to the movement of the three phases: solid, liquid and gas. The latent heat inherent to phase changes may also have significant thermal effects *(Gens and Olivella, 2001).*

The advective flows of liquid and gas are the main hydraulic phenomena which occur in porous multiphase materials. These flows are controlled uniquely by liquid pressure *($\boldsymbol{P_l}$)* and gas pressures *($\boldsymbol{P_g}$)*. Liquid and gas pressures are used rather than water and air pressures. This is accordance with the assumption that each phase may contain more than one species. As more than one species may be present in the fluid phases, non-advective flows are potentially significant (diffusion). The most important one is the diffusion of water vapour in the gas phase, especially in non-isothermal situations. Vapour diffusion is controlled by gradients of vapour concentration. The same consideration can be made for dissolved air diffusion in the liquid phase, but its importance is generally less than water vapour diffusion *(Gens and Olivella, 2001).*

The mechanical behavior of unsaturated porous media will be associated with the usual stress-strain relationship and additional contributions from changes in suction (matric and osmotic) and changes in temperature *(Gens and Olivella, 2001)*.

The transport phenomena mentioned above are strongly coupled and they must be considered as parts of a single interconnected system. Figure 2.1 shows the thermal and hydraulic interaction in an unsaturated porous media subjected to hydration from one end and to heating from the other end. The mechanical phenomena have not been added in the figure in order to clarify the picture.

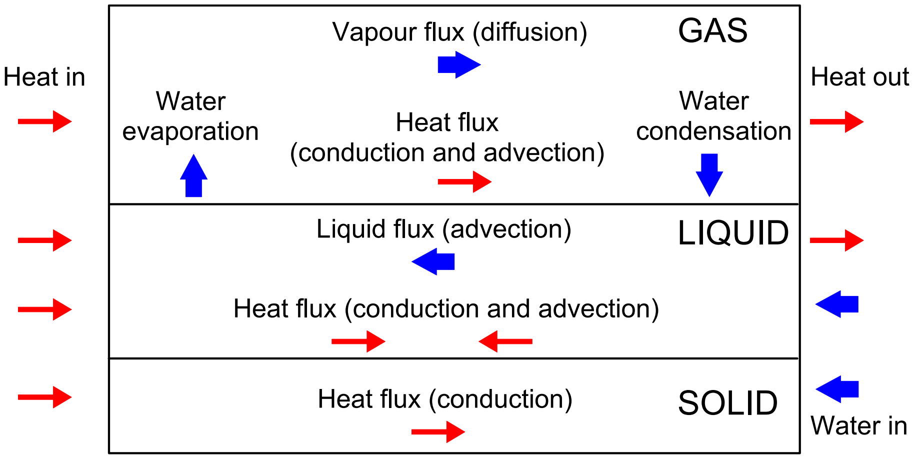

Figure 2.1: Coupled thermo-hydraulic phenomena in an unsaturated porous medium subjected to heating and hydration (Gens and Olivella, 2001)

2.2 Formulation Features

An unsaturated porous medium composed by solid grains, water and gas is shown in schematic form in Figure 2.2. The problem is formulated under a multiphase and multispecies approach. Thermal, hydraulic and mechanical aspects are considered and the coupling between them in all possible directions is taken into account.

Three phases are considered: the solid phase (*s*) is constituted by the mineral, the liquid phase (*l*) is constituted by water and air dissolved; and the gas phase (*g*) is formed by a mixture of dry air and water vapor. Three species are considered, solid (*s*) where the mineral is coincident with solid phase, water (*w*) as liquid or evaporated in the gas phase and air (*a*) constituted by dry air, either in gas phase or dissolved in the liquid phase.

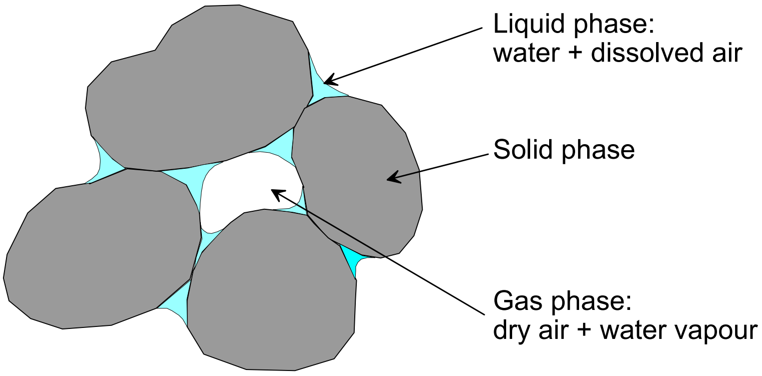

Figure 2.2: Schematic representation of an unsaturated porous media

The following assumptions and aspects are taken into account in the formulation of the problem:

- Dry air is considered a single species and it is the main component of the gaseous phase. Henry's law is used to express equilibrium of dissolved air.
- Thermal equilibrium between phases is assumed. This means that the three phases are at the same temperature
- Vapour concentration is in equilibrium with the liquid phase. The psychometric law expresses its concentration.
- State variables (unknowns) are: solid displacements, $\mathbf{u}$ (three spatial directions); liquid pressure, P_l; gas pressure, P_g; and temperature, T.
- Balance of momentum for the medium as a whole is reduced to the equation of stress equilibrium together with a mechanical constitutive model to relate stresses with strains. Strains are defined in terms of displacements.
- Small strains and small strain rates are assumed for solid deformation.
- Balance of momentum for dissolved species and for fluid phases are reduced to constitutive equations (Fick's law and Darcy's law).
- Physical parameters in constitutive laws are function of pressure and temperature. For example: concentration of vapour under planar surface (in psychometric law), surface tension (in retention curve), dynamic viscosity (in Darcy's law), strongly depend on temperature.

The formulation proposed by *Olivella et al., (1994) and Olivella et al., (1996)* has been widely validated and employed with useful results in many THM applications *(Olivella, (1995); Olivella et al., (1996); Alonso & Alcoverro, (1999); Sanchez, (2004); FEBEX project, Mont Terri project, among others)*. Table 2.1 summarizes the main equations and variables proposed in the THM formulation.

Table 2.1: Summary of Equations and Variables (Olivella et al., 1994)

Equation Name	**Variable**	
Balance Equations		
Solid mass balance	ϕ	Porosity
Water mass balance	P_l	Liquid Pressure
Air mass balance	P_g	Gas pressure
Energy balance	T	Temperature
Momentum balance	$\dot{\mathbf{u}}$	Solid velocity
Constitutive equations		
Fick's law (Vapour and air)	$\mathbf{i}_g^w$; $\mathbf{i}_l^a$	Non-advective mass flux
Darcy's law (Liquid and gas)	$\mathbf{q}_l$; $\mathbf{q}_g$	Volumetric flux with respect to the solid
Fourier's law	$\mathbf{i}_c$	Non-advective heat flux
Mechanical constitutive law	$\boldsymbol{\sigma}$	Total stress tensor
Liquid density	ρ_l	Liquid density
Gas law	ρ_g	Gas density
Equilibrium restrictions		
Henry's law	ω_l^a	Mass fraction of air in liquid phase
Psychrometric law	ω_g^w	Mass fraction of water in gas phase
Definitions Constrains		
$\dot{\boldsymbol{\varepsilon}} = \frac{1}{2}\left(\nabla\dot{\mathbf{u}} + \nabla\dot{\mathbf{u}}^t\right)$	$\dot{\boldsymbol{\varepsilon}}$	Strain rate tensor

$\omega_l^w + \omega_l^a = 1$	ω_l^w	Mass fraction of liquid phase
$\omega_g^w + \omega_g^a = 1$	ω_g^a	Mass fraction of gas phase
$S_l + S_g = 1$	S_g	Volumetric fraction of pore volume occupied by liquid and gas phases
$\mathbf{i}_l^w + \mathbf{i}_l^a = 0$	$\mathbf{i}_l^w$	Non-advective mass flux of liquid phase
$\mathbf{i}_g^w + \mathbf{i}_g^a = 0$	$\mathbf{i}_g^a$	Non-advective mass flux of gas phase

2.3 Governing Equations

The equations that govern the THM problem can be categorized into four main groups, namely, balance equations, constitutive equations, equilibrium restrictions and definition constraints. Equations for mass balance were established following the compositional approach *(Olivella et al., 1994)*. That is, mass balance is performed for water, air and mineral species instead of using solid, liquid and gas phases. In this way the phase change terms do not appear explicitly, which is useful when equilibrium is assumed. As salt dissolution is not considered in this approach, the mineral species coincide with the solid phase. Equation for balance of energy is established for the medium as a whole. The equation of momentum balance for the porous medium is reduced to that of stress equilibrium (*Olivella et al., 1996*).

2.3.1 Balance Equations

The macroscopic balance of any thermodynamic property ψ (per unit mass) in a continuum can be expressed by equation (2.1) *(Olivella et al., 1994)*:

$$\frac{\partial}{\partial t}(\rho\psi) + \nabla \cdot (\mathbf{j}_\psi) - f^\psi = 0 \qquad \text{Eq 2.1}$$

where ρ is the mass density of the species containing ψ. $\mathbf{j}_\psi$ is the total flux of ψ with respect to the fixed reference system and f^ψ is the rate of production/removal of ψ per unit of volume. The total flux $\mathbf{j}_\psi$ may be decomposed into two components: an advective (phase motion) and a non advective (motion of the species inside the phase), see equation (2.2).

$$\mathbf{j}_{\psi} = \rho\psi\mathbf{v}_{\psi} + \mathbf{i}_{\psi} \qquad \text{Eq 2.2}$$

where $\mathbf{v}_{\psi}$ is the mean velocity of mass and $\mathbf{i}_{\psi}$ is the non advective flux of ψ.

Volumetric mass of a species $i(s,w,a)$ in a phase $\alpha(s,l,g)$, θ_{α}^{i}, is the product of the mass fraction of that species ω_{α}^{i} and the bulk density of the phase ρ_{α}, see equation (2.3).

$$\theta_{\alpha}^{i} = \omega_{\alpha}^{i} \cdot \rho_{\alpha} \qquad \text{Eq 2.3}$$

2.3.2 Mass balance of solid

The mass balance of solid present in the medium is written in equation (2.4) *(Olivella et al., (1994)*; *CODE_BRIGHT user's guide, 2004)*, as follows:

$$\frac{\partial}{\partial t}\left(\theta_{s}\left(1-\phi\right)\right)+\nabla\cdot\left(\mathbf{j}_{s}\right)=0 \qquad \text{Eq 2.4}$$

where θ_{s} is the mass of solid per unit volume of solid, ϕ the porosity and $\mathbf{j}_{s}$ is the flux of solid.

A more convenient form of the balance equations is obtained considering the definition of material derivate with respect to the solid velocity given in equation (2.5):

$$\frac{D\left(\circ\right)}{Dt}=\frac{\partial\left(\circ\right)}{\partial t}+\dot{\mathbf{u}}\nabla\left(\circ\right) \qquad \text{Eq 2.5}$$

Using the previous definition, the solid mass balance (equation (2.4)) is expressed in equation 2.6 as follows:

$$\frac{D_{s}\phi}{Dt}=\frac{1}{\theta_{s}}\left(\left(1-\phi\right)\frac{D_{s}\theta_{s}}{Dt}\right)+(1-\phi)\nabla\cdot\frac{d\mathbf{u}}{dt} \qquad \text{Eq 2.6}$$

Equation (2.6) expresses the variation of porosity caused by volumetric deformation and solid density variation.

2.3.3 Mass balance of water

Water is present in liquid an gas phases. The total mass of water per unit of volume in the porous medium is expressed in equation (2.7) as follow:

$$\frac{\text{Mass Water}}{\text{Total Volume}} = \left(\theta_l^w S_l \phi + \theta_g^w S_g \phi\right) \qquad \text{Eq 2.7}$$

where θ_l^w, θ_g^w are the masses of water per unit of volume in liquid and gas phases, respectively. S_l, S_g are the volumetric fraction of pore volume occupied by the (*l*, *g*) phases, respectively.

The total mass balance of water is expressed in equation (2.8) as:

$$\frac{\partial}{\partial t}\left(\theta_l^w S_l \phi + \theta_g^w S_g \phi\right) + \nabla \cdot \left(\mathbf{j}_l^w + \mathbf{j}_g^w\right) = f^w \qquad \text{Eq 2.8}$$

where f^w is an external supply of water. An internal production term is not included because the total mass balance inside the medium is performed.

The water fluxes in each phase can be written as:

$$\mathbf{j}_l^w = \mathbf{i}_l^w + \theta_l^w \mathbf{q}_l + \theta_l^w S_l \phi \dot{\mathbf{u}} = \mathbf{j}'^w_l + \theta_l^w S_l \phi \dot{\mathbf{u}} \qquad \text{Eq 2.9}$$

$$\mathbf{j}_g^w = \mathbf{i}_g^w + \theta_g^w \mathbf{q}_g + \theta_g^w S_g \phi \dot{\mathbf{u}} = \mathbf{j}'^w_g + \theta_g^w S_g \phi \dot{\mathbf{u}} \qquad \text{Eq 2.10}$$

$\mathbf{j}'$ is the flux relative to the solid phase. It corresponds to the total flux minus the advective part caused by solid motion. When solid deformation is negligible, then $\mathbf{j}' = \mathbf{j}$. The relative contribution of each flux term to the total flux is not always the same. For instance, diffusion will become more important if advection is small.

The use of the material derivative, equation (2.5), leads to:

$$\phi \frac{D_s\left(\theta_l^w S_l + \theta_g^w S_g\right)}{Dt} + \left(\theta_l^w S_l + \theta_g^w S_g\right)\frac{D_s \phi}{Dt} + \left(\left(\theta_l^w S_l + \theta_g^w S_g\right)\phi\right)\nabla \cdot \frac{d\mathbf{u}}{dt} + \nabla \cdot \left(\mathbf{j}'^w_l + \mathbf{j}'^w_g\right) = f^w \qquad \text{Eq 2.11}$$

2.3.4 Mass balance of air

Dry air is considered a single species and the gaseous phase is a mixture of air and water vapor. Air is also dissolved in liquid phase. The total air content per unit volume of porous medium is expressed by equation (2.12) as follow:

$$\frac{\text{Mass of air}}{\text{Total Volume}} = \left(\theta_l^a S_l \phi + \theta_g^a S_g \phi\right) \qquad \text{Eq 2.12}$$

where it is assumed that air cannot be present in the solid phase. The mass fluxes of air in each fluid phase are:

$$\mathbf{j}_l^a = \theta_l^a \mathbf{q}_l + \theta_l^a S_l \phi \dot{\mathbf{u}} = \mathbf{j}'^a_l + \theta_l^a S_l \phi \dot{\mathbf{u}} \qquad \text{Eq 2.13}$$

$$\mathbf{j}_g^a = \mathbf{i}_g^a + \theta_g^a \mathbf{q}_g + \theta_g^a S_g \phi \dot{\mathbf{u}} = \mathbf{j}'^a_g + \theta_g^a S_g \phi \dot{\mathbf{u}} \qquad \text{Eq 2.14}$$

where $\mathbf{i}_g^a$ is the non advective air flux in the gas phase; and non advective air flux in the liquid phase is neglected.

Once the other mass balance equations have been written it is straightforward to obtain the mass balance of air taking into account that air is the main component of the gas phase and that it may be also present as dissolved in air in the liquid phase.

$$\phi \frac{D_s\left(\theta_l^a S_l + \theta_g^a S_g\right)}{Dt} + \left(\theta_l^a S_l + \theta_g^a S_g\right)\frac{D_s \phi}{Dt} + \left(\left(\theta_l^a S_l + \theta_g^a S_g\right)\phi\right)\nabla \cdot \frac{d\mathbf{u}}{dt} + \nabla \cdot \left(\mathbf{j}'^a_l + \mathbf{j}'^a_g\right) = f^a \qquad \text{Eq 2.15}$$

2.3.5 Momentum balance for the medium

The balance of momentum for the porous medium reduces to the equilibrium equation for macroscopic total stresses, if the inertial terms are neglected:

$$\nabla \cdot \boldsymbol{\sigma} + \mathbf{b} = \mathbf{0} \qquad \text{Eq 2.16}$$

where $\boldsymbol{\sigma}$ is the stress tensor and $\mathbf{b}$ is the vector of body forces. This assumption is usually accepted because both, velocities and accelerations, are small. Providing an adequate mechanical constitutive model, the equilibrium equation is transformed into a form in terms of the solid velocities, fluid pressure and temperature. A possible decomposition of strains is:

$$\dot{\varepsilon} = \dot{\varepsilon}^e + \dot{\varepsilon}^{vp} + \dot{\varepsilon}^T \qquad \text{Eq 2.17}$$

where $\dot{\varepsilon}^{e}$ is the elastic strain rate due to stress, $\dot{\varepsilon}^{vp}$ is the viscoplastic strain rate and $\dot{\varepsilon}^{T}$ is the strain rate due to temperature changes. $\dot{\varepsilon}$ is the total strain rate which is related with solid velocities through the compatibility conditions that can be written as:

$$\dot{\varepsilon} = \frac{1}{2}\left(\nabla \dot{\mathbf{u}} + \nabla \dot{\mathbf{u}}^{t} \right) \qquad \text{Eq 2.18}$$

2.3.6 Internal energy balance for the medium

Following the proposal of *Olivella et al., (1994*) the balance of energy is expressed in terms of internal energy. In this approach a thermal equilibrium between phases is assumed, the temperature is the same in all phases and only one equation of total energy is required. Adding the internal energy of each phase, the total internal energy per unit volume of porous media can be written as follow:

$$\frac{\text{Total internal energy}}{\text{Total Volume}} = E_s \rho_s \left(1-\phi\right) + E_l \rho_l S_l \phi + E_g \rho_g S_g \phi \qquad \text{Eq 2.19}$$

where E_s, E_l, E_g are the specific internal energy corresponding to each phase, that is, internal energy per unit mass of phase.

The most important processes of energy transfer in a porous medium are conduction, advection (due to mass flux) and phase change *(Bear et al., (1991) in Olivella et al., (1994))*. Heat conduction $\mathbf{i}_c$ is usually computed by means Fourier's law with an effective thermal conductivity coefficient to account for the characteristics of the medium and also including heat dispersion *(Olivella et al., 1994)*.

Using the specific internal energies of the species and the species mass fluxes, the energy fluxes due to phase motion can be written as follow:

$$\mathbf{j}_{E_s} = E_s \rho_s \left(1-\phi\right) \dot{\mathbf{u}} \qquad \text{Eq 2.20}$$

$$\mathbf{j}_{E_l} = \mathbf{j}'^{w}_{l} E^{w}_{l} + \mathbf{j}'^{a}_{l} E^{a}_{l} + E_l \rho_l S_l \phi \dot{\mathbf{u}} = \mathbf{j}'_{E_l} + E_l \rho_l S_l \phi \dot{\mathbf{u}} \qquad \text{Eq 2.21}$$

$$\mathbf{j}_{E_g} = \mathbf{j}'^{w}_{g} E^{w}_{g} + \mathbf{j}'^{a}_{g} E^{a}_{g} + E_g \rho_g S_g \phi \dot{\mathbf{u}} = \mathbf{j}'_{E_g} + E_g \rho_g S_g \phi \dot{\mathbf{u}} \qquad \text{Eq 2.22}$$

where $\mathbf{j}'_{E_l}$ and $\mathbf{j}'_{E_g}$ are the advective fluxes of energy with respect to solid phase.

The equation for internal energy balance for the porous medium is established taking into account the internal energy in each phase E_s, E_l, E_g:

$$\frac{\partial}{\partial t}\left(E_s\rho_s(1-\phi)+E_l\rho_l S_l\phi+E_g\rho_g S_g\phi\right)+\nabla\cdot(\mathbf{i}_c+\mathbf{j}_{E_s}+\mathbf{j}_{E_l}+\mathbf{j}_{E_g})=f^E \qquad \text{Eq 2.23}$$

where $\mathbf{i}_c$ is energy flux due to conduction through the porous medium, the other fluxes $\mathbf{j}_{E_s}, \mathbf{j}_{E_l}, \mathbf{j}_{E_g}$ are advective fluxes of energy caused by mass motions and f^E is an internal/external energy supply.

The use of the material derivative, allows obtaining an equation formally similar to the mass balance of water, as shown in equation 2.24:

$$\phi\frac{D\left(E_l\rho_l S_l+E_g\rho_g S_g\right)}{Dt}+(1-\phi)\frac{D(E_s\rho_s)}{Dt}+E_s\rho_s\nabla\cdot\frac{d\mathbf{u}}{dt}+\nabla\cdot\left(\mathbf{i}_c+\mathbf{j}'_{E_l}+\mathbf{j}'_{E_g}\right)=f^E \qquad \text{Eq 2.24}$$

The reason for the similarity is that both water and internal energy are considered present in the three phases.

2.3.7 Constitutive equations

The constitutive equations establish the link between the independent variables (or unknowns) and the dependent variables. There are several categories of dependent variables depending on the complexity with which they are related to the unknowns. Here, some of the basic constitutive laws, divided in thermal, hydraulic and mechanical are presented. The governing equations are finally written in terms of the unknowns when the constitutive equations are substituted into the balance equations.

2.3.7.1 Thermal constitutive law

Heat conduction is assumed to be governed by Fourier's law:

$$\mathbf{i}_c=-\lambda\nabla T \qquad \text{Eq 2.25}$$

where λ is the thermal conductivity of the porous medium which depends on degree of saturation, porosity and temperature.

2.3.7.2 Hydraulic constitutive law

The advective fluxes of fluid phase will be computed using generalized Darcy's law *(Bear, (1979) in Olivella et al., (1994))* which is expressed in equation 2.26 as follows:

$$\mathbf{q}_\alpha = -\mathbf{K}_\alpha \left(\nabla P_\alpha - \rho_\alpha \mathbf{g} \right) \qquad \alpha = l, g \qquad \text{Eq 2.26}$$

where P_α is the pressure of α phase. $\mathbf{K}_\alpha$ is the permeability tensor of α phase in the porous medium, evaluated as:

$$\mathbf{K}_\alpha = \mathbf{k} \frac{k_{r_\alpha}}{\mu_\alpha} \qquad \alpha = l, g \qquad \text{Eq 2.27}$$

where $\mathbf{k}$ is the intrinsic permeability tensor of the medium, that depends on its pore structure. μ_α is the dynamic viscosity of the α phase in the medium. Finally, k_{r_α} is the relative permeability of the α phase in the porous medium. The Kozeny's model was used to consider the porosity dependence of intrinsic permeability. It is expressed as follows:

$$\mathbf{k} = \mathbf{k}_o \frac{\phi^3}{(1-\phi)^2} \frac{(1-\phi_o)^2}{\phi_o^{\ 3}} \qquad \text{Eq 2.28}$$

where ϕ_o is the reference porosity and $\mathbf{k}_o$ the intrinsic permeability for matrix ϕ_o. In general, the relative permeability can be expressed as a function of the phase degrees of saturation $k_{r_\alpha} = f\left(S_{r_\alpha} \right)$. The relative permeability law of liquid phase may be expressed by means of Van Genuchten model as follow:

$$k_{rl} = \sqrt{S_{rl}} \left(1 - \left(1 - S_{rl}^{\ 1/\lambda} \right)^\lambda \right)^2 \qquad \text{Eq 2.29}$$

where S_{rl} is the degree of saturation of liquid phase and λ is a power parameter. The relative permeability of the gas phase may be expressed by means of a generalized power, as follow:

$$k_{rg} = A S_{rg}^{\ \lambda_g} \qquad \text{Eq 2.30}$$

where A is a constant, S_{rg} the degree of saturation of gas phase and λ_g is a power parameter.

The non advective fluxes of species inside the fluid phase are computed through Fick's law, which expresses them in terms of gradients of mass fraction of species by means of a hydrodynamic dispersion tensor *(Olivella et al., 1994)*:

$$\mathbf{i}_\alpha^i = -\mathbf{D}_\alpha^i \nabla \omega_\alpha^i \qquad i = w, a \qquad \alpha = l, g \qquad \text{Eq 2.31}$$

where $\mathbf{D}_\alpha^i$ is the dispersion tensor and ω_α^i is the mass fraction of i species in α phase.

Finally, the water retention curve establishes the link between the degree of saturation of the medium and the water potential (suction). The water retention curve has been determined in laboratory and may be fitted by means of a Van Genuchten model as equation 2.32 indicate;

$$S_e = \frac{S_l - S_{rl}}{S_{ls} - S_{rl}} = \left(1 + \left(\frac{P_g - P_l}{P}\right)^{\frac{1}{1-\lambda}}\right)^{-\lambda} \qquad P = P_o \frac{\sigma}{\sigma_o} \qquad \text{Eq 2.32}$$

where S_e is effective saturation ($0 \le S_e \le 1$), P is a material parameter, λ is a parameter associated to the shape function for retention curve, S_{rl} is the residual saturation and S_{ls} is the maximum saturation.

2.3.7.3 Mechanical constitutive law

Generally, a THM constitutive equation shows explicitly the contributions of strains, temperature and fluid pressure. It can be expressed as:

$$\dot{\boldsymbol{\sigma}} = \mathbf{D}\dot{\boldsymbol{\varepsilon}} + \mathbf{f}\dot{s} + \mathbf{t}\dot{T} \qquad \text{Eq 2.33}$$

where $\boldsymbol{\sigma}$ is the stress tensor (net or effective stress), $\mathbf{D}$ is the constitutive stiffness matrix, $\boldsymbol{\varepsilon}$ is the tensor, $\mathbf{f}$ is the generic constitutive tensor relating the changes in the fluid pressures and stresses, s is a variable related to the fluid pressures, $\mathbf{t}$ is the constitutive tensor which related stresses and temperatures and T is a variable related to temperature.

Different constitutive models have been implemented in CODE_BRIGHT in order to describe the mechanical behaviour of different materials, see *(Code_Bright user's manual, 2004)*. The mechanical constitutive models available in CODE_BRIGHT are the following: a- Elasticity (with a thermal and pore pressure term); b- Nonlinear elasticity; c- Viscoplasticity for saline materials; d- Viscoplasticity for granular materials; e- Viscoplasticity for unsaturated soils; f- Thermoelastoplastic model for soils and g- Damage-elastoplastic model for argillaceous rocks. These models are able of reproduce only the isotropic behaviour of porous media.

The thermoelastoplastic model (f) has been used to analyze the coupled (THM) behaviour of bentonite buffer in the heater experiment, whereas the damage-elastoplastic model for argillaceous materials (g) has been used to analyze the THM behavior of the Opalinus clay rock in the heater experiment (Chapter V). These mechanical constitutive models will be described in paragraphs 2.3.9 and 2.3.10, respectively.

A new mechanical constitutive model has been developed in order to consider the anisotropic behavior of argillaceous rocks. This constitutive model has been formulated within a viscoplastic framework and implemented in CODE_BRIGHT. This anisotropic constitutive model will be described in chapter VI.

2.3.8 Equilibrium restrictions

Another type of relationships that relate dependent variables with unknowns are the equilibrium restrictions. The species air in liquid phase and water in gas phase are expressed through Henry's law and psychrometric law, respectively. Henry's law expresses a linear relationship between the concentration of air in dissolution and the partial pressure of air in gaseous phase (*Olivella et al., 1994*). It is expressed in equation 2.34

$$\omega_l^a = \frac{P_a}{H}\frac{M_a}{M_w} \qquad \text{Eq 2.34}$$

where $P_a = P_g - P_w$ is the air partial pressure, H is the Henry's constant (10000 MPa), M_a is the molecular mass of dry air and M_w is the molecular mass of water. The psychrometric law expresses the variation of vapor density (or partial vapor pressure) in gas due to the curvature of the surface of the liquid phase and the temperature *(Edlefson and Anderson, (1943) in Olivella et al., (1994))*. The psychrometric law is expressed in the equation 2.35 as follow:

$$\theta_g^w = \rho_g \omega_g^w = \left(\theta_g^w\right)^0 \exp\left(\frac{-\left(P_g - P_l\right) M_w}{RT\rho_l}\right) \qquad \text{Eq 2.35}$$

where $\left(\theta_g^w\right)^0$ is the vapor density in the gaseous phase in contact with planar surface $P_g - P_l = 0$ and depends on temperature. R is the universal gas constant (R = 8.3143 J mol K^{-1}), T is the absolute temperature (ºK) and M_w is the molecular mass of water (M_w = 18.016 g mol^{-1}).

2.3.9 Thermoelastoplastic constitutive model

The THM behaviour of bentonite barrier will be modeled using a thermoelastoplastic model for unsaturated soils *(Gens (1995) in CODE_BRIGHT user's guide, (2004))*, which is explained as follow:

The mechanical constitutive equation takes the incremental general form:

$$d\sigma' = \boldsymbol{D} d\varepsilon + \boldsymbol{h} ds \qquad \text{(Eq 2.36)}$$

This equation is derived from:

$$d\varepsilon = d\varepsilon^e + d\varepsilon^p = (\mathbf{D}^e)^{-1} d\sigma' + \alpha \mathbf{I} ds + \Lambda \frac{\partial G}{\partial \sigma'} \qquad \text{(Eq 2.37)}$$

where $\mathbf{D}^e$ is the elastic stiffness matrix, α is the parameter that consider elastic strain due suction change, I is the identity tensor, Λ the plastic multiplier and G is the plastic potential.

An elasto-plastic constitutive law has been selected. It is based on a generalized yield surface that depends on stresses and suction as well:

$$F = F\left(\sigma', \varepsilon_v^p, s\right) \tag{Eq 2.38}$$

Volumetric strain is defined as:

$$\varepsilon_v = \varepsilon_x + \varepsilon_y + \varepsilon_z \tag{Eq 2.39}$$

and ε_v^p is the plastic volumetric strain.

Using stress invariants this equation depends on:

$$F = F\left(p', J, \theta, \varepsilon_v^p, s\right) \tag{Eq 2.40}$$

where:

$$p' = \frac{1}{3}\left(\sigma'_x + \sigma'_y + \sigma'_z\right) = p - \max(p_g, p_l) \tag{Eq 2.41}$$

$$J = \sqrt{\frac{1}{2} trace(\mathbf{s}:\mathbf{s})} \quad ; \quad \mathbf{s} = \sigma' - p'\mathbf{I} \tag{Eq 2.42}$$

$$\theta = -\frac{1}{3}\sin^{-1}\left(1.5\sqrt{3}\ \det \boldsymbol{s}/J^3\right) \quad \text{(Lode's angle)} \tag{Eq 2.43}$$

where **I** is the identity tensor.

For simplicity, a form of the classical Modified Cam-Clay model is taken as the reference isothermal saturated constitutive law:

$$F = \frac{3J^2}{g_y{}^2} - L_y{}^2\left(p' + p_s\right)\left(p_o - p'\right) = 0 \tag{Eq 2.44}$$

where g_y is a function of the Lode angle and

$$L_y = M / g_y\Big|_{\theta = -\pi/6} \tag{Eq 2.45}$$

The preconsolidation p_o is considered dependent on suction (BBM Model):

$$p_o = p^c \left(\frac{p_o^*(T)}{p^c}\right)^{\frac{\lambda(o) - kio}{\lambda(s) - kio}} \tag{Eq 2.46}$$

$$p_o^*(T) = p_o^* + 2(\alpha_1 \Delta T + \alpha_3 \Delta T \left|\Delta T\right|) \tag{Eq 2.47}$$

$$\lambda(s) = \lambda(o)\left[(1 - r)\exp\left(-\beta s\right) + r\right] \tag{Eq 2.48}$$

$$p_s = p_{s0} + ks\exp(-\rho\Delta T) \quad ; \quad \Delta T = T - T_{ref} \tag{Eq 2.49}$$

Hardening depends on plastic volumetric strain according to:

$$dp_o^* = \frac{1+e}{\lambda(0) - k_{io}} p_o^* d\varepsilon_v^p \tag{Eq 2.50}$$

The plastic potential is taken as:

$$G = \alpha \frac{3J^2}{g_p{}^2} - L_p^2 \left(p' + p_s\right)\left(p_o - p'\right) \tag{Eq 2.51}$$

where g_p is a function of the Lode angle and

$$L_p = M / g_p\big|_{\theta=-\pi/6} \tag{Eq 2.52}$$

α is a non-asociativity parameter.

The variation of stress-stiffness with suction and, especially, the variation of swelling potential with stress and suction have been considered. The elastic components of the model (volumetric strains) are:

$$d\varepsilon_v^e = \frac{k_i(s)}{1+e}\frac{dp'}{p'} + \frac{k_s(p',s)}{1+e}\frac{ds}{s+0.1} + (\alpha_o + 2\alpha_2 \Delta T)dT \tag{Eq 2.53}$$

where:

$$k_i(s) = k_{io}\left(1 + \alpha_i s\right) \tag{Eq 2.54}$$

$$k_s(p',s) = k_{so}\left(1 + \alpha_{sp} \ln p'/p_{ref}\right)\exp\left(\alpha_{ss} s\right) \tag{Eq 2.55}$$

For deviatoric elastic strains, a constant Poisson’s ratio is used.

2.3.10 Damage-elastoplastic constitutive model

The mechanical behaviour of the argillaceous rocks will be modeled by means of the mechanical constitutive law proposed by *Vaunat & Gens, (2003)*. Argillaceous rocks are considered as a composite material, made of a clay matrix interlocked by bonds, see Figure 2.3. Bonding is formed by deposition of cementing agents, such as, silica, carbonates and hydroxides. The brittle behaviour of argillaceous rocks can be due to bonds. Different local values of stresses and strains are experienced by the two materials. The local strains must be compatible with external deformations applied and the local stresses must be in equilibrium with the external load. Bond response is modeled through a damage model proposed by *Carol et al., (2001)*, whereas clay matrix can be represented by any model used to characterize a clay soil.

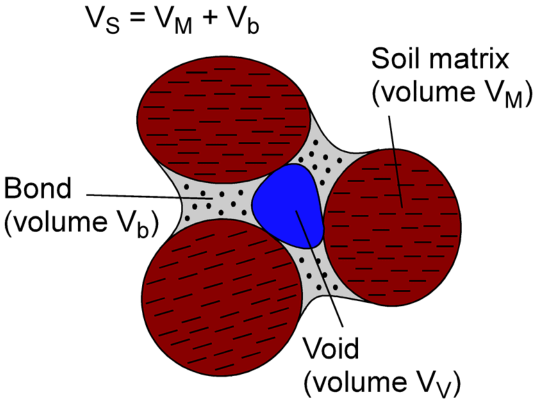

Figure 2.3: Schematic representation of the argillaceous rock (Vaunat & Gens, 2003).

The total volume of solids is defined as: $V_s = V_M + V_b$, where V_M is the matrix volume and V_b is the bond volume. Different volumetric ratios can be defined as:

$$e = \frac{V_V}{V_S} \tag{Eq 2.56}$$

$$e_b = \frac{V_b}{V_S} \tag{Eq 2.57}$$

$$e_N = \frac{(V_b + V_V)}{V_S} \tag{Eq 2.58}$$

where, e is the void ratio, e_b is the volume occupied by bond and e_N is the volume not occupied by the clay particles.

The associated volumetric strains are expressed as follows:

$$d\varepsilon_v = -\frac{de}{(1+e)} \tag{Eq 2.59}$$

$$d\varepsilon_{vb} = -\frac{de_b}{(1+e)} \tag{Eq 2.60}$$

$$d\varepsilon_{vN} = -\frac{de_N}{(1+e)} \tag{Eq 2.61}$$

Because $e_N = e_b + e$ the three volumetric strains are related by (Eq 2.56) as follows:

$$d\varepsilon_{vN} = d\varepsilon_{vb} + d\varepsilon_v \tag{Eq 2.62}$$

Constitutive law for bond

According to scalar damage theory, the response of the material is linear elastic, but over an area that progressively reduces as micro-cracks develops during loading.

Mean and deviatoric bond stresses p_b and q_b are expressed by (Eq 2.63) as follow:

$$\begin{aligned} p_b - p_{b0} &= (1-D)K_{b0}\varepsilon_{vb} = K_{b0}\hat{\varepsilon}_{vb} = K_b\varepsilon_{vb} \\ q_b - q_{b0} &= (1-D)G_{b0}\varepsilon_{qb} = G_{b0}\hat{\varepsilon}_{qb} = G_b\varepsilon_{qb} \end{aligned} \qquad \text{(Eq 2.63)}$$

where K_{b0} and G_{b0} are the bulk and shear moduli of the undamaged material, D is the scalar damage variable. $\hat{\varepsilon}_{vb}$ and $\hat{\varepsilon}_{qb}$ are the strains inside the damaged bond, K_b and G_b are the damaged moduli.

Adopting an alternative damage variable L equal to the natural logarithm of 1/(1 – D) proposed by *Carol et al. (2001),* the terms $\hat{\varepsilon}_{vb}$, $\hat{\varepsilon}_{qb}$, K_b and G_b are expressed in (Eq 2.64) as follow:

$$\begin{aligned} \hat{\varepsilon}_{vb} &= e^{-L}\varepsilon_{vb}, \qquad & \hat{\varepsilon}_{qb} &= e^{-L}\varepsilon_{qb} \\ K_b &= e^{-L}K_{b0} & G_b &= e^{-L}G_{b0} \end{aligned} \qquad \text{(Eq 2.64)}$$

In this model, no damage occurs while the bond stresses remain below the maximum energy (Eq 2.65):

$$u_{b\max} = \left[\frac{(p_b - p_{b0})^2}{2K_b} + \frac{(q_b - q_{b0})^2}{2G_b}\right]_{\max} \qquad \text{(Eq 2.65)}$$

Local equilibrium

Local equilibrium is ensured when work of external stresses during any increment of strain is equal to work of the stresses inside the bonds and the matrix. Local equilibrium is expressed as follow:

$$p d\varepsilon_v + q d\varepsilon_q = p_M d\varepsilon_{vM} + q_M d\varepsilon_{qM} + (p_b - p_{b0}) d\varepsilon_{vb} + (q_b - q_{b0}) d\varepsilon_{qb} \qquad \text{(Eq 2.66)}$$

where p and q are the external stresses, p_M and q_M are the stresses inside the matrix and ε_v, ε_q, ε_{vM}, ε_{qM}, ε_{vb} and ε_{qb} are the strains defined previously. Equation 2.66 can be re-written as:

$$p = p_M\left(1+\frac{d\varepsilon_{vb}}{d\varepsilon_v}\right)+\left(p_b - p_{b0}\right)\frac{d\varepsilon_{vb}}{d\varepsilon_v}$$
$$q = q_M\left(1+\frac{d\varepsilon_{qb}}{d\varepsilon_q}\right)+\left(q_b - q_{b0}\right)\frac{d\varepsilon_{qb}}{d\varepsilon_q} \quad \text{(Eq 2.67)}$$

The key assumption of the model is that $d\varepsilon_{vb}/d\varepsilon_v$ and $d\varepsilon_{qb}/d\varepsilon_q$ are constant and equal to χ_0 in the undamaged state. When micro-cracks develop inside the bonds ($L > 0$), the resisting area decreases and the strains inside the bond $\hat{\varepsilon}_{vb}$ and $\hat{\varepsilon}_{qb}$ are expressed by equation (2.64). Local equilibrium becomes as follows:

$$p = (1+\chi)p_M + \chi(p_b - p_{b0})$$
$$q = (1+\chi)q_M + \chi(q_b - q_{b0}) \quad \text{(Eq 2.68)}$$

where, $\chi = (\varepsilon_{vb}\, e^{-L})/\varepsilon_v = \chi_0\, e^{-L/2}$ (degradation law)

Application to argillaceous rock

Due to the low porosity of argillaceous rocks ($n < 0.13$) this material exhibits a linear elastic response under isotropic loading up to a strain of 2%. During shearing a brittle response is observed at a volumetric strain close to 1%. Envelopes of peak and residual strengths are curved for the range of applied stresses (up to a mean value of 40 MPa). As a consequence, Hoek & Brown criterion in conjunction with a linear elastic law is considered for the destructured matrix. The failure locus of the intact rock takes the following expression:

$$\frac{(q+q_t)^2}{R_c} - \frac{m}{3}(q+q_t) - m(p+p_t) - R_c = 0 \quad \text{(Eq 2.69)}$$

where $R_c = R_{cM}(1+\chi)$. Parameter χ_0 is given by $(R_c - R_{cM})/R_{cM}$, and it is computed as the relative post-peak drop in strength measured in triaxial tests. R_c and R_{cM} are uniaxial compression strengths of the composite material and the clay matrix, respectively. m is the ratio of uniaxial compressive strength divided by tensile strength. It is a parameter that determines the shape of the yield locus.

Young modulus of destructured mudstone E_M is finally determined in order to recover the Young modulus of the intact mudstone E. The Young modulus of intact rock is related to E_M, E_{b0} and χ_0 by:

$$E = (1+\chi_0)E_M(1+\chi_0) + \chi_0 E_{b0}\chi_0 \qquad \text{(Eq 2.70)}$$

where E, E_M and E_{b0} are the Young's modulus of the rock, the clay matrix and the bonds, respectively. The parameter χ is related to the amount of bonding. It takes the value χ_0 when bonds are intact (undamaged rock) and progressively degrades as damage proceeds (measured by the logarithmic damage variable L). The logarithmic damage variable L takes a null value in the undamaged state and an infinite value in the fully damaged state. L appears thus to be simply related to the degradation of bond Young modulus, following the expression $L = \ln(E_0/E)$ where E_0 and E are the undamaged and damaged bond Young's modulus, respectively. A representation of Opalinus clay model in p-q space is shown in Figure 2.4.

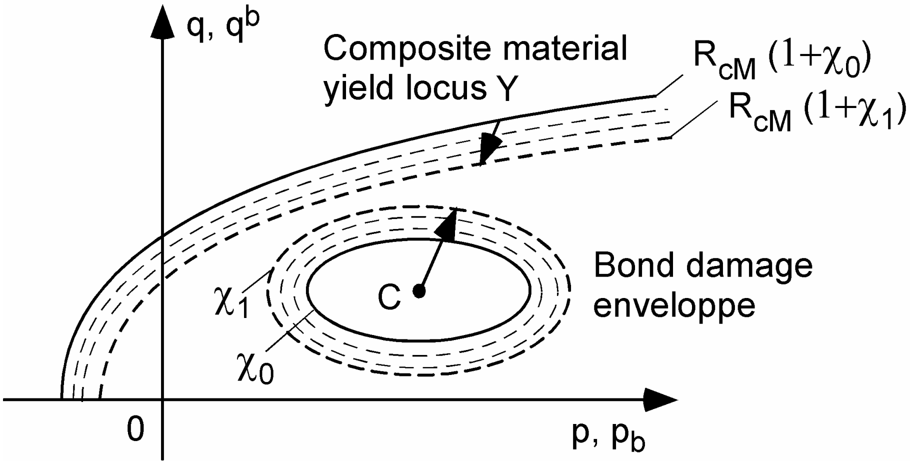

Figure 2.4: Representation of Opalinus clay model in a p-q diagram (Vaunat & Gens, 2003).

CHAPTER III

OPALINUS CLAY
ROCK LABORATORY CHARACTERIZATION

3.1 Introduction

In this chapter the results of laboratory tests performed in order to characterize some aspects of the hydro-mechanical behaviour of Opalinus Clay are presented. Mineralogical analysis by means of X-ray diffraction was carried out in powder of rock. Determinations of the bulk density, dry density, particle density, water content and initial suction were performed on core samples. Water retention curve and saturated hydraulic conductivity were performed in order to acquire parameters for use in the numerical simulations. Unsaturated hydraulic conductivity has been estimated by the back-analysis of infiltration test, using a numerical model and the computer code "CODE_BRIGHT". Mercury intrusion porosimeter (MIP) was performed to determine the pore size distribution (PSD). From (PSD) was possible estimate the water retention curve, saturated hydraulic conductivity and relative permeability of rock. Direct observations of the fabric of Opalinus Clay rock were performed by means of Scanning Electron Microscope (SEM). Finally, compression uniaxial test were performed to obtain deformation and strength parameters of the rock.

3.2 Opalinus Clay Mineralogy

The Opalinus Clay was formed as marine sediment consisting of fine mud particles. It contains between 40 to 80 % clay minerals, 10 % of which are capable of swelling. Its mineralogy consists mainly of sheet silicates (illite, illite-smectite mixed layers, chlorites, kaolinites), framework silicates (albites, K-feldspar), carbonates (calcite, dolomite, ankerite and siderite) and quartz *(Thury and Bossart, (1999)*; *Bossart et al., (2002))*. The mineralogy of Opalinus Clay has been reported by *Hohner and Bossart, (1998)*, see Table 3.1.

A qualitative characterization of the mineralogical composition of Opalinus Clay rock has been performed by means of X-ray diffraction using a powdered sample. It was performed in the X-ray diffraction department of the University of Barcelona. The equipment used was a D-500 Siemens diffractometer. The different phases observed in the powder sample are indicated in Table 3.2. The phase intensity has been classified in heavy, intermediated and weak intensity. The most intense reflections for mineral found in the powder sample of the Opalinus Clay rock are shown in Figure 3.1.

Pore water squeezed from Opalinus Clay rock is highly mineralized, sodium-chlorite water with total dissolved solids of up to 20 g/l. The water contains a significant component of seawater that is millions of years old *(Thury and Bossart, (1999))*. The pore water chemistry is described in Table 3.3 *(Hohner and Bossart, (1998))*.

Table 3.1: Mineralogy of Opalinus clay (Hohner and Bossart, (1998))

Minerals	**[%]**
Quartz	9 - 14
Pyrite	0.3 - 1.7
Carbonates	
Calcite	4 - 25
Siderite	1 - 7
Ankerite	< 1
Clay minerals	
Illite	16.6 - 27
Chlorite	9.2 - 13.2
Kaolinite	16.6 - 25.7
Illite/smectite ML [%]	7.6 - 15.9
Feldspars	
K-feldspars	0 - 2
Albite	0 - 2
Organic carbon	0.3 – 1.3
Others: gypsum, ahydrit and celestin	

Table 3.2: Phases of minerals observed in powder samples of Opalinus Clay by means of X-ray diffraction.

Minerals		**Intensity**
Non clayed minerals	Quartz	Heavy
	Calcite	Heavy
	Pyrite	Weak
Clayed minerals	kaolinite	Intermediate
	Illite	Intermediate
	Chlorite	Intermediate

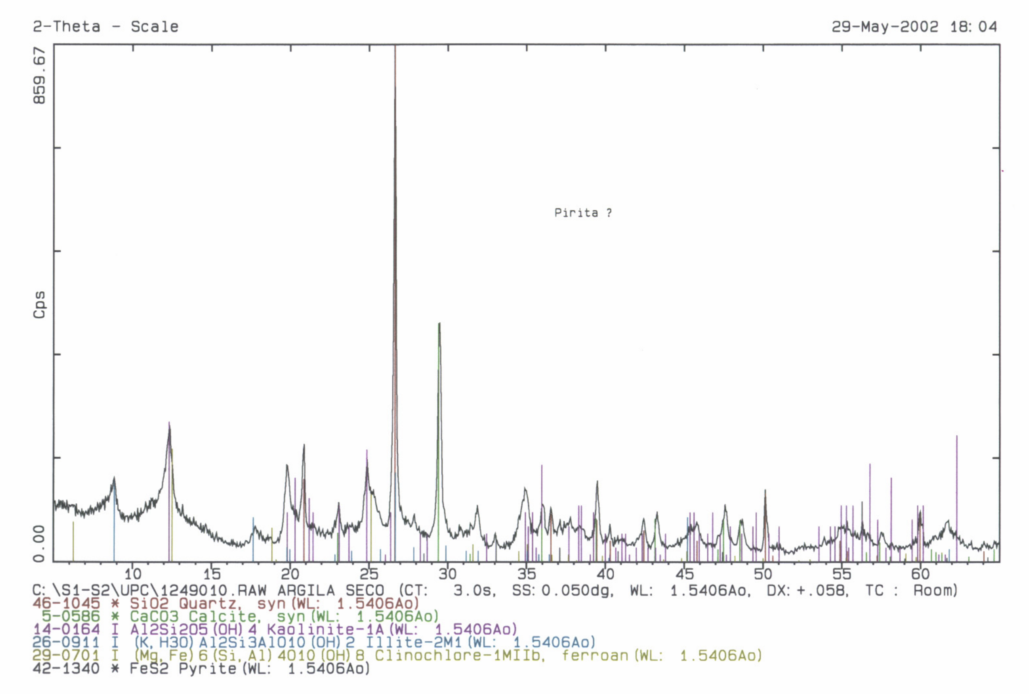

Figure 3.1: X-ray diffraction of Opalinus Clay powder.

Table 3.3: Pore water chemistry of Opalinus Clay (squeezed) (Hohner and Bossart, (1998))

Water type	Na - Cl
Mineralization TDS [mg/l]	18525
Concentration of components [mg/l]	
Na	5320
Ca	789
Mg	502
SO_4	1620
Cl	9970
HCO_3	113
pH	7.54

3.3 Initial determinations

Determinations of water content (w), bulk density (ρ), particle density (ρ_s) and suction (s) were performed in samples of Opalinus Clay rock. Cores of 72 mm in diameter with a total length of 5.6 m were received at the UPC Geotechnical laboratory from the Mont Terri underground laboratory. The samples were obtained from borehole BVE-1, at depth ranging from 7.98 m to 13.62 m. Table 3.4 shows the length and position of each sample.

The weight of each sample was measured using a balance with an accuracy of 1.0E-02 g, and the volume was measured using the mercury immersion method. The particle density was determined with the aid of a Le Chatelier bottle and the test was performed at 25 ºC. The initial suction was measured at 22 ºC with a transistor psychrometer, previously calibrated with salt solutions *(Delage et al., (1998); Romero, (1999); Romero, (2001))*. Figure 3.2 shows a photograph of the psychrometer sensor used to measure the suction *(Dimos, (1991))*. Once water content (w), bulk density (ρ) and particle density (ρ_s) were determined, it was possible to calculate the dry density (ρ_d), void ratio (e), porosity (n) and degree of saturation (S_r). Table 3.5 shows a summary of the values obtained for the different parameters for each sample.

Table 3.4: Details of the samples from BVE-1

Sample	Depth [m]		Length [cm]
	from	to	
BVE-1/3	7.98	8.78	80
BVE-1/4	8.78	9.54	76
BVE-1/5	9.54	10.44	90
BVE-1/6	11.08	11.75	67
BVE-1/7	11.75	12.51	76
BVE-1/8	12.51	13.02	51
BVE-1/9	13.62	13.61	59

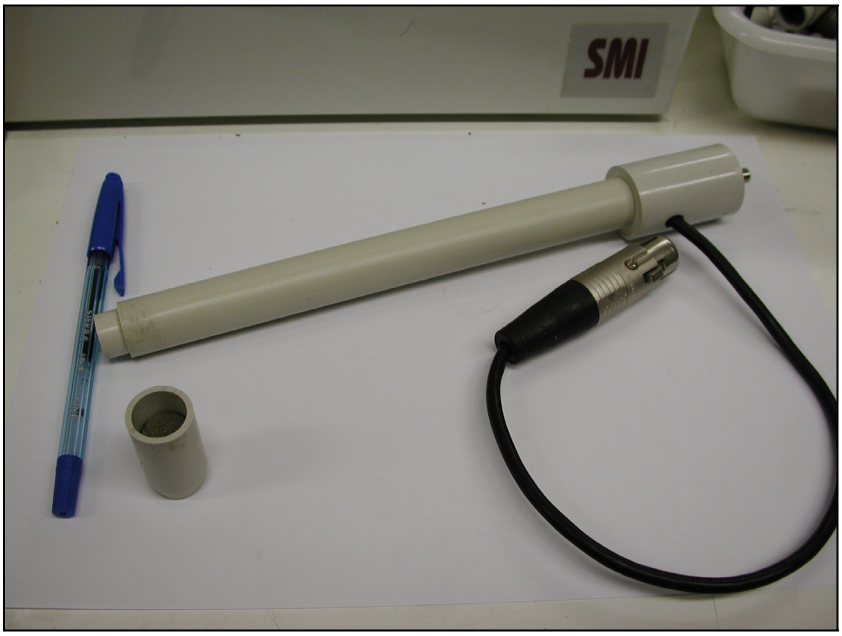

Figure 3.2: Transistor psychrometer sensor (Soil Mechanics Instrumentation, SMI) used to measure the total suction in Opalinus clay rock (Dimos, (1991)).

Table 3.5: Results of the determination of water content (w) bulk density (ρ), dry density (ρ_d), particle density (ρ_s) and initial suction (s) in samples at different depths.

Sample	Depth [m]	***w*** [%]	ρ [g/cm^3]	ρ_d [g/cm^3]	ρ_s [g/cm^3]	***Suction*** [MPa]	***e***	***n***	S_r [%]
BVE-1/3	8.70	6.40	2.41	2.26	2.73	16.77	0.206	0.171	84.73
BVE-1/4	9.50	6.80	2.42	2.26	2.72	13.25	0.200	0.167	92.24
BVE-1/5	10.30	6.80	2.40	2.25	2.73	18.30	0.217	0.179	85.53
BVE-1/6	11.10	7.00	2.40	2.24	2.76	11.67	0.233	0.189	82.93
BVE-1/7	12.50	7.00	2.40	2.24	2.74	12.28	0.222	0.182	86.13
BVE-1/8	13.00	6.60	2.41	2.26	2.74	14.88	0.213	0.175	84.91
BVE-1/9	13.60	7.00	2.41	2.26	2.74	14.25	0.215	0.177	89.25
Average value		6.80	2.41	2.25	2.74	14.49	0.215	0.177	86.533

3.4 Water retention curve

The water retention curve was obtained in drying and wetting paths, by means of the vapor equilibrium technique *(Delage et al., (1998) and Romero, (1999))*. This technique consists in the application of a specified relative humidity in the air of a system thermodynamically closed where the sample is placed. The relative humidity is controlled by means of different saturated or partially saturated salt solutions in direct contact with the air.

Specimens were extracted from the borehole BHE-8 at a depth of 5.4 to 5.8 m. Figure 3.3 shows the locations of different boreholes performed at the HE niche. Specimens showed bedding planes with angles ranging 65º to 70º with respect to the borehole longitudinal axis. Small rock specimens of 25x25x10 mm were equilibrated in hermetic containers at a specified relative humidity (RH) of the air, where the volume change of the specimens was allowed, see Figure 3.4.

The relative humidity was imposed by means of partially saturated solutions of NaCl, saturated salt solutions and sulphuric acid with different concentrations. Table 3.6 shows values of suction generated with NaCl and sulphuric acid solutions with different concentrations, as well as some saturated salt solutions (*Delage et al., (1998), Romero, (1999), UPC-DIT., (1999), Perry, (1992))*.

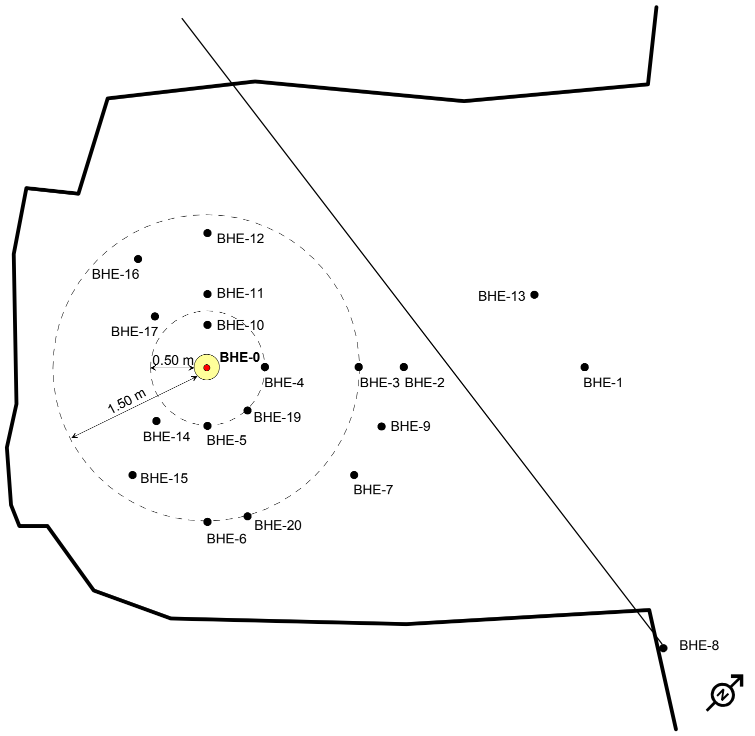

Figure 3.3: Upper view of the HE niche. Location of different boreholes.

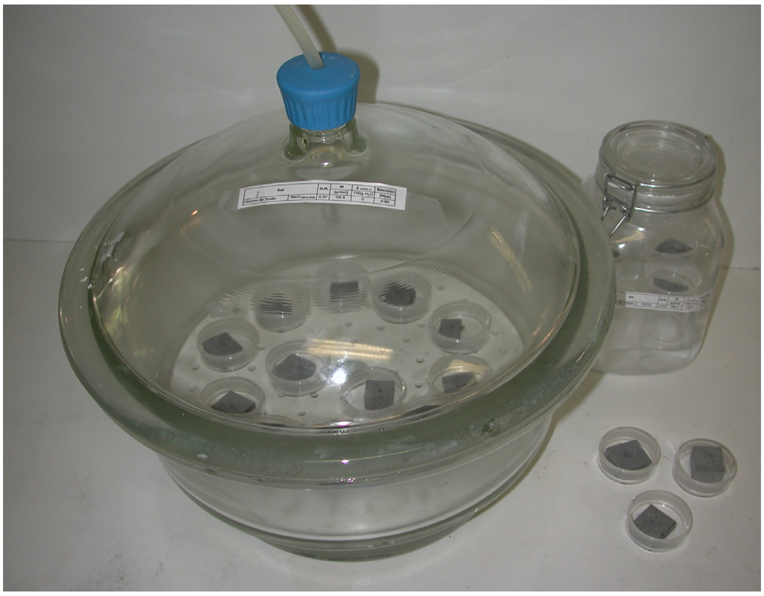

Figure 3.4: Specimens and containers used to evaluate the water retention curve.

The specimens were equilibrated for a period of four weeks in a temperature controlled room at T = 22 ºC. The samples were weighted and measured with an accuracy of 1.0E-04 g and 1.0E-02 mm in order to obtain their water content and volume changes. The measurement of the final dimensions of each specimen allowed the calculation of the final dry density. The average measured value of bulk density, dry density, mineral particle density, water content and degree of saturation of these specimens were equal to 2.39 g/cm^3, 2.24 g/cm^3, 2.70 g/cm^3, 6.67 % and 0.82, respectively.

Relative humidity controlled by NaCl solutions is related to salt concentration through the following expression *(Romero, (1999))*:

$$\begin{aligned} RH &= 1 - 0.035 \cdot m - 1.1421\times10^{-3} \cdot m(m-3) && \text{for m} < 3 \\ RH &= 1 - 0.035 \cdot m - m(m-3)\cdot(1.9772\times10^{-3} - 1.193\times10^{-5} \cdot T) && \text{for m} \geq 3 \end{aligned} \qquad \textbf{(}\text{Eq 3.1)}$$

where: m is molality of solute (mol of NaCl/Kg. of pure water) and T is the temperature in ºC.

When saturated salt solutions were used to control the relative humidity, solutions were prepared using concentrations that were at least 20 % greater than the solubility corresponding to the temperature of the test. When using solutions of sulfuric acid, concentration (C) defined as the percentage in weight of sulfuric acid in the dissolution, is related to relative humidity by means of empirical relations *(UPC-DIT., (1999), Perry, (1992))*.

Table 3.6: RH values and their consequent suction for solutions with different NaCl molality, sulphuric acid concentrations and saturated salts solutions.

Solution	R.H.	Suction [MPa]
NaCl $_{[m = 0.856]}$	0.97	3.8
NaCl $_{[m = 1.369]}$	0.95	6.3
KNO_3	0.94	8
$ZnSO_4$	0.91	13
$(NH_4)_2SO_4$	0.84	25
NaCl $_{[m = 5.647]}$	0.78	34
$NaNO_2$	0.66	57
$Mg(NO_3)_2$	0.54	84
K_2CO_3	0.44	112
$MgCl_2$	0.33	151
H_2O_4S $_{[C = 64\%]}$	0.10	310
H_2O_4S $_{[C = 66\%]}$	0.08	345

m = NaCl solution molality [mol of NaCl/Kg. of pure water], C = sulphuric acid concentration [%]

The relative humidity of the air in the container was related to the total suction in the specimens by means of the Kelvin law (*Delage et al., 1998*), as follows:

$$s = -\frac{R \cdot T}{M_w \cdot g} \ln(RH) \qquad \text{(Eq 3.2)}$$

where s is the total suction, R is the universal gas constant (R = 8.3143 J mol K^{-1}), T is the absolute temperature (T = 295 K at 22 ºC), M_w is the molecular mass of water (M_w = 18.016 g mol^{-1}), g is the gravity acceleration (g = 9.81 m s^{-2}) and RH is the relative humidity of air.

The water retention curve is expressed using the Van Genuchten analytical equations, as follows:

$$S_e = \frac{S_l - S_{rl}}{S_{ls} - S_{rl}} = \left(1 + \left(\frac{P_g - P_l}{P}\right)^{\frac{1}{1-\lambda}}\right)^{-\lambda} \qquad \text{(Eq 3.3)}$$

where S_e is the effective saturation ($0 \le S_e \le 1$), P is a material parameter [MPa], λ the shape function for retention curve, S_{rl} the residual saturation and S_{ls} the maximum saturation. In the high suction range (Sr < 0.2) the Van Genuchten model is not able to adjust correctly these measurements. In order to increase the range of applicability of the original analytical expression, it was necessary to use a modification of the Van Genuchten function *(Huertas et al., 2000)* which is more suitable for higher values of suction (Sr < 0.2), as follows:

$$S_e = \frac{S_l - S_{rl}}{S_{ls} - S_{rl}} = \left(1 + \left(\frac{P_g - P_l}{P}\right)^{\frac{1}{1-\lambda}}\right)^{-\lambda} \left(1 - \frac{P_g - P_l}{P_s}\right)^{\lambda_s} \qquad \text{(Eq 3.4)}$$

where P_s and λ_s are two new material parameters.

The values of the parameters obtained fitting the measured water retention curve are shown in Table 3.7. On the drying path, the specimens were initially wetted in an atmosphere with a RH of 97 %, corresponding suction $s = 3.8\ \text{MPa}$. Under these conditions water content increases and reached a mean value of 8.0 %. Once the specimens reach equilibrium, each specimen was dried at different values of suction in hermetic containers. On other hand, wetting path was performed with specimens which were dried in an atmosphere with a RH of 8.0%, corresponding to a suction $s = 345\ \text{MPa}$, until its water content decreased a mean value of 1%. When the specimens reached the equilibrium, each specimen was wetted applying different suction values in hermetic containers. Figure 3.5 shows the water retention curve in terms of suction-water content following drying and wetting paths. The water retention curve in terms of suction-degree of saturation in drying and wetting paths is shown in Figure 3.6. Values of measured water content and applied suction for both drying and wetting paths are shown in the appendix A (Table A.1 to A.5). The final void ratios obtained after the equilibrium of rock with the relative humidity are shown in Figure 3.7. Despite the dispersion, mainly due to the difficulty to measure the dimensions of the rock specimen, it can be observed a tendency to reduce the pore volume when the suction increases.

Table 3.7: Parameters of the Van Genuchten model which fit the water retention curve of Opalinus clay in wetting and drying path.

Parameter	Drying Path	Wetting Path
P [MPa]	8.12	8.60
λ	0.19	0.32
P_s [MPa]	700	700
λ_s	2.38	0.66

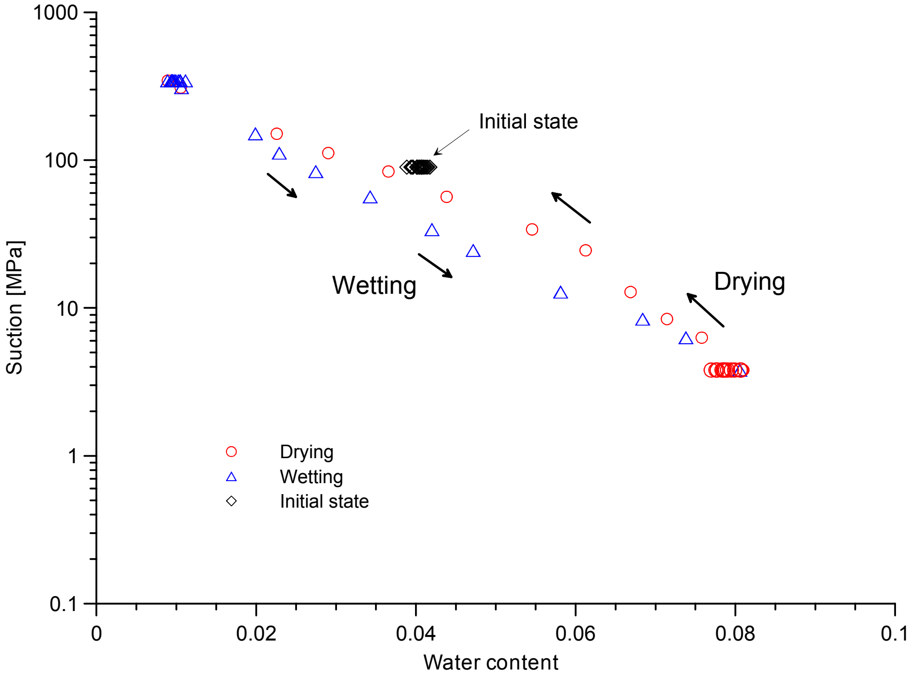

Figure 3.5: Water retention curve of Opalinus Clay rock in terms of suction-water content in drying and wetting paths.

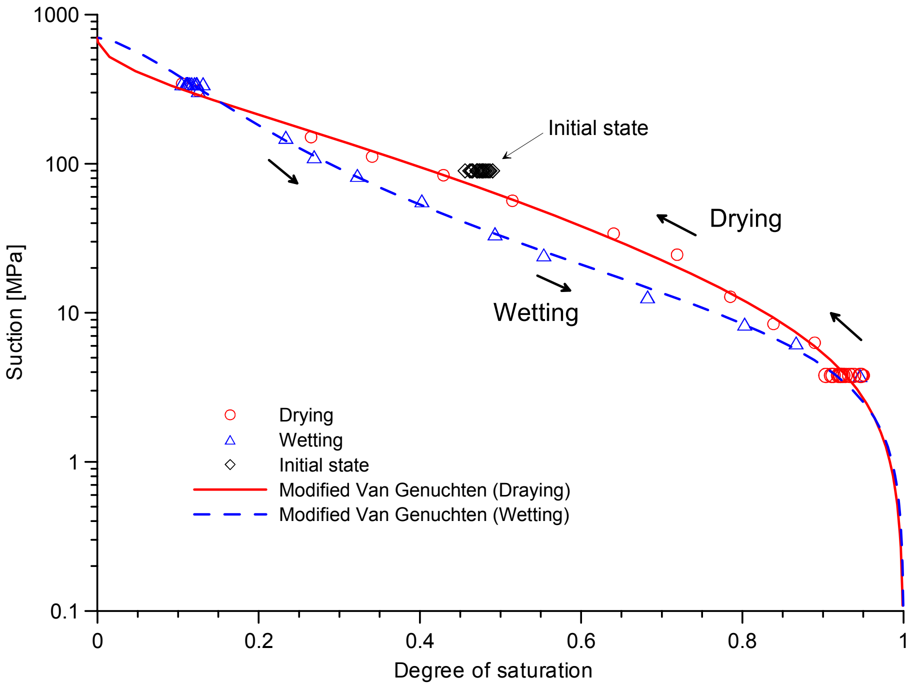

Figure 3.6: Water retention curve of Opalinus Clay rock in terms of suction-degree of saturation in drying and wetting paths.

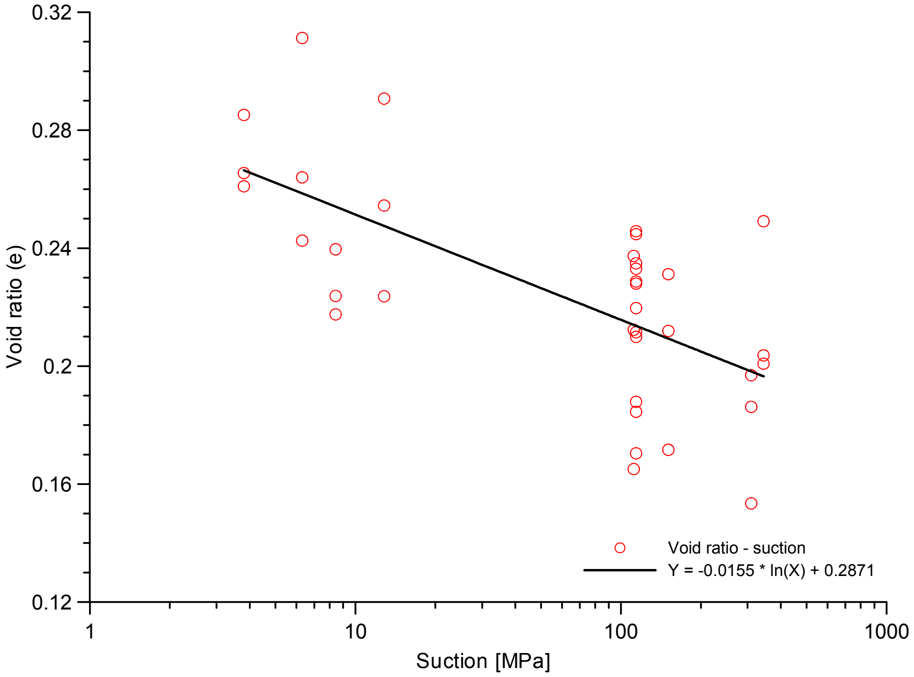

Figure 3.7: Measured final void ratio of the specimens

3.4.1 Water retention curve at constant volume

In order to obtain the suction-water content relationship at low suctions values, a second water retention curve was obtained with suctions values ranging from 0 MPa to 83.0 MPa following the drying path. Two specimens of 50 mm in diameter and 20 mm height were extracted from sample BVE-1/4, at 9.0 m depth. The samples presented bedding planes parallel to the longitudinal axis of the borehole. The laboratory test was carried out in a room with a controlled temperature of 22 ºC.

The equipment used was an isochoric cell developed in the UPC laboratory, which does not allow any volume change of the specimens. Figure 3.8 shows a photograph of the isochoric cell and the different parts of this device. Figure 3.9 shows a vertical section of the isochoric cell.

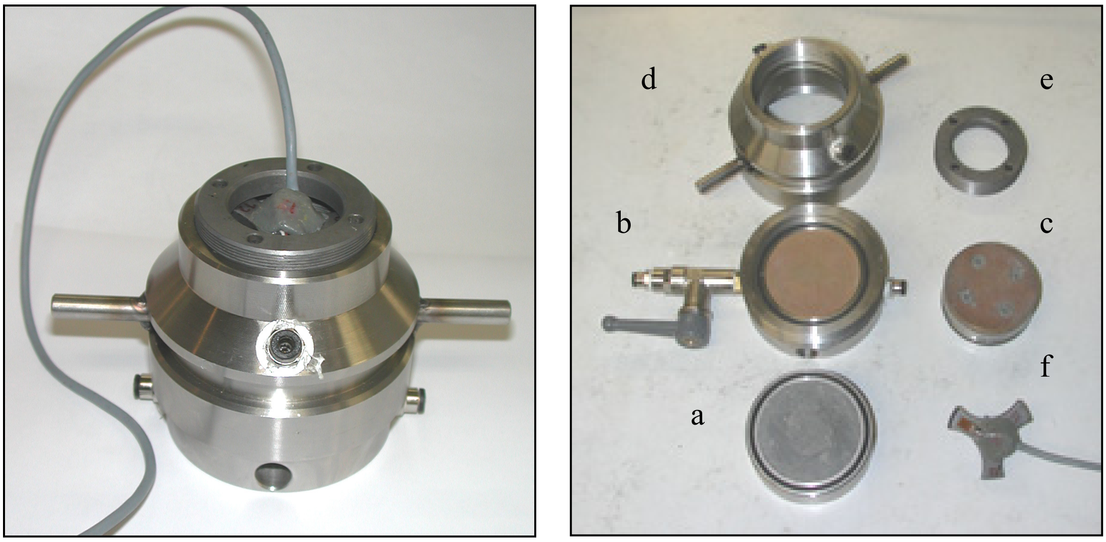

Figure 3.8: Left: Isochoric cell. Right: different isochoric cell components. a- stainless steel ring of 50 mm in diameter and 20 mm in height, b- lower cap with a porous disc, c- upper head with porous disc, d- top cap that is threaded to the lower cap, e- steel ring to tighten the upper head against the specimen and f- load cell to measure the swelling pressure.

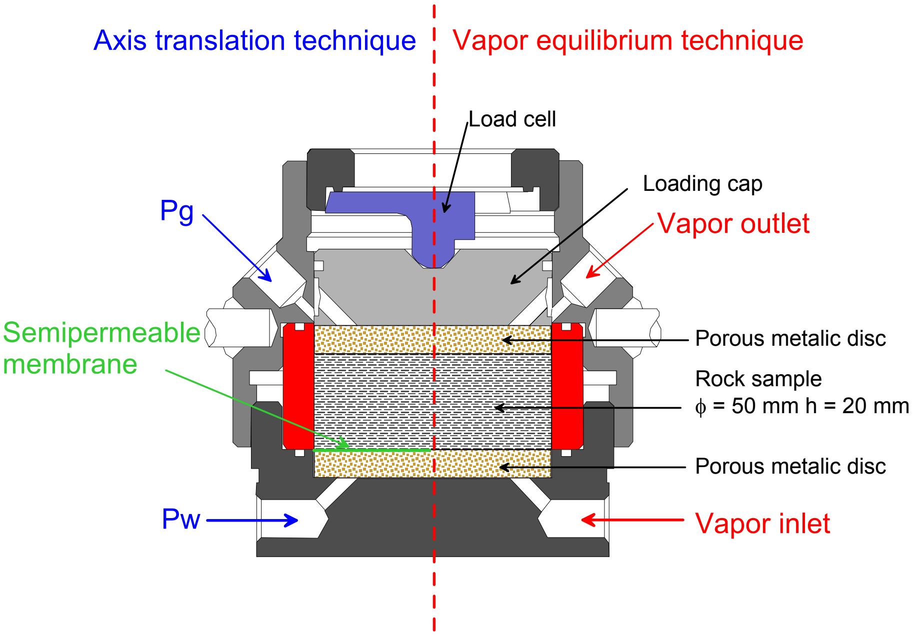

Figure 3.9: Isochoric cell used to perform the water retention curve at constant volume.

Initially, the specimens were saturated with Pearson water *(Pearson, 1998)* maintaining their volume constant. Then both specimens were dried in steps applying increasing suctions from 0 MPa to 83 MPa.

The axis translation technique was used to control the matrix suction, $\left(p_a - p_w\right)$, where p_a is the air pressure and p_w is the water pressure *(Romero, 2001)*. This technique was implemented to apply suctions smaller than 3.0 MPa. In the equipment used, water pressure was applied on the lower porous disc and was maintained a constant pressure of 0.1 MPa. The air pressure was applied on the top porous disc and its value was changed from 0.1 MPa to 3.0 MPa. A membrane (cellulose acetate), located between the specimen and the bottom porous disc, acts as a semi-permeable interface between the air and water pressures. The liquid phase with dissolved salts can flow through the membrane but the air remains confined over the membrane.

The vapor equilibrium technique was implemented to apply suctions ranging from 3.0 to 83.0 MPa *(Delage et al., (1998); Romero, (2001))*. In this technique, the vapor can be transported by simple diffusion or by forcing its circulation with an air pump. In the present case, a forced flow of humid air was established on the boundaries of the sample, through the top and lower porous discs. At each suction change step, the required time to achieve the equilibrium between the rock water and the solution was approximately two weeks. Saturated salt solutions were used to control the relative humidity. Partially saturated salt solutions of NaCl were also used. Table 3.8 shows the different suction values applied by means of axis translation and vapor equilibrium techniques.

Table 3.8: R.H. and suction value imposed in drying paths by means of axis translations and vapor equilibrium techniques.

TECHNIQUE		R.H. %	SUCTION (MPa)
AXIS TRASLATIONS Air overpressure method		-	0
		-	0.1
		-	0.3
		-	0.5
		-	1
		-	2
		-	3
VAPOR EQUILIBRIUM	$NaCl_{[m=1.369]}$	95.4	6.3
	$(NH_4)_2SO_4$	83.1	25
	$NaCl_{[m=5.647]}$	77.7	34
	$Mg(NO_3)_2$	54.0	83

The initial state of the samples was defined by a bulk density $\rho = 2.39$ g/cm^3, a water content $w = 0.065$, and a porosity $n = 0.178$ for the specimen 1; and by $\rho = 2.40$ g/cm^3, $w = 0.062$, and $n = 0.172$ for the specimen 2. In both cases, the density of minerals was $\rho_s = 2.73$ g/cm^3 and the initial suction $s = 15.0\ \text{MPa}$. If these initial porosities are considered unchanged during the initial wetting, degrees of saturation greater than one are computed using the water contents measured at null suction. This discrepancy can be associated with small increases of volume due to device deformability or to the fact that the density of water tightly bound to the clay particles is higher than of the free water *(Villar, 2002)*.

The values of the water content and degree of saturation associated with each suction step are summarized in Appendix A (Table A.6). Figure 3.10 shows the water retention curve obtained in terms of suction-water content relationship during the drying path. The fitted parameters of equation 3.4 are: $S_{rl} = 0$, $S_{ls} = 1$, $P = 3.9\ \text{MPa}$, $\lambda = 0.128$, $P_s = 700\ \text{MPa}$ and $\lambda_s = 2.73$. The water retention curve in terms of suction-degree of saturation relationship and the analytically function (3.4) are plotted in the Figure 3.11.

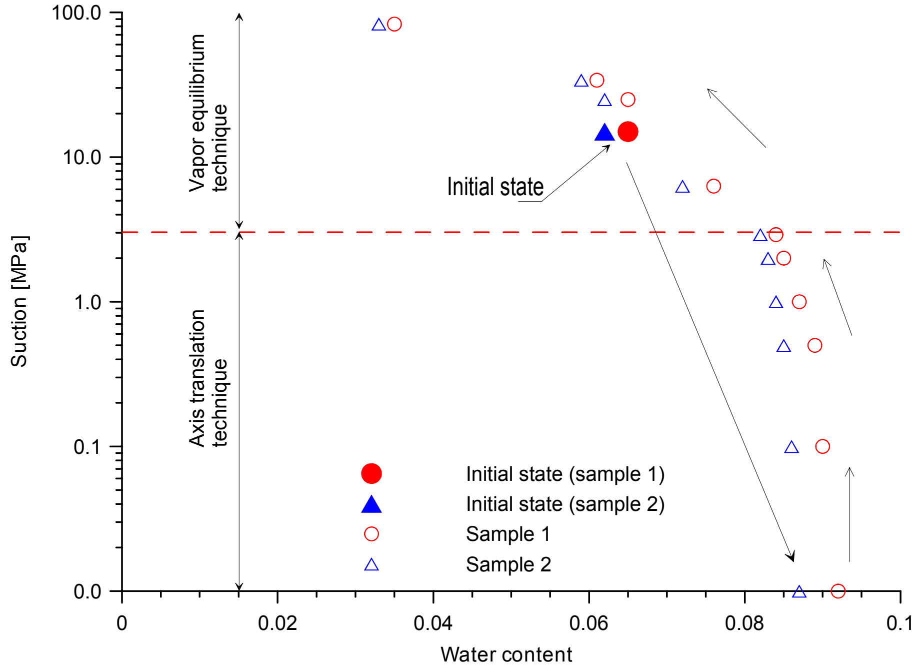

Figure 3.10: Water retention curve in terms of suction-water content relationship in the drying path for specimens 1 and 2 maintained at a constant porosity n = 0.178 and n = 0.172, respectively.

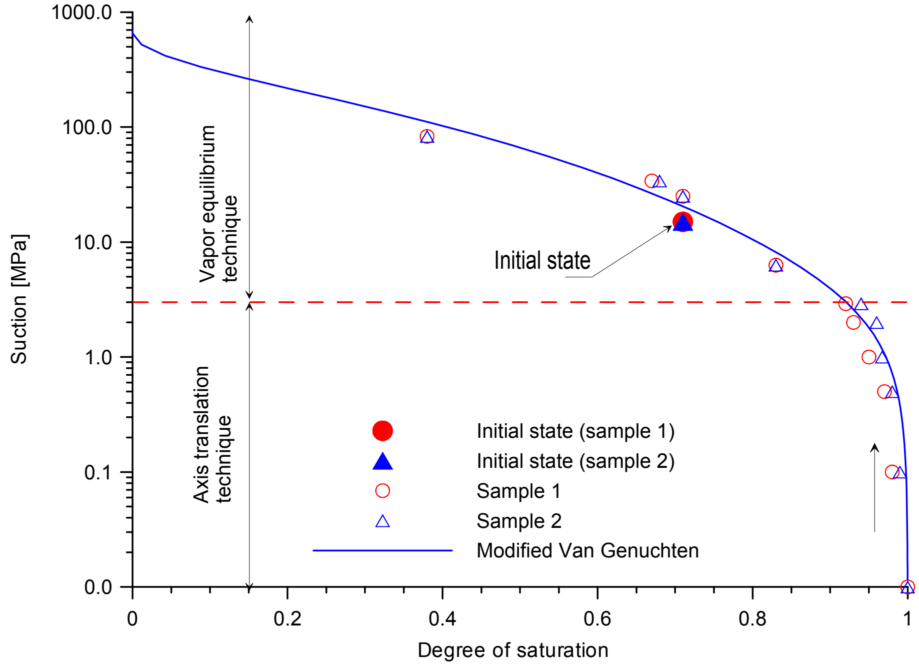

Figure 3.11: Water retention curve in terms of suction-degree of saturation relationship in the drying path for specimens 1 and 2 maintained at a constant porosity n = 0.178 and n = 0.172, respectively.

3.4.2 Suction – swelling pressure relationship

The laboratory test was performed in an isochoric cell previously described in the section 3.4.1. The swelling pressure of the rock was measured by the load cell placed against the upper end of the specimen. The load cell was calibrated in a high pressure oedometer frame with a load ratio of 1/20. The calibration curve can be seen in the Appendix A, Figure A.1. The sample underwent a wetting and drying cycle. The total suction was applied by means of the vapor equilibrium technique, where the different suctions values were applied by means of saturated salt solutions. The vapor transfer was performed using a forced convection system driven by an air pump. The vapor was passed through or along the boundaries of the sample. Changes in the water content of the sample were registered measuring the weight of it, and measuring the evolution in time of the weight of the salt solutions container. The saturation condition was obtained by means of synthetic water injected (*Pearson, 1998*). Changes in water content induce changes in the swelling pressure. A swelling pressure of 1.85 MPa was measured under saturated conditions. A sudden drop of swelling pressure to 0.10 MPa was registered when the rock was dried. Figure 3.12 shows the suction-water content relationship of the sample under isochoric conditions in a wetting and drying path. The temporal evolution of the swelling pressure and water content of the sample can be seen in the Figure 3.13. Swelling pressure values ranging from 0.6 MPa to 1.2 MPa have been reported by (*Bock, 2001).*

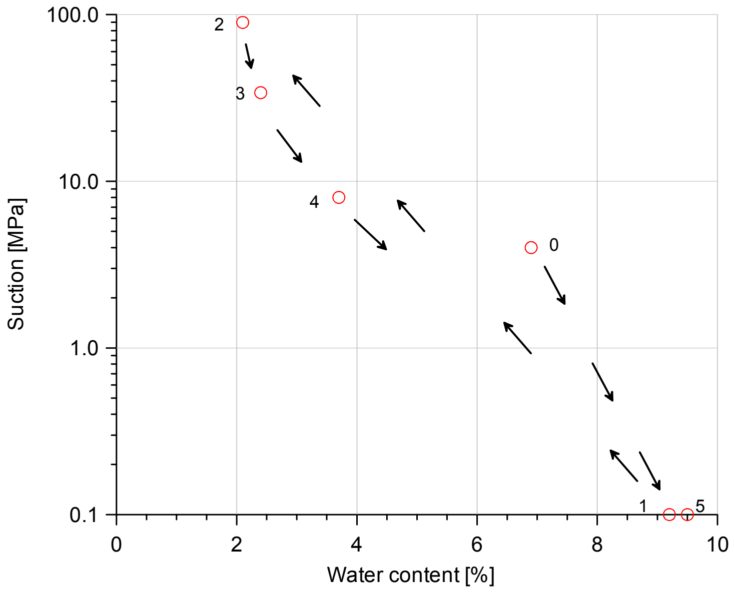

Figure 3.12: Wetting and draying paths performed in Opalinus Clay sample under isochoric conditions.

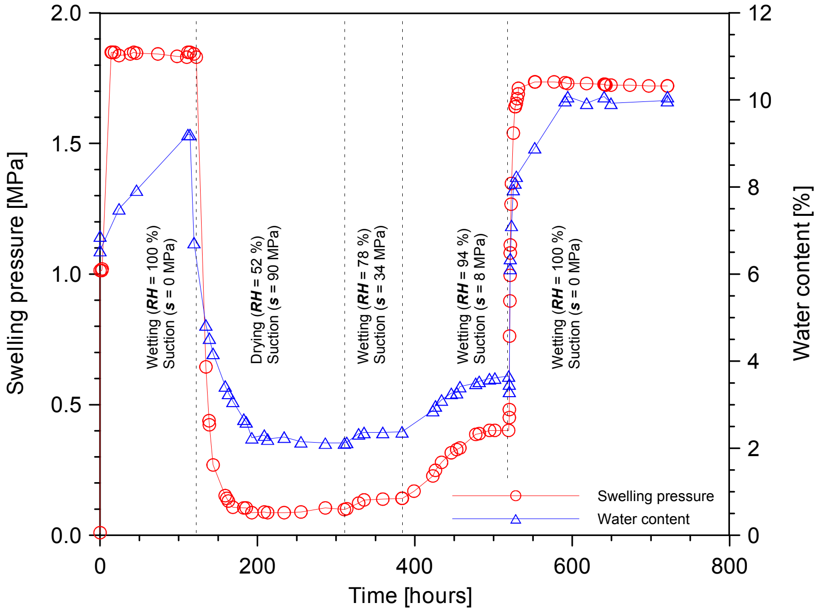

Figure 3.13: Temporal evolution of swelling pressure and water content of the sample underwent wetting and draying paths.

3.5 Hydraulic conductivity

The hydraulic conductivity of the Opalinus Clay rock under saturated conditions was measured in laboratory tests by means of infiltration tests. The value of unsaturated permeability cannot be obtained directly from the results of the infiltration test performed. The influence of the degree of saturation on water permeability can be modeled using a relative permeability function $k_{rl}\left(S_r\right)$, that can be expressed using the Van Genuchten model:

$$k_{rl} = \frac{K(S_r)}{K(S_r = 1)} = \sqrt{S_e}\left(1-\left(1-S_e^{1/\lambda}\right)^{\lambda}\right)^2 \qquad \textbf{(Eq 3.5)}$$

where S_e is the effective saturation and λ a material parameter. Note that the value of parameter λ in the unsaturated permeability law, (Eq. 3.5), may be different from the value parameter λ used in the water retention curve.

In order to know the relative permeability function, the value of parameter λ has been determined by the back-analysis of the infiltration and drying tests, using the finite element code “CODE_BRIGHT”. The infiltration tests were performed in an especially designed and built permeameters made in stainless steel. The drying test was performed by AITEMIN during 2001 and was analyzed by DM Iberia (*Velasco and Pedraza, 2002)* and COLENCO (*Croisé and Klubertanz, 2002*).

3.5.1 Permeameters description

The permeameters consists of a ring of 75 mm in diameter and 50 mm high, where the sample is placed; and two caps with its respective porous filters and inlet/outlet water valves. The joining between the ring and the caps is a screw-on type and the hydraulic closure between them is assured by rubber "O"-rings. The samples were stuck to the ring by epoxi resin throughout the perimeter ensuring the flow through the rock. In order to assure the appropriate contact between the filter and the sample, they were polished until they reached the ring level. Figure 3.14 shows a section of the permeameter and Figure 3.15 shows a sample of Opalinus Clay fitted to the stainless steel ring by means of epoxi resin.

Water enters through the bottom of the sample at a pressure of 0.50 MPa and exits the sample through the top at atmospheric pressure. The pressure was applied using a mercury column system. The amount of water entering to the samples was measured in a burette with a resolution of 0.05 ml. The water used in this test had a chemical composition that represented the water existing in the rock formation (*Pearson, 1998*).

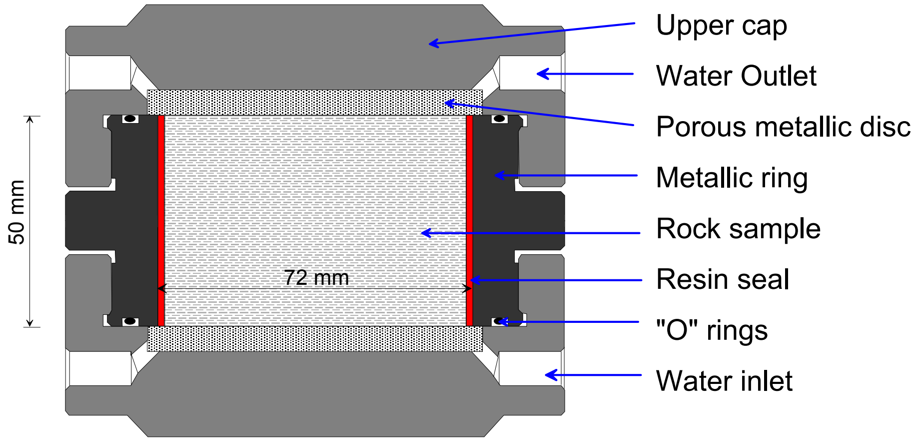

Figure 3.14: Scheme of permeameter built to perform permeability test.

Figure 3.15: Sample pasted to the ring by means of epoxi resin

3.5.2 Infiltration test 1

The objective of this test was to determine the hydraulic conductivity of the Opalinus clay under saturated and unsaturated conditions *(Muñoz et al., 2001)*. Permeability tests at constant infiltration water pressure of 0.5 MPa were carried out on four samples (P1 to P4) extracted from borehole BHE-8, at depths of 6.00, 6.30, 6.60 and 8.60 m. The samples tested were 72 mm in diameter and 50 mm height. These samples present stratification planes ranging from 65º to 70º with respect to the borehole longitudinal axis. Due to the dimensions of the permeameter, the discontinuity planes do not cross entirely the specimen in the direction of the hydraulic gradient. Initially, the specimens were dried using the vapor equilibrium technique until they reached an initial degree of saturation $S_r = 36\ \%$.

In order to model the test, a hydraulic analysis under one-dimensional conditions was performed with CODE_BRIGHT using a mesh with 40 elements and 41 nodes. The modified Van Genuchten expression (Eq. 3.4) was used to model the water retention curve. The parameters of the water retention curve used in this model are indicated in Table 3.7.

The hydraulic conductivity under saturation conditions was determined applying the Darcy's law in specimen P4. The value obtained was $K = 1.33 \text{ x } 10^{-13}$ m$/s$, and the intrinsic permeability, $k = 1.35 \text{ x } 10^{-20}$ m^2. A hydraulic conductivity value of $K = 2.0 \text{ x } 10^{-13}\ m/s$ has been reported by *Thury and Bossart, (1999*). Values ranging from $K_{//} = 2.0 \text{ x } 10^{-13}\ m/s$ to $K_{\perp} = 8.0 \text{ x } 10^{-14}\ m/s$ were reported by *Bock, (2001*). Figure 3.16 shows the volume of water infiltrated in samples P1 to P4 as a function of time, obtained from laboratory tests and the computed water volume obtained with 1-D numerical simulations.

Samples P1, P2 and P3 were used to observe the water content distribution as time increase. These samples were tested at different infiltration times, 96, 240 and 600 hours, respectively. Once the time prefixed for each sample was reached, they were extracted from the ring using a coring devise and cut in slices of 10 mm (approx.) to determine their water content. Figure 3.17 shows the comparison between measured and computed profiles of degree of saturations along the specimens at different times. In this case the value of the parameter $\lambda = 0.31$ in the relative permeability law was obtained by the back-analysis.

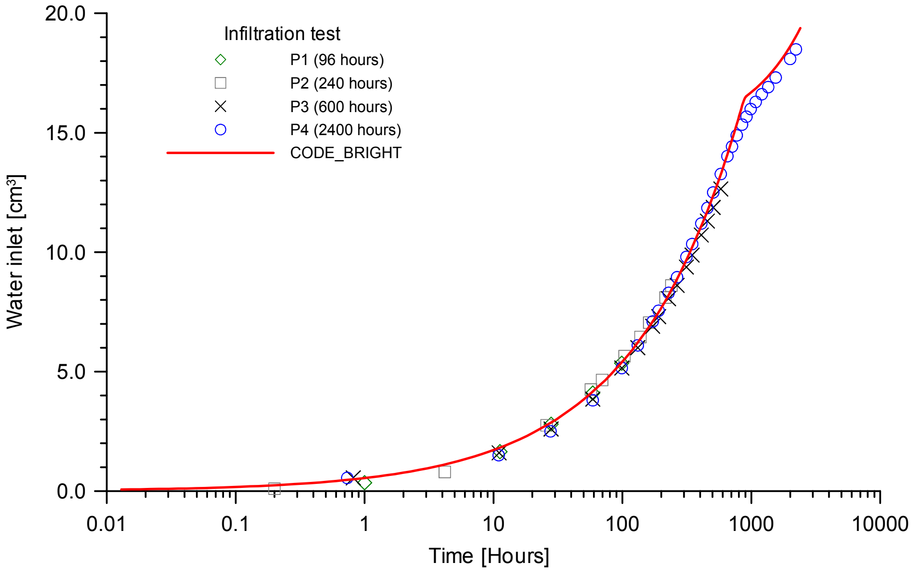

Figure 3.16: Volume of water infiltrated in samples P1 to P4 measured in laboratory test and computed with CODE_BRIGHT.

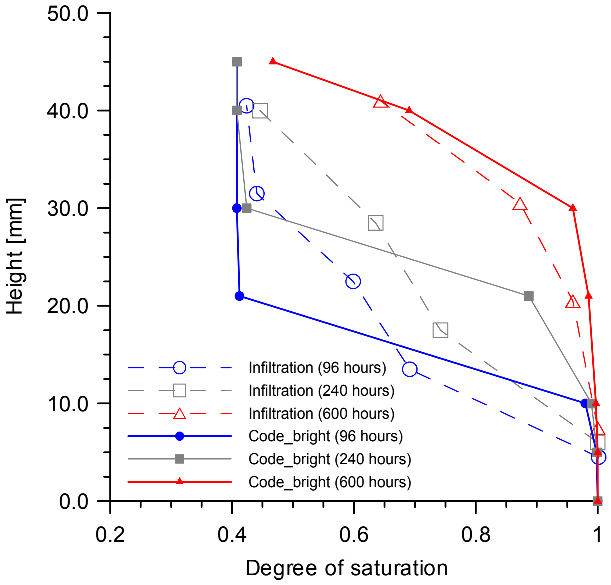

Figure 3.17: Measured and computed profiles of degree of saturations in the samples P1 to P3.

3.5.3 Infiltration test 2

The test was carried out on a sample extracted from borehole BVE-1/5 at a depth of 10.40 m. The sample was 72 mm in diameter and 50 mm height, and presented stratification planes parallel to the borehole longitudinal axis. Once the sample was inside the ring, it was dried using the vapor equilibrium technique until it reached a degree of saturation of about 70 %. A suction of 34 MPa was applied by means of a solution of sodium chloride (NaCl) with a molality *m* = 5,647. Humid air was circulated in a closed circuit using a small pump. Changes in the water content of the sample were registered measuring the evolution in time of the weight of salt solution. Equilibrium conditions required times close to eight weeks, see Figure 3.18.

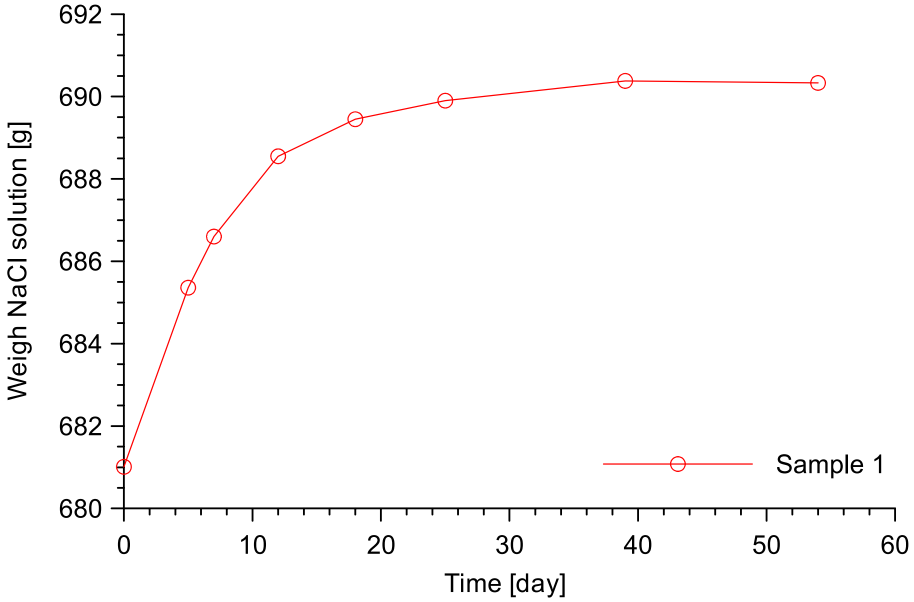

Figure 3.18: Time evolution of weight of the salt solution during the drying process of the sample.

Pearson water was injected through the bottom of the sample with a constant pressure of 0.5 MPa, whereas the atmospheric pressure was imposed at the top of the sample. The water pressure was applied using a mercury column system. The water inflow volume was measured using a burette with a resolution of 0.05 ml. The temperature during the drying and injection processes was 20 ± 2 ºC. After reaching stationary conditions, the hydraulic conductivity under saturated conditions was determined by means of Darcy's law. The value obtained was $K = 7.35E-13\ \mathrm{m}/s$, and the intrinsic permeability was $k = 7.50E-20\ \mathrm{m}^2$. These values belong to the high range of usual values for hydraulic conductivity of Opalinus Clay. This is due to the favorable orientation of bedding planes, which were parallel to the direction of the hydraulic gradient.

In order to model the test, a hydraulic analysis under one-dimensional conditions was performed with CODE_BRIGHT using a mesh with 40 elements and 41 nodes. The modified Van Genuchten expression (Eq. 3.4) was used to model the water retention curve. The parameters used in the equations (Eq. 3.4) correspond to the water retention curve determined at constant volume. The model parameters used in numerical simulations are indicated in Table 3.9. Taking into account the amount of water that fills the pores of the sample, a porosity of 0.192 was considered in the numerical simulation. Figure 3.19 illustrates the water volume infiltrated in the sample obtained from the laboratory test and from the numerical simulations. A good agreement between measured and predicted infiltrated volume can be achieved using a value of $\lambda = 0.135$ to define the relative permeability law. Note that small changes in the value of parameter λ lead to significant changes in the computed infiltration rate during the unsaturated stage.

The small value obtained for parameter λ indicates an abrupt reduction of the permeability when the degree of saturation decreases below 0.95, see Figure 3.20. This reduction in permeability comes from the fact that in the infiltration test, the permeability necessary to fit the rate of saturation under unsaturated conditions is much smaller than the permeability measured directly under saturated conditions. A reason of this reduction may be that, due to the small porosity of the Opalinus clay, the amount of free water able to flow under suction gradients is much smaller that the water bound to clay particles. Consequently, near the state of saturation, small changes in water content represent significant changes in the amount of water which is free to flow. However what may be more relevant is the presence of discontinuities in the rock specimen, which in this infiltration test, were oriented parallels to the direction of the hydraulic gradient. Two simultaneous processes occur during the rock hydration. On the one hand, the reduction of the thickness of fissures occurs when the rock is hydrated, due to rock's swelling. On the other hand, under saturated conditions a great part of the flow passes through the more permeable planes of discontinuity, whereas under unsaturated conditions these fissures may be dry and the flow fundamentally takes place through the rock matrix. Although the rock's matrix is more impermeable, it has a greater capacity of water retention. Only when the rock is practically saturated, the water occupies the discontinuities and the permeability increase abruptly.

In order to fit the rate of saturation under unsaturated conditions a second modeling of the test was performed. In this case, a change in the intrinsic permeability due to changes in pores structure was performed. During unsaturated infiltration (time no longer than 26 days) intrinsic permeability was supposed to be of $k = 6.20E-21\ \mathrm{m}^2$. When saturation of the specimen was reached, an intrinsic permeability of $k = 7.50E-20\ \mathrm{m}^2$ was considered (measured hydraulic conductivity). In this case, a good fit between measured and calculated values of infiltrated water is obtained with a value of $\lambda = 0.6$. This value is more in agreement with the typical values obtained for this parameter in clayey materials. Figure 3.21 shows the comparison between the measured and computed values of water mass infiltrated into the specimen versus time, using this new approach. It can be observed how in this case, this relationship is similar to a potential law $k_{rl} = S_r^{4.5}$, which is in the range of recommended values for the scoping calculations presented by DM Iberia *(Velasco and Pedraza, 2002)*, see Figure 3.20. The new set of model parameters used in numerical simulations is indicated in Table 3.10.

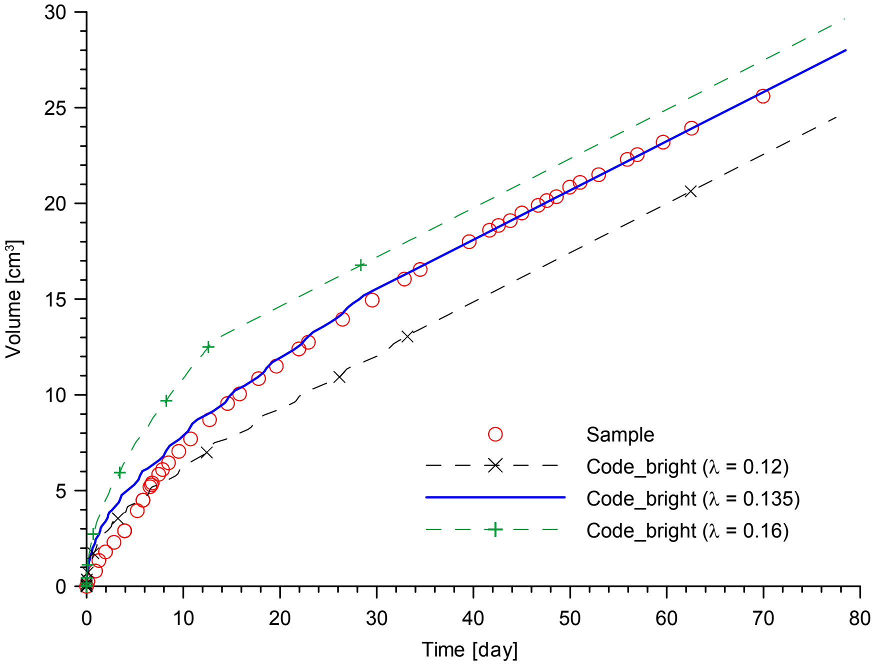

Figure 3.19: Volume of water infiltrated in the sample measured in laboratory test and calculated using three different values for parameter λ. Intrinsic permeability is the same under saturated or unsaturated conditions.

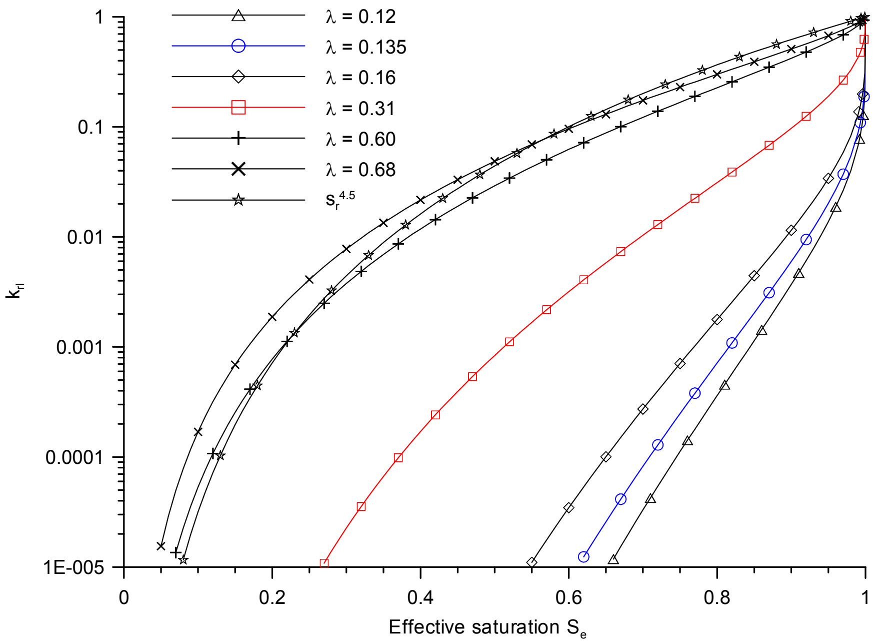

Figure 3.20: Relative permeability laws and the associated values of λ used in the numerical simulations.

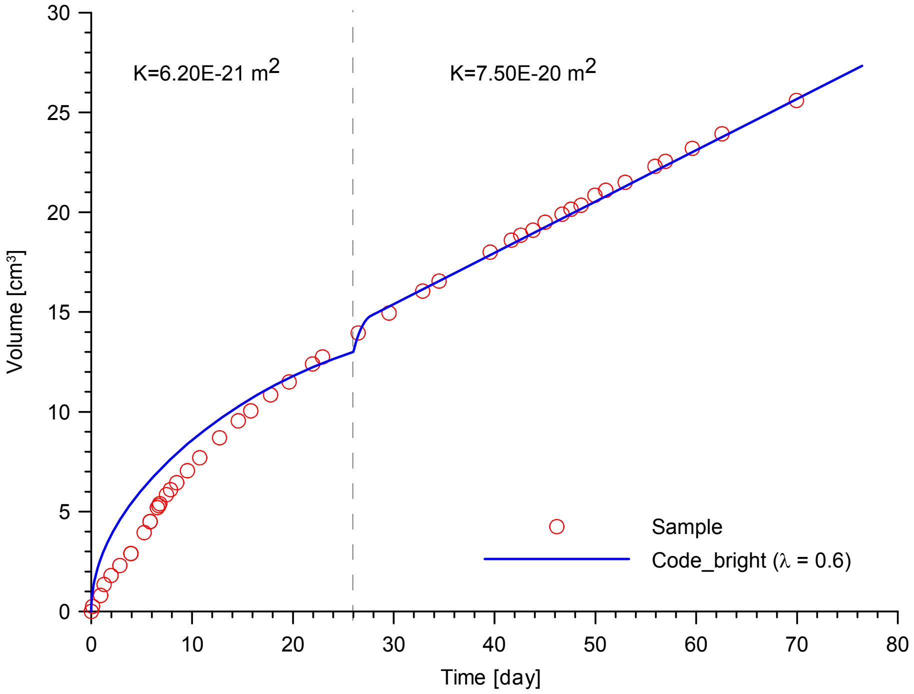

Figure 3.21: Water volume infiltrated in the sample measured in laboratory and calculated using different intrinsic permeability values under unsaturated conditions (t < 26 days) and under saturated conditions.

Table 3.9: Hydraulic parameters used in the numerical modeling of test

Properties	**Value**
Intrinsic permeability **k** (Kozeny model)	$k = k_0 \dfrac{\phi^3}{(1-\phi)^2} \dfrac{(1-\phi_0)^2}{\phi_0^3}$ ϕ_0: reference porosity (0.192) k_0: intrinsic permeability for matrix ϕ_0 (7.50E-20) [m^2]
Retention Curve (Modified Van Genuchten model)	$S_e = \dfrac{S_l - S_{rl}}{S_{ls} - S_{rl}} = \left(1 + \left(\dfrac{P_g - P_l}{P}\right)^{\frac{1}{1-\lambda}}\right)^{-\lambda} \left(1 - \dfrac{P_g - P_l}{P_s}\right)^{\lambda_s}$ S_e: Effective saturation ($0 \le S_e \le 1$) P : Material parameter (3.90) [MPa] λ : Shape function for retention curve (0.128) P_s: Material parameter (700.00) [MPa] λ_s: (2.73) S_{rl}: Residual saturation (0.00) S_{ls}: Maximum saturation (1.00)
Relative permeability $\mathbf{k_{rl}}$ (Van Genuchten model)	$k_{rl} = \sqrt{S_e}\left(1 - \left(1 - S_e^{1/\lambda}\right)^{\lambda}\right)^2$ S_e: Effective saturation ($0 \le S_e \le 1$) λ : Power (0.12, 0.135 and 0.16) S_{rl}: Residual saturation (0.00) S_{ls}: Maximum saturation (1.00)
Porosity	(0.192)
Initial suction	(-34.00) [MPa]

Table 3.10: Hydraulic parameters used in the numerical modeling of infiltration test carried out with two intrinsic permeability values (unsaturated and saturated) and different relative permeability law.

Properties	**Value**
Intrinsic permeability **k** (Kozeny model)	$k = k_0 \dfrac{\phi^3}{(1-\phi)^2} \dfrac{(1-\phi_0)^2}{\phi_0^3}$ ϕ_0: reference porosity (0.192) k_0: intrinsic permeability for unsaturated condition; $t < 26$ days (6.20E-21) [m^2] k_0: intrinsic permeability for saturated condition; $t > 26$ days (7.50E-20) [m^2]

Retention Curve (Modified Van Genuchten model)	$S_e = \frac{S_l - S_{rl}}{S_{ls} - S_{rl}} = \left(1 + \left(\frac{P_g - P_l}{P}\right)^{\frac{1}{1-\lambda}}\right)^{-\lambda} \left(1 - \frac{P_g - P_l}{P_s}\right)^{\lambda_s}$ S_e: Effective saturation ($0 \le S_e \le 1$) P : Material parameter (3.90) [MPa] λ : Shape function for retention curve (0.128) P_s: Material parameter (700.00) [MPa] λ_s: (2.73) S_{rl}: Residual saturation (0.00) S_{ls}: Maximum saturation (1.00)
Relative permeability $\mathbf{k_{rl}}$ (Van Genuchten model)	$k_{rl} = \sqrt{S_e}\left(1 - \left(1 - S_e^{1/\lambda}\right)^{\lambda}\right)^2$ S_e: Effective saturation ($0 \le S_e \le 1$) λ : Power (0.60) S_{rl}: Residual saturation (0.00) S_{ls}: Maximum saturation (1.00)
Porosity	(0.192)
Initial suction	(-34.00) [MPa]

3.5.4 Drying test

The drying test was performed by AITEMIN *(Floría et al. 2002)* during 2001 and was analyzed by DM Iberia *(Velasco and Pedraza, 2002)* and COLENCO *(Croisé and Klubertanz, 2002)*. The evaporation rate was measured in three samples extracted from boreholes BLT 1 and 2 from SHGN niche *(Floría et al. 2002)*. These samples were placed in a drying chamber under controlled atmospheric conditions. Samples were 101 mm in diameter and 280 mm in height and the average relative humidity, temperature and air velocity in the chamber during the test was of 33 %, 30 ºC and 0.52 m/s respectively. Bedding planes were parallel to the core axis. Evaporation was only allowed across the upper surface of the specimens. The core samples were wrapped with latex and then with an insulation foam in order to prevent evaporation from the base and lateral surface. Sample A acted as reference sample and it remained at the drying chamber up to the end of test (142 days). The other two specimens were used to measure the water content profile at different times from the beginning of the test. During 142 days of test the following parameters were recorded:

a- Temperature (T), Relative Humidity (RH), and airflow velocity (V) inside the drying chamber

b- Potential rate of evaporation of a surface of free water c- Environmental temperature and humidity out of drying chamber

d- Continuous measurement of loss weight of samples (A, B and C)

e- Temperature of the reference sample (A) along a vertical profile (4 positions)

Figure 3.22 shows in schematic form the drying chamber used to develop the test and the location of the different sensors.

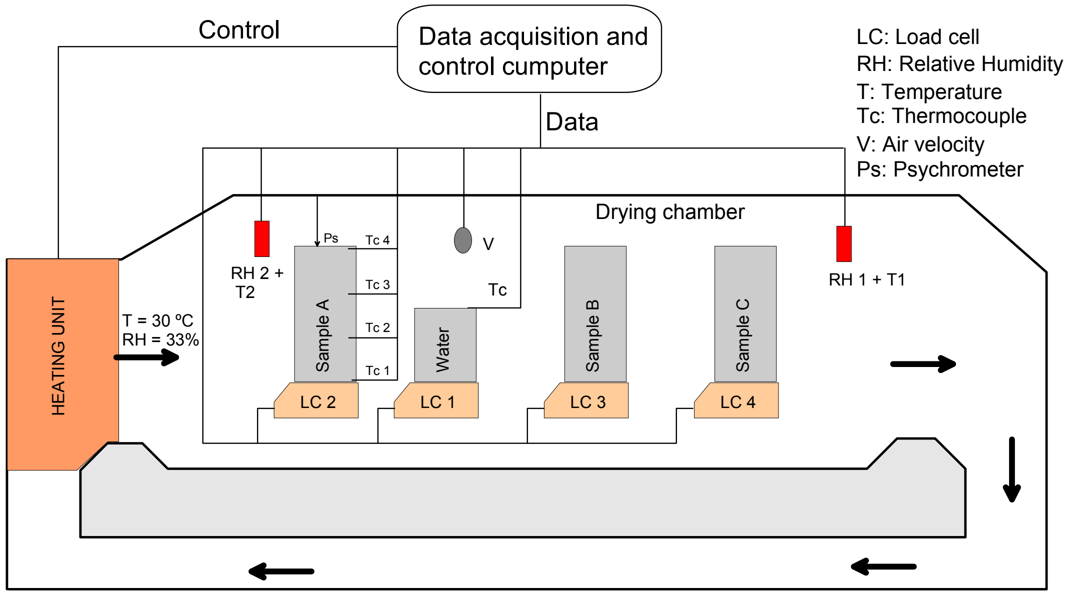

Figure 3.22: Drying test performed by AITEMIN (Floría et al. 2002).

A 1-D thermo-hydraulic analysis was performed with CODE_BRIGHT. The numerical model carried out was similar to the model used by *Velasco and Pedraza, (2002)*. In order to evaluate the evaporation flow at the sample-air interface, the turbulence coefficient (β_g) was used (Dalton-type equation). The turbulence coefficient $\beta_g = 7.10E-03$ m/s was deduced from the evaporation of free water recorded from the water container located into the drying chamber *(Velasco and Pedraza, (2002))*. The good agreement between measurements and simulation results shown in Figure 3.23 may be obtained using a water conductivity K= $2.0\cdot10^{-13}$ m/s, a relative permeability characterized by a parameter λ = 0.68 and the water retention curve determined in laboratory (section 3.4). The hydraulic parameters of the model are shown in Table 3.11. Figure 3.24 shows the computed and measured water content profiles at different times.

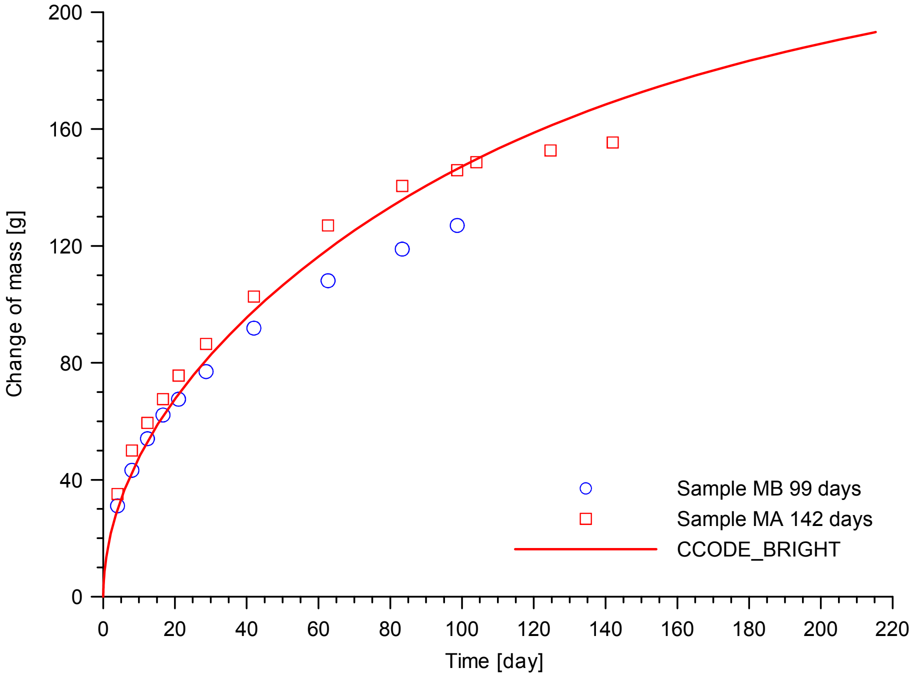

Figure 3.23: Values measured and computed of water mass extracted in the drying test.

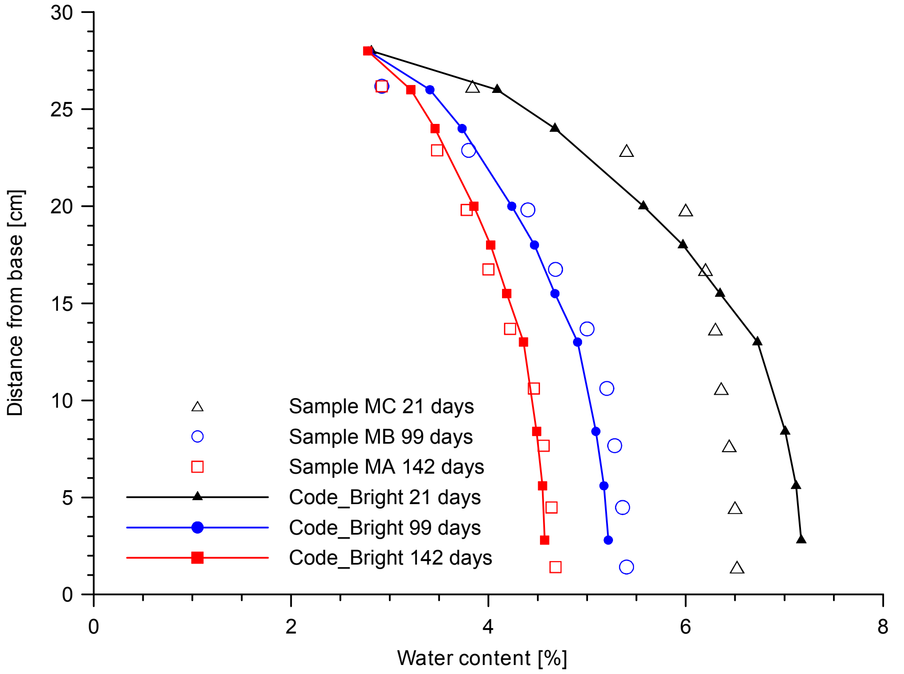

Figure 3.24: Computed and measured water content profiles at different times during the drying test.

Table 3.11: Hydraulic parameters used in the numerical modeling of the drying test.

Properties	**Value**
Intrinsic permeability **k** (Kozeny model)	$k = k_0 \frac{\phi^3}{(1-\phi)^2} \frac{(1-\phi_0)^2}{\phi_0^3}$ ϕ_0: reference porosity (0.160) k_0: intrinsic permeability for matrix ($2.0 \cdot 10^{-20}$) [m^2]
Retention Curve (Modified Van Genuchten model)	$S_e = \frac{S_l - S_{rl}}{S_{ls} - S_{rl}} = \left(1 + \left(\frac{P_g - P_l}{P}\right)^{\frac{1}{1-\lambda}}\right)^{-\lambda} \left(1 - \frac{P_g - P_l}{P_s}\right)^{\lambda_s}$ S_e: Effective saturation ($0 \le S_e \le 1$) P : Material parameter (3.90) [MPa] λ : Shape function for retention curve (0.128) P_s: Material parameter (700.00) [MPa] λ_s: (2.73) S_{rl}: Residual saturation (0.00) S_{ls}: Maximum saturation (1.00)
Relative permeability $\mathbf{k_{rl}}$ (Van Genuchten model)	$k_{rl} = \sqrt{S_e}\left(1 - \left(1 - S_e^{1/\lambda}\right)^{\lambda}\right)^2$ S_e: Effective saturation ($0 \le S_e \le 1$) λ : Power (0.68) S_{rl}: Residual saturation (0.00) S_{ls}: Maximum saturation (1.00)
Porosity	(0.160)
Initial suction	(0.00) [MPa] Full saturated

3.6 Mercury Intrusion Porosimetry and Electronic Microscopy

The pore size distribution (PSD) of the Opalinus Clay rock was determined by means of mercury intrusion porosimetry (MIP) carried out in the mercury intrusion porosimeter of the Geotechnical laboratory of the UPC. From the (PSD) the water retention curve, the saturated hydraulic conductivity and relative permeability were estimated; following the methodology presented by *(Romero et al., 1999)*.

The (MIP) consist in the application of pressure (p) on a non-wetting fluid (mercury), which is introduced into the pores of soil. The relationship between intrusion pressure

(p) and pore diameter (d), for pores of cylindrical shape and parallel infinite wall, is established by the equation 3.6:

$$p = -\frac{4\sigma_{Hg}\cos\theta_{nw}}{d} \qquad \text{(Eq 3.6)}$$

where σ_{Hg} is the surface tension of the mercury, θ_{nw} is the contact angle between the mercury and the pore wall, and d is the apparent pore diameter. The surface tension value adopted was $\sigma_{Hg} = 0.484\ \text{N/m a } 25\ ^{\circ}\text{C}$. The contact angle was taken as $\theta_{nw} = 140^{\circ}$. This value is usually assumed to vary between 139º to 147º for clayey minerals *(Romero et al., 1999).*

The equipment performs the MIP in two phases. At the first phase the equipment performs the mercury intrusion at low pressure. The applied pressure was increased from 0.015 MPa to 0.15 MPa, measuring apparent pore diameter ranging from 98.8 µm to 9.8 µm, respectively. In this phase, the air sample was evacuated by means of vacuum and subsequently the sample was surrounded by mercury. In the second phase, the MIP was carried out at high pressure. The mercury pressure was increased from 0.17 MPa to 219 MPa, measuring pores diameters ranging between 8.7 µm and 6.8 nm.

Previous to carrying out the MIP test, samples undergone a freezing-drying process in order to remove the pore water. The freezing-drying process involve temperatures and pressure conditions to eliminate the surface tension forces caused by air-water interfaces and therefore it is assumed that no shrinkage occurs during the drying, which could alter the rock microstructure. The details of the freezing-drying procedure can be seen in (*Mitchell, 1993*). The samples tested were taken from the borehole BVE 90/1, at a depth of 1.85 m depth. The initial conditions of samples were: water content *w* = 7.0%, porosity *n* = 18.2% and dry density ρ_d = 2.24 g/cm^3. The freeze dried samples weight around of 1.5 g.

Figure 3.25 shows the PSD of the samples tested. The pore size has been divided in four levels, such as: macro-porosity, meso-porosity, micro-porosity and ultra micro-porosity. The macro-porosity covers pore diameters from 100 µm to 1 µm. The meso-porosity covers pore diameters between 1000 nm and 100 nm. The micro-porosity covers pore diameters from 100 nm to 20 nm. The ultra micro-porosity covers pore diameters lower than 20 nm, *(Romero, (1999))*. Table 3.12 summarizes the total porosity distribution as a function of pore size determined in the test.

Table 3.12: Total porosity distribution as a function of pore size of samples.

Pore diameters (*d*)	**Porosity [%]**
Macro-porosity $1000 \leq d < 100000$ nm	20.8
Meso-porosity $100 \leq d < 1000$ nm	12.5
Micro-porosity $20 \leq d < 100$ nm	24.2
Ultra micro-porosity $d \leq 20$ nm	42.5

Figure 3.26 shows the volume of mercury intruded versus the pore size, normalized by the dry weight of the samples. The mercury volume intruded, normalized by the total volume of the samples is equivalent to the cumulative porosity (n), see Figure 3.27. A large difference between theoretical porosity values and porosity value obtained by MIP was found. The difference can be due to existing fissures in samples with size bigger than 100 μm and also to the existence of pore sizes smaller than the resolution of the porosimeter (7.0 nm). Porosity difference of $(\Delta n = 0.077)$, $(\Delta n = 0.072)$ and $(\Delta n = 0.090)$ for samples 1, 2 and 3, were determined, respectively.

The pore size distribution normalized by the total porosity (n_0) represents the porosity which can be absorbed by the mercury intrusion to high pressures, see Figure 3.28. The values of n/n_0 are equivalent to the mercury degree of saturations Sr_{nw} (non-wetting fluid). Figure 3.28 shows the mono-modal pore size distributions which define the inflexion point (maximum frequency of pores) at 20 nm approximately.

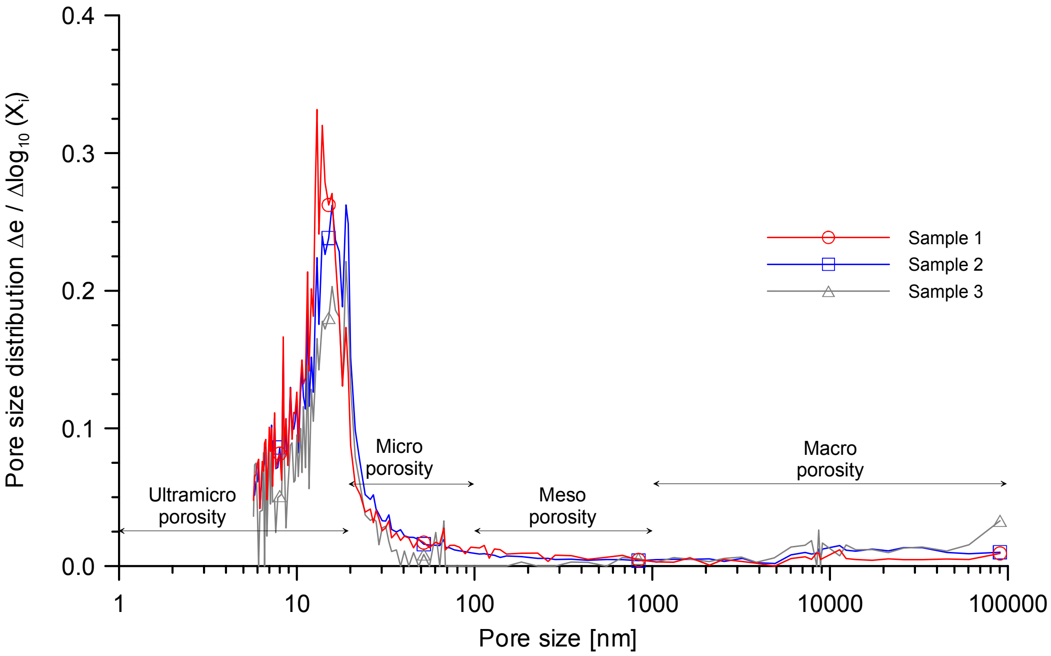

Figure 3.25: Pores size distribution of the Opalinus Clay samples

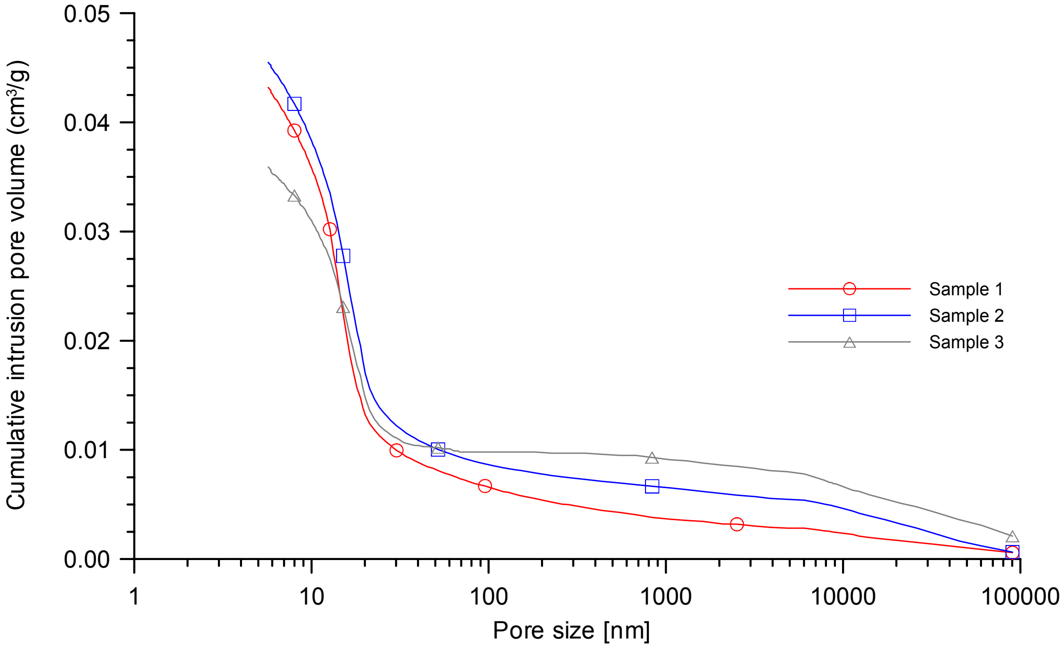

Figure 3.26: Volume of mercury intruded, normalized by dry weight of the samples.

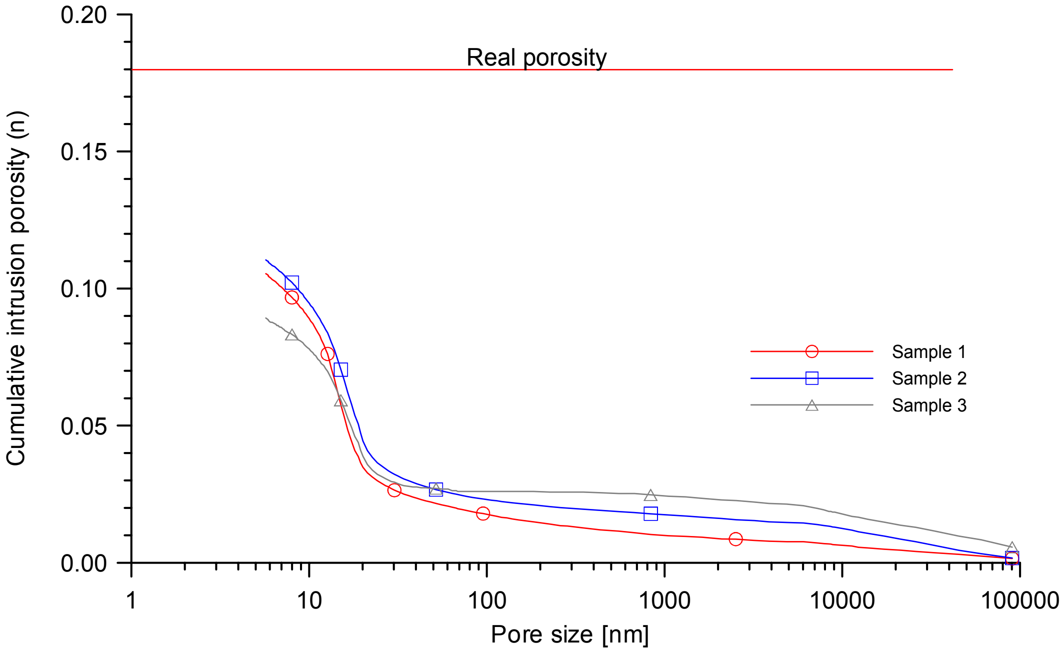

Figure 3.27: Cumulative total porosity obtained in the mercury intrusion porosimetry.

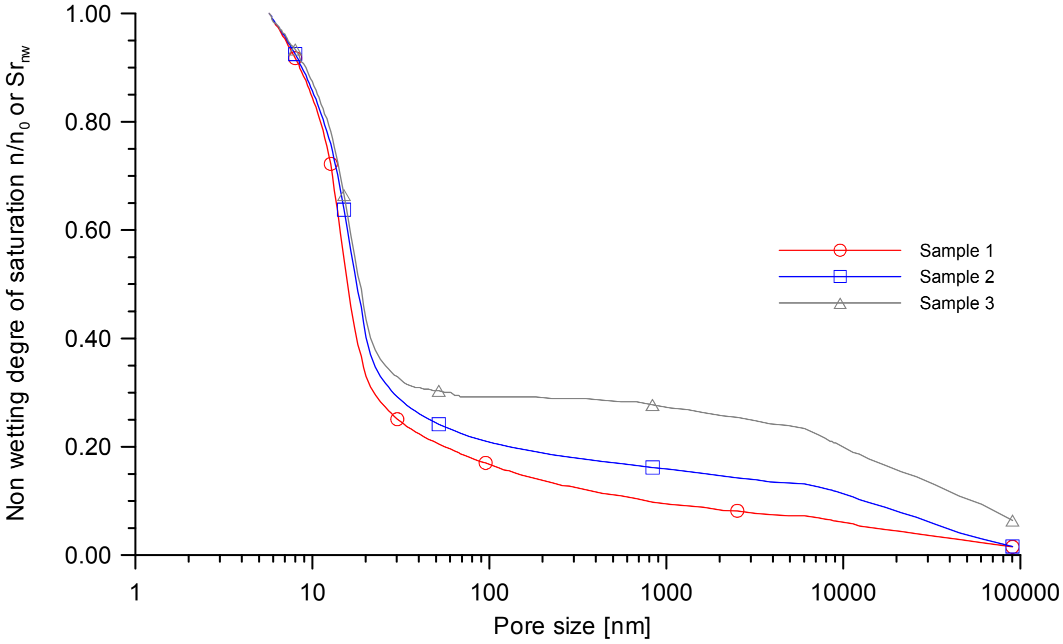

Figure 3.28: Mercury degree of saturations.

3.6.1 Water retention curve

The MIP was used to estimate the suction-water content relationship of the Opalinus Clay rock. MIP can be interpreted as a drying path of a saturated sample. The mercury intrusion into the rock pores, produced by pressure increments, is equivalent to extraction of pore water. The relationship between the pressure of the non-wetting fluid and suction can be established by means of equation 3.9, which combines the equations 3.7 and 3.8, as follows:

$$p = -\frac{4\sigma_{Hg}\cos\theta_{nw}}{d} \qquad \text{(Eq 3.7)}$$

$$\left(u_a - u_w\right) = \frac{4\sigma\cos\theta_w}{d} \qquad \text{(Eq 3.8)}$$

$$\left(u_a - u_w\right) = -\frac{\sigma\cos\theta_w}{\sigma_{Hg}\cos\theta_{nw}}p = 0.196p \qquad \text{(Eq 3.9)}$$

where σ is the water surface tension and $\cos\theta_w = 1$ is the coefficient of wetting for air-water interface.

The water content $\left(w\right)$ and degree of saturations $\left(Sr\right)$ can be estimated by means of following relations:

$$Sr_{nw} + Sr = 1 \qquad \text{(Eq 3.10)}$$

$$w = \left(1 - Sr_{nw}\right)\left(w_{sat} - w_r\right) + w_r \qquad \text{(Eq 3.11)}$$

$$Sr = \left(1 - Sr_{nw}\right) + \frac{w_r}{w_{sat}}Sr_{nw} \qquad \text{(Eq 3.12)}$$

where $\left(Sr\right)$ is the water degree of saturation, $\left(w_{sat}\right)$ the water content for $Sr = 1$ and $\left(Sr_{nw}\right)$ the mercury degree of saturation. $\left(w_r\right)$ is the residual water content, where the value $w_r = 4.5\%$ corresponds to the maximum value of suction $s = 42.6$ MPa, obtained with the maximum intrusion pressure $p = 219.2$ MPa. The water content at saturation $w_{sat} = 9.5\%$ was determined from the water retention curve at constant volume. Figure 3.29 and Figure 3.30 show the water retention curve obtained by MIP in terms of water content and degree of saturation, respectively and its comparison with the experimental water retention curve *(Muñoz et al. 2003).*

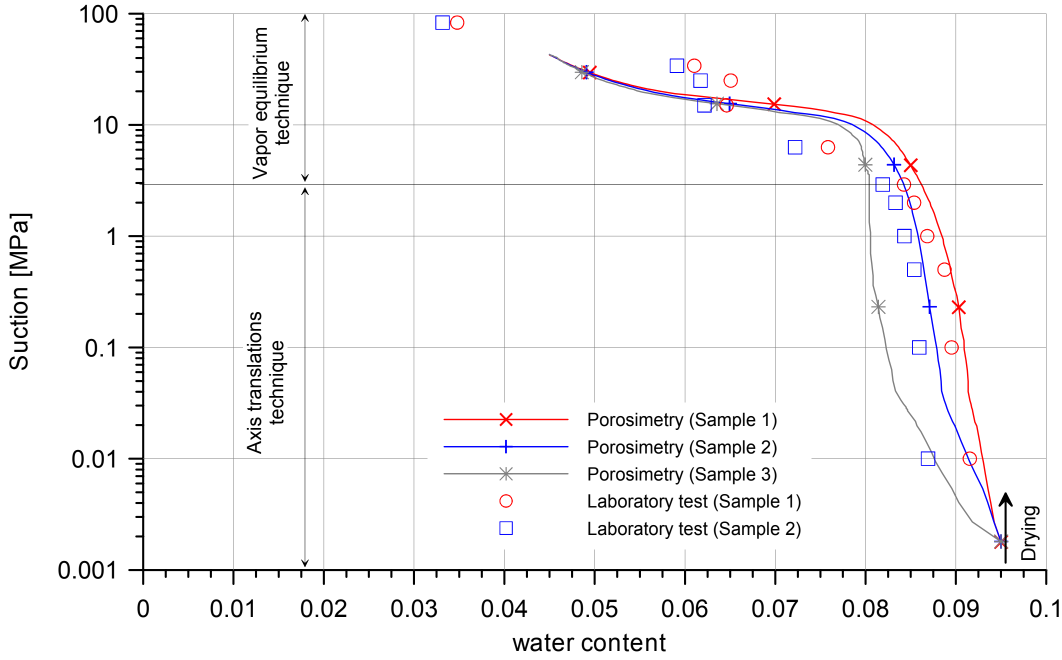

Figure 3.29: Water retention curve of Opalinus Clay rock, expressed in terms of water content, obtained with MIP.

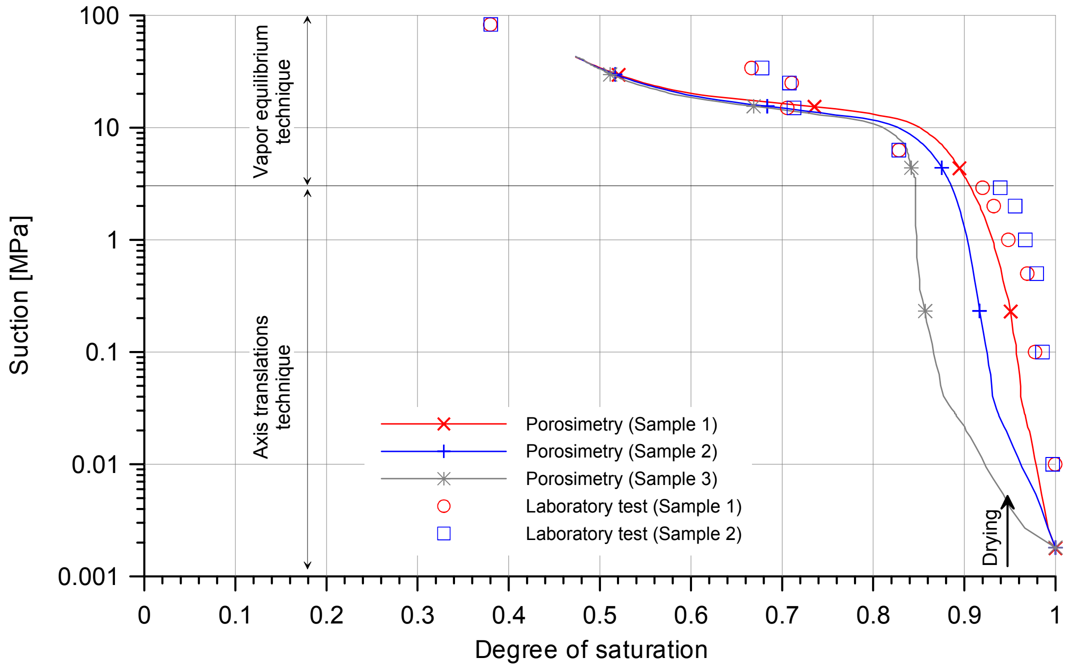

Figure 3.30: Water retention curve of Opalinus Clay rock, expressed in terms of degree of saturation. MIP and comparison with experimental determination.

3.6.2 Hydraulic conductivity

MIP can be used to estimate the value of saturated permeability by means of the following equations, (*García-Bengochea et al. 1979, in Romero, 1999*):

$$k_w\left(d_m\right)=\frac{\rho_w g n}{32\mu}\sum_i^m x_i^2\overline{f}\left(x_i\right) \qquad \text{(Eq 3.13)}$$

where ρ_w is the water density at 22 ºC, g the gravitational acceleration, μ the coefficient of absolute viscosity of water at 22 ºC, n the porosity and $\overline{f}\left(x_i\right)$ the relative frequency of pore diameter $\left(x_i\right)$. Figure 3.31 represents the relative frequency of pore diameter $\left(x_i\right)$.

The value of the permeability function $\sum_i^m x_i^2\overline{f}\left(x_i\right)$ obtained for the samples 1, 2 and 3 were: 1.97E+08 nm^2, 1.46E+08 nm^2 y 1.36E+08 nm^2, respectively. The values of the saturated permeability determined with MIP for samples 1, 2 and 3were: 6.31E-12 m/s, 4.90E-12 m/s and 3.70E-12, respectively. Note that the relevant values to estimate permeability are mainly related to the bigger pore size $\left(x_i > 10\ \mu\text{m}\right)$.

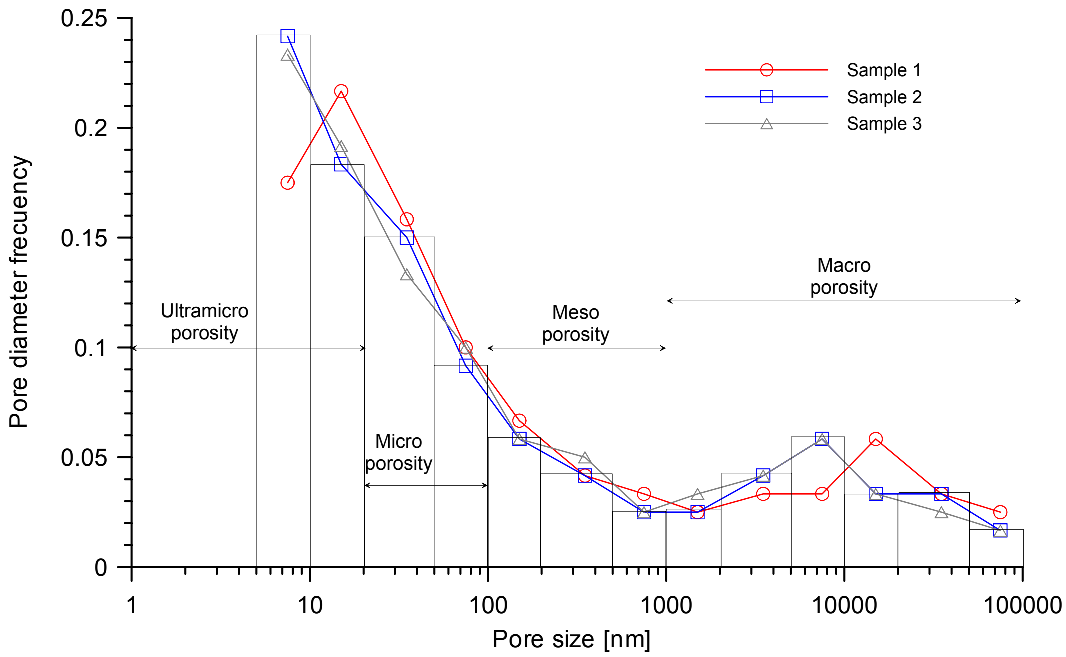

Figure 3.31: Relative frequency of pores diameters.

The relative permeability of water can be influenced by the pore size and pore distribution of the rock. The MIP can be used to evaluate the relative permeability following the equation 3.14 *(Romero, 1999)*:

$$\frac{k_{(w)}}{k_{(w)sat}}(x) \cong \frac{\int_{x_{\min}}^{x} x^2 f(x)\,dx}{\int_{x_{\min}}^{x_{\max}} x^2 f(x)\,dx} \qquad \text{(Eq 3.14)}$$

where the porous media is characterized by the pore diameter (x) and the relative frequency $f(x)$. The relative permeability was determined by integration of the pores from $x_{\min} = 6.8\ \text{nm}$ until the pore diameter associated with each degree of saturation. Figure 3.32 shows the relative permeability curves as a function of degree of saturation, obtained by MIP.

Figure 3.33 shows the relative permeability curves as a function of degree of saturation obtained by back-analysis of infiltration tests performed with Code_Bright *(Muñoz et al., 2003)*, using the Van Genuchten expression, equation 3.15.

$$k_{rl} = \sqrt{S_r}\left(1-\left(1-S_r^{1/\lambda}\right)^{\lambda}\right)^2 \qquad \text{(Eq 3.15)}$$

where S_r is the degree of saturation $(0 \le S_r \le 1)$, S_{rl} the residual degree of saturation (0), S_{ls} maximum degree of saturations (1.0), λ rock parameter (0.135).

In order to obtain the relative permeability law by means of fits of MIP data, the expression 3.15 and a generalized power law were used. The parameter obtained for the expression 3.15 was $\lambda = 0.245$, whereas the generalized power law was the following:

$$k_{rl} = A S_e^{\alpha} \qquad \text{(Eq 3.16)}$$

where A is a constant (1), α the power (16), S_e the effective degree of saturation $S_e = \frac{S_r - S_{r0}}{1 - S_{r0}}$ and S_{r0} the residual degree of saturations (0.6).

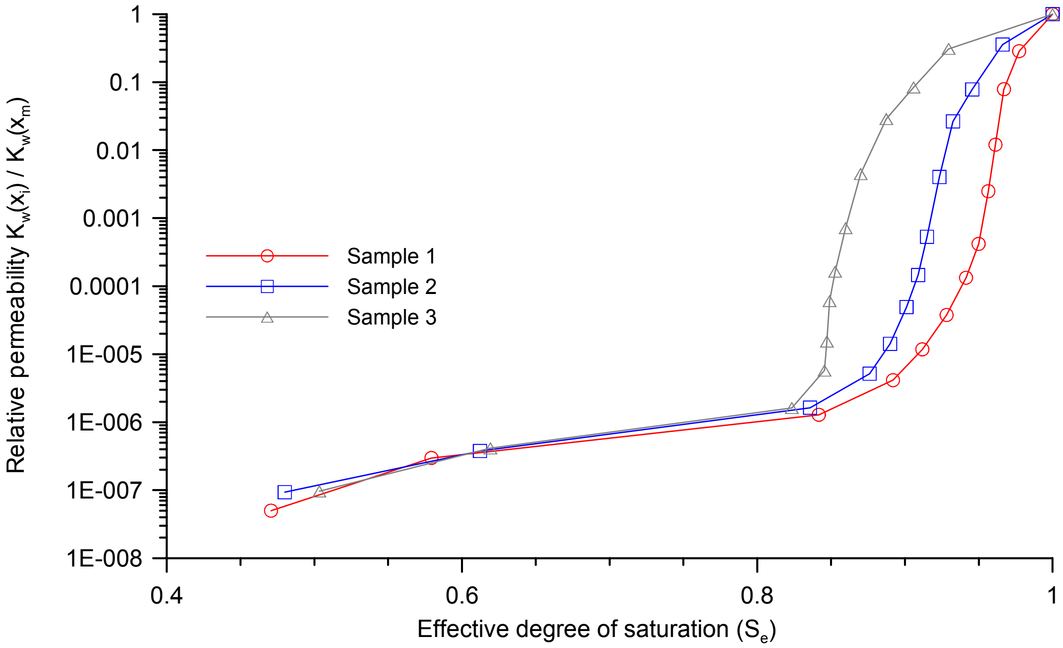

Figure 3.32: Relative permeability law obtained by means of mercury intrusion porosimetry.

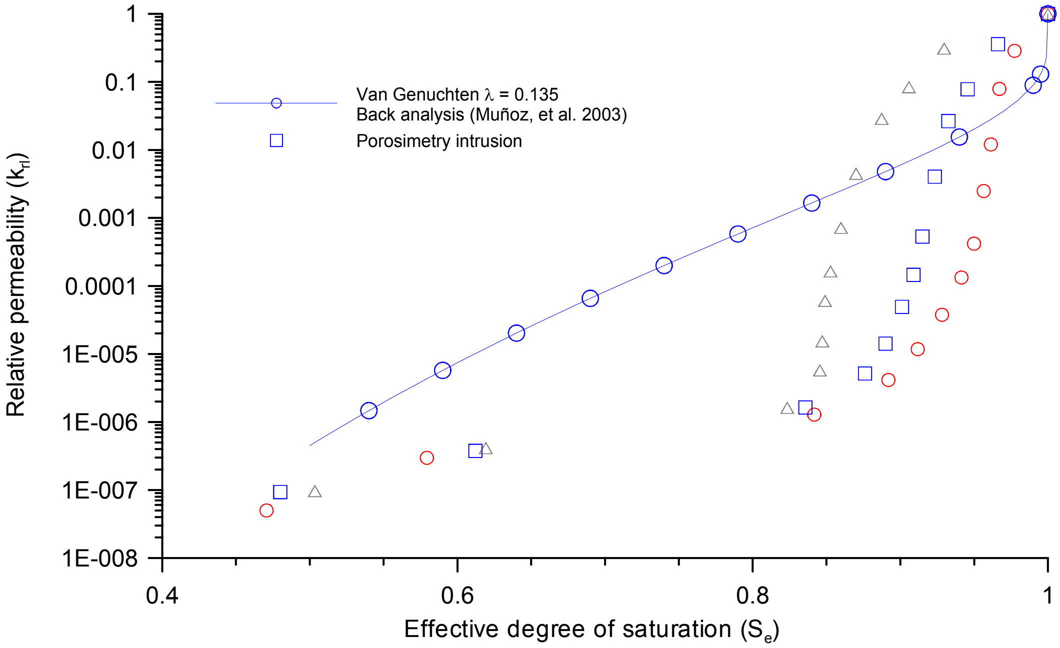

Figure 3.33: Relative permeability law obtained by back analysis of infiltration tests and by means of fits with least squares method of MIP.

3.6.3 Scanning electron microscopy

Direct observations of the fabric of Opalinus Clay rock were performed by means of Scanning Electron Microscope (SEM), where photomicrographs with zoom of 500x and 2000x were taken. Samples were taken from the borehole BVE 90/1 at 1.85 m depth. Figure 3.34 shows the photomicrograph taken with zoom of 500x, where can be seen a very compact fabric of the rock. The clay aggregates are shown in Figure 3.35, where the photomicrograph was taken with zoom of 2000x. The pore size indicated in this figure (ellipses in dashes line) varies between 5 μm to 15 μm. It corresponds to the macro-porosity determined with MIP. The maximum size of the clay aggregates indicated in Figure 3.35 is 32 μm.

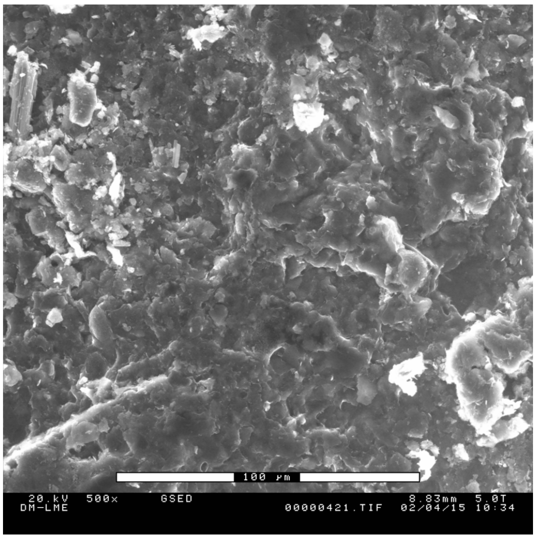

Figure 3.34: Photomicrograph of the Opalinus Clay fabric taken with a zoom of 500x.

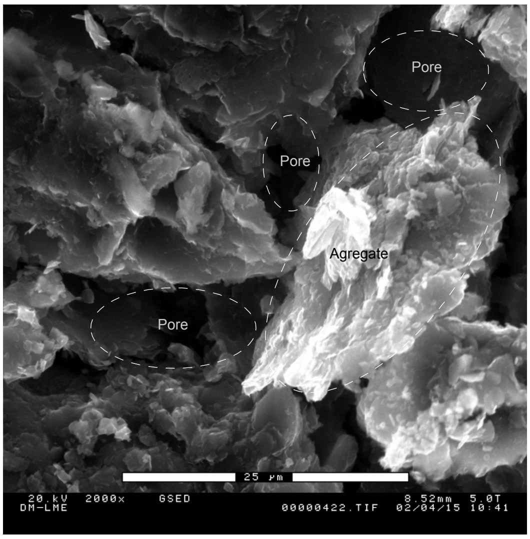

Figure 3.35: Photomicrograph of the Opalinus Clay fabric taken with a zoom of 2000x.

3.7 Uniaxial compression test

Uniaxial compression tests were carried out in three cores of Opalinus clay rock in order to determine the Young modulus and Poisson's ratio at different water contents. The samples were extracted from borehole BHE-8 at 7.00, 7.50 and 9.00m depth. They were cut with a diamond saw, without water flushing, and were then topped using a sulphur mortar. They were then placed under different humidity contents using the vapour equilibrium techniques. Due to its size, it was necessary to impose an air flow through the dissolution and desiccator vessels in order to reduce the time needed to reach equilibrium. The samples were called C1, C2 and C3 and their size, applied suctions, water contents and degree of saturation are shown in Table 3.13.

Table 3.13: Size, suctions, water contents and degrees of saturation values for test samples C1, C2 and C3.

Sample	Diameter [mm]	Length [mm]	Suction [MPa]	HR [%]	*w* [%]	Sr [%]
C1	72	143.3	70.0	60.0	3.22	40.0
C2	72	146.5	30.0	80.0	4.45	55.0
C3	72	145.0	15.0	90.0	5.94	73.0

The samples present stratification planes inclined from 65° to 70° with respect to the longitudinal axis. The failure was brittle and took place in a plane dipping between 40° and 43° with respect to the longitudinal axis.

Tests were performed in a strain controlled equipment. The displacement rate was of 0.01 mm/min for samples C1 and C3, whereas the displacement rate applied to sample C2 was 0.01mm/min until a vertical stress of 7.40 MPa was reached. Then the rate was increased to 0.1 mm/min, until failure. Longitudinal strains were measured using displacement transducers (LVDT) and strain gages. Radial strains were measured using strain gages. Figure 3.36 shows the instrumentation used in the samples and Figure 3.37 shows the sample C3 after failure. Figure 3.38, Figure 3.39 and Figure 3.40 show the longitudinal and radial stress-strain behaviour for the samples C1, C2 and C3, respectively.

The deformation and strength parameters determined are presented in Table 3.14. The Young's modulus of the samples C1 and C3 were calculated in the reloading phase. Previous in-situ and rock laboratory tests suggest a Young's modulus for Opalinus Clay which ranges between 1000 and 7000 MPa (*Thury and Bossart, 1999*). Young's modulus of $E = 6000\ \text{MPa}$, Poisson's ratio of $\upsilon = 0.27$ and uniaxial compressive strengths of $\sigma_{f(//)} = 10.0\ \text{MPa}$ and $\sigma_{f(\perp)} = 16.0\ \text{MPa}$ have been reported by (*Bock, 2001)*.

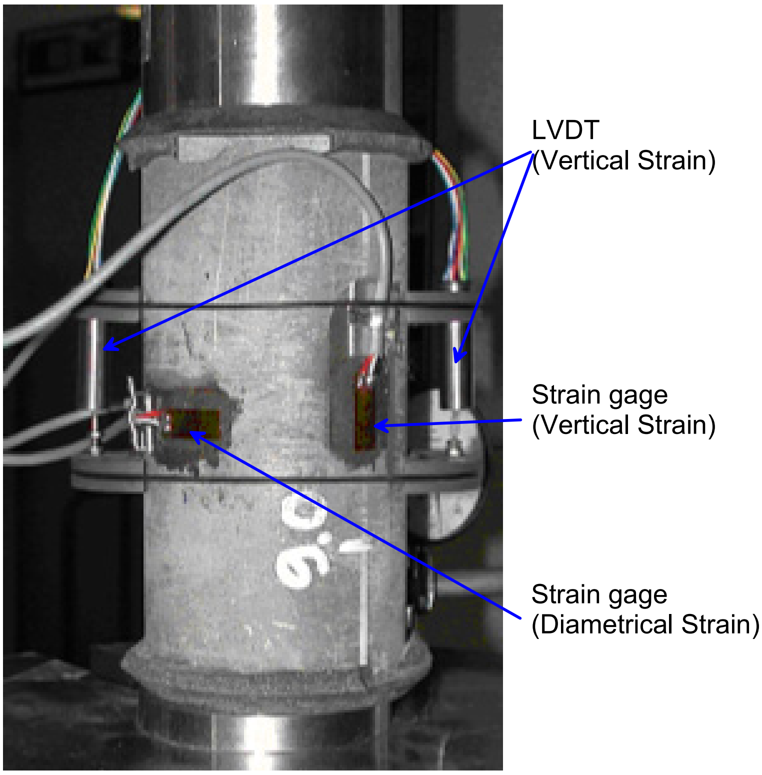

Figure 3.36: Instrumentation of samples with two displacement transducers (LVDT) and two strain gages in order to measure the longitudinal strain. Radial strain was measured using two strain gages placed horizontally.

Figure 3.37*: Sample C3 after the failure. Sample C3 presents the stratification planes inclined between 65° and 70° with respect to the longitudinal axis. Failure occurs in a plane inclined between 40° and 43° with respect to the longitudinal axis.*

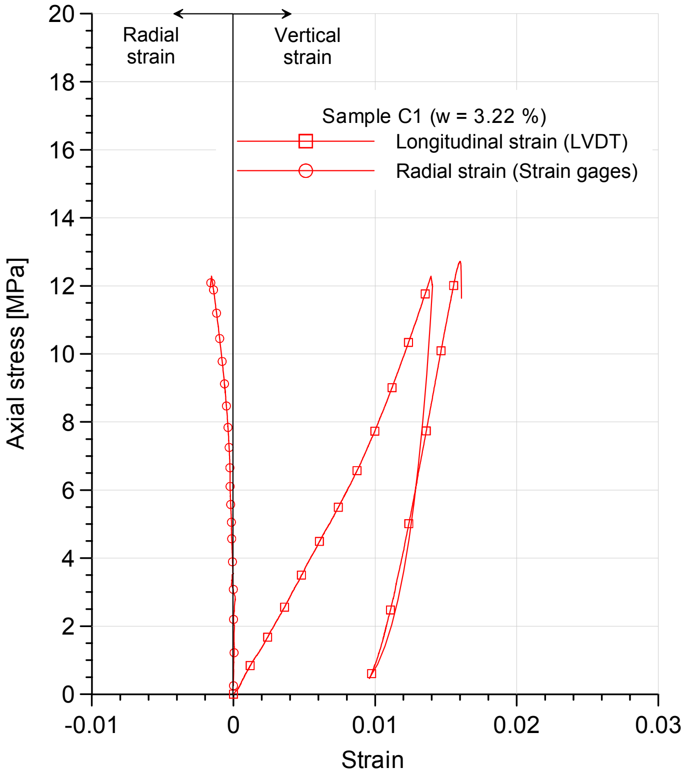

Figure 3.38: Stress-strain curves of uniaxial compressive test of sample C1

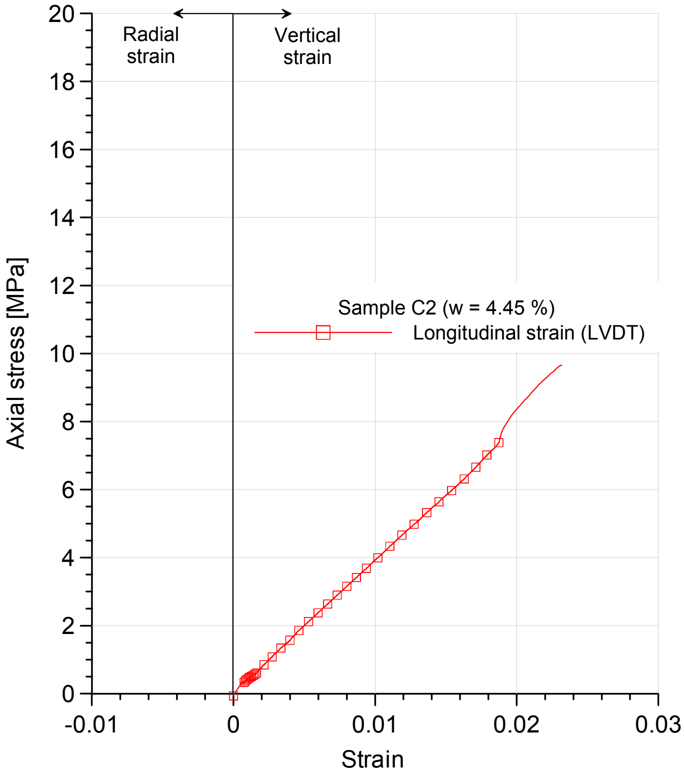

Figure 3.39: Stress-strain curves of uniaxial compressive test of sample C2.

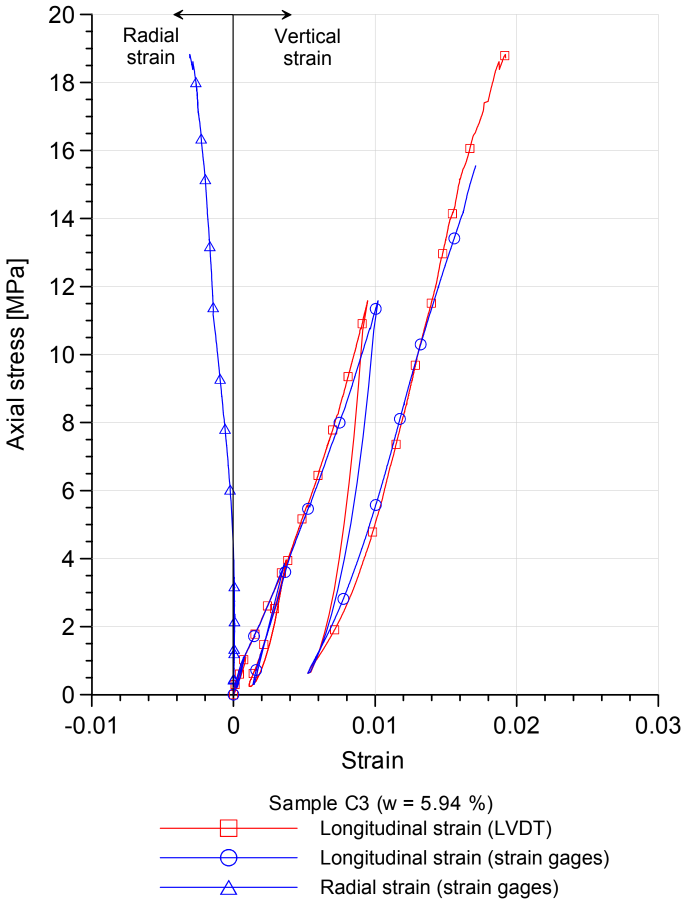

Figure 3.40: Stress-strain curves of uniaxial compressive test of sample C3

Table 3.14: Determined parameters of deformation and strength of Opalinus clay rock in uniaxial compressive laboratory tests.

Sample	Water content (w) [%]	Young's modulus (**E**) [MPa]	Poisson's ratio (ν)	Uniaxial compressive strength (σ_{failure}) [MPa]
C1	3.22	1055	0.210	12.72
C2	4.45	350	-	9.65
C3	5.94	1440	0.330	18.82

CHAPTER IV

T-H-M FIELD AND SMALL SCALE EXPERIMENTS
HE EXPERIMENT AND PULSE HEATING TEST

4.1 Introduction

In this chapter, the behaviour of the Opalinus Clays rock under thermal actions will be analyzed. The coupled T-H-M behaviour of the rock and the interactions with bentonite is analyzed in a large scale heating experiment carried out in the Mont Terri Underground Rock Laboratory. The thermal expansion coefficient of the rock by means of heating-cooling cycles will be determined. Finally, a pulse heating test carried out in the laboratory will be presented. In this test, the water saturated permeability, gas permeability, the rock swelling pressure and the rock reaction against a pulse of heat will be determined.

4.2 Description of Heating Experiment (HE)

The Heating Experiment (HE) is a large scale heating test carried out in the Mont Terri Underground Rock Laboratory. The objectives of the Heating Experiment were to acquire knowledge about the coupled Thermo-Hydro-Mechanical (THM) processes developed in the argillaceous rock and in the saturated bentonite buffer. Special emphasis was given to the study of the interaction between rock and bentonite. The concept of the experiment was to simulate, in a controlled way, thermal and hydraulic conditions which could be similar to those found in a high level waste repository built in an argillaceous rock of the type of “Opalinus clay”.

The HE experiment was located on the so-called “HE niche” on the west wall of the New Gallery of the underground rock laboratory, in the shaly facies of the Opalinus clay formations. The HE niche is 5.4 m wide, 7.0 m long and 4.70 m height. Figure 4.1

shows the 3D view of the Mont Terri Underground Rock Laboratory and the location of the HE niche, *(http://www.mont-terri.ch)*.

The HE experiment was instrumented with sensors of temperature, pore water pressure and inclinometers located in boreholes performed around the heating borehole BHE-0. The instrumentation provides data on the rock reaction against the bentonite swelling and thermal load. Figure 4.2 shows the upper view of the niche, where it can be seen the instrumentation boreholes (BHE-1 to BHE-20) that were drilled around the heater borehole BHE-0 to monitor different parameters of the host rock, such as, temperature, pore water pressure and radial deformation *(Fuentes-Cantillana et al., 2001)*.

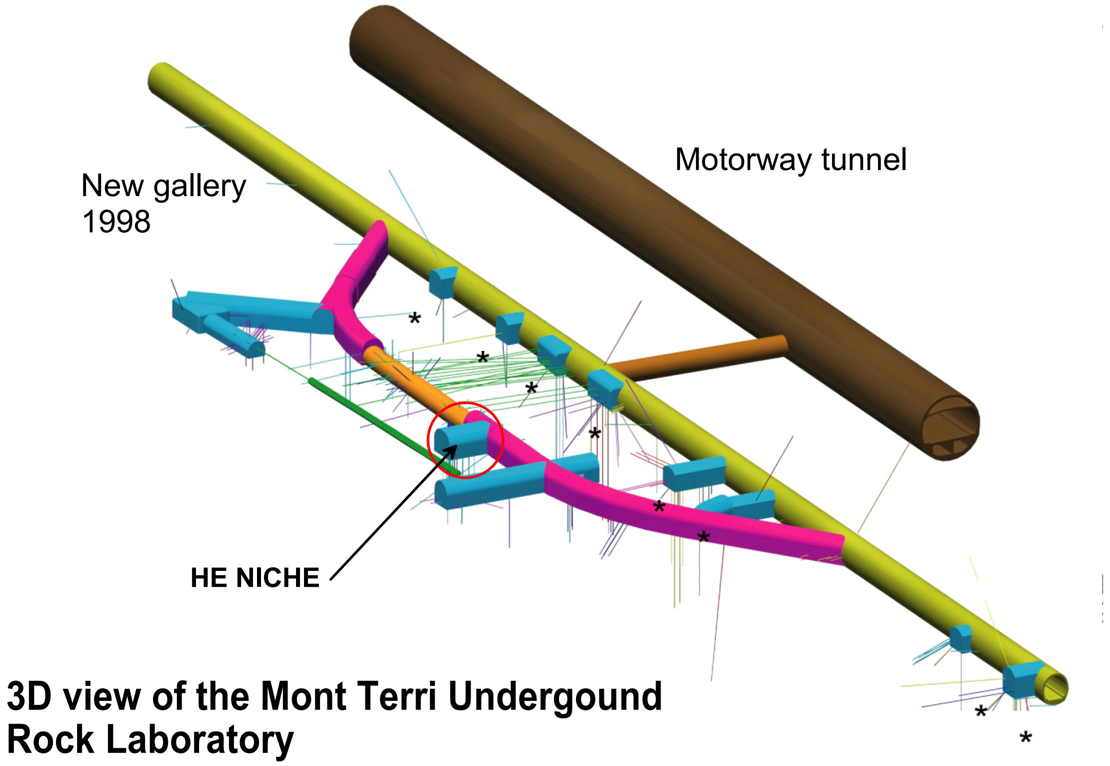

Figure 4.1: 3D view of the Mont Terri Underground Rock Laboratory and the location of the Heating Experiment, HE niche (http://www.mont-terri.ch).

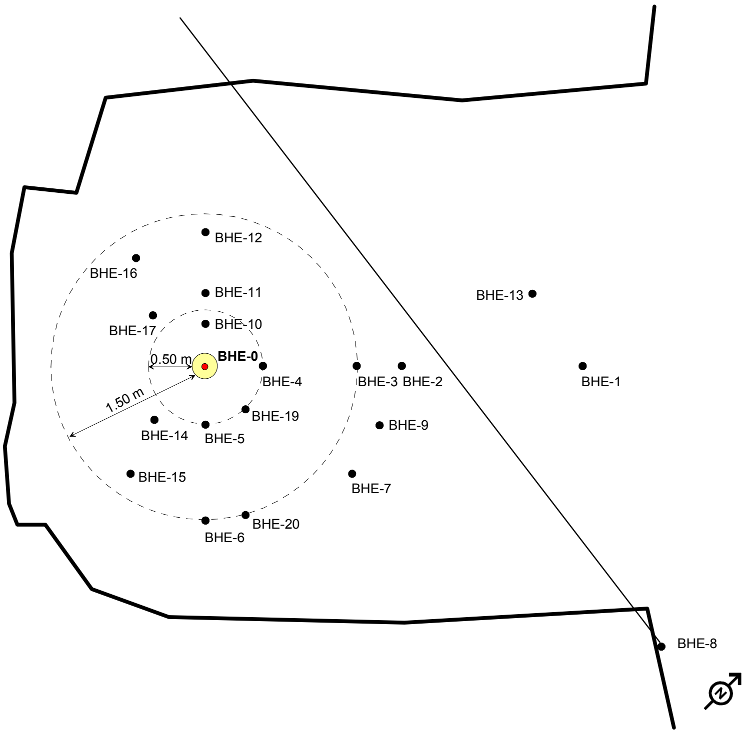

Figure 4.2: Upper view of the HE niche, (Fuentes-Castillana J.L., et al., 2001)

A vertical borehole 300 mm in diameter and 7.0 m depth, identified as BHE-0, was drilled in the niche floor. A heating tube with an external diameter of 100 mm was placed in the axis of the borehole BHE-0. A heater of 75 mm in diameter and 2.00 m length was placed into the heating tube from 4.0 m to 6.00 m depth. Cylindrical ceramic filter elements were installed to accelerate the hydration of the bentonite buffer. These filters were fixed to the outer part of the heating tube. The gap between the ceramic filters and the rock was backfilled with ring-shaped compacted bentonite blocks, 0.10 m thick, from 2.0 m to 7.0 m depth. The rest of the borehole, from 0.40 m to 2.0 m depth, was backfilled with dry sand. The upper part of borehole BHE-0, from 0.00 m to 0.40 m depth was sealed with resin to avoid leakages of water and gas. It also supports the vertical thrust caused by the bentonite swelling, *(Fuentes-Cantillana et al., 2001)*. The Figure 4.3 shows the vertical section of the borehole BHE-0 with all components of the experiment. Details of test components such as buffer bentonite, heater, heater tube and sintered filter are shown in Figure 4.4.

The HE experiment was developed in three different phases. The first phase consists of the hydration of the bentonite buffer using a synthetic water of similar composition to the water rock formation (*Pearson, 1998*). The hydration phase lasted 982 days, from

16/06/1999 (t = 0) until 22/02/2002 (t = 982 days). The hydration of the bentonite buffer was performed at four different depths, -6.90 m, -5.60 m, -4.40 m and -3.00 m at piezometric head of 2.0 m over the niche floor, *(Fuentes-Cantillana et al., (2001); García-Siñeriz and Rey (1999-2004))*.

The heating phase began once the bentonite buffer was fully saturated. Power was initially applied in steps of 140W, 150W, 285W and 580W, until the heater-buffer contact (r = 0.05m) reached a temperature of 100 ºC. Then, a constant temperature of 100 ºC was maintained at the heater-bentonite contact. A heating period of 540 days was considered, from 22/02/2002 (t = 982) until 22/02/2004 (t = 1522). After 18 months of heating the electric power was switched off, then the initial conditions of temperatures was recovered, *(García-Siñeriz and Rey (1999-2004))*. The temperature sensors TB00_05.00, TB05_05.00, TB06_05.00 and TB01_05.00 have been chosen in order to plot the temporal and spatial distribution of the measured temperatures. The time evolution of recorded temperature during the heating phase can be seen in Figure 4.5. The sensor TB06_05.00 failed after 1050 days of test. The distribution of temperature as a function of distance for different times during the heating phase is shown in Figure 4.6.

The measured time evolution of water pressure during the heating phase is shown in Figure 4.7. Sensors QB19/2, QB19/3 and QB20/2 were selected to plot the temporal and spatial pore water pressure evolution. Sensor QB19/3 failed after 1200 days of test. Temperature increments generate positive water pressures. Water pressure increments from 0.12MPa to 0.73MPa were measured by the sensor QB19/2 at time t = 1050 days, whereas the water pressure increment of 0.07MPa to 0.30MPa at time t = 1080 days was measured by the sensor QB20/2. Note that 30 days have elapsed between the maximum water pressure measured by sensors QB19/2 and QB20/2. At constant temperature, dissipation of water pressures is produced and they tend towards the initial condition.

A fast temperature increment generates a pulse of water pressure which is then dissipated with time. Figure 4.8 shows the increments of water pressure measured for different times during the heating phase. In this figure, the point 1 shows the water pressure measured by the sensors QB19/2 and QB20/2 at time t = 980 days (end of hydrations phase). The point 2 shows an increment of water pressure recorded by the sensor QB19/2 at time t = 1030 (Pw = 0.53MPa), whereas the sensor QB20/2 did not detect any increase. Point 3 shows the maximum water pressure increment (Pw = 0.65MPa) recorded by the sensor QB19/2 at time t = 1050 days. At the same time the sensor QB20/2 began to read water pressure increments (Pw = 0.14 MPa). The point 4 shows the beginning of water pressure dissipation at the sensor QB19/2 at time t = 1060 days, whereas the water pressure at sensor QB20/2 continues its increasing rate. In point 5 the dissipation of water pressure at sensor QB19/2 at time t = 1080 days can be observed, whereas the sensor QB20/2 records the maximum water pressure (Pw = 0.30MPa). Finally the point 6 shows the dissipation of water pressure at both sensors QB19/2 and QB20/2.

The measured values of radial displacements during hydration, heating and cooling phases have been plotted in Figure 4.9. The maximum measured value after the heating is in the order of 5.4 mm, whereas the measured values increase until 5.6mm during the cooling phase.

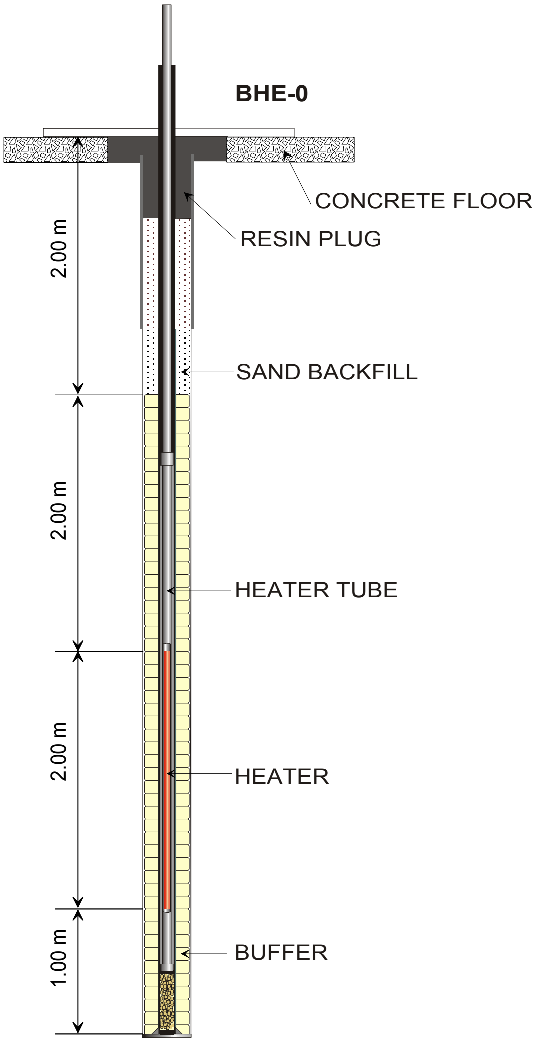

Figure 4.3: Vertical section of the borehole BHE-0. All test components are emplaced.

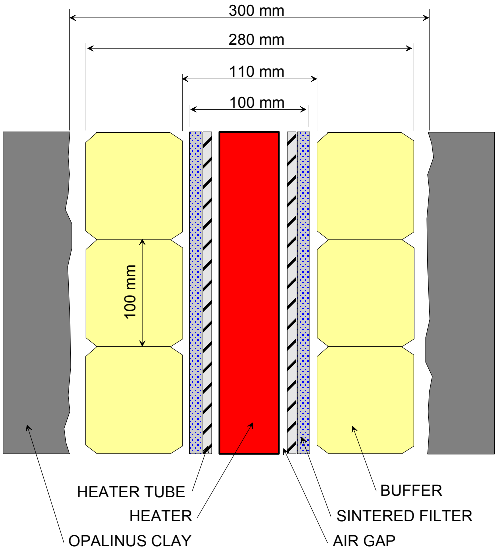

Figure 4.4: Detail of the test components.

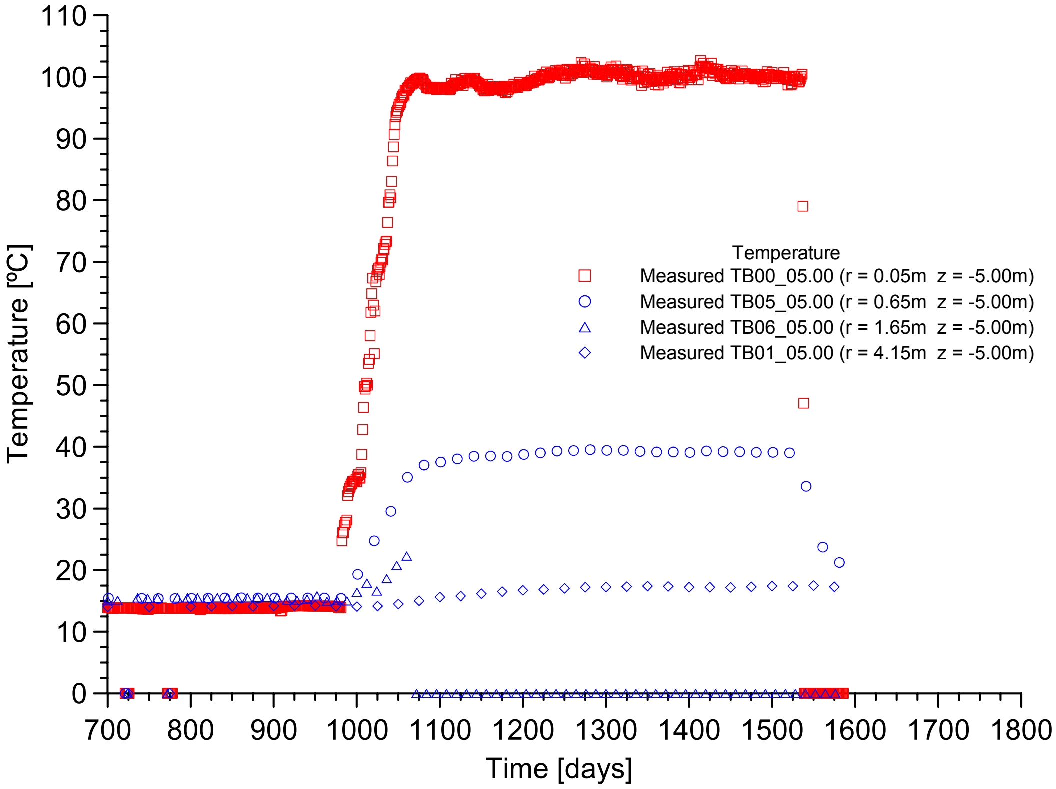

Figure 4.5: Time evolution of temperatures measured during the hydration, heating and cooling phases, in points located in the rock.

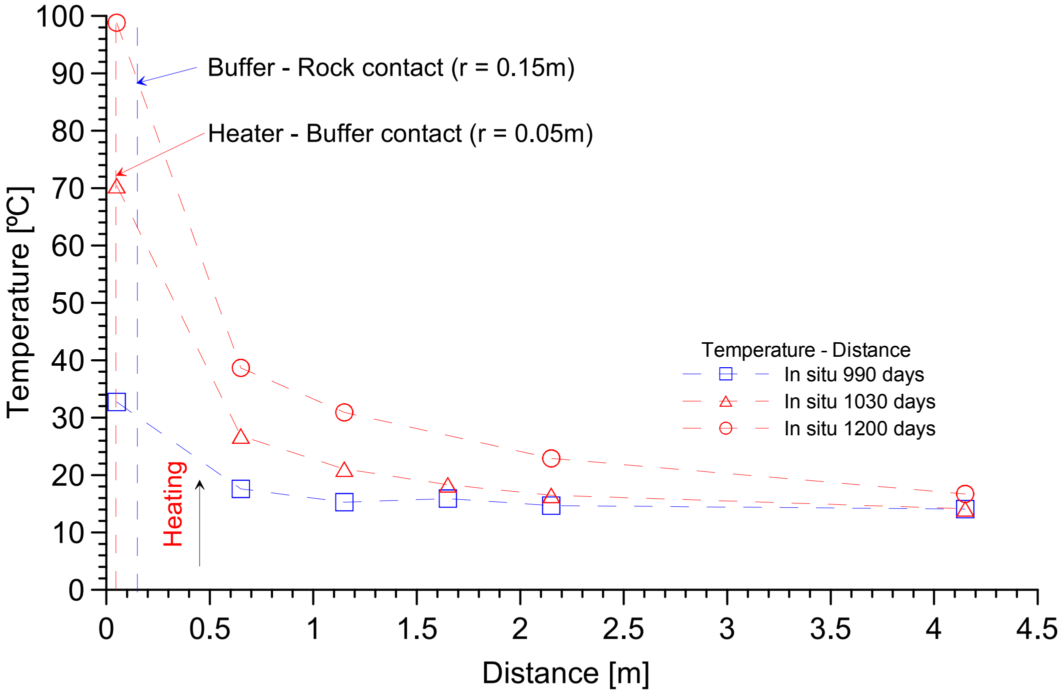

Figure 4.6: Measured distribution of temperature as a function of distance for different times during the heating phase.

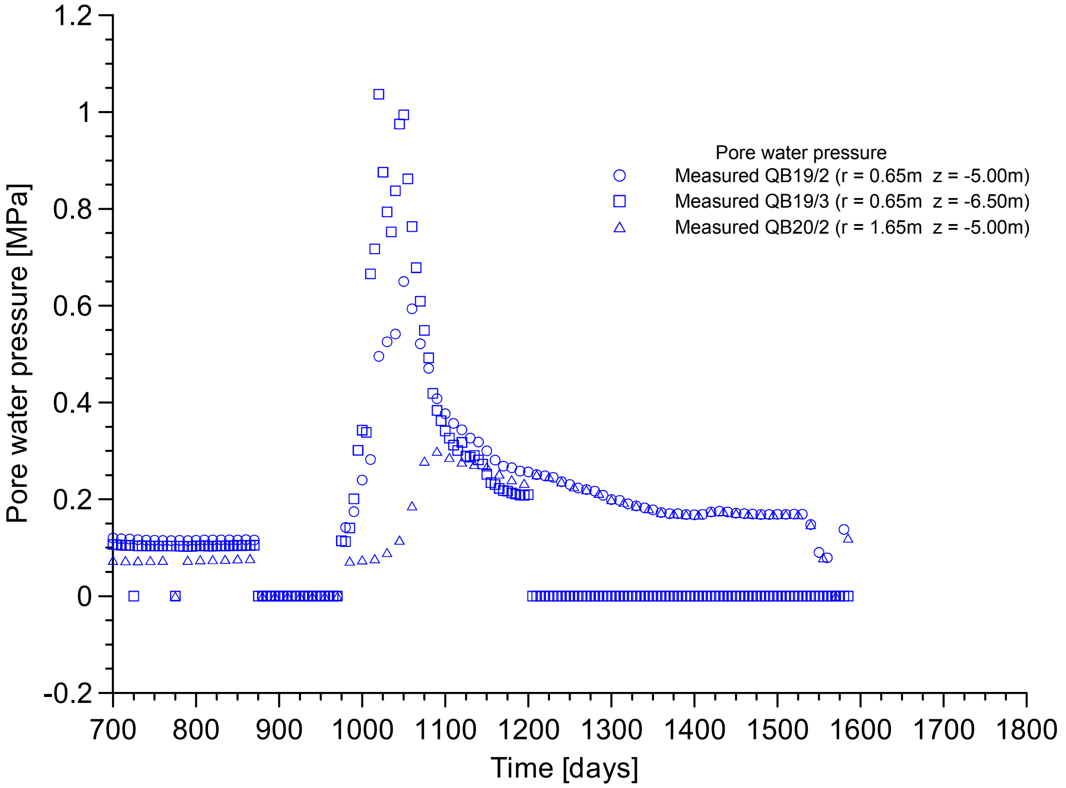

Figure 4.7: Time evolution of pore water pressure in points located in rock during hydration, heating and cooling phase.

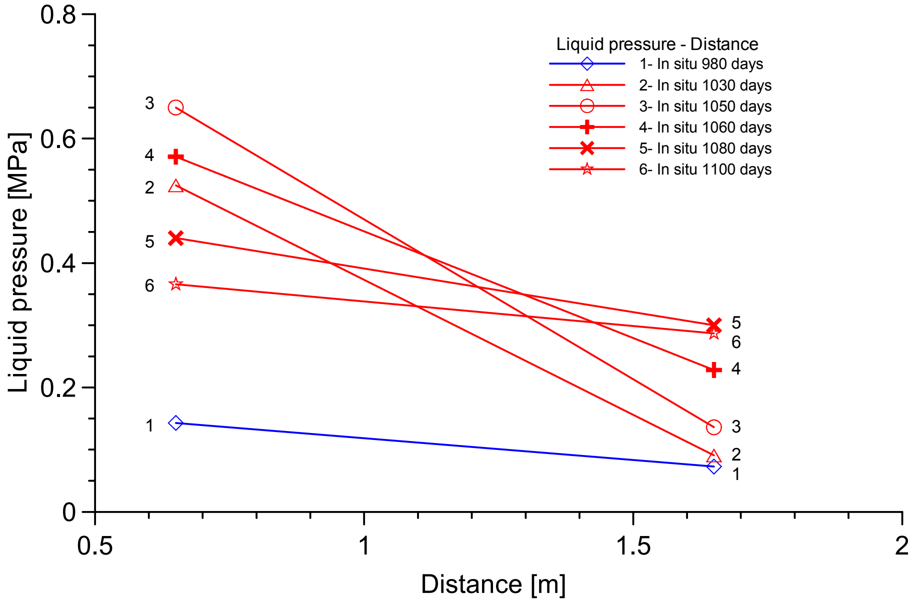

Figure 4.8: Measured distribution of liquid pressure as a function of distance for different times during the heating phase.

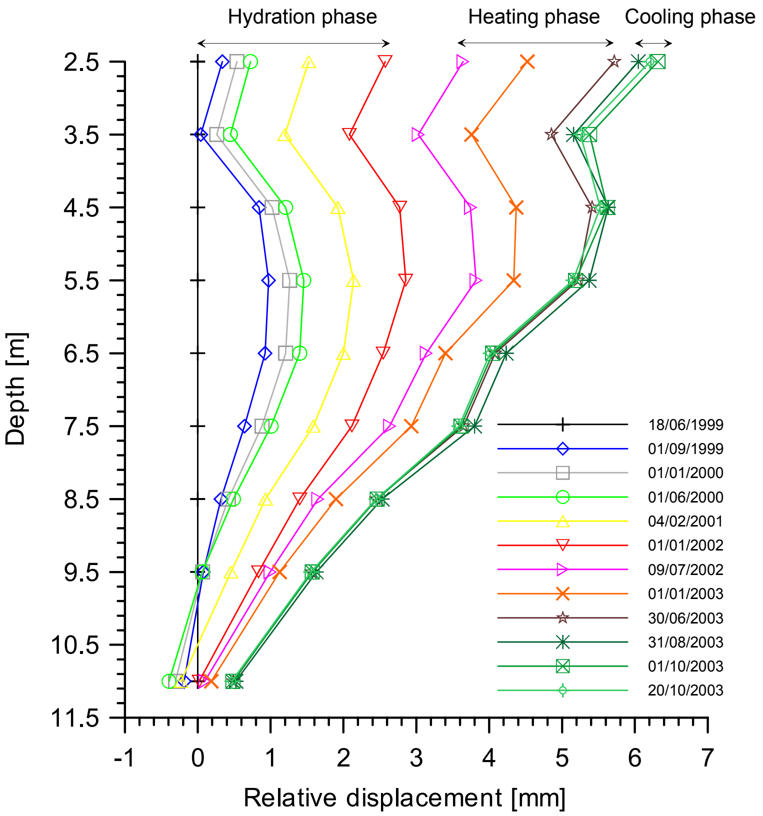

Figure 4.9: Profile of measured radial displacements versus depth (Garcia-Siñeriz & Rey, 1999-2004).

4.3 Thermal expansion test

The behaviour of the Opalinus clay rock under temperature changes was measured in laboratory tests. Rock samples were subjected heating-cooling cycles which ranged from 22 ºC to 65 ºC. The laboratory test was performed in a metallic frame, containing a sample of 72 mm in diameter and 60 mm height *(Pintado, (2002))*. The samples were extracted from borehole BH8-1 at 6.50 m depth. The initial bulk density, dry density, water content and degree of saturation of the samples tested were equal to 2.37 g/cm^3, 2.24 g/cm^3, 5.67 % and 76.5%, respectively. The samples have bedding planes ranging between 65º and 70º with respect to borehole axis.

The measuring system consists of two Pyrex glass rods, one on top of the sample and another one at the side of the sample. The vertical strain of the sample was measured by a mechanical micrometer placed over the upper end of the glass rod. The temperature of the sample was measured by means of three thermocouples. These were installed, one at each side and another one in the middle of the sample. The whole system was plunged in water bath. The sample was isolated of the water by a latex membrane. The temperature was imposed with four electric heaters of 125 Ohms per unit, and connected at 220 Volt. A scheme of the test can be seen in the Figure 4.10.

The first sample was tested with a water content of $\boldsymbol{w}$ = 5.67 %. Figure 4.11 shows the time evolution of the temperature and vertical strain, respectively. Figure 4.12 shows the vertical strain of expansion with the temperature. The second sample was dried until it reached a degree of saturation, Sr = 38 %, that corresponds to a water content of 2.80%. Drying was induced in a desiccator, where a relative humidity of 51% was imposed using a sulphuric acid solution. It took 6 weeks to achieve equilibrium. This sample was subjected to heating and cooling cycles ranging from 22 ºC to 65 ºC. Figure 4.13 shows the evolution of temperature and vertical strain with time, respectively. Figure 4.14 shows the vertical strain (expansion) with the temperature. Changes in temperature were slowly applied, at a rate of 2 ºC per hour in heating and at a rate of 1ºC per hour during cooling. It can be observed that deformations in heating cycles are greater than in cooling. Consequently there is an irreversible strain, which accumulates in each cycle. The obtained values for the linear thermal expansion coefficient (α) are indicated in Table 4.1. According to thermal expansion values presented in Table 4.1 the coefficient (α) increase slightly with the water content. A thermal conductivity of Opalinus Clay in the range $1.02 \text{ to } 2.16 \text{ WmK}^{-1}$ has been reported by *Hohner and Bossart, (1998)*.

Values for the linear thermal expansion coefficient are indicated for different kinds of rocks, such as $\alpha = 2.80E-06\,^{\circ}\mathrm{C}^{-1}$ for granite *(Keusen et al., (1989))*, and $\alpha = 4.00E-05\,^{\circ}\mathrm{C}^{-1}$ for salt *(Janssen et al., (1984))*. A thermal expansion coefficient of $\alpha = 4.13E-05\,^{\circ}\mathrm{C}^{-1}$ determined in Boom Clay has been reported by *Hueckel et al., (1998)*.

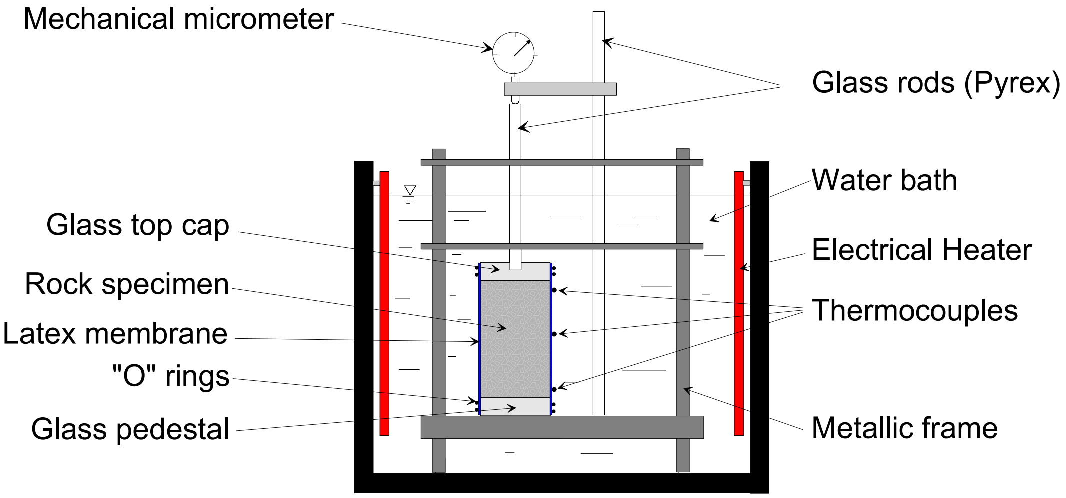

Figure 4.10: Equipment built to carry out the linear thermal expansion test.

Table 4.1: Linear thermal expansion coefficient for heating and cooling cycle in samples with different water contents.

Samples		**α** **[1/ºC]**
Heating	**w** =5.67%	1.40E-04
Cooling	**w**=5.67%	9.00E-05
Heating	**w** =2.80%	1.20E-04
Cooling	**w**=2.80%	8.00E-05

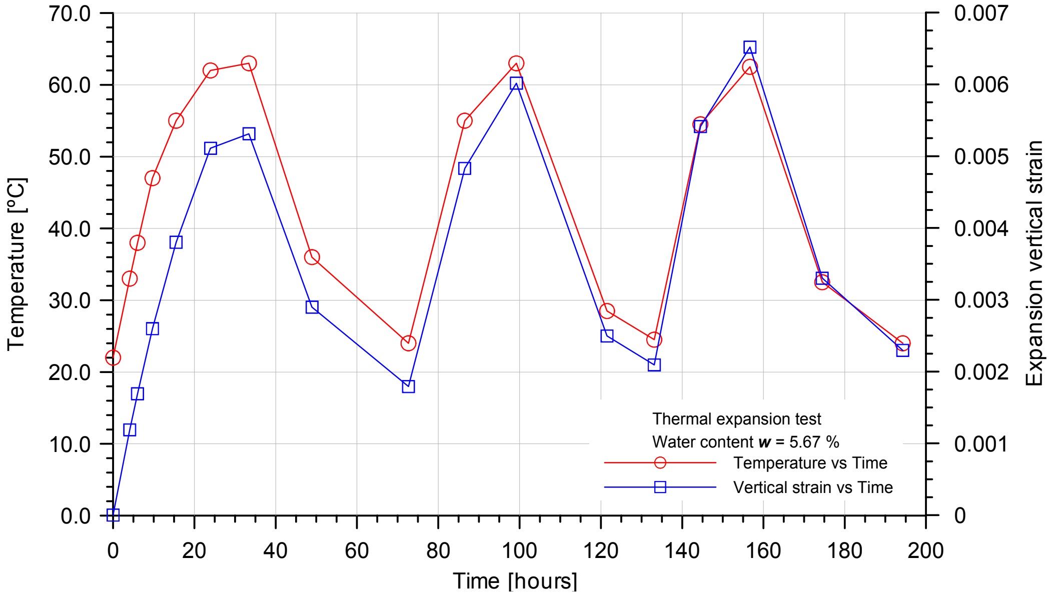

Figure 4.11: Time evolution of temperature and vertical strain during heating and cooling cycle. Water content w = 5.67%.

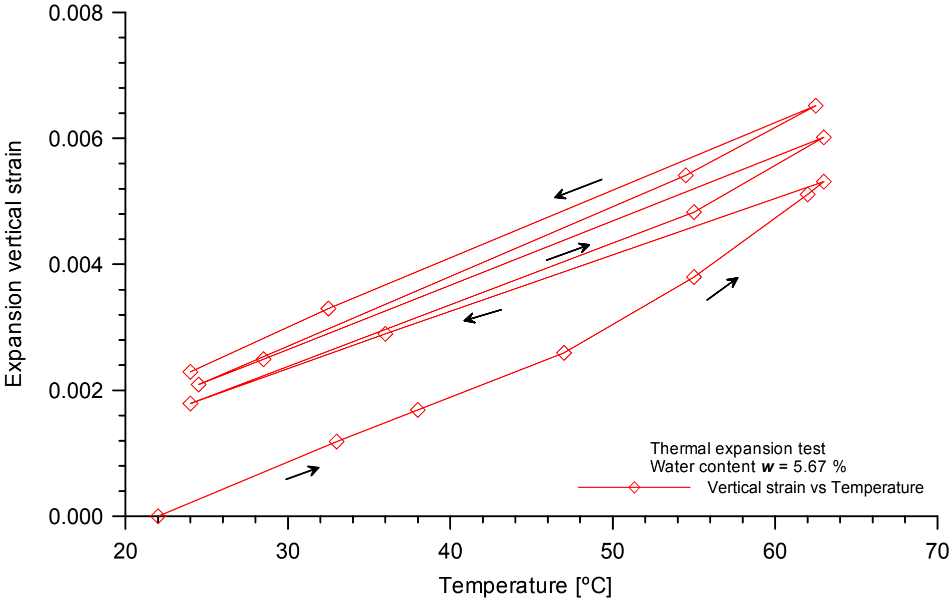

Figure 4.12: Vertical strain versus temperature during heating and cooling cycles. Water content w = 5.67%.

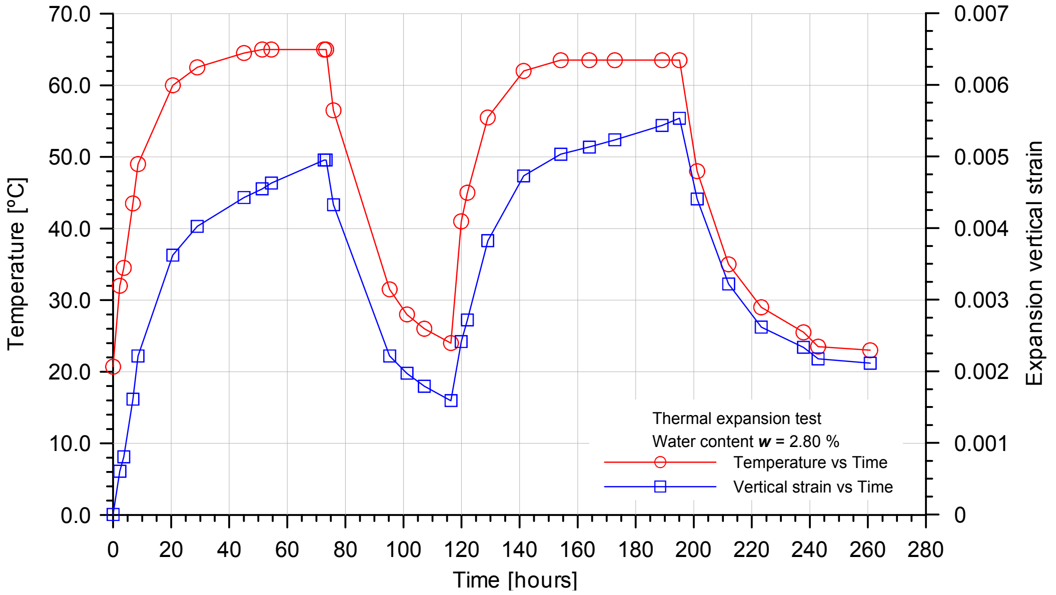

Figure 4.13: Time evolution of temperature and vertical strain with the time during heating and cooling cycles. Water content w = 2.80%.

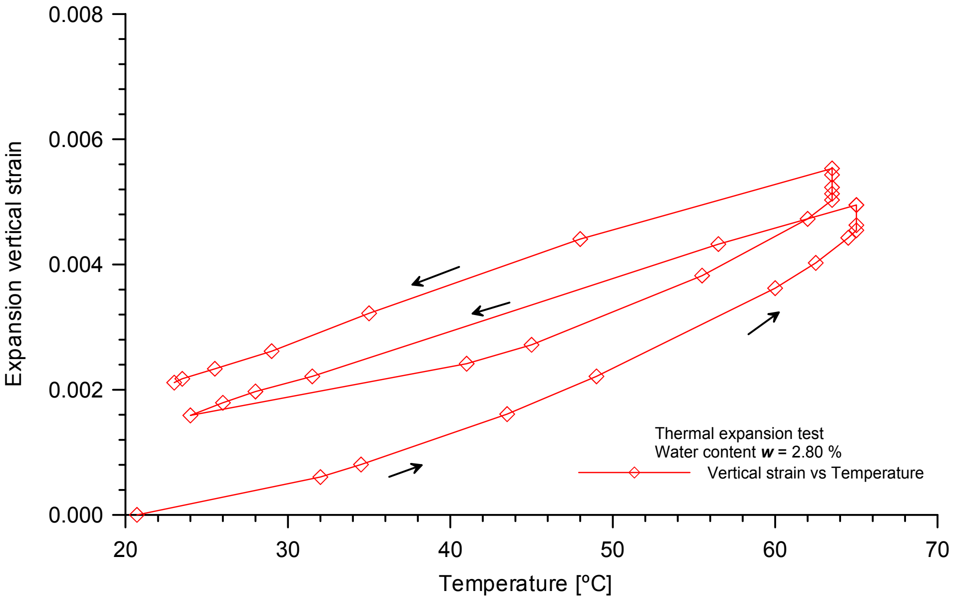

Figure 4.14: Vertical strain versus temperature during heating and cooling cycles. Water content w = 2.80%.

4.4 Pulse heating test

A laboratory test has been performed in order to analyze the coupled T-H-M behaviour of the Opalinus Clay rock. Laboratory equipment was designed and built to measure the rock reaction against a thermal load. The objective of this laboratory test is to measure the pore water pressure and temperature evolutions of the rock, during hydration and heating phases.

4.4.1 Description of the equipment

The equipment designed consists in a stainless steel ring of 75 mm in diameter and 100 mm height, where the sample is located. The ring has eight inlets which allow the installation of different types of sensors into the rock sample. An upper lid and bottom lid are screwed to the ring in order to maintain the sample tightly sealed. The sample is 70 mm in diameter and 100 mm height. The annular gap between the sample and the ring is filled with epoxi resin. The joining between the ring and the lids is a screw-on type and the hydraulic closure between them is assured by rubber "O"-rings. Figure 4.15 shows in schematic form the cell built.

The swelling pressure is registered by means of strain gages placed in a ring section with reduced thickness of wall. A thickness of the ring wall of 2.0 mm was determined after numerical simulations of the mechanical behaviour of the cell using Code_Bright. The vertical strain of the ring was measured by means of two strain gages diametrically opposed. Strain gages of the type $CEA-06-062UW120$, 6.0 mm length and 120 Ω, were provided by Vishay. In order to complete the Wheatstone bridge it was necessary to add two calibrated electric resistances of 120 Ω. The circumferential strain of the ring was measured with two strain gages diametrically opposite. The circumferential strain gages are rotated 90º respect to the vertical strain gages. The Wheatstone bridge was also completed with two calibrated electric resistances. The outlet voltage of each Wheatstone bridge was calibrated by means of water pressure. The strain gages were protected against environmental actions.

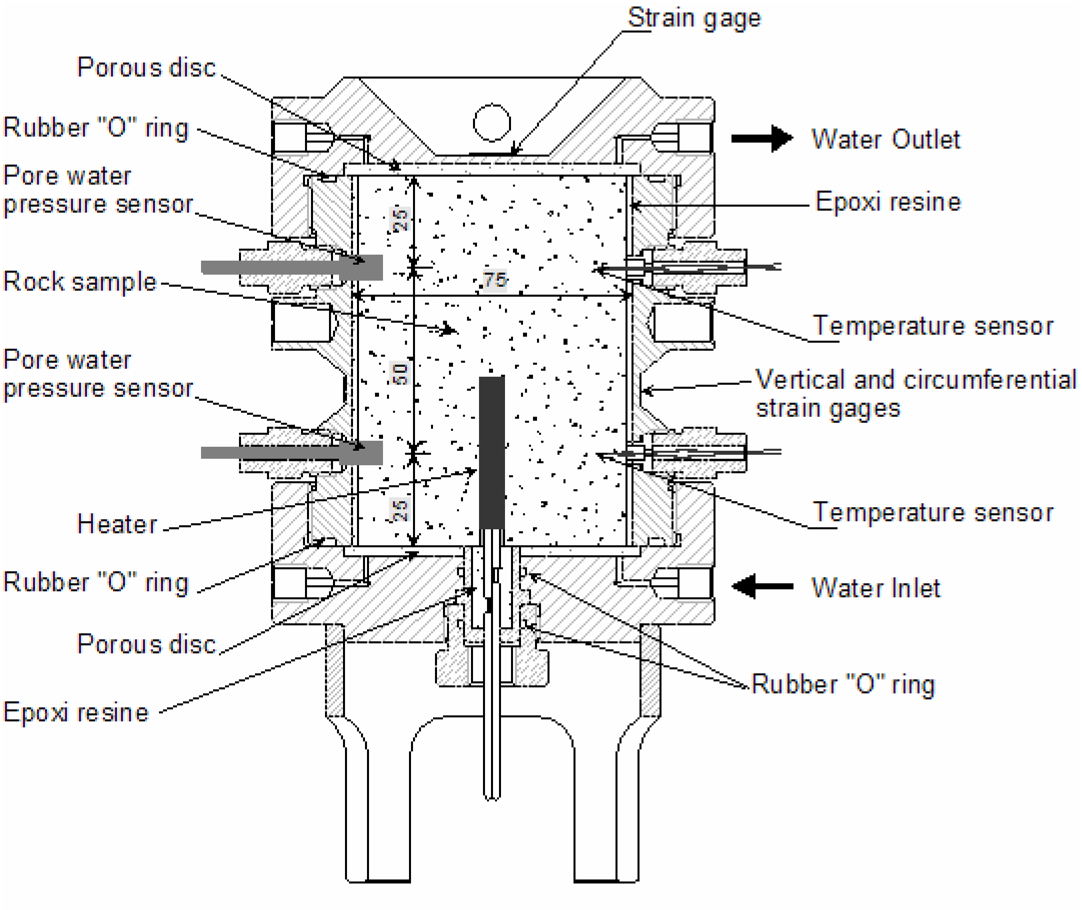

Figure 4.15: Cell built to perform laboratory pulse heating test.

Both upper and bottom lids has two spherical closing valves of water inlet/outlet. In the central part of upper lid two strain gages were installed in an area of reduced thickness. A thickness of 2.0 mm was decided after numerical simulations of the cell. The strain gages measure the bending deformation of the lid produced by the inner pressure. The Wheatstone bridge was completed with two calibrated electric resistances and the outlet voltage was calibrated by means of water pressure. In order to minimize the water volume between the sample and the outlet pipe, a porous disc of 3.0 mm thickness and outlet pipe of 0.79 mm (1/32”) in diameter were adopted.

A heater was installed in the bottom lid of the cell, coincident with the longitudinal axis of sample. The heater consists in an electrical resistance of cartridge type of 6.0 mm in diameter and 40 mm length. It is connected to a power supply variable between 12 to 40 Volts (CC). In order to ensure a correct thermal conductivity between the heater and the rock, a thin layer of silicone oil was applied to the heater-rock contact. The silicone oil acts as thermal conductor and avoids the existence of occluded air that acts as thermal insulating in the heater-rock contact. A plastic ring of low thermal conductivity (BLAUHÖG ®, *http://www.sertu.es*) was placed between the heater and the bottom lid in order to avoid heat flow towards the metallic components. The cables of heater were glued with epoxi resin into the metallic cylinder to avoid water leak through them. The metallic cylinder is pressed against the lid by means of a screw. A system of double rubber "O"-rings was built to ensure a reliable hydraulic seal.

The pore water pressure evolution during the hydrations and heating was registered with two miniature pore water pressure sensors (DRUC, model PDCR 81). The pore water pressure sensors are 6 mm in diameter and 12 mm length. They measure in a pressure range from 0.0 to 3.5 MPa. These sensors are located at 25 mm and 75 mm from the bottom part of the sample, respectively. The water pressure sensors were placed inside the sample. Once the sample was emplaced into the metallic ring, two holes of 6 mm in diameter and 5 mm depth were drilled in the sample. In order to avoid water leak through sensors connection, a hydraulic seal was ensure by means of rubber "O"-rings. Figure 4.16 shows in detail the lay out of pore water pressure sensor installation. The sensor is supported in its end by a plastic ring (ring carrier sensor), where the rubber "O"-ring is leaning. The sensor is pressed against the rock by means a screw (sensor's retain).

Four temperature sensors were installed in the cell (thermocouple type K, with weld point). The evolution of temperatures in the inner of the sample is measured with two sensors diametrically opposed to the pore water pressure sensors. These sensors are located at 25 mm and 75 mm from the bottom part of the sample, respectively. Figure 4.17 shows in detail the temperature sensor installation into the rock. The hydraulic closure is similar to the pore water pressure sensors described previously. The cables of the thermocouple are glued with epoxi resin to avoid water leak through them. A rubber "O"-ring placed in the plastic top is pressed against the metallic ring by means of screw (sensor retain). A third temperature sensor was located in the heater-rock contacts in order to measure the heater temperature evolutions.

The cell was operated within a temperature controlled water bath (T = 22 ºC), where the cell was submerged during the heating phase. The water bath had a volume of 20 l and its temperature was measured with a fourth temperature sensor.

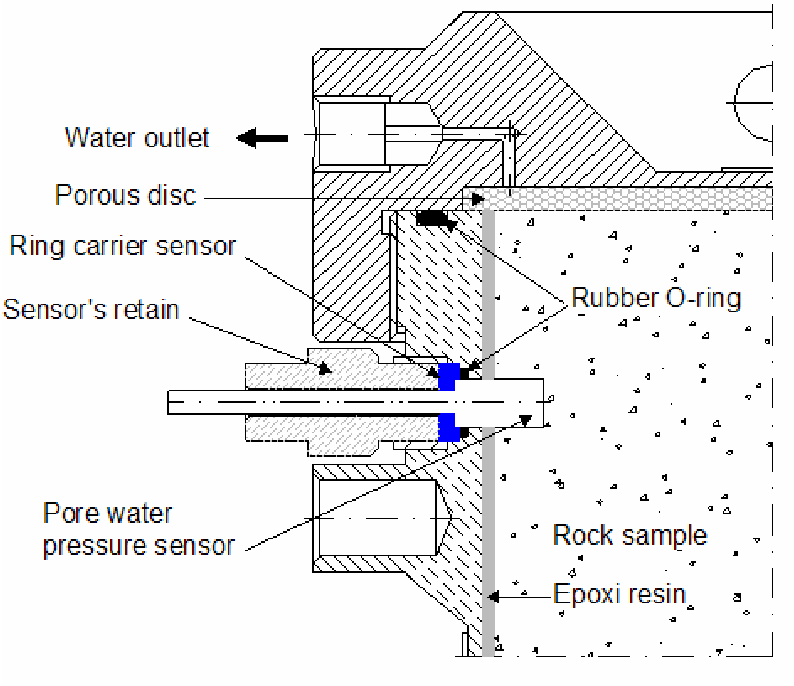

Figure 4.16: Pore water pressure sensor installation.

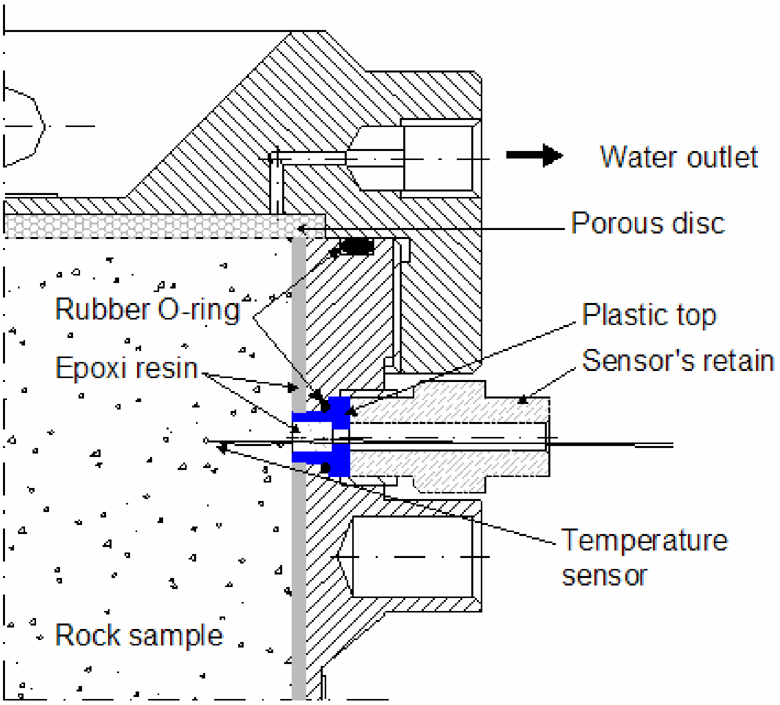

Figure 4.17: Temperature sensor installation.

Data was recorded by means of data acquisition board installed in a PC. The data acquisition board was provided by National Instruments, model NI PCI-6035E, with 16 bit analogical inputs at 200 kS/s. The interface between the sensors and the data acquisition board is performed whit modular signals conditioners of 5B series, provided by National Instruments. The modules 5B38-5 were used in signals conditioning of full bridge from strain gages. Modules 5B31-01 (millivolt input module, -1 V to +1 V input rage) was used to condition signals from pore water pressure sensors. The modules 5B47-K-05 were used to condition signals from thermocouples type K (0 ºC to 500 ºC). All modules were connected to a backplane of 16 channels with power supply voltage of +5.0 VCC. A Visual Basic code was developed to control the experiment.

The water infiltrated into the rock had similar composition of the Opalinus Clay formations (*Pearson, 1998*). The water volume infiltrated was measured manually with a traditional system double wall burette, whose resolution is 0.05 ml.

Figure 4.18 and Figure 4.19 show the pore water pressure sensor and temperature sensor used in the cell. Figure 4.20 and Figure 4.21 show the ring with the strain gages installed, which measure the vertical and circumferential strain, respectively. Figure 4.22 shows the upper lid with the strain gages installed, whereas Figure 4.23 shows the bottom lid with the heater already installed. Figure 4.24 shows the cell built to perform the pulse heating test. An overall view of the cell with all its components is given in Figure 4.25.

The calibration curves of different sensors are presented in the Appendix B. Figure B2 shows the calibration curves of the pore water pressures sensors. Figure B3 shows the thermocouple calibration curve, whereas Figure B4 shows the calibration curves of the strain gages. The curve of input (V) - power (W) of the heater is given in Figure B5.

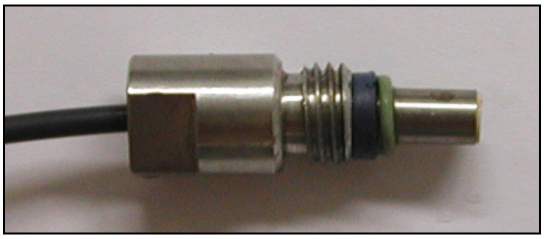

Figure 4.18: Miniature pore water pressure sensors (DRUC, model PDCR 81).

Figure 4.19: Temperature sensor (thermocouple type K with weld point).

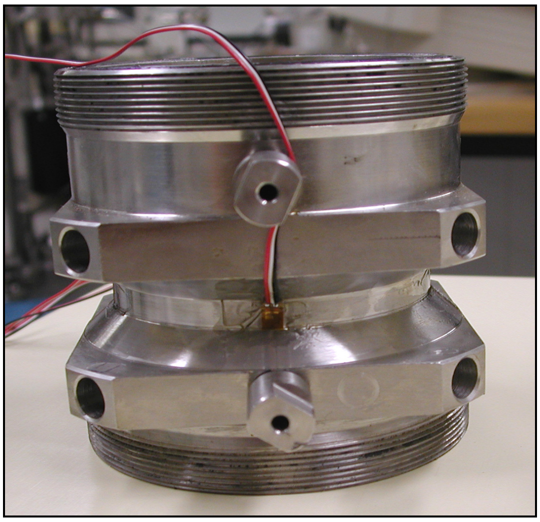

Figure 4.20: Strain gages to measure the vertical strain of the ring.

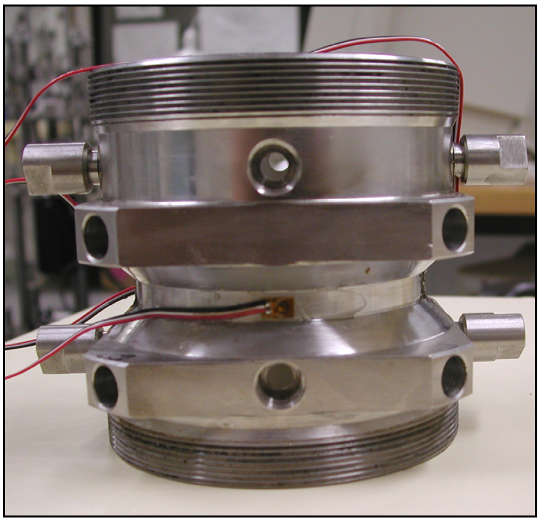

Figure 4.21: Strain gages to measure the circumferential strain of the ring.

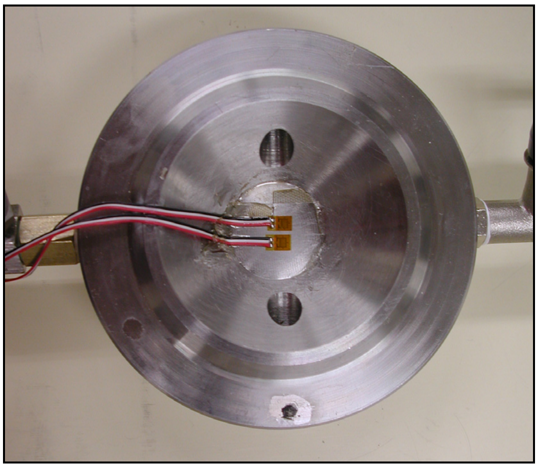

Figure 4.22: Upper lid with strain gages installed.

Figure 4.23: Bottom lid with the heater already installed.

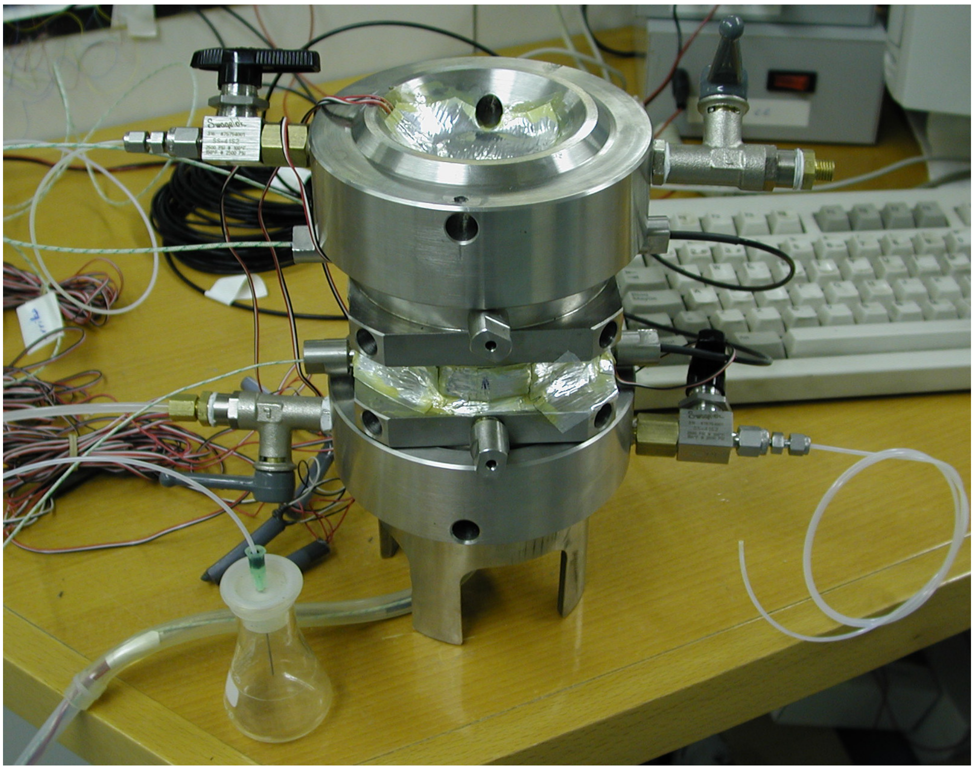

Figure 4.24: Cell built to perform the pulse heating test.

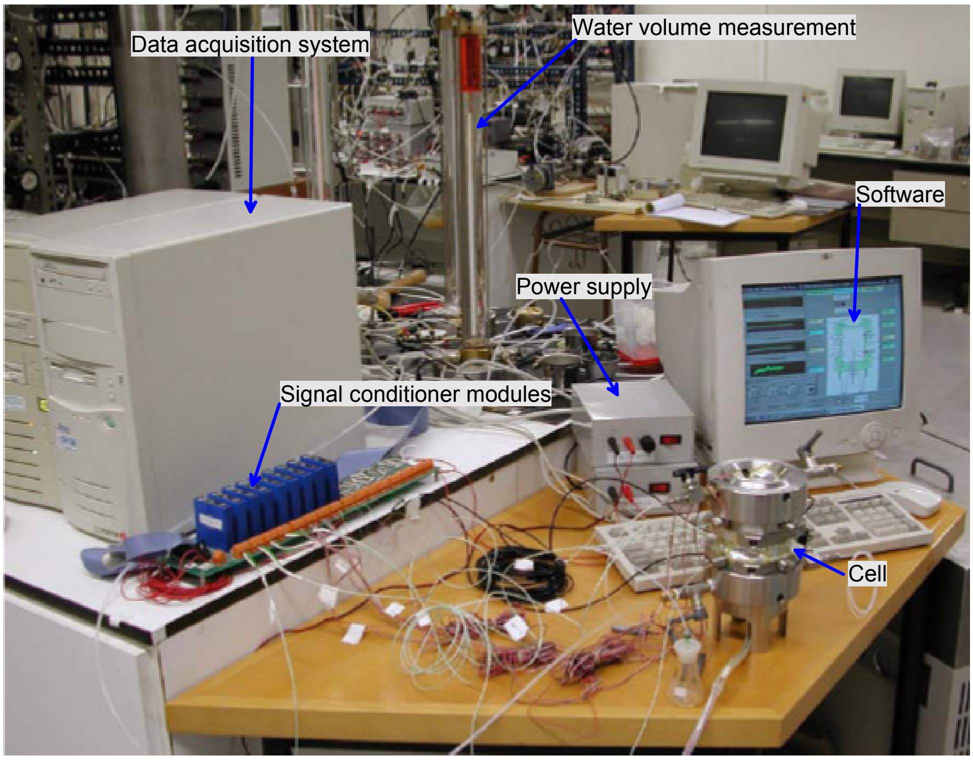

Figure 4.25: Cell and its component, data acquisition system, signals conditioner modules, power supply, water volume measure and software.

4.4.2 Experimental results

The sample tested was extracted from the borehole BVE 90/1 at 1.70m depth; it had 68.5 mm in diameter and 100 mm height. The sample had a water content of $w = 7.35\ \%$ $\left(S_l = 0.85\right)$ and bedding planes were parallel to its longitudinal axis. In Figure 4.26 can be seen the sample of Opalinus Clay before being placed into the cell ring. Figure 4.27 shows the bottom view of the sample already fit into the cell ring. In this figure it can be seen a drilling of 6.5 mm in diameter performed to place the heater into the rock and the silicone oil filling inner of the drill. The measured separation between the vertical fissures produced by drying of the rock (1.33 cm to 1.72 cm) is indicated in the photograph.

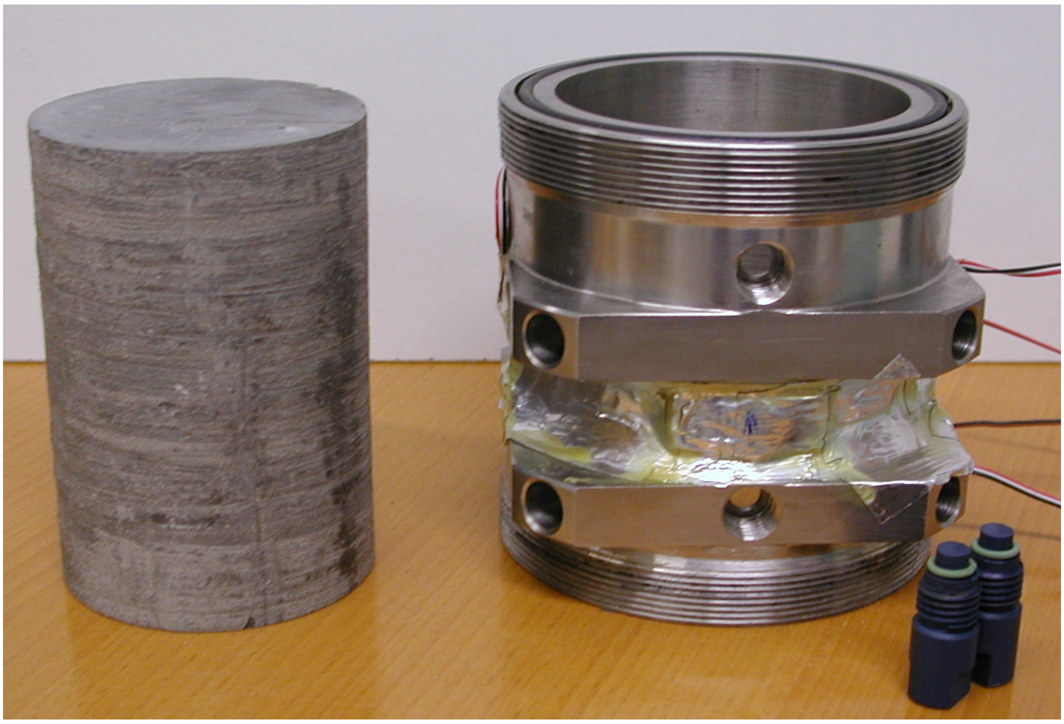

Figure 4.26: Rock sample of 68.5 mm in diameter and 100 mm height previously to be placed into the cell ring.

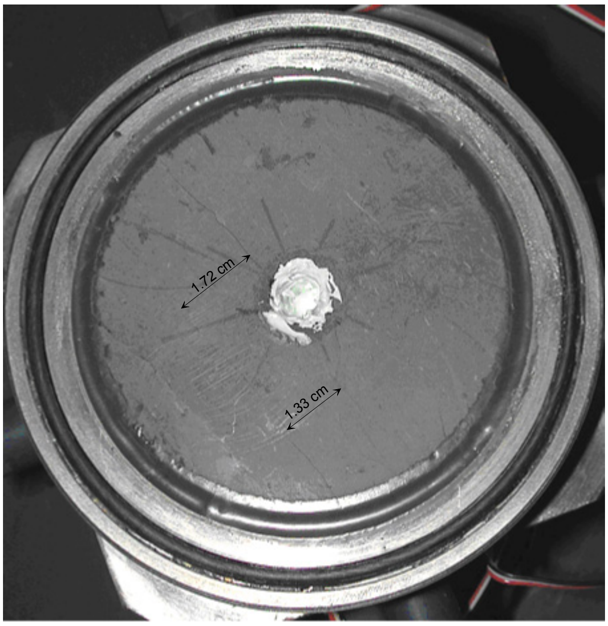

Figure 4.27: Bottom view of the sample already placed into the cell ring. In the center of the sample 6.5 mm diameter hole was drilled to place the heater into the rock which was later filled with silicone oil to avoid occluded air in the heater-rock contact. The separation between vertical fissures is also indicated.

4.4.2.1 Initial gas permeability

Previous to the water infiltration phase the gas permeability of the sample was determined. The bottom valve of the cell was connected to a tank of known volume. The tank was filled with gas at a pressure of $P_g = 0.21$ MPa . The upper valve of the cell is open to the atmosphere. The gas can flow through the sample, whereas the fall of gas pressure in the inner of tank is recorded as function of time.

The gas permeability was calculated by means of equation (4.1) from *Yoshimi & Osterberg, (1963)* as follow:

$$k_g = \left[\frac{2.3 \cdot V \cdot L \cdot \mu_a}{A \cdot \left(p_a + \frac{p_0}{4} \right)} \right] \cdot \left[\frac{-Log_{10}\left(\frac{p_t}{p_0} \right)}{t} \right] \qquad \text{(Eq 4.1)}$$

where:

V : is the tank volume (3.99E-03) [m^3]

L : is the length of the sample (1.0E-01) [m]

μ_a : is the fluid dynamic viscosity (1.78E-05 at 22 ºC) [Nsm^{-2}]

A : is the horizontal area of the sample (3.68E-03) [m^2]

p_a : is the atmospheric pressure (1.01E+05) [N/m^2]

p_0 : is the initial gas pressure into the tank, t = 0 [N/m^2]

p_t : is the gas pressure in the tank a time t = t [N/m^2]

t : is the time [s]

Figure 4.28 shows the gas pressure evolution in the tank and in the two pressure sensors of the cell. Figure 4.29 shows the evolution of the gas pressure profile (gas pressure-height of sample) in the sample. The recorded data, gas pressure vs. time, provides a lineal relationship between $-Log_{10}\left(\frac{p_t}{p_0}\right)$ and time t, as can be observed in Figure 4.30, (the slope is 2.45E-03). The intrinsic gas permeability obtained in this test was $k_g = 8.07E-14$ m^2. This value provides the opportunity to estimate the fracture thickness by means of cubic permeability law, equation 4.2.

$$k_g = \frac{b^3}{12 \cdot a} \qquad \text{(Eq 4.2)}$$

Assuming the gap between fractures to be $a = 0.017$ m (derived from direct measurement) the fracture thickness calculated is $b = 25.5\ \mu$m. This fracture thickness corresponds to the diameter's size of "macro-porosity" determined with mercury intrusion porosimetry (MIP) (see section 3.6).

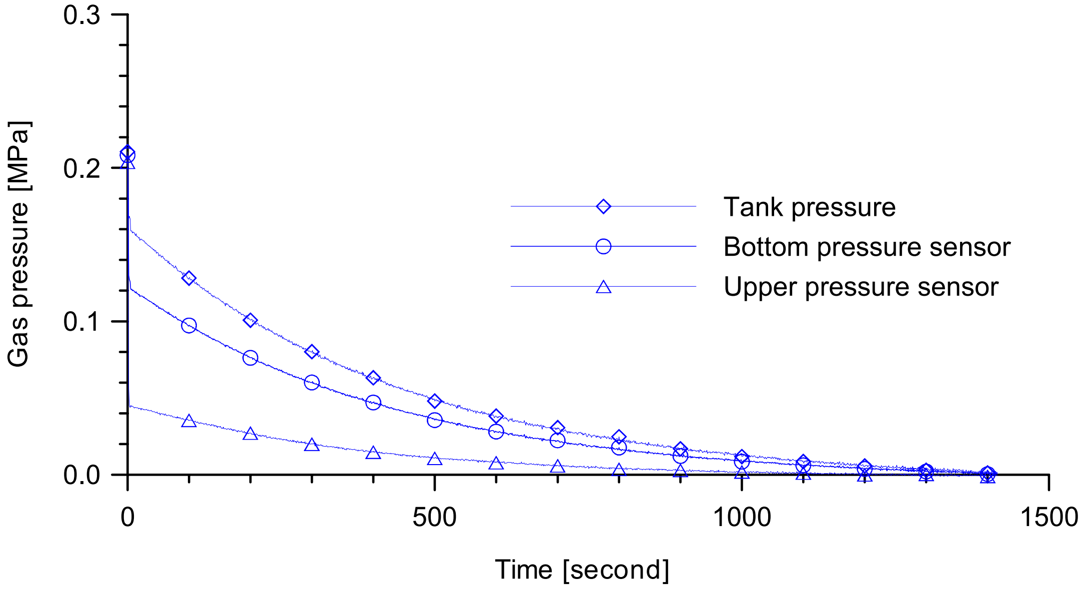

Figure 4.28: Time evolution of gas pressure in the inner of tank and both pressure sensor of the cell.

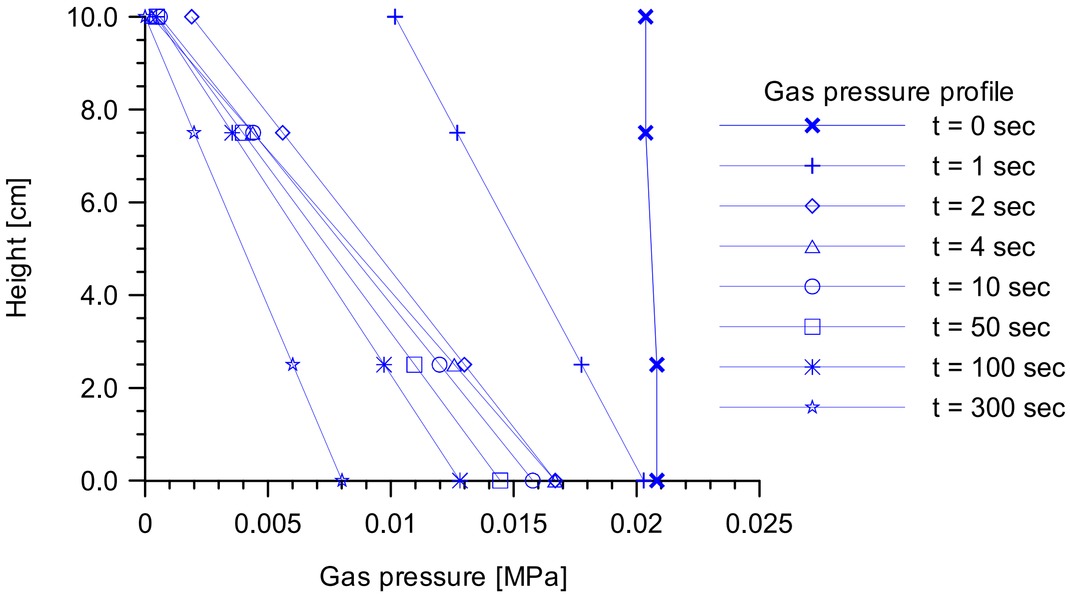

Figure 4.29: Gas pressure profile evolution into the sample.

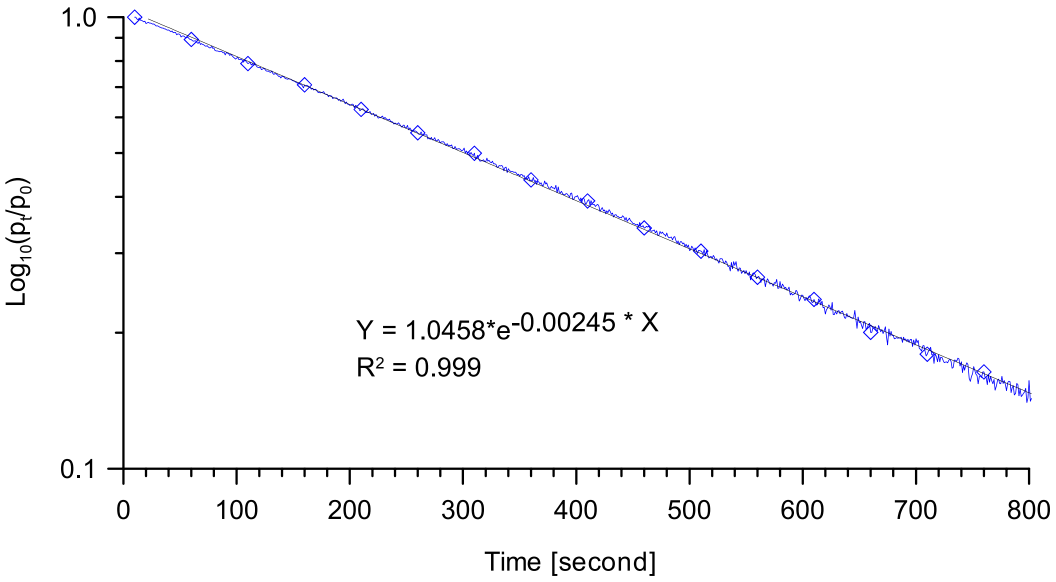

Figure 4.30: Record data of gas pressure and time in the inner tank.

4.4.2.2 Operational phase

The operational phase of the heating experiment consists in an initial hydration of rock and subsequent cycles of heating-cooling with different power inputs. These heating tests were carried out in drained or undrained conditions. Figure 4.31 shows in schematic form the location and identification of different types of sensors.

Figure 4.32 shows the time evolutions of temperature, recorded by the thermocouples (T2), (T3) and (T4) during the whole history of the experiment. The temperature evolution at the heater-rock contact could not be recorded because the sensor (T1) was damaged. Figure 4.33 shows the time evolutions of pore water pressure recorded by sensors (P_w1) and (P_w2). This figure show also the history of water pressure which was applied at the inlet of the cell. The upper pore water pressure sensor (P_w2) failed after 125 days of test. A new pore water pressure was installed at time t = 250 days. The bottom pore water pressure sensor (P_w1) became damaged after 315 days of test. A new pore water pressure was installed after 385 days of test. The water was infiltrated at an initial pressure of 0.50 MPa during the first 55 days of test. Subsequently, the water pressure was increased up to 0.85 MPa, between 55 and 70 days of test. In the period between day 70 and day 127 the water pressure inlet was increased to 1.0 MPa. After that, the water pressure inlet was reduced to 0.65 MPa until the end of the test.

The time evolution of swelling pressure recorded by the strain gages (SV), (SC) and (SL) is shown in Figure 4.34. At the beginning of the rock hydration (t = 2 days), the vertical pressure developed by the rock increased suddenly to 2.50 MPa (SV). Subsequently, the vertical pressure was continuously increasing with time until it reached a value of 4.0 MPa. In similar way, the radial pressure developed by the rock increased suddenly to 2.0 MPa (SC). After that, the radial pressure was continuously increasing up to a value of 3.0 MPa. The water outlet valve (upper) was closed after 105 days of test. The strain gages located on the upper lid (SL) recorded the water pressure evolution when the water outlet valve was closed. The hydration phase and cycles of heating-cooling will be explained in more detail in the next section.

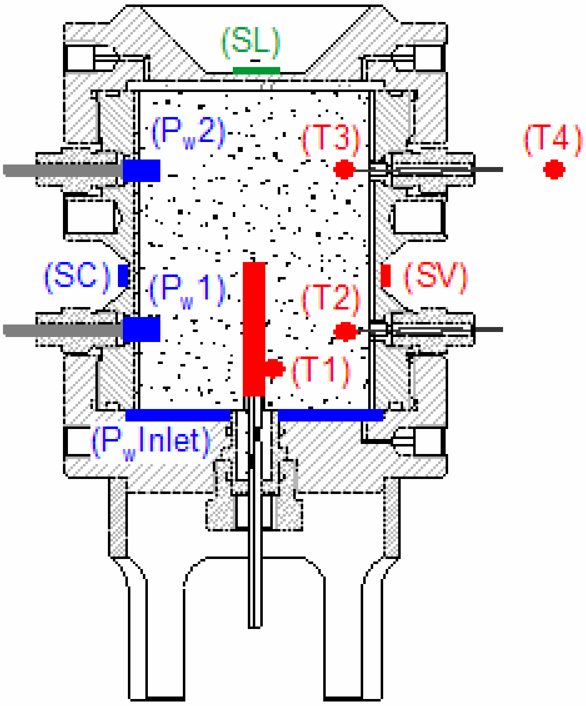

Figure 4.31: Identification and location of different sensors.

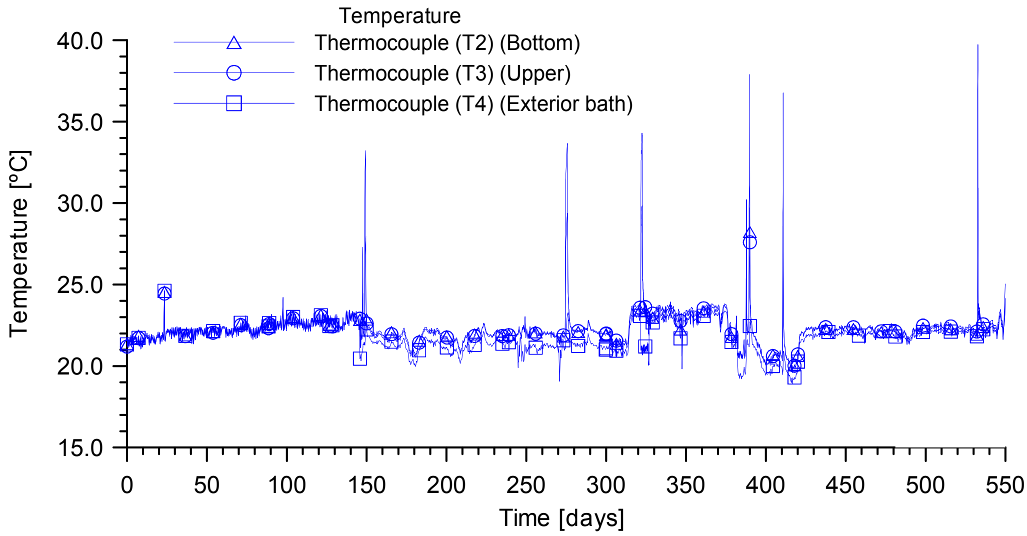

Figure 4.32: Time evolution of rock temperature.

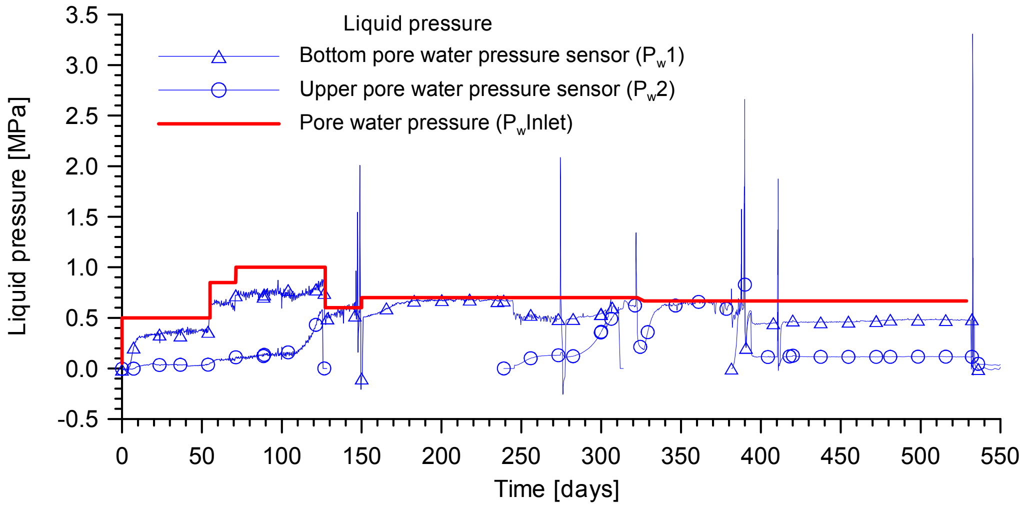

Figure 4.33: Time evolution of rock pore water pressure.

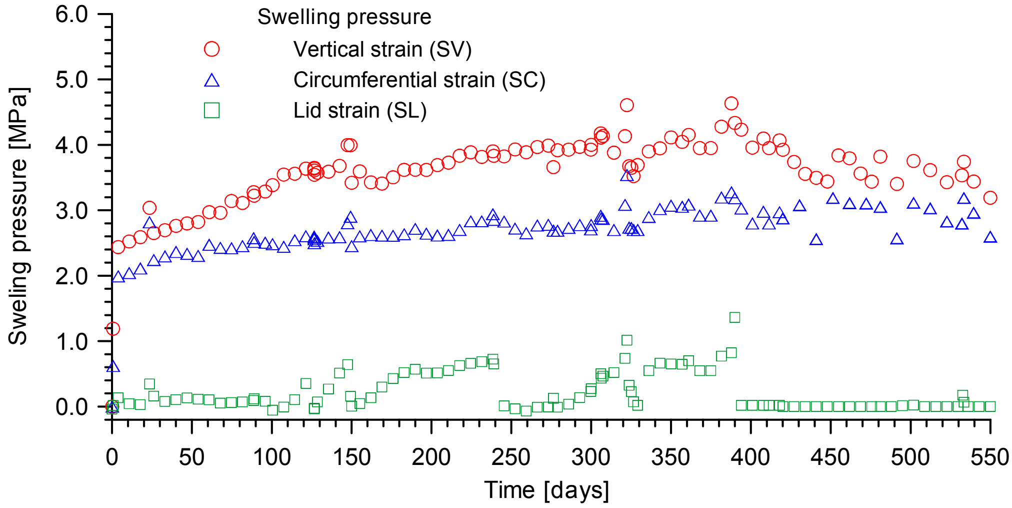

Figure 4.34: Time evolution of swelling pressure developed by the rock.

Hydration phase

The hydration phase (started at t = 0 days) was performed under isothermal conditions at 22±1 ºC during a period of 100 days. Figure 4.35 shows the time evolution of temperatures recorded during the hydration phase. The time evolution of pore water pressure measured in the rock and the history of water pressure applied in the inlet of the cell are shown in Figure 4.36.

The saturation phase began with a water pressure inlet of 0.5 MPa. After 55 days of hydration the water pressure inlet was increased to 0.85 MPa during a period of 15 days. After that, the water pressure was increased to 1.0 MPa. The bottom pore water pressure sensor (P_w1) began to record positive pressure after 5 days of testing. A water pressure value of 0.35 MPa was reached in the sensor (P_w1) after 15 days of hydration. It remained constant until the new water pressure increment (t = 55 days). The upper pore water pressure sensor (P_w2) began to record positive values after 10 days of hydration. Figure 4.37 shows the time evolution of water volume infiltrated during the first 100 days of hydration. A period of 20 days, approximately, was necessary to saturate the rock. The time evolution of water inflow is shown in Figure 4.38. A saturated water permeability of $K = 8.1E-13 \text{ m/s}$ was measured between 80 and 100 days of test, assuming steady state flow. It corresponds to a water inflow of $q = 3.285E-12 \text{ m}^3/\text{s}$, a hydraulic gradient of 1000 and an area of sample of 4.07E-03 m^2. Figure 4.39 shows the measured water inflow as a function of hydraulic gradient. A linear fit to the water inflow rate provides a hydraulic permeability average of $K = 1.04E-12 \text{ m/s}$ (see Figure 4.39). Figure 4.40 shows the time evolution of rock swelling pressure developed during the hydration phase.

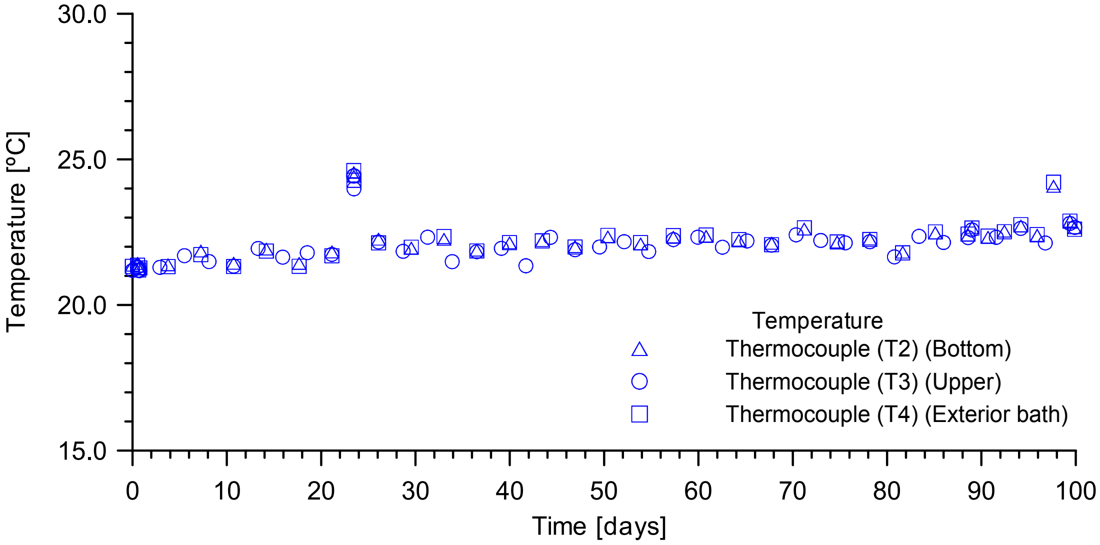

Figure 4.35: Time evolution of temperature measured during the hydration phase (isothermal conditions).

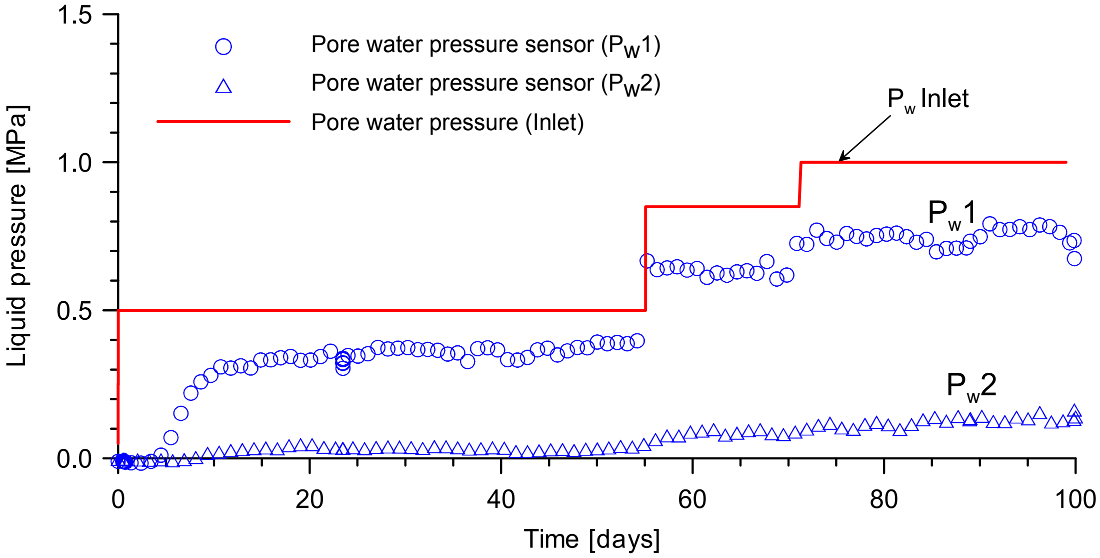

Figure 4.36: Time evolution of pore water pressure measured during hydration phase.

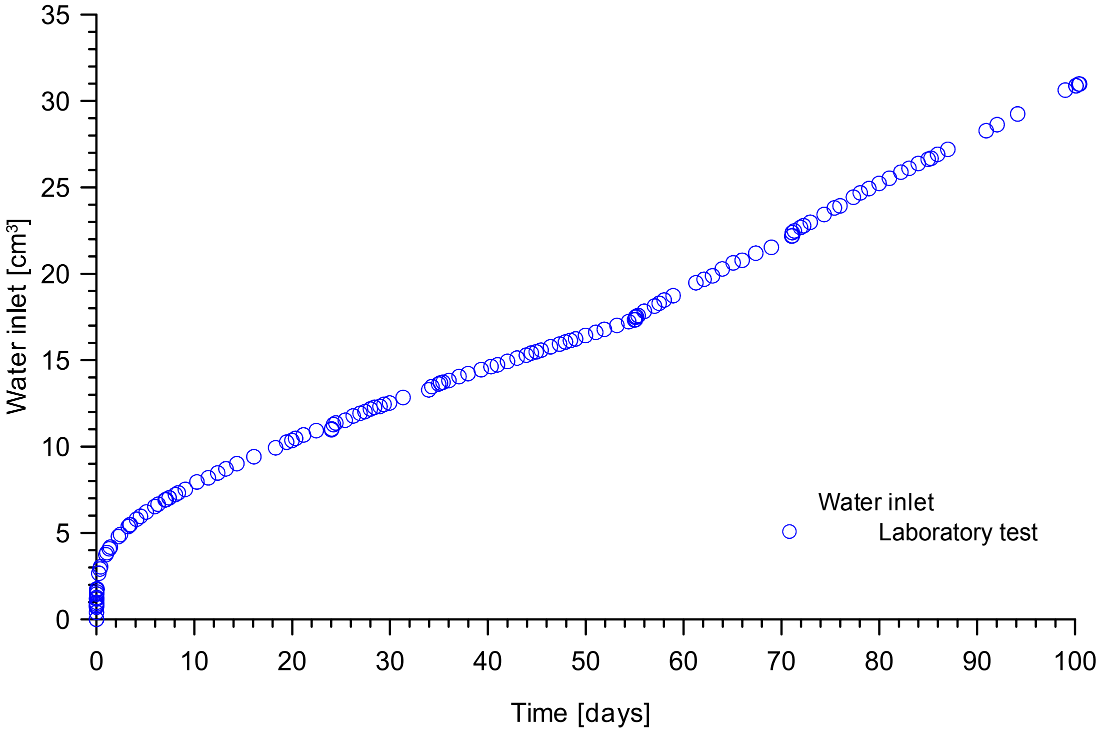

Figure 4.37: Volume of water infiltrated during the hydration phase.

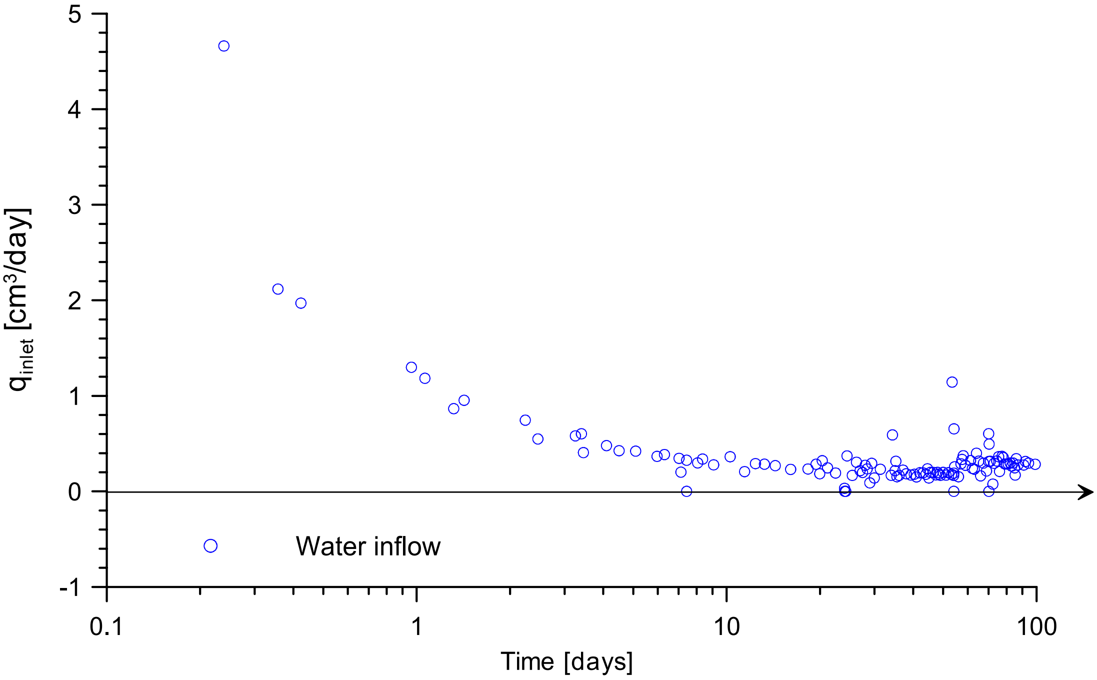

Figure 4.38: Time evolution of water inflow rate measured during hydration phase.

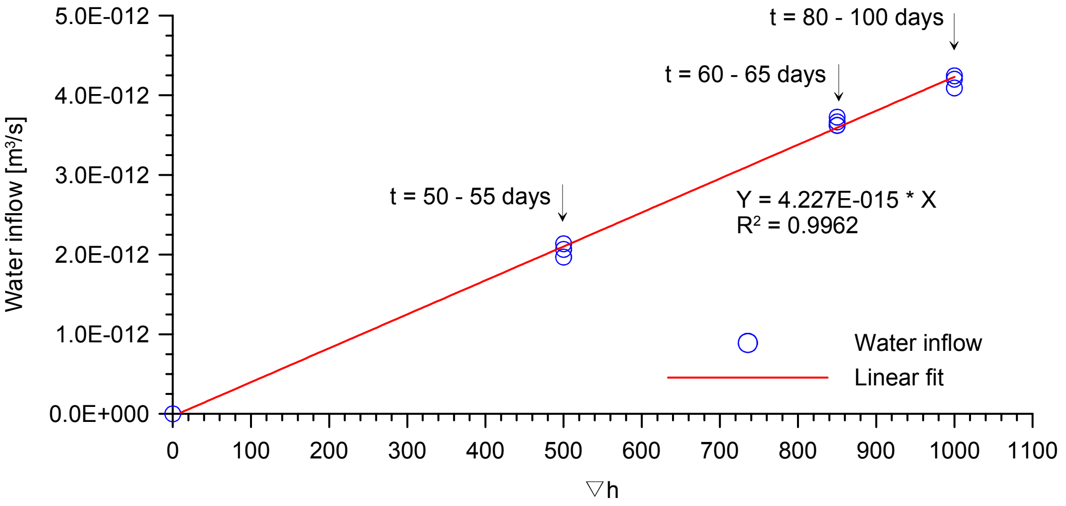

Figure 4.39: Water inflow rate as a function of pressure head. A average hydraulic permeability of K = 1.04E-12 m/s (area of sample 4.07E-03 m^2) is derived.

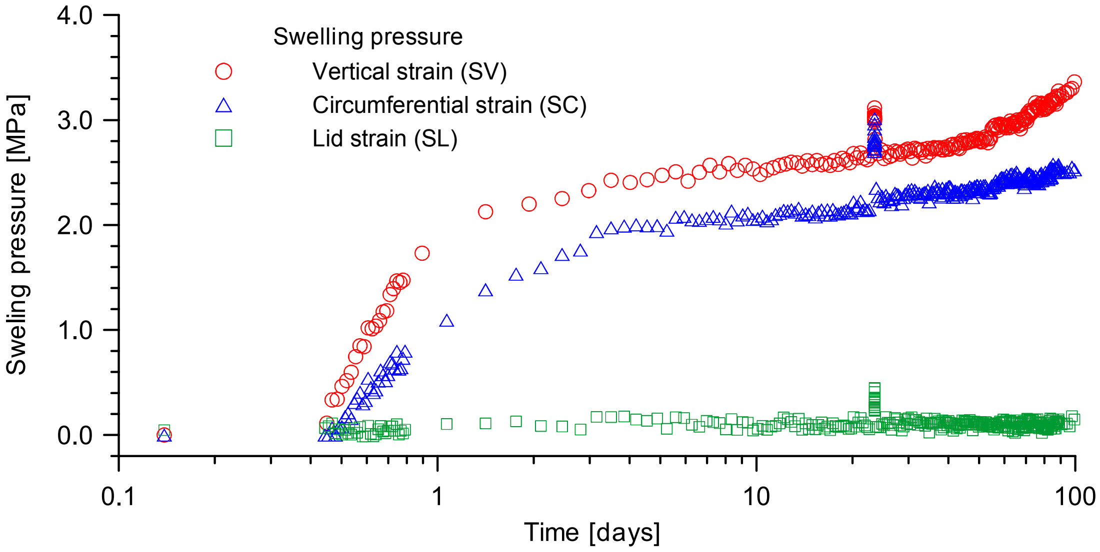

Figure 4.40: Time evolution of swelling pressure measured during the hydration phase.

Heating phase

A total of six cycles of heating-cooling were performed during the experiment. The four cycles of heating-cooling called: Heating A, B, C and D will be described now in detail.

Heating A

This heating test was carried out between 148.5 to 151 days of test. The heater was switched with a constant power input of 5.10 W during 17.15 hours. This test was performed under drained conditions. The upper water outlet of the cell remains open to the atmosphere.

Figure 4.41 (upper) shows the time evolution of temperature recorded by sensors (T2), (T3) and (T4). The maximum temperature recorded by the sensors (T2) and (T3) at the end of the heating were of 33.0 ºC and 27.8 ºC, respectively. A small increment of temperature of 1 ºC was recorded in the exterior bath by sensor (T4) at the end of the heating phase. It is due to a loss of heat through the bottom part of the cell. The heater was switch-off after 17.15 hours of test, when a rapid drop of temperature was recorded. Time evolution of pore water pressure recorded by sensor (P_w1) is shown in Figure 4.41 (middle). A sudden pore water pressure increment of 1.65 MPa and a subsequent pore water pressure dissipation was recorded by sensor (P_w1) during heating. Once the power was removed, a sudden drop in pore water pressure of 0.60 MPa was measured. Negative value of pore water pressure (Pw = -0.3 MPa) was recorded as a result of cooling. The increase in pore water pressure due to heating may induce the rock fracture. On the other hand, a rapid cooling induces a transient increase of suction. In drained conditions can be observed that the temperature effect in pore water pressure produce an irreversible process, because the final pore water pressure is lower than the initial value. The water inlet was open a time t = 150.5 days with a liquid pressure of 0.60 MPa. Figure 4.41 (bottom) shows the time evolution of stresses induced by thermal strains measured by the strain gages. Both vertical and circumferential strain gages recorded a stress increment of 0.60 MPa during heating. A small stress increment of 0.20 MPa was recorded by the strain gages placed in the upper lid. The effect of the heating-cooling cycle in the rock pressures is a reversible process.

Figure 4.42 (upper) shows the rate of heating and temperature increment recorded by sensors (T2), between 3570 and 3576 hours of test (148.75 to 149 days). A maximum rate of heating of 0.52 ºC/min was recorded by bottom sensor (T2). It decreased rapidly with time. Temperature increments of 11 ºC and 5 ºC with regards to the initial temperature were recorded by sensors (T2) and (T3), respectively. Figure 4.42 (bottom) shows the pore water pressure increment recorded by bottom sensor (P_w1). Both radial and vertical increments of stresses recorded by strain gages are also indicated in bottom figure. Pore water pressure dissipation began when the rate of heating was lower than 0.05 ºC/min.

Figure 4.43 (upper) shows the rate of cooling and the decrease of temperature measured by sensor (T2), between 3586 and 3592 hours of test. A maximum rate of cooling of 0.55 ºC/min was recorded by sensor (T2). Figure 4.43 (bottom) shows the pore water pressure decrease recorded by sensor (P_w1) during the cooling phase. A decrease of vertical and radial stresses of 0.50 MPa was measured by both vertical and circumferential strain gages, whereas a stress decrease of 0.20 MPa was measured by the strain gages placed in the upper lid, see Figure 4.43 (bottom).

A volume of drained pore water $\Delta V_{dr} = 0.285\ \text{cm}^3$ was measured during the heating phase. This was produced by an increment of temperature $\Delta T = 9.6$ ºC as can be seen in Figure 4.44. The thermal expansion of a volume of pore water subjected to a temperature increment is equal to:

$$\Delta V_W = \alpha_W V_W \Delta T \qquad \text{(Eq 4.3)}$$

where α_W is the thermal expansion coefficient of free water, V_W is the volume of pore water and ΔT is the temperature increment.

The rock volumetric strain ε_v during a drained heating test is obtained by substracting both, the volume due to the thermal expansion of free water and the solid skeleton from the total volume of drained pore water ΔV_{dr} *(Delage et al. (2000))* as follows:

$$\varepsilon_v = \frac{\left[\Delta V_{dr} - \left(\alpha_W n V + \alpha_S \left(1-n\right) V\right) \Delta T\right]}{V} \qquad \text{(Eq 4.4)}$$

where α_W and α_S are the thermal expansion coefficient of water and solid skeleton, respectively; n the porosity and V the volume of the sample. The sample volumetric strain $\varepsilon_v = 1.12E-04$ was computed from (Eq 4.4) using the following parameters

$\alpha_W = 3.4E - 04$ ºC^{-1}, $\alpha_S = 1.0E - 05$ ºC^{-1}, $n = 0.18$ and $V = 407.15$ cm^3. The corresponding volumetric thermal expansion coefficient of the rock $\alpha_{rock} = 1.17E - 05$ ºC^{-1} was determined by (Eq 4.5).

$$\varepsilon_v = \alpha_{rock}\Delta T \tag{Eq 4.5}$$

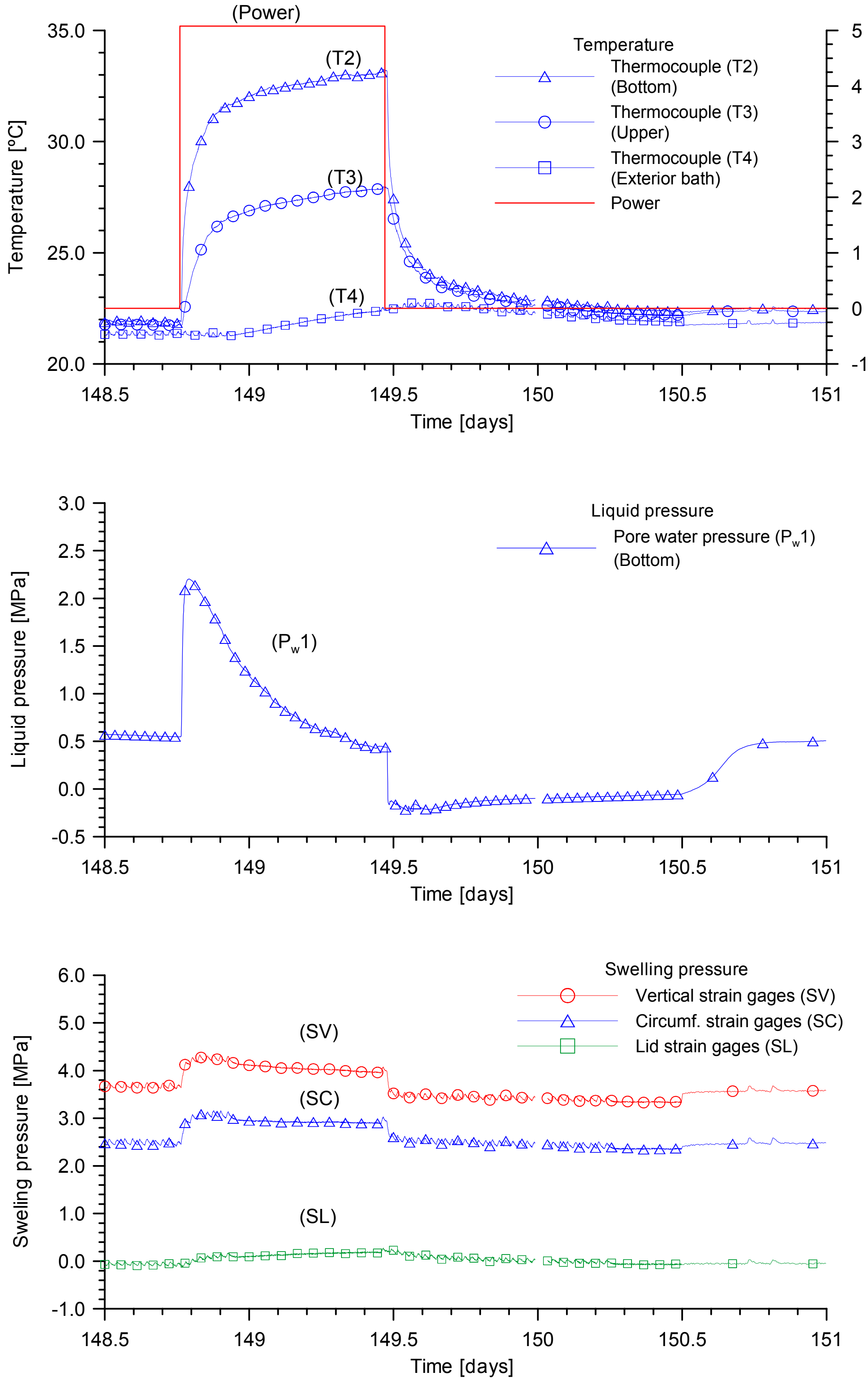

Figure 4.41: Heater test (A) performed under drained condition. (Upper): Time evolution of temperature measured into the rock. (Middle): Time evolution of pore water pressure measured in the rock. (Lower): Time evolution of stresses induced by temperature strain measured during the heating phase.

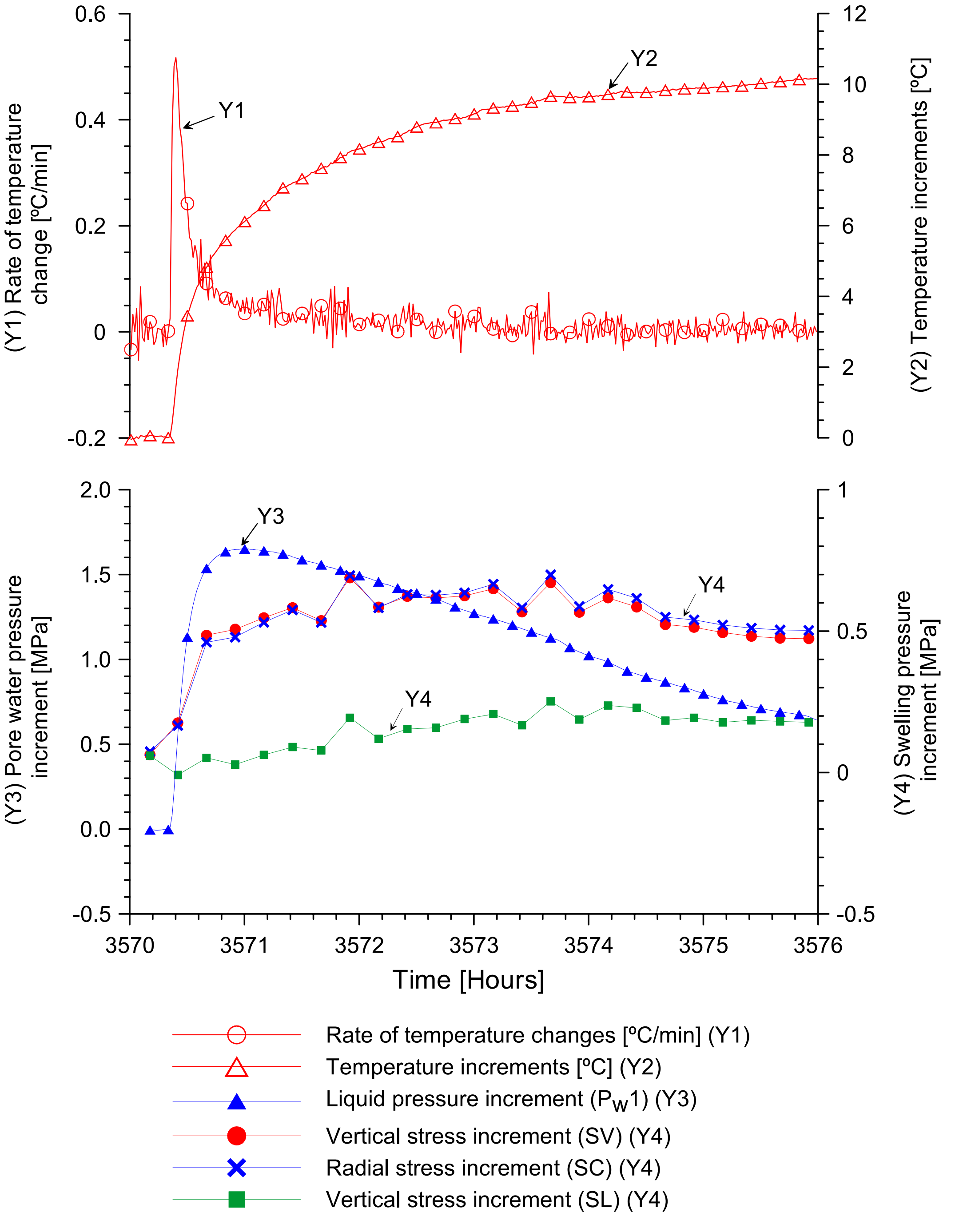

Figure 4.42 (Upper): Rate of heating and temperature increments recorded by sensors (T2), (Bottom): Pore water pressure increments recorded by sensor ($P_{w}1$) and stress increments recorded by strain gages.

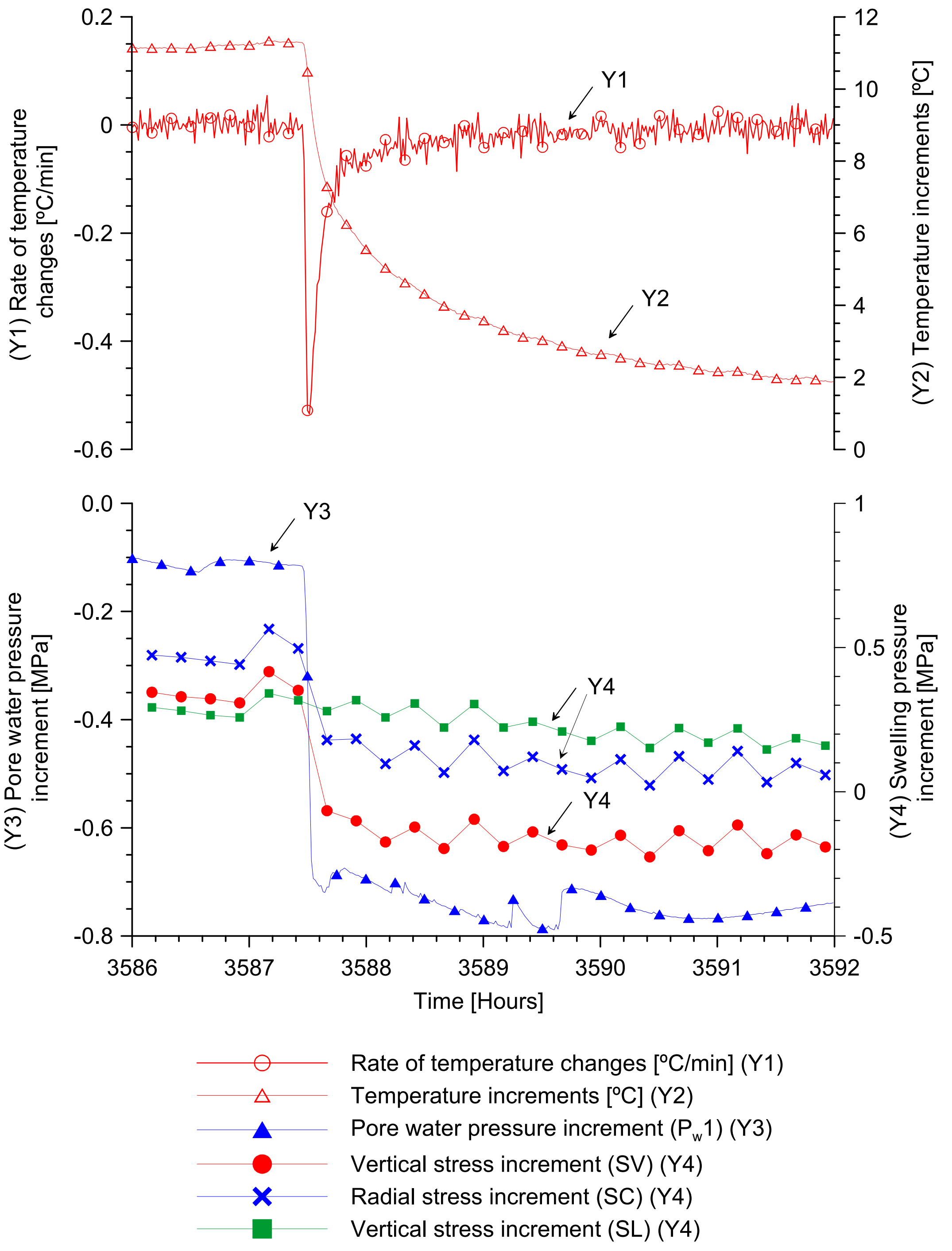

Figure 4.43: (Upper): Rate of cooling and temperature decrease recorded by sensor (T2), (Bottom): Pore water pressure increments recorded by sensor (Pw1) and stress decrease recorded by strain gages.

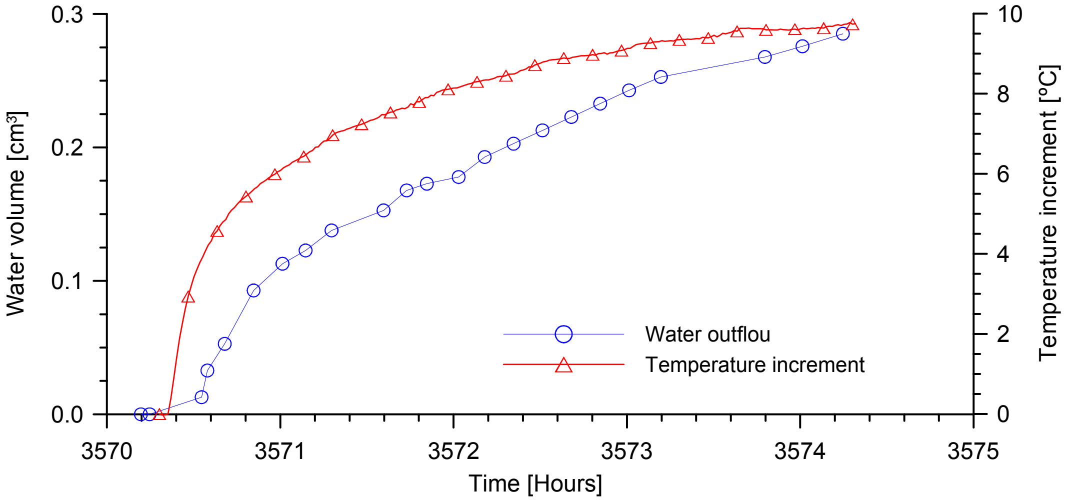

Figure 4.44: Water outflow measured during the heating (A).

Heating B

The second cycle of heating-cooling was carried out between 389 to 391 days of test. The heating was performed in two phases. In the first heating phase a power input of 4.90 Watt was applied during 10.8 hours. After that, the power was increased up to 8.85 Watt during 3.05 hours. This heating test was performed under undrained conditions. Figure 4.45 (top) shows the time evolution of temperature recorded by the temperature sensors (T2) and (T3). Temperature changes of 9 ºC and 5 ºC were recorded during the first heating phase by the sensors (T2) and (T3), respectively. In the second heating phase temperature increments of 7 ºC and 3 ºC were recorded by sensors (T2) and (T3), respectively.

Time evolution of pore water pressure recorded by sensors (P_w1) and (P_w2) can be seen in Figure 4.45 (middle). The initial water pressure recorded by both sensors was 0.60 MPa. At the first heating phase the sensor (P_w1) records a rapid water pressure increase of 1.2 MPa and a subsequent small and slow dissipation. In a similar way, a rapid increment of water pressure of 1.0 MPa was recorded by sensor (P_w2) and then it remained constant. During the second heating phase pore water pressure increments of 1.2 MPa and 0.8 MPa were recorded by sensors (P_w1) and (P_w2), respectively. A rapid drop of temperature was produced when the power was removed. As a result of the cooling, a sudden decrease in pore water pressure occurs.

Figure 4.45 (bottom) shows the time evolution of stresses measured by the strain gages. A vertical stress of 4.2 MPa was recorded before heating by the vertical strain gages. At the first heating phase a vertical stress increment of 0.8 MPa was measured. A subsequent vertical stress increment of 0.80 MPa was recorded at the second heating phase. During the cooling phase a sudden drop in vertical stress of 1.6 MPa was measured. A radial stress of 2.8 MPa was recorded before the heating by the circumferential strain gages. Radial stress increments of 0.8 MPa were measured at the first and second heating phase, respectively. During the cooling phase a sudden drop of 1.4 MPa of radial stress was recorded. The time evolution of water pressure was measured by the strain gages placed on the upper lid due to this test was undrained. An initial water pressure of 0.5 MPa was recorded before the heating. A water pressure increment of 1.10 MPa and a subsequent increment of 0.80 MPa were recorded during the first and second heating phase, respectively. A drop of water pressure of 2.40 MPa occurs during the cooling phase. The magnitudes of water pressure increments measured by the strain gages placed on the upper lid are the same as the values recorded by the pore water pressure sensors. In Figure 4.45 it can be seen that the heating effects in pore water pressure and swelling pressure is a reversible process.

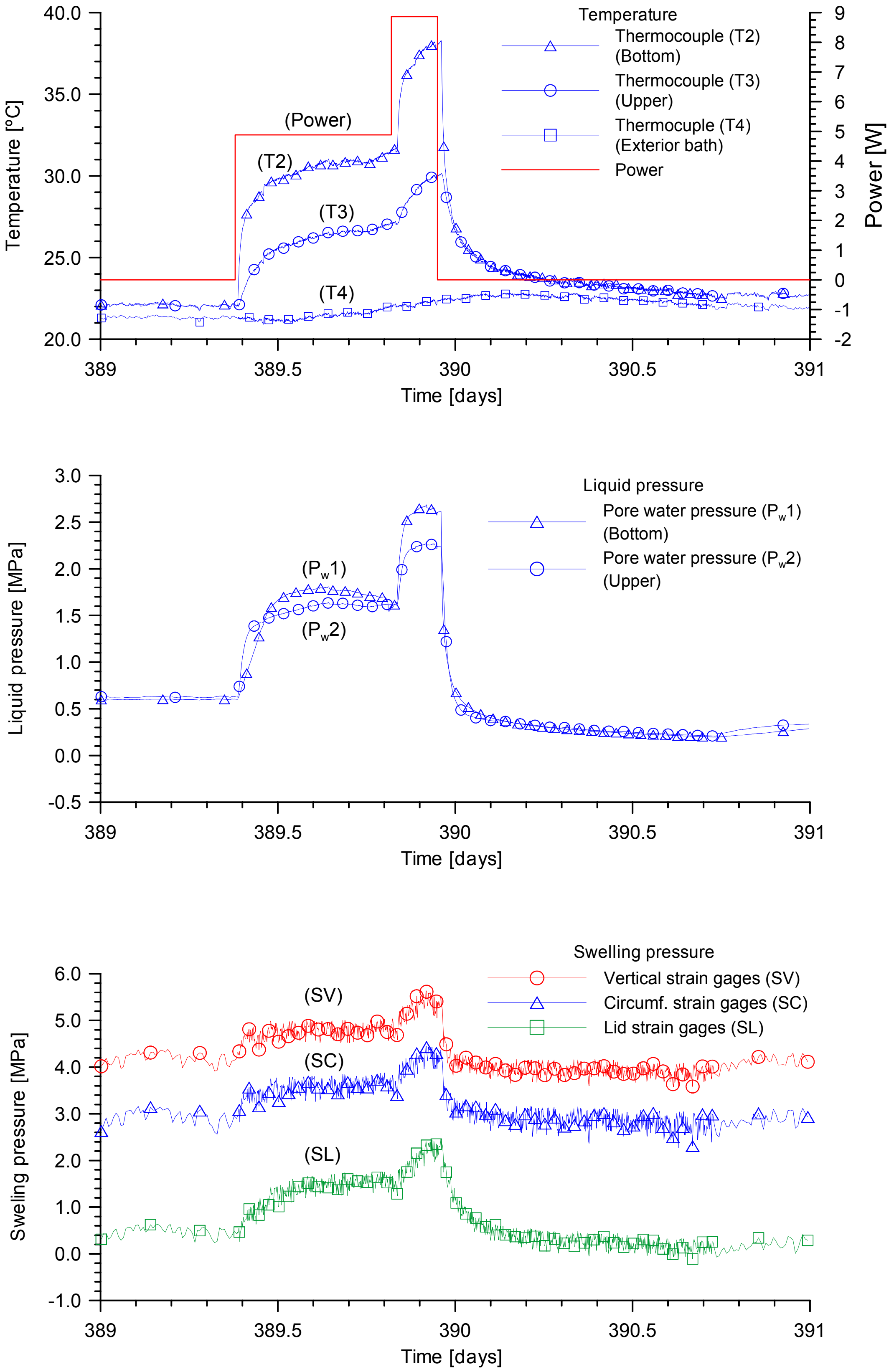

Figure 4.45: Heater test (B) performed under undrained condition. (Upper): Time evolution of temperature measured in the rock. (Middle): Time evolution of pore water pressure measured in the rock. (Lower): Time evolution of stresses measured by strain gages during heating phase.

Heating C

A hydraulic permeability of $K = 8.14E - 13$ m/s was determined before the third heating was performed. This value corresponds to a water inflow of $q = 0.192\ cm^3/day$ and a hydraulic gradient of 670. Figure 4.46 shows the time evolution of infiltrated water between 398 to 410 days of test.

The heating test was carried out between 410 to 412 days of test. The heating was performed in two phases. In the first heating phase a power input of 5.15 W was applied during 7.2 hours. After that, the power was increased to 9.36 W during 2.78 hours. This heating test was performed in drained conditions (the upper water outlet remains open to atmosphere). Figure 4.47 (upper) shows the time evolution of temperature recorded by the temperature sensors (T2) and (T3). Temperature changes of 12 ºC and 6 ºC were recorded in the first heating phase by sensors (T2) and (T3), respectively. In the second heating phase a temperature increments of 5 ºC and 3 ºC were recorded by sensors (T2) and (T3), respectively.

The time evolution of pore water pressures recorded by sensors (P_w1) and (P_w2) can be seen in Figure 4.47 (middle). Initial water pressures of 0.45 MPa and 0.10 MPa were recorded by the sensors (P_w1) and (P_w2), respectively. At the first heating phase the sensor (P_w1) recorded a sudden water pressure increment of 1.0 MPa and a subsequent rapid dissipation. A rapid water pressure increment of 0.50 MPa and a subsequent pore water dissipation was measured by sensor (P_w2). During the second heating phase pore water increments of 1.0 MPa and 0.4 MPa were recorded by the sensors (P_w1) and (P_w2), respectively. A rapid drop of temperature was produced when the power was removed. As a result of the cooling a sudden decrease in pore water pressure of 1.80 MPa and 0.50 MPa were recorded by sensors (P_w1) and (P_w2), respectively.

The time evolution of stresses measured by the strain gages is plotted in Figure 4.47 (bottom). A vertical stress of 4.0 MPa was recorded before the heating by the vertical strain gages. At the first heating phase a vertical stress increment of 0.6 MPa was measured. A subsequent vertical stress increment of 1.0 MPa was recorded at the second heating phase. During the cooling phase a sudden drop in vertical stress of 1.6 MPa was measured. A radial stress of 2.8 MPa was recorded before heating by the circumferential strain gages. Radial stress increments of 0.6 MPa and 1.0 MPa were measured at the first and second heating phase, respectively. During the cooling phase a sudden drop of radial stress of 1.2 MPa was recorded. A small stress increment of 0.20 MPa was recorded by the strain gages placed in top lid during the heating.

Rock damage was caused by successive heating cycles. This damage may be interpreted as an increment of the hydraulic permeability. Figure 4.48 shows the water pressure increments measured in heating phases A and C. Both heating phases were performed under drained conditions with a common power applied of 5.0 W. The maximum pore water pressure of 2.2 MPa was recorded during the heating A, whereas a maximum water pressure of 1.4 MPa was recorded during the heating C.

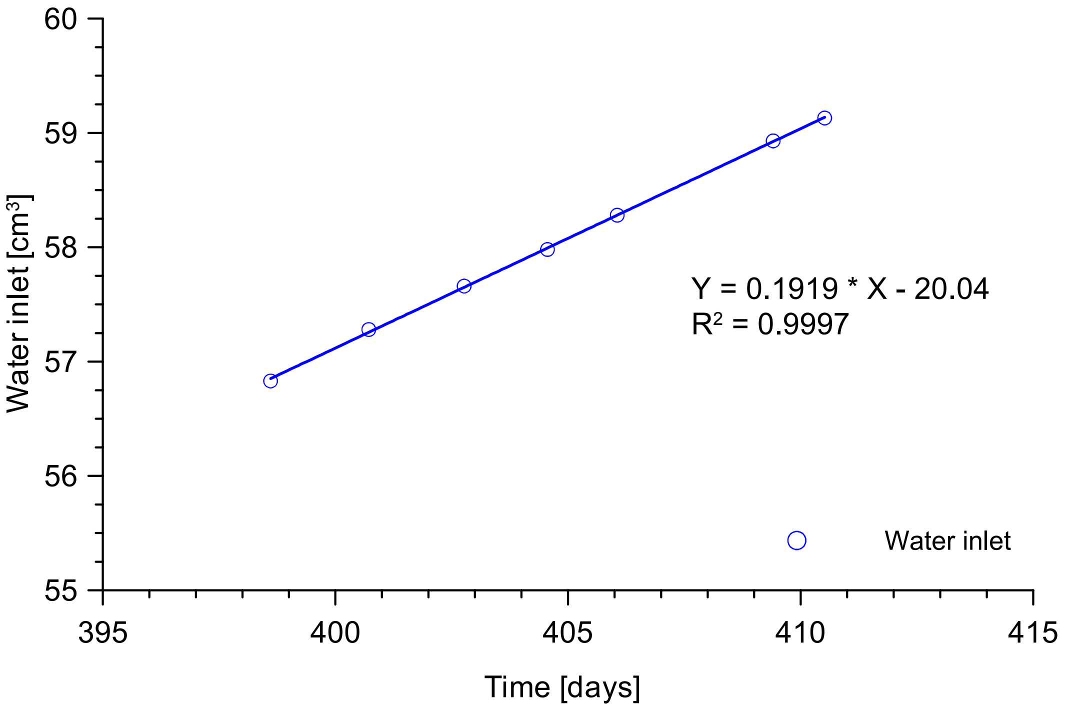

Figure 4.46: Time evolution of water inlet.

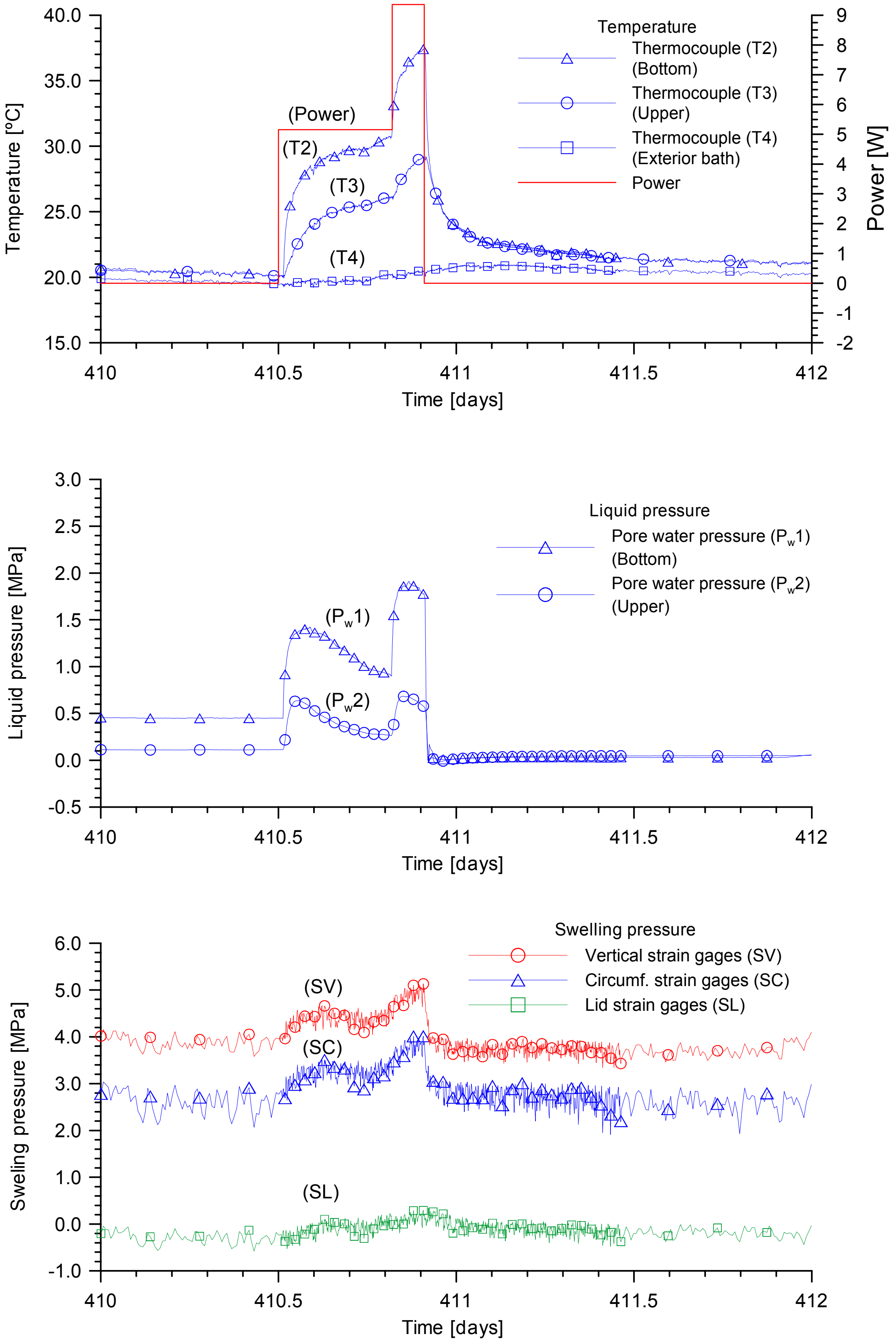

Figure 4.47: Heating test (C) performed under drained condition. (Upper): Time evolution of temperature measured in the rock. (Middle): Time evolution of pore water pressure measured in the rock. (Lower): Time evolution of stress measured by strain gages during heating phase.

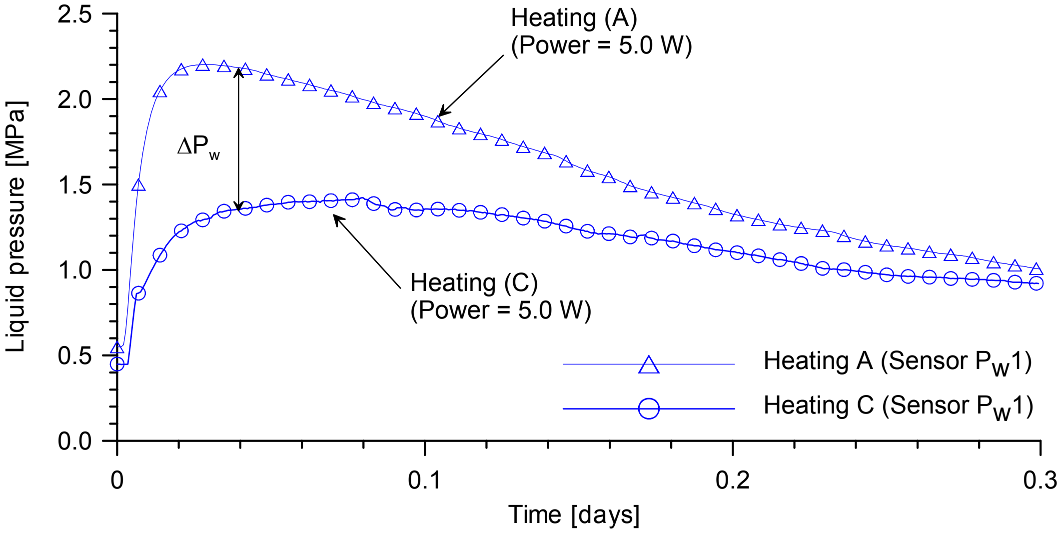

Figure 4.48: Comparison of generated pore water pressure in Tests A and C performed at a power of 5.0 W under drained conditions.

Heating D

The fourth cycle of heating-cooling was carried out between 532.5 to 533 days of test. The test was performed in three phases of heating in drained conditions. Figure 4.49 (upper) shows the time evolution of temperature recorded by the temperature sensors (T2) and (T3). In the first heating phase a power input of 19.0 W was applied during 0.30 hours. After that, the power was reduced to 12.5 W during 0.25 hours because the maximum range of measure of the water pressure sensor (3.5 MPa) was reached. In the second heating phase the power was increased to 19.0 W during 0.08 hours and a subsequent decreasing of power to 12.5 W during 0.17 hours. In the third heating phase the power applied was increased to 19.0 MPa during 0.10 hours. After that the power was reduced to 12.5 MPa during 3.0 hours. After that, the power input was reduced to 0, where a temperature change of 18 ºC and 9 ºC were recorded by sensors (T2) and (T3), respectively.

Time evolution of pore water pressure recorded by sensors (P_w1) and (P_w2) can be seen in Figure 4.49 (middle). The initial water pressure of 0.45 MPa and 0.10 MPa was recorded by sensors (P_w1) and (P_w2), respectively. The maximum pore water pressure of 3.6 MPa was recorded by the sensor (P_w1). Subsequent dissipation of pore water pressure occurs when the rate of heating was reduced. A maximum pore water pressure increment of 1.20 MPa and a subsequent dissipation was recorded by the sensor (P_w2). A rapid drop of temperature was produced when the power input was removed. The fast cooling was recorded and a sudden decrease in pore water pressure of 2.20 MPa and 0.70 MPa were recorded by the sensors (P_w1) and (P_w2), respectively. In this case, the water pressure recorded by the sensor (P_w1) after cooling is lower than the water pressure before the heating.

Figure 4.49 (bottom) shows the time evolution of stresses measured by the strain gages. A vertical stress of 3.6 MPa was recorded before the heating by the vertical strain gages. At the heating phase a vertical stress increment of 1.40 MPa was measured. During the cooling phase a sudden drop of vertical stress of 1.4 MPa was measured. A radial stress of 3.0 MPa was recorded before the heating by the circumferential strain gages. A radial stress increment of 1.2 MPa was measured during the heating phase. At the cooling phase a sudden drop of radial stress of 1.2 MPa was recorded. The changes in stresses induced by thermal strain have been reversible in this case.

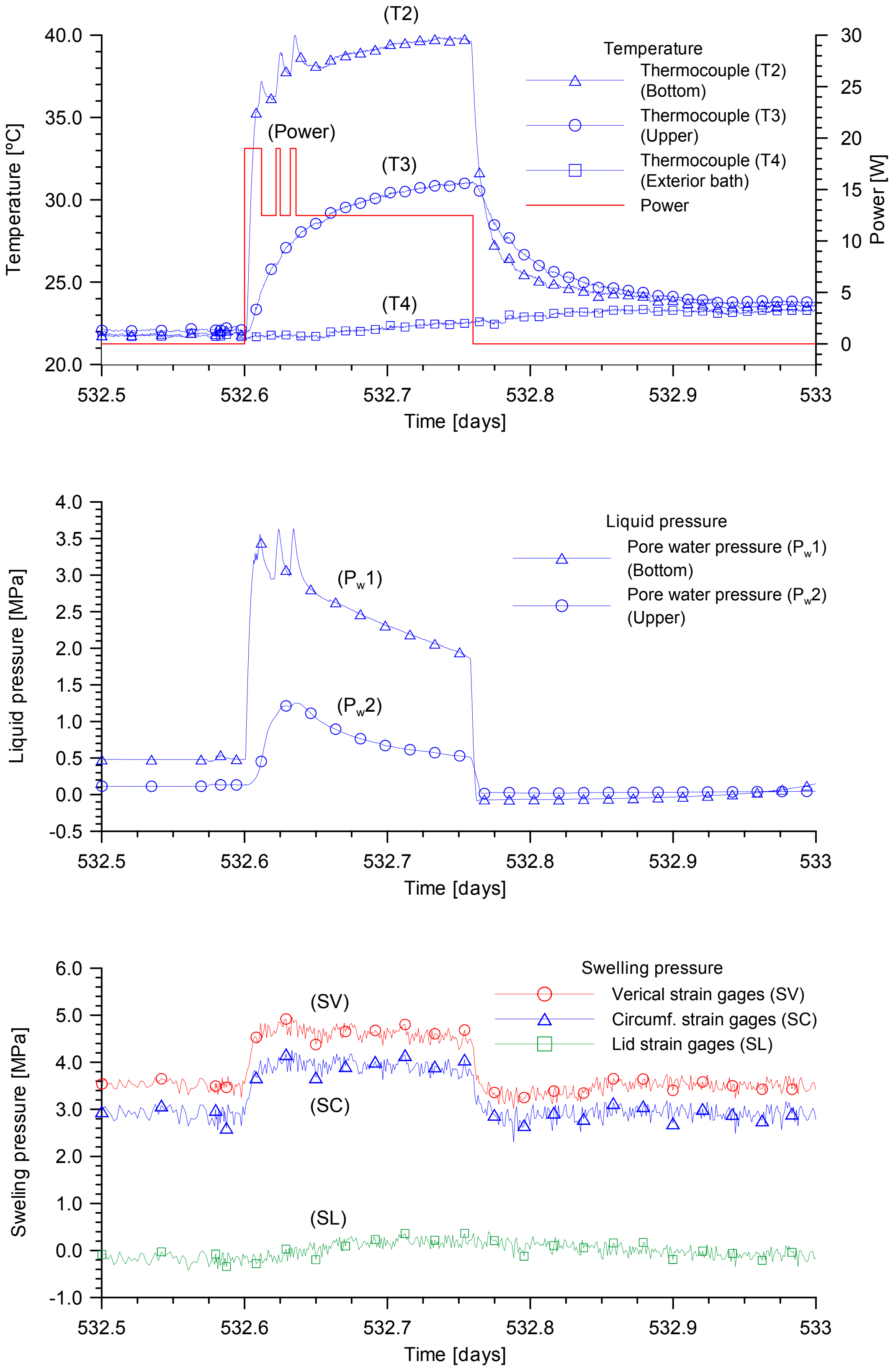

Figure 4.49: Heating test (D) performed under drained condition. (Upper): Time evolution of temperature measured in the rock. (Middle): Time evolution of pore water pressure measured in the rock. (Lower)Time evolution of stresses measured during heating phase.

4.4.2.3 Final gas permeability

The intrinsic gas permeability was determined after the heating phase. This test was carried out under saturated conditions. Figure 4.50 shows pressure-time records which were used to determine the intrinsic gas permeability under unsaturated and saturated conditions. The intrinsic gas permeability under unsaturated conditions has been described previously in the paragraph 4.4.2.1. This test was performed before the water infiltration and it provide a value $k_g = 8.07E-14$ m^2 for a rock degree of saturation of $S_l = 0.85$.

An intrinsic gas permeability of $k_g = 2.62E-17$ m^2 was determined under saturated conditions after heating phase. The gas permeability was computed by means of equation (4.1) from *Yoshimi & Osterberg (1963)* as explained previously in the paragraph 4.4.2.1. Water outflow was not recorded in the drainage during the gas permeability test.

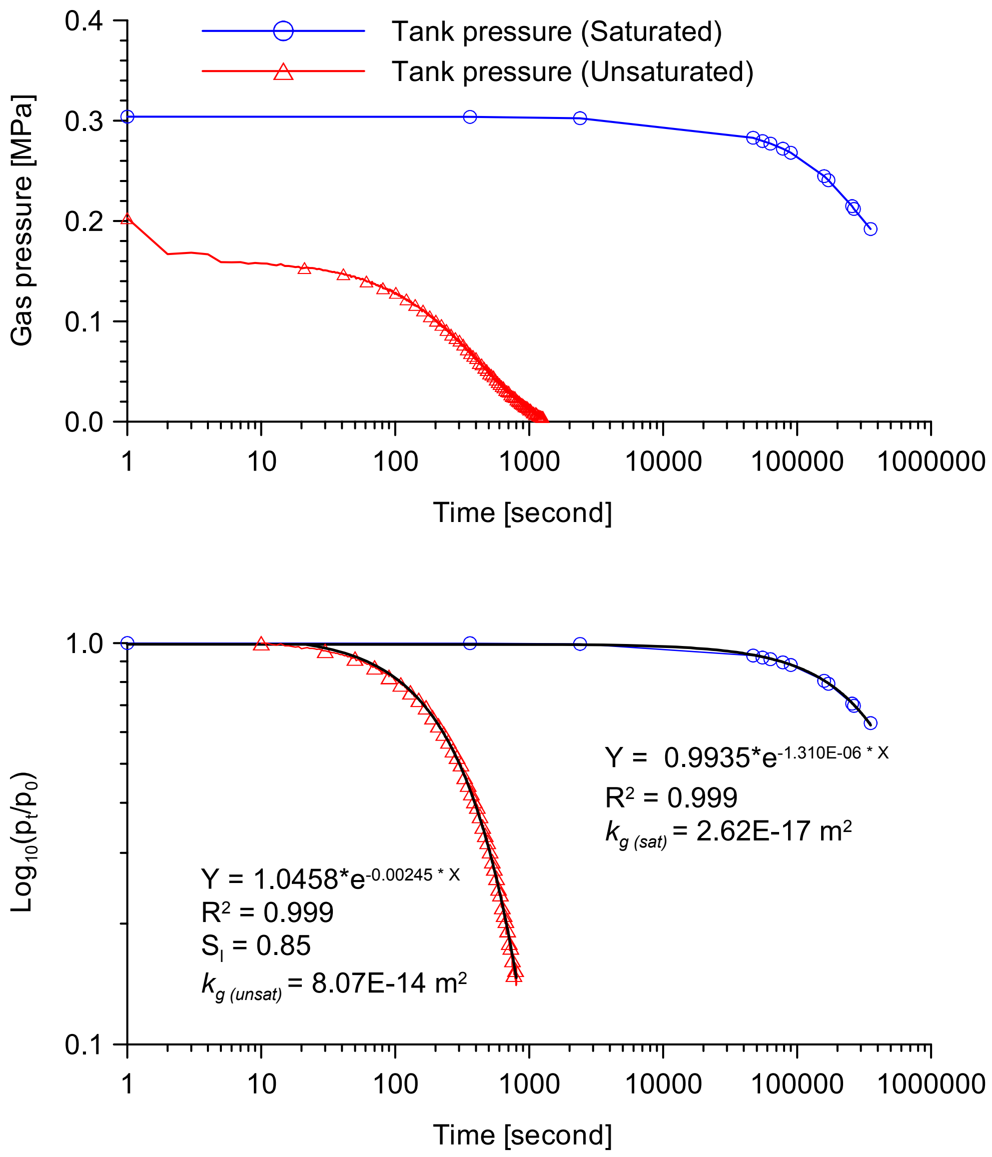

Figure 4.50: Gas permeability of the rock determined under saturated and unsaturated conditions.

CHAPTER V

T-H-M AXISYMMETRIC ANALYSIS WITH ISOTROPIC CONSTITUTIVE MODELS

5.1 Introduction

In this chapter the numerical simulations of the "in situ" HE experiment and a heating laboratory test will be presented. The coupled Thermo-Hydro-Mechanical (THM) processes developed in both, the host rock "Opalinus clay" and in the saturated bentonite buffer have been modeled with CODE_BRIGHT (*Olivella et al., 1994* and *Olivella et al., 1996*). The full formulation has been previously presented in Chapter II.

5.2 Modeling of the HE experiment

The numerical simulation of the HE experiment was divided basically in two parts. The first part covers the excavation of the HE niche and drilling the borehole BHE-0, in order to obtain a suitable stress state, pore water pressures and temperatures values in the near field of the experiment. The second part of the numerical simulations covers the bentonite buffer emplacement, bentonite buffer hydration phase, heating phase and cooling phase. Special interest was given to the interaction between bentonite buffer and host rock in the near field. In order to observe rock degradation the effects of the bentonite suction, swelling pressure and thermal load have been analyzed.

The HE experiment was instrumented with sensors of temperature, water pressure and inclinometers located in boreholes performed around the heating borehole BHE-0. The instrumentation provides data on the rock reaction against the bentonite swelling and thermal load. The numerical results are compared with experimental data in all phases of the experiment.

5.2.1 Geometry of the HE experiment

Given the characteristic of the HE experiment, an axisymmetric numerical model with respect to the longitudinal axis of the borehole BHE-0 has been adopted. In the model the HE niche is 5.40 m wide and 4.70 m height, and the borehole BHE-0 is 300 mm in diameter and 7.00 m deep. The coordinate system has its origin at the intersection between the floor of the HE niche and the longitudinal axis of borehole BHE-0. The domain is 50 m length and 40 m height. Figure 5.1 shows the finite element mesh and the boundary conditions adopted. A finite element mesh having 4790 quadrilateral elements and 4917 nodes was developed. Each node has four degrees of freedom, namely, two displacements (radial and vertical), the liquid pressure and the temperature. The geometry of the HE experiment, i.e., the HE niche and borehole dimensions, and the different position of the all components has been taken from *Fuentes-Canstillana et al. (2001)*.

A total of six different materials have been considered: 1- The host rock Opalinus clay, 2- The bentonite buffer, 3- The heater tube, 4- The sintered filter, 5- The dry sand which fills the upper part of the borehole, 6- The resin to seal the upper part of borehole. Figure 5.2 shows the geometry of the HE and a detail of all different materials placed into the borehole BHE-0. The heater tube is 75 mm in diameter and 7.0 m length. However, the heater element is placed from -4.0 m to -6.0 m depth. The sintered filters are 13.0 mm in thickness and extend from -1.5 m to -7.0 m depth. The gap between sintered filters and host rock is filled with compacted bentonite blocks of 100 mm in thickness. They are placed from -2.0 m to -7.0 m depth. The gap between the heater tube and rock, from -2.00m to -0.40m depth, is filled with sand. No account is given to the possible gaps between buffer bentonite and rock, and between buffer bentonite and heater. The upper part of borehole BHE-0, from 0.0 m to -0.40 m is sealed with resin to avoid leakages of water and gas.

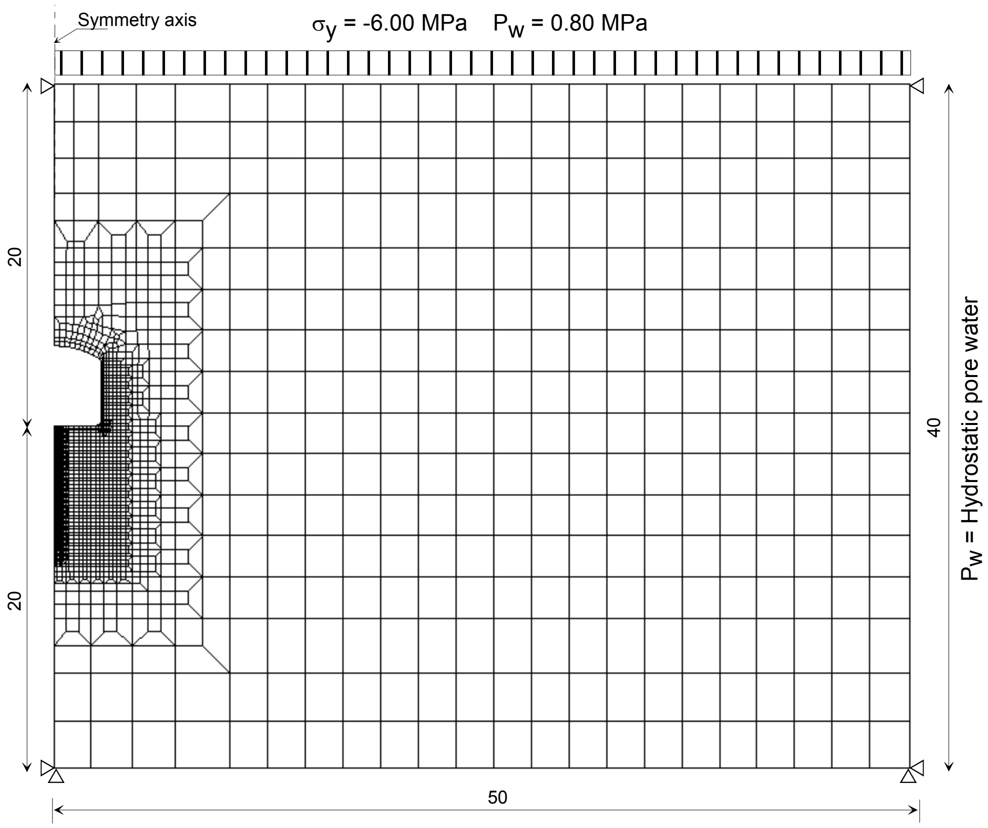

Figure 5.1: Axisymmetric finite element mesh used in the model.

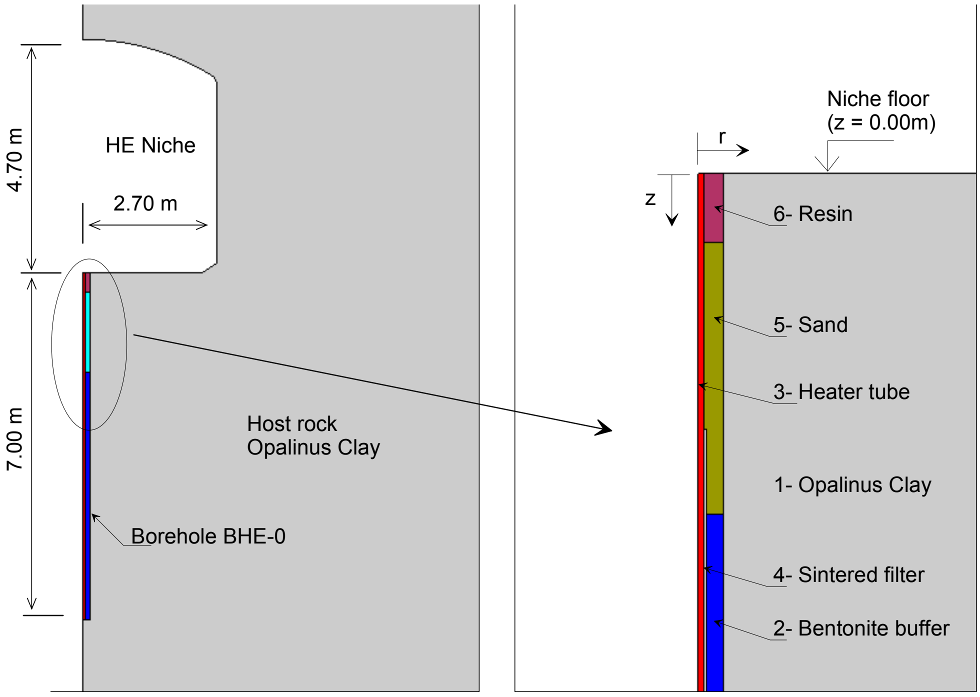

Figure 5.2: (Left): Geometry of HE niche and borehole BHE-0. (Right): Different components emplaced into the borehole BHE-0.

5.2.2 Initial and boundaries conditions

The initial phase of the calculations covers a period of 420 days, from March 1997 until May 1999, when the HE niche was already excavated. The initial stress state at the host rock was the following: σ_y = -6.0 MPa (vertical), σ_x = -4.8 MPa (radial) and σ_z = -4.8 MPa (circumferential) *(Bossart et al., 2002 and Martin and Lanyon, 2003).* A vertical stress σ_y = -6.0 MPa was applied at the upper boundary. A vertical stress σ_y = -0.5 MPa was applied on the niche floor. It is the vertical load due to concrete floor built in the niche. A hydrostatic absolute pore water pressure distribution was applied, where P_w = 1.0 MPa correspond to at the HE niche floor. The initial temperature at the host rock was 15 ºC. A hydraulic boundary condition of suction $s = 6.8\text{ MPa}$, equivalent relative humidity (RH) of 95 %, was applied on all the perimeter of the HE niche, as can be seen in Figure 5.3 (left).

The initial calculation phase corresponds to excavation of the borehole BHE-0. A period of 10 days was considered. Then a new boundary condition of suction $s = 6.8\text{ MPa}$ was applied on the wall of the borehole. The hydraulic boundary condition applied previously in the HE niche was maintained, see Figure 5.3 (Right).

Once the excavation phase was finished, a new numerical model was built with all the components of the HE experiment emplaced into the borehole BHE-0. The initial conditions in host rock were the stresses, pore water pressures and temperatures calculated at the end of the borehole excavation phase. An isotropic initial stress state of $\sigma_x = \sigma_y = \sigma_z = -0.15\text{ MPa (compression)}$ was applied to the bentonite buffer. The initial degree of saturation at the bentonite buffer was 60 %, that corresponds to a suction of $s = 136\text{ MPa}$. The initial temperature at the bentonite buffer was 15 ºC. The boundary conditions applied during the hydration phase is shown in Figure 5.4 (Left).

The hydration phase covers a period of 982 days, in which the hydraulic boundary condition applied to the HE niche was maintained. The boundary condition at the wall of the borehole BHE-0 was removed. A hydrostatic water pressure was applied to the sintered filter at four different depths, -6.90 m, -5.60 m, -4.40 m and -3.00 m. The water pressure at each injection point corresponds to a common piezometric head of 2.0 m over the niche floor. The hydration phase was performed under isothermal conditions at a temperature of 15º C.

The heating phase started after 982 days of hydration, when a temperature of 100 ºC was applied at the contact between heater and bentonite. A heating period of 554 days was considered. The hydraulic boundary condition applied to the HE niche and the four injections points were maintained, see Figure 5.4 (Right).

A cooling phase of 365 days was considered in calculations, from t = 1536 until t = 1901. The boundary condition of temperature at the contact between bentonite and heater was removed, allowing the temperature to recover the initial conditions.

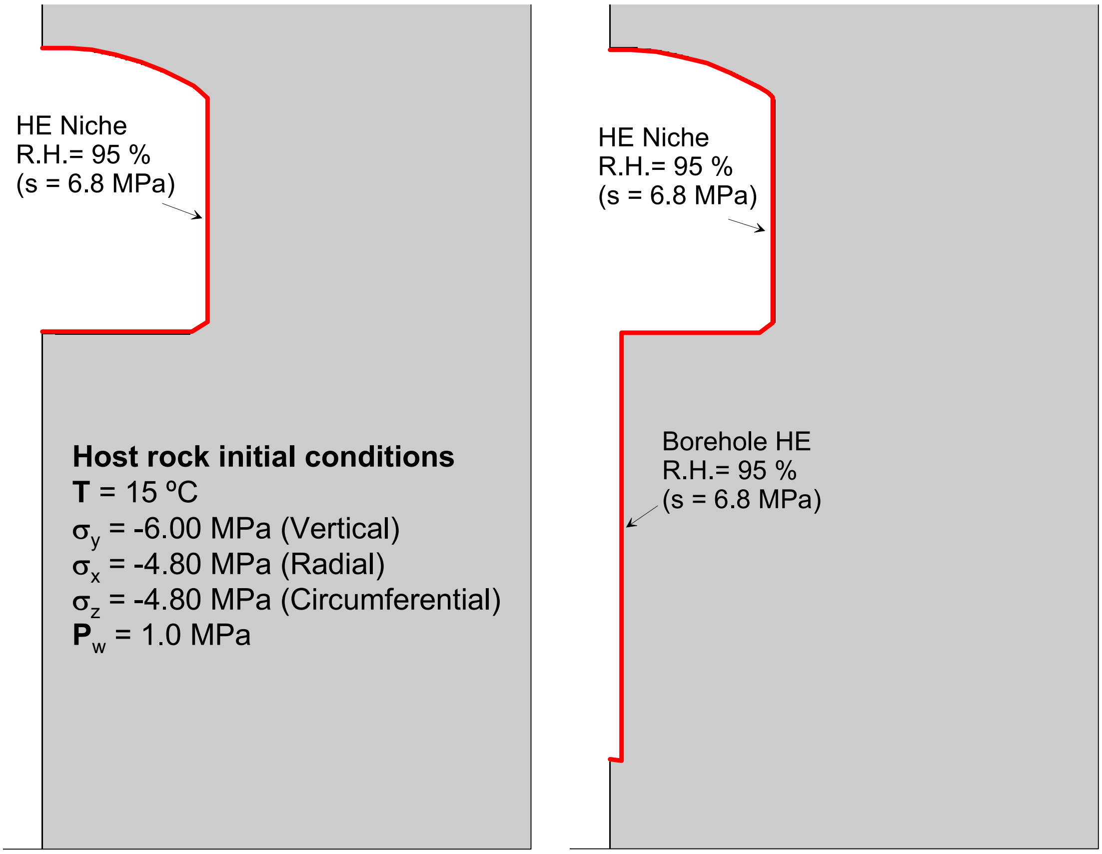

Figure 5.3: (Left): Boundary conditions applied on the niche perimeter at the niche excavation phase. (Right): Boundary conditions applied on the wall of the borehole at the borehole excavation phase.

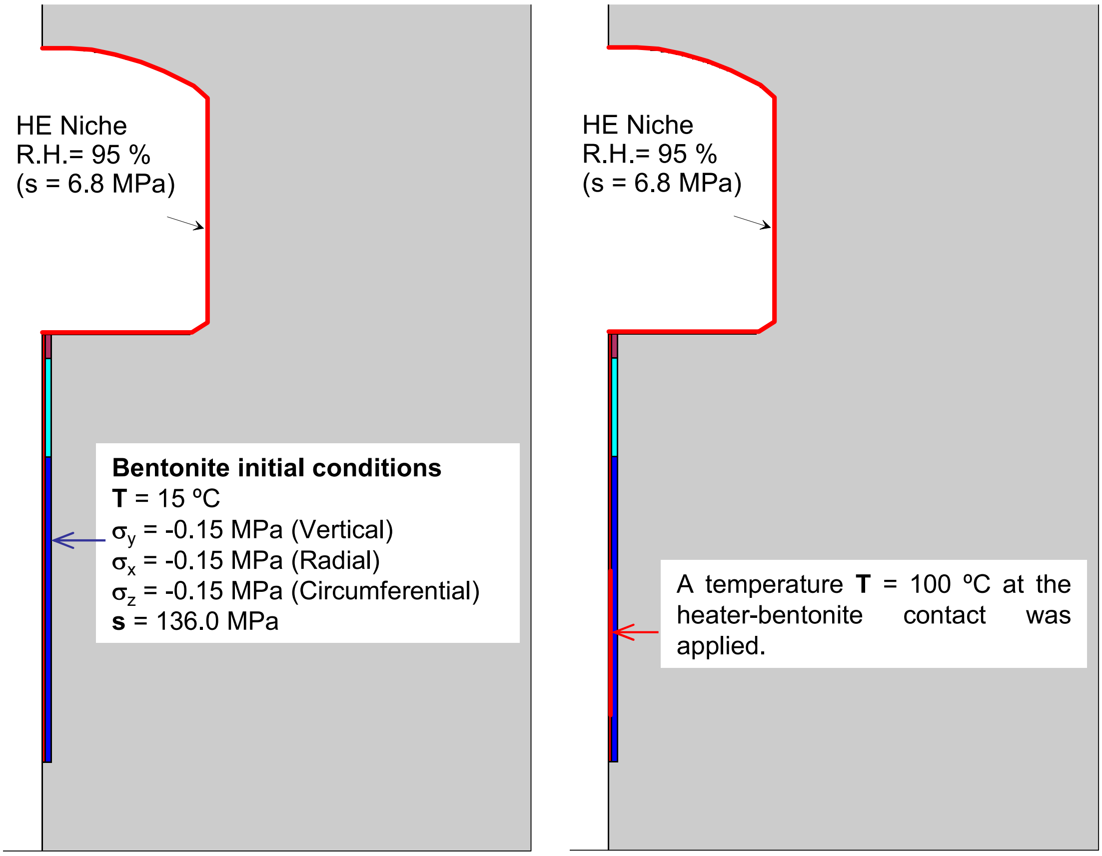

Figure 5.4: (Left): Boundary conditions applied during hydration phase. (Right): Boundary conditions applied to the heater during heating phase.

5.2.3 Host rock parameters

The mechanical, hydraulic and thermal parameters used in the model have been taken from available information on Opalinus Clay rock (*Hohner M. & Bossart P., 1998; Bock H., 2001; Muñoz J. et al., 2001; Muñoz J. et al., 2003*). They are summarized in Table 5.1, Table 5.2 and Table 5.3. The mechanical constitutive law proposed by *Vaunat and Gens (2003)*, described in chapter II, was used to simulate the rock.

Table 5.1: Mechanical parameters of Opalinus Clay

Properties	**Value**
E (Young's modulus)	(6000) [MPa]
ν (Poisson's ratio)	(0.27)
UCS (Unconfined Compressive Strength)	(16.0) [MPa]
UTS (Unconfined Tensile Strength)	(2.0) [MPa]
m	(8.0)
χ_0	(2.0)

Table 5.2: Hydraulic parameters of Opalinus Clay

Properties	**Value**
Intrinsic permeability, **k** (Kozeny model)	$k = k_0 \frac{\phi^3}{(1-\phi)^2} \frac{(1-\phi_0)^2}{\phi_0^3}$ ϕ_0: reference porosity (0.137) k_0: intrinsic permeability for matrix ($3.50 \cdot 10^{-19}$) [m^2]
Water Retention Curve (Modified Van Genuchten model)	$S_e = \frac{S_l - S_{rl}}{S_{ls} - S_{rl}} = \left(1 + \left(\frac{P_g - P_l}{P}\right)^{\frac{1}{1-\lambda}}\right)^{-\lambda} \left(1 - \frac{P_g - P_l}{P_s}\right)^{\lambda_s}$ S_e: Effective saturation ($0 \leq S_e \leq 1$) P : Material parameter (3.90) [MPa] P_s : Material parameter (700.00) [MPa] λ : Shape function for retention curve (0.128) λ_s : Material parameter (2.73) S_{rl}: Residual saturation (0.00) S_{ls}: Maximum saturation (1.00)
Relative permeability, $\mathbf{k_{rl}}$ (Van Genuchten model)	$k_{rl} = \sqrt{S_e}\left(1 - \left(1 - S_e^{1/\lambda}\right)^{\lambda}\right)^2$ S_e: Effective saturation ($0 \leq S_e \leq 1$) λ : Power (0.29) S_{rl}: Residual saturation (0.00) S_{ls}: Maximum saturation (1.00)
Molecular diffusion of vapour	$D_m^{vapor} = \tau D \left(\frac{(273.15 + T)^n}{P_g}\right)$ *D:* diffusion coefficient ($5.60 \cdot 10^{-10}$) [$m^2\ s^{-1}\ K^{-1}\ Pa$] *n:* (2.3) τ: Coefficient of tortuosity (1)
Porosity, **n**	(0.137)

Table 5.3: Thermal parameters of Opalinus Clay

Properties	**Value**
Thermal conductivity, λ	(2.10) [W m^{-1} K^{-1}]
Linear thermal expansion coefficient, $\boldsymbol{\beta}_s$	($1.00 \cdot 10^{-05}$) [ºC^{-1}]
Specific heat, **Cs**	(874.00) [J kg^{-1} K^{-1}]

Bentonite parameters

The bentonite parameters are derived from the information on the FEBEX project *(FEBEX Project (2000), Lloret A. et al., (2002), Sanchez and Gens (2005))*. The parameters are summarized in Table 5.4, Table 5.5 and Table 5.6. The thermoelastoplastic model for unsaturated soils proposed by *Gens (1995),* explained in chapter II, was used to simulate the bentonite.

Table 5.4: Mechanical parameters of FEBEX bentonite

Elastic Parameters		**Plastic Parameters**	
Properties	**Value**	**Properties**	**Value**
γ_d	1.80 [g/cm^3]	$\lambda_{(0)}$	0.158
		r	0.75
k_{io}	0.02	β	0.05 [MPa^{-1}]
k_{so}	0.3	ρ	0.2 [ºC^{-1}]
ν	0.3	k	0.1
α_{ss}	-0.03	p^c	0.1 [MPa]
α_{is}	-0.003	M	1
α_{sp}	-0.135	α	0.395
P_r	0.01 [MPa]	P_0*	22.0 [MPa]

Table 5.5: Hydraulic parameters of FEBEX bentonite

Properties	**Value**
Intrinsic permeability, **k** (Kozeny model)	$k = k_0 \dfrac{\phi^3}{(1-\phi)^2} \dfrac{(1-\phi_0)^2}{\phi_0^3}$ ϕ_0: reference porosity (0.40) k_0: intrinsic permeability for matrix ($1.1 \cdot 10^{-21}$) [m^2]

Water Retention Curve (Van Genuchten model)	$S_e = \frac{S_l - S_{rl}}{S_{ls} - S_{rl}} = \left(1 + \left(\frac{P_g - P_l}{P}\right)^{\frac{1}{1-\lambda}}\right)^{-\lambda}$ S_e: Effective saturation ($0 \le S_e \le 1$) P : Material parameter (90.00) [MPa] λ : Shape function for retention curve (0.45) S_{rl}: Residual saturation (0.00) S_{ls}: Maximum saturation (1.00)
Relative permeability, $\mathbf{k_{rl}}$ (Generalized power)	$k_{rl} = Se^{\lambda}$ S_e: Effective saturation ($0 \le S_e \le 1$) λ : Power coefficient (3.5)
Porosity, ***n***	(0.40)

Table 5.6: Thermal parameters of FEBEX bentonite

Properties	**Value**
Thermal conductivity	$\lambda = \lambda_w^{S_l} \cdot \lambda_d^{(1-S_l)}$ λ_w: (1.28) [W m^{-1} K^{-1}] λ_d: (0.50) [W m^{-1} K^{-1}]
Linear thermal expansion coefficients, $\mathbf{b_s}$	($0.35 \cdot 10^{-05}$) [ºC^{-1}]
Specific heat, **Cs**	(732.00) [J kg^{-1} K^{-1}]

5.2.4 Results of the analysis

The results of the numerical model are presented and compared with in situ data, following the main phases of the experiment. In all phases the displacement field, stress state, pore water pressure distribution and temperature field around of the borehole BHE-0 were analyzed. The experimental data were provided by *(García-Siñeriz and Rey, 1999 – 2004).*

5.2.4.1 HE niche excavation phase

As it was previously explained, the numerical model began with the HE niche already excavated. At the end of niche excavation phase, the maximum downward vertical displacements calculated takes place at the crown of niche, and reach a value of 6.7 mm. The upward vertical displacement on the niche floor, at symmetry axis, reaches a value of 1.6 mm. A maximum horizontal displacement of 2.2 mm is calculated at a half height of the niche wall. The shady zone in the Figure 5.5 shows the deformation of the HE niche at the end of niche excavation period.

The minor and major principal stresses are shown in Figure 5.6 and Figure 5.7, respectively. The horizontal stress distribution is shown in Figure 5.8. The horizontal stress in the niche wall decreases from -4.8 MPa to -0.1 MPa. A significant change in the stresses state reaches a depth of 2.5m from the wall. Vertical stress distribution can be seen in Figure 5.9. Vertical stresses under the niche floor decrease from -6.0 MPa to -0.50 MPa (vertical stresses applied on the niche floor). The significant disturbed zone produced by excavation reach a depth of 4.0m. At the crown of the niche, tensile vertical stresses of 0.5 MPa are computed, and the disturbed zone over the crown reaches a depth of 2.8 m. Plastic strain are developed in the floor-wall joint as shows Figure 5.10.

The distribution of the liquid pressures around the HE niche is shown in Figure 5.11 at 420 days after excavation. The distribution of degree of saturation (S_r) around of the niche can be seen in Figure 5.12. An unsaturated zone around of HE niche, which reaches a thickness of 1.5m around the wall, has been developed. This unsaturated zone is due to the water evaporation in the niche (R.H. = 95 %). The computed degree of saturation in the niche perimeter is about Sr = 85.0 %.

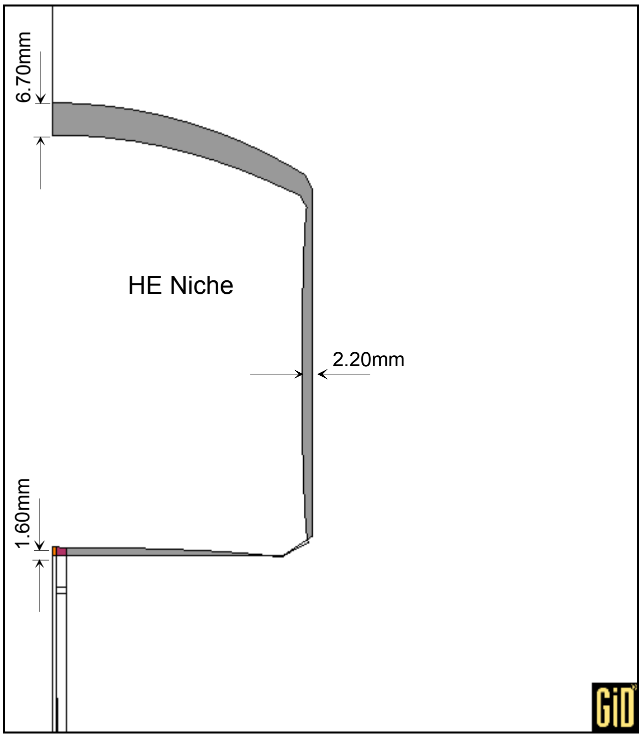

Figure 5.5: Deformation of the HE niche calculated after 420 days of the niche excavation.

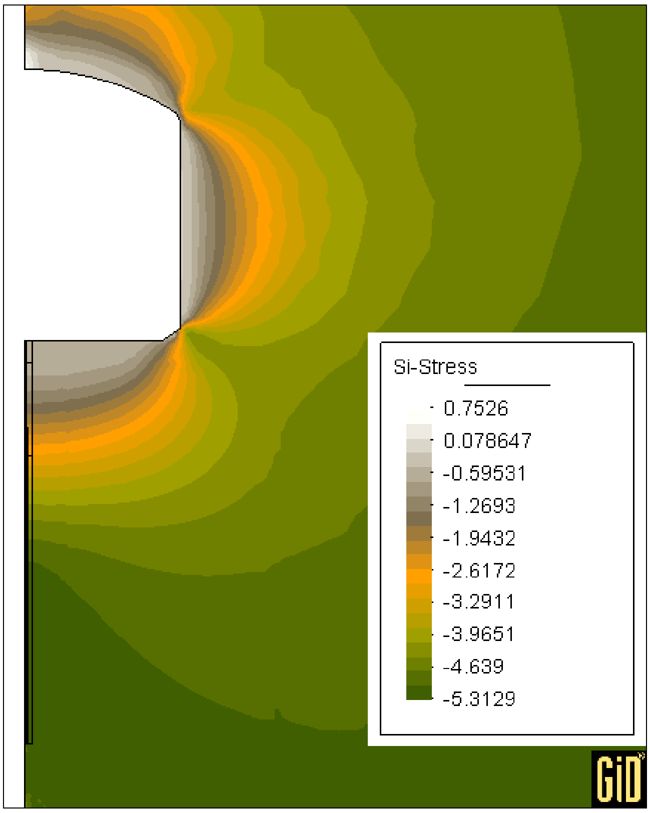

Figure 5.6: Minor principal stress (MPa) calculated after 420 days of niche excavation.

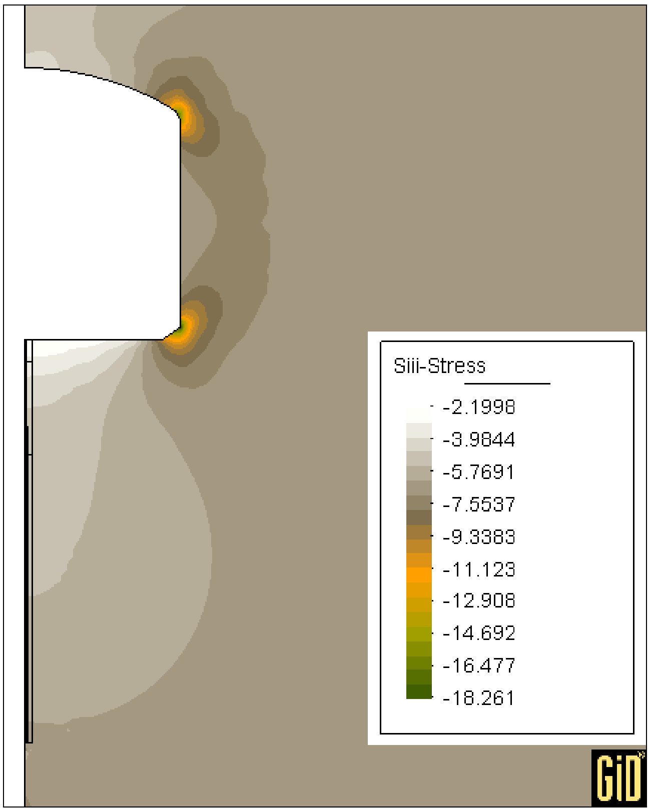

Figure 5.7: Major principal stress (MPa) calculated after 420 days of niche excavation.

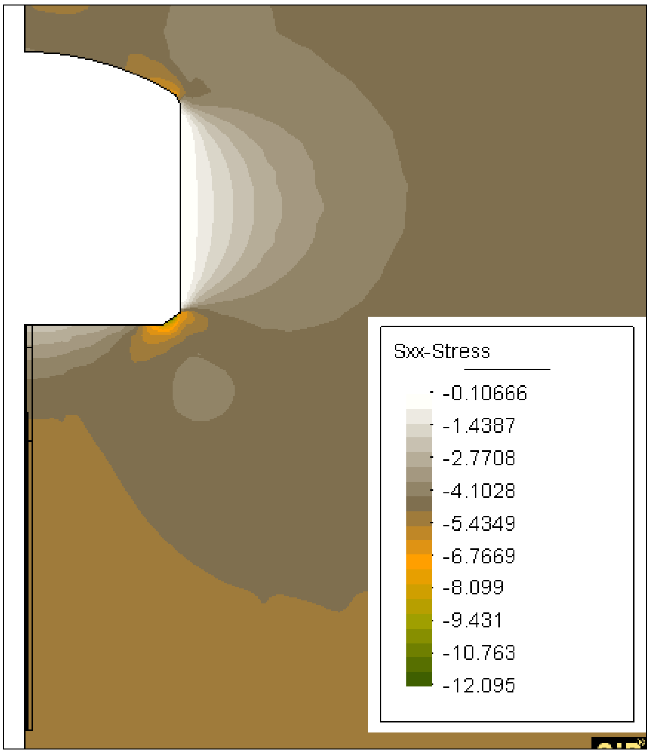

Figure 5.8: Horizontal stress (MPa) calculated after 420 days of niche excavation.

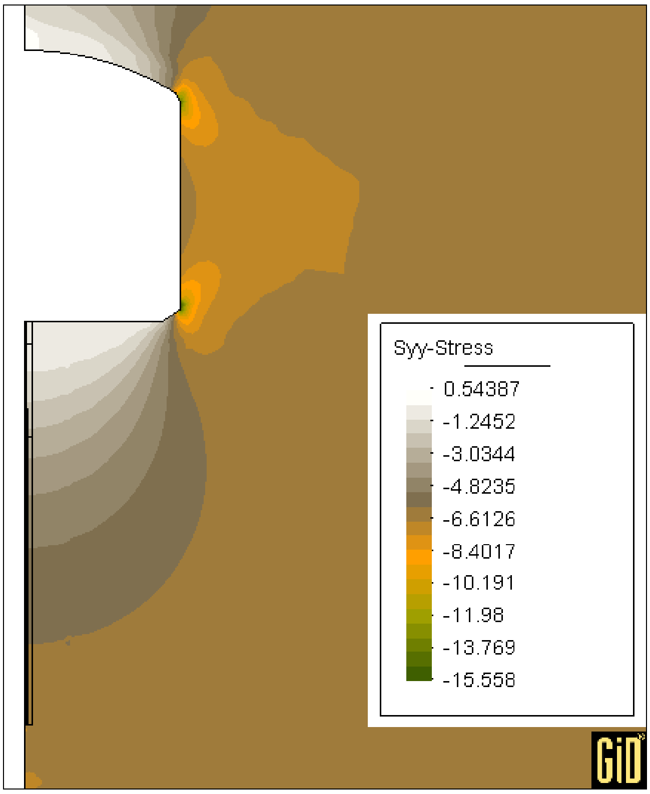

Figure 5.9: Vertical stress (MPa) calculated after 420 days of niche excavation.

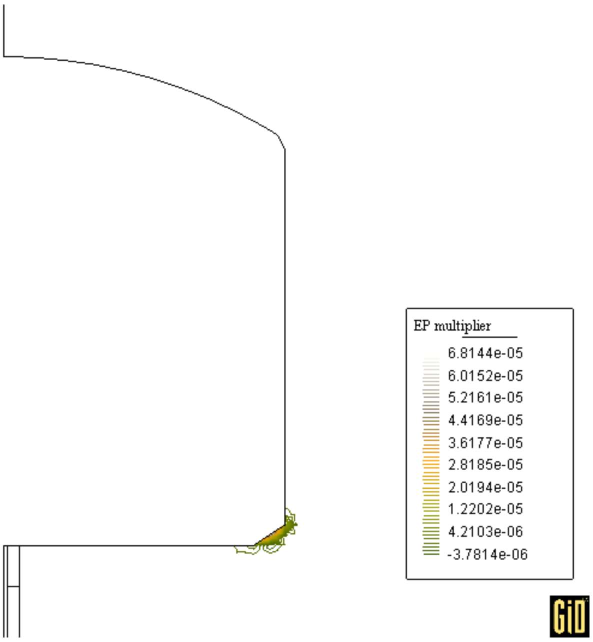

Figure 5.10: Plastic zone developed after 420 days of niche excavation.

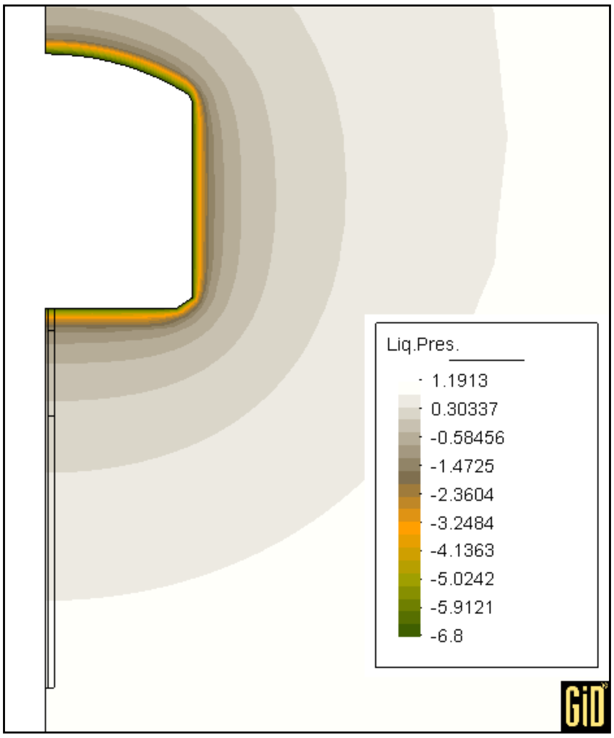

Figure 5.11: Distribution of the liquid pressure (MPa) around of the HE niche after 420 days.

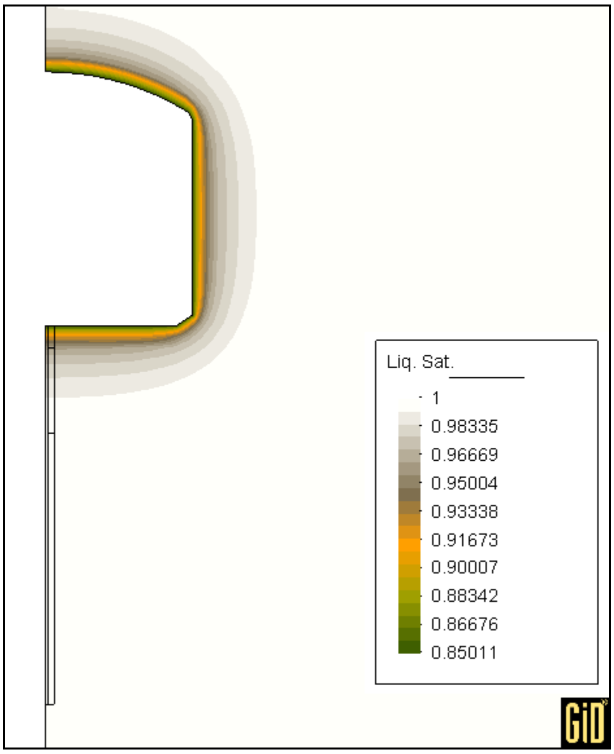

Figure 5.12: Degree of saturation (Sr) around of the HE niche after 420 days.

5.2.4.2 Drilling borehole BHE-0

The drilling of the borehole BHE-0 was simulated by removing the finite elements placed at radial distance between 0.0 m and 0.15 m and depth ranging from 0.0 m to -7.0 m. This phase lasted 10 days, from day 420 until day 430. In this stage, a boundary condition of suction (***s*** = 6.8 MPa) was applied on the wall of the borehole BHE-0.

The total radial and circumferential stresses are shown in Figure 5.13 and Figure 5.14 respectively. Due to excavation, the total radial stress in the wall of borehole decrease from -4.8 MPa to -0.1 MPa. On the other hand, the circumferential stresses increase from the initial value of -4.8 MPa to -9.5 MPa. The stress changes affect an annulus zone of 0.8 m in thickness around the borehole.

The distribution of liquid pressure around of borehole BHE-0 at t = 430 days is shown in Figure 5.15, whereas the distribution of the degree of saturation around the borehole is shown in the Figure 5.16. A relatively thin annulus having thickness of 0.15m was unsaturated around the borehole.

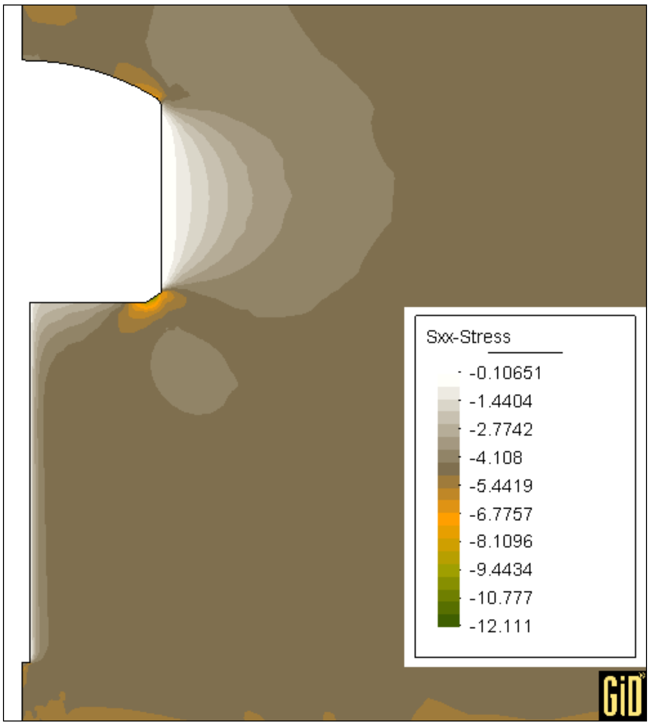

Figure 5.13: Distribution of the total radial stress (MPa) around of the borehole BHE-0 after 430 days.

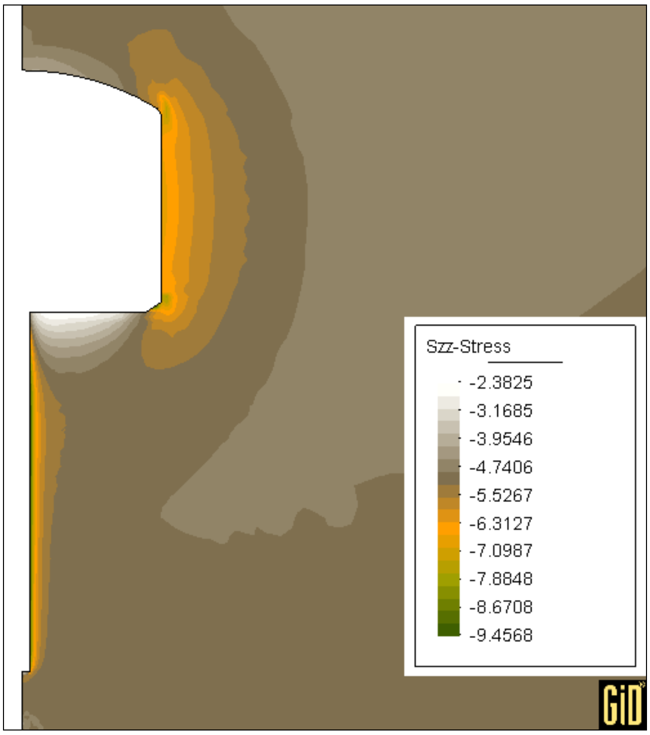

Figure 5.14: Distribution of the total circumferential stress (MPa) around of the borehole BHE-0 after 430 days.

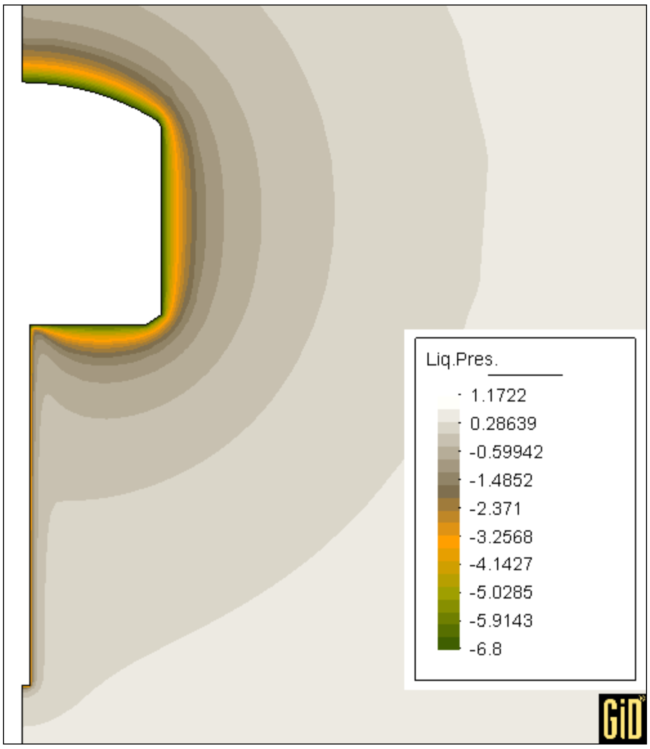

Figure 5.15: Distribution of the liquid pressure (MPa) around of the borehole BHE-0 after 430 days.

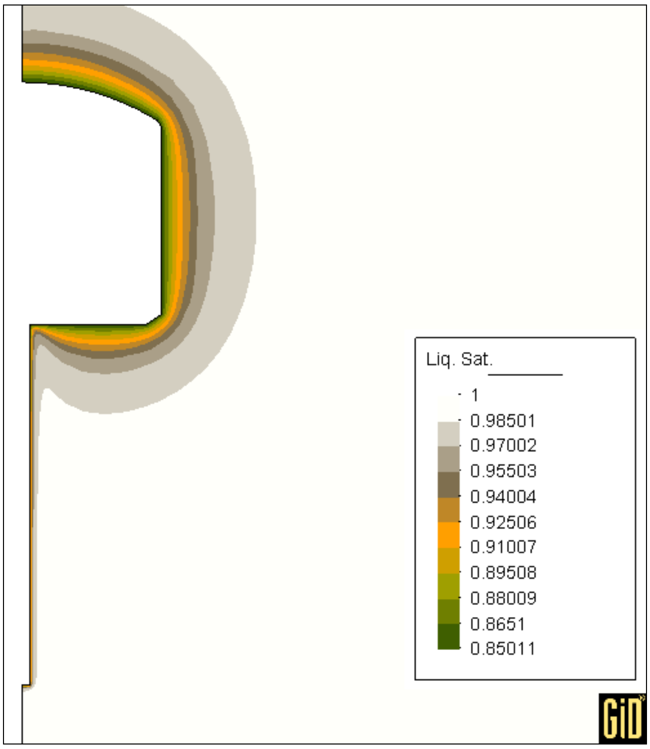

Figure 5.16: Degree of saturation (Sr) around of the borehole BHE-0 after 430 days.

5.2.4.3 Hydration phase

The temperature sensors TB00_05.00, TB05_05.00, TB06_05.00 and TB01_05.00 were chosen in order to plot the temporal and spatial distribution of the measured temperatures. The sensors were located in a horizontal plane 5.0 m deep and at radial distances of 0.05 m, 0.65 m, 1.65 m and 4.15 m, respectively. The water pressure sensors QB 19/2 and QB 20/2 were chosen represent the measured pore water pressure evolution in points located in a horizontal plane 5.0 m depth and radial distance of 0.65 m and 1.65 m, respectively.

Figure 5.17 shows the time evolution of the computed and measured temperature during the operational phase of the HE experiment in points located at the same position of the temperature sensors. Figure 5.18 shows the time evolution of the computed and measured liquid pressure in the location of the water pressure sensors. The radial stress, circumferential stress and radial displacement computed in a plane at 5.0 m depth and radial distance of 0.15 m, 0.65 m and 1.65 m are shown in Figure 5.19, Figure 5.20 and Figure 5.21, respectively.

At the beginning of the hydration phase the water enters into the sintered filter and rises towards the upper part of the borehole, where the sand was saturated quickly. After that, the water began to saturate the bentonite buffer slowly. The high initial suction of bentonite (136MPa) produces a desaturation on the surrounding rock of 0.7 m thickness. Figure 5.22 (Left) shows the liquid pressure and degree of saturation (Right) in bentonite blocks and in the rock, calculated after 45 days of hydration. The time evolution of the degree of saturation in points located into the bentonite at 5.0 m depth, are shown in Figure 5.23. The required time to saturate the bentonite was 200 days approximately. Figure 5.24 shows the transitory process of the desaturation and resaturation produced in the surrounding rock at 5.0 m depth. The rock reaches the full saturation after 250 days of hydration.

The measured and computed water inflow during the hydration phase is shown in Figure 5.25. The theoretical quantity of water required to reach the full saturation of bentonite and sand is 116.45 l. An amount of 105.5 l of injected water was calculated with CODE_BRIGT, whereas the total amount of 150.16 l of injected water was measured. The discrepancy between unaccounted for the computed and measured quantity of injected water can be due to leaks. In fact, the heater tube was broken at the beginning of the hydrations phase due to high bentonite swelling pressure (*García-Siñeriz et al. 1999-2004*). Table 5.7 shows the history of the measured injected water into the borehole BHE-0.

The high swelling pressures of bentonite produce changes in the stress state of the surrounding rock, during the hydration phase. The significant change of the stress state extends to a maximum distance of 1.0 m. The radial stress increases from -0.15 MPa to -14.0 MPa, whereas the circumferential stress decreases from the initial value of -9.2 MPa until it reaches a tensile stress of 1.0 MPa in points located at the bentonite-rock contact, as shown Figure 5.19 and Figure 5.20, respectively. Figure 5.26 shows the distribution of radial stress and circumferential stress after 980 days of hydration. A maximum radial displacement of 1.05 mm was calculated in a point located at the bentonite-rock contact (r = 0.15 m). Radial displacements of 0.24 mm and 0.05 mm were calculated at radial distances of 0.65 m and 1.65 m, respectively. As a consequence of the high swelling pressures of bentonite, plastic strains are produced in some points of the rock. The calculated plastic zone was located in a narrow annulus of rock immediate to the bentonite buffer. It reaches a maximum thickness of 0.05 m. The radial displacements and plastic zone around the Borehole BHE-0 during hydration phase can be seen in Figure 5.27.

5.2.4.4 Heating phase

The heating phase began at time t = 982 days, once the hydration phase was completed. The heating phase lasted 18 months, where the power was initially applied in steps of 140 W, 150 W, 285 W and 580 W. This power is applied to the axis of the heater, until the heater-buffer contact (r = 0.05m) reaches a temperature of 100 ºC. The time evolution of temperature during heating phase can be seen in Figure 5.17. The calculated and measured distribution of temperature as a function of distance for different times during the heating phase is shown in Figure 5.28. As it can be seen in Figure 5.17 and Figure 5.28 the temperature field is well captured by the model.

The computed and measured evolution of water pressure during heating phase is shown in Figure 5.18. Temperature increments generate significant positive water pressures. Water pressure increments from 0.12 MPa to 0.73 MPa were measured by sensor QB19/2 at time t = 1050 days, whereas a water pressure increment from 0.07 MPa to 0.30 MPa at time t = 1080 days was measured by sensor QB20/2. Note that 30 days have passed between the maximum water pressure measured by the sensor QB19/2 and QB20/2. At constant temperature, dissipation of water pressures is produced and they tend towards the initial condition. The liquid pressure increments are well reproduced by the model. Liquid pressure increments are induced by the thermal expansion of the water. In fact, the coefficient of thermal expansion of water is higher than the thermal expansion coefficient of the solid skeleton. The magnitude of the increments of liquid pressures is controlled by several factors, such as the rate of temperature increase, the rock permeability, the rock porosity, the rock stiffness and geometry and boundary conditions of the experiment.

Total radial and circumferential stresses increments computed are shown in Figure 5.19 and Figure 5.20, respectively. Successive temperature increments produce small increments of radial and circumferential stress (load effect). Plastic strains are produced in the rock around the borehole BHE-0 by temperature increments. The plastic zone reaches a maximum thickness of 0.08 m. Figure 5.29 shows the temperature field and liquid pressure distribution developed around BHE-0 during the heating phase at time t = 1050 days. Temperature changes reach a maximum radial distance of 5.0 m.

5.2.4.5 Cooling phase

The cooling phase began 1536 days after the beginning of the experiment. In the calculations, it lasted 365 days more. In this phase, the power was removed. Calculations indicate that the temperature decreases quickly. The evolution of temperature in the cooling phase can be seen in Figure 5.17. The profile of temperature versus radial distance is shown in Figure 5.30. After 25 days of cooling, the temperature drops to less than 25° C in the whole area of influence of the test. The liquid pressure evolution at sensors QB19/2 and QB20/2 during the cooling phase can be seen in Figure 5.18. The cooling induces negative liquid pressure, and its magnitude depends on the rate of temperature decrease. The transitory radial and circumferential stresses produced by cooling are shown in Figure 5.19 and Figure 5.20, respectively. This transitory stress changes represent a radial displacement towards the heater (unloading effect). Long term, steady state stresses do not seem to be affected by the heating and cooling phases except for a narrow zone immediate to the bentonite buffer.

The rock's stresses in the near field of the borehole BHE-0 are a consequence of the complete history of the HE experiment, such as HE niche excavation, borehole BHE-0 drilling, the development of swelling pressures and the thermal dilation of materials. The effective stress path followed by a point of the rock close to the interface with the bentonite (r = 0.18 m) has been plotted in Figure 5.31. The plot shows that this point reaches limiting conditions at some instant during hydration. Once the initial strength envelope is hit, limited rock degradation is produced. The stress path shows how the stresses are maintained at the current limiting strength surface. Some additional yielding is calculated during the heating phase. During the cooling phase, an unloading of the point of rock was produced. The rock degradation computed in a narrow zone around of the borehole can be seen in Figure 5.32. This figure shows the time evolution of plastic multiplier (upper) and time evolution of tensile strength (bottom) computed at radial distance of 0.16m and 0.18m in all phases of the experiment.

The computed and measured values of radial displacements have been plotted in Figure 5.33 and Figure 5.34, respectively. Large discrepancies are found between measured and calculated displacements. The maximum computed displacements at (z = -5.0 m) at the end of the heating phase is 0.12 mm, whereas the measured values is in order of 5.4 mm. During the cooling phase negative displacements were predicted by the model (displacements toward the heater) on the contrary, the measured displacements continue to increase until they reach 5.6mm.

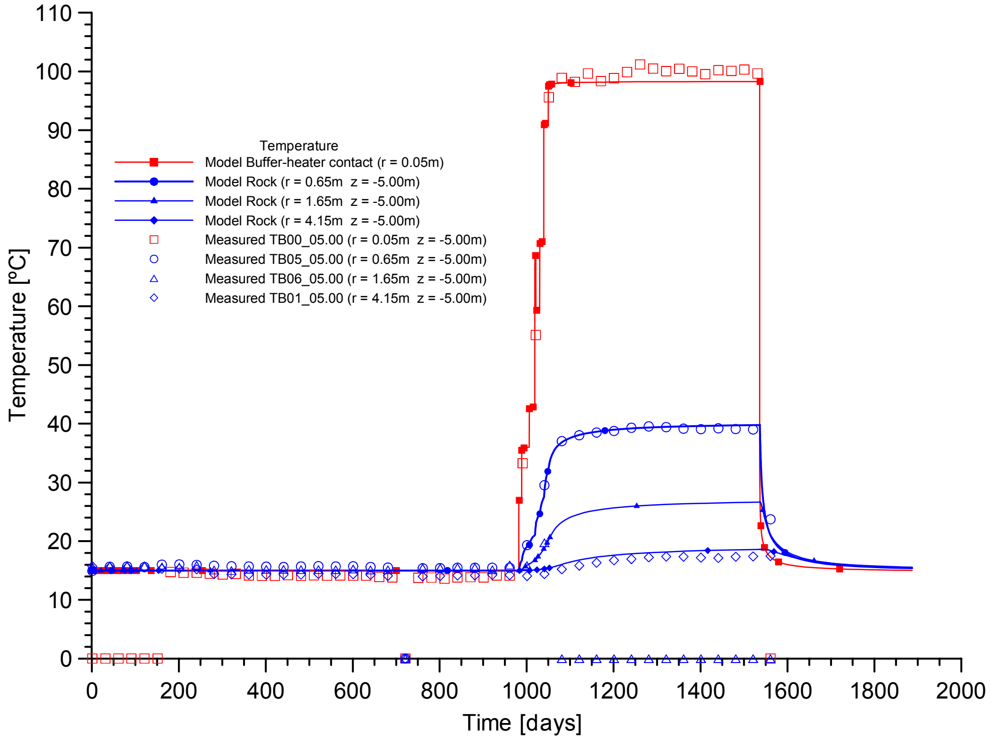

Figure 5.17: Time evolution of temperatures computed and measured during the hydration, heating and cooling phases, in points located in bentonite and rock.

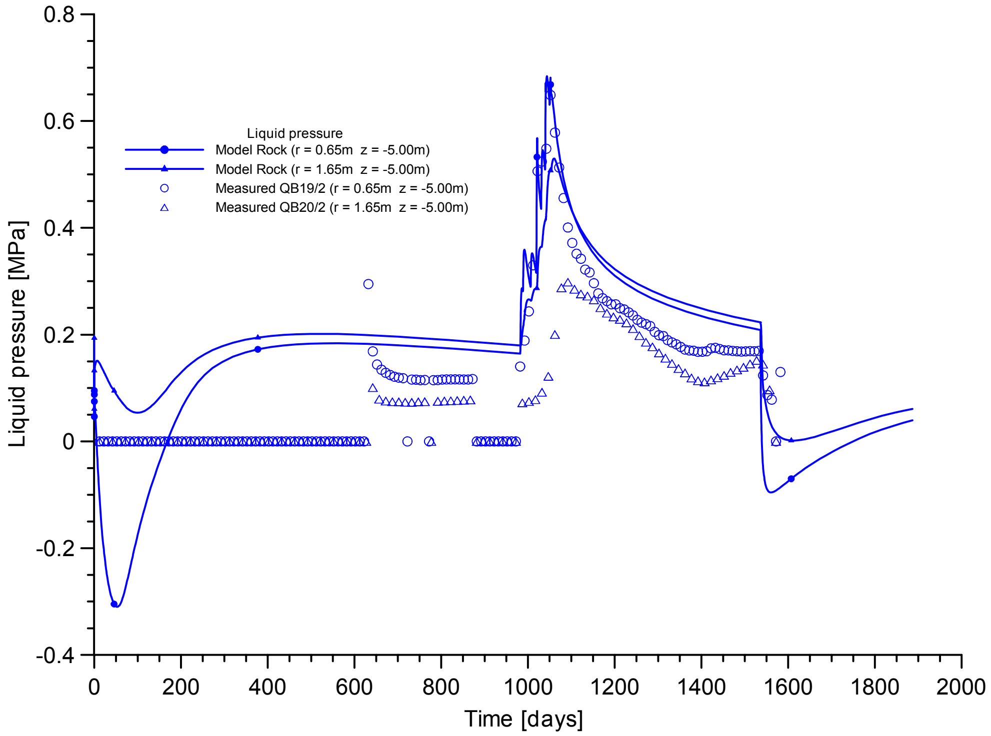

Figure 5.18: Time evolution of liquid pressure in points located in rock during hydration, heating and cooling phase.

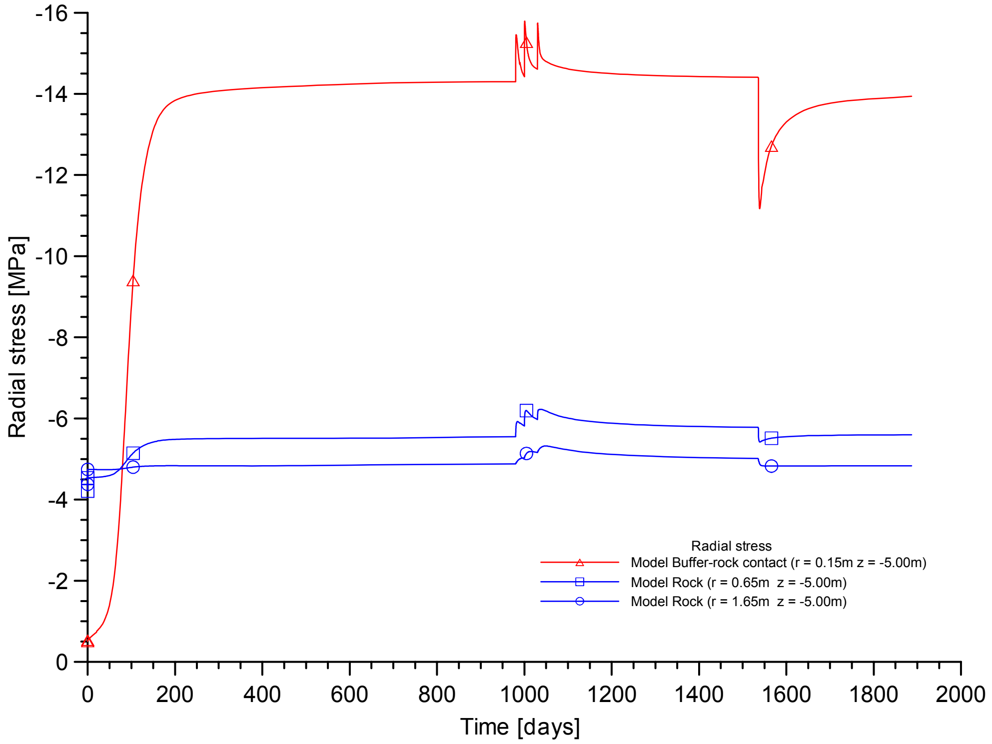

Figure 5.19: Time evolution of the radial stress computed during the hydration, heating and cooling phases, in points located in rock.

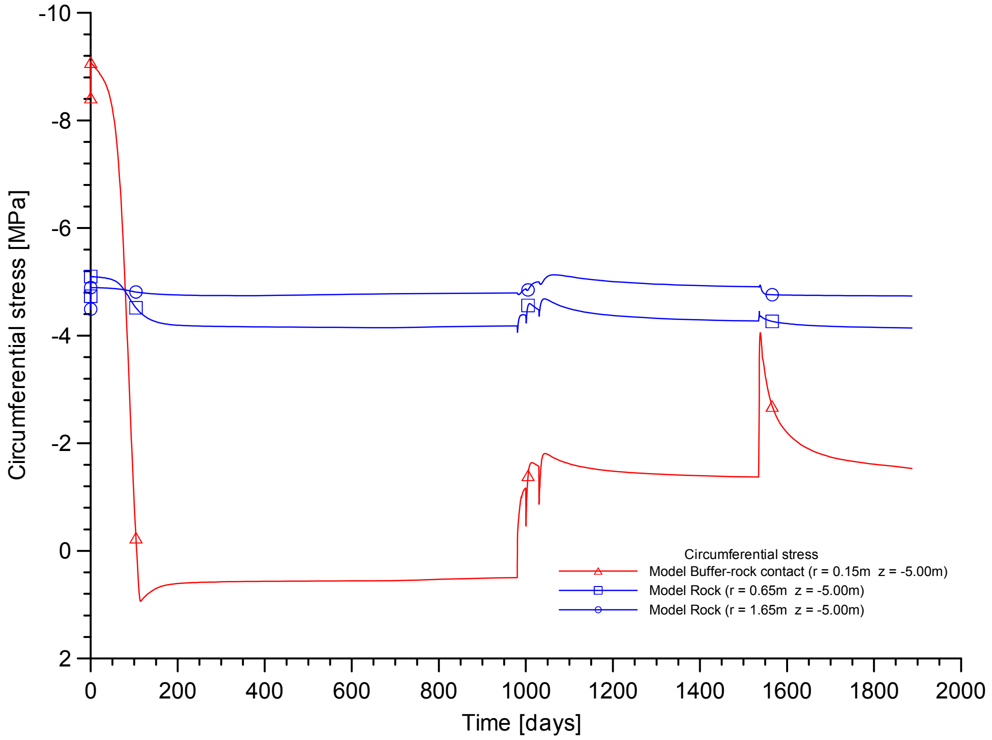

Figure 5.20: Time evolution of the circumferential stress in points located in rock during hydration, heating and cooling phase.

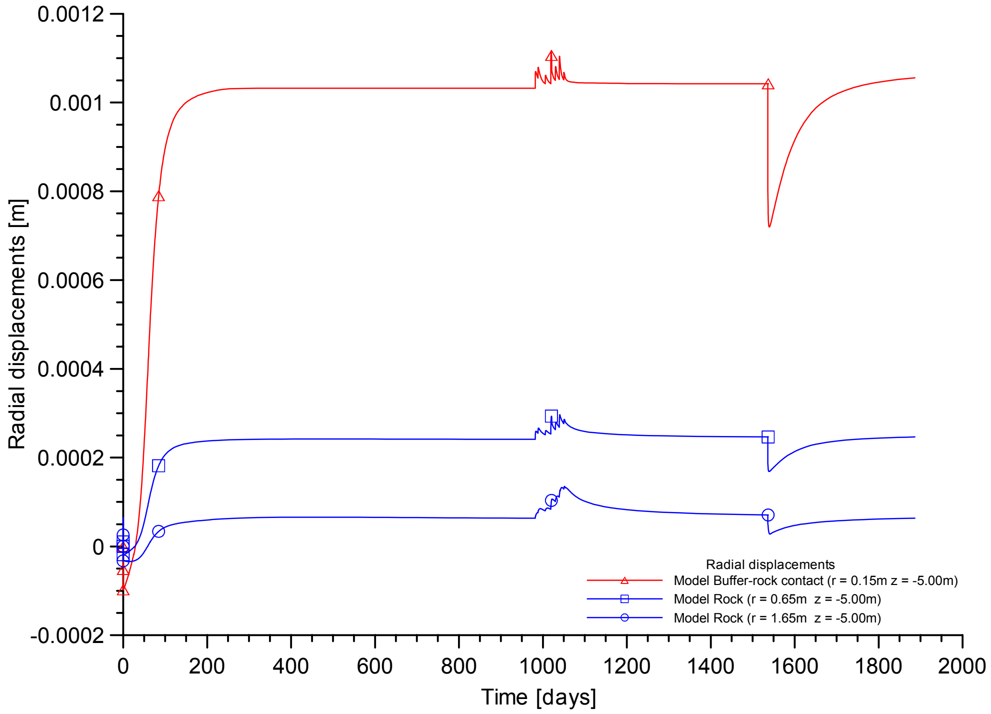

Figure 5.21: Computed radial displacements of rock during hydration phase, heating phase and cooling phase. Points located at 5.0 m depth and radial distances of 0.15m, 0.65m and 1.65m.

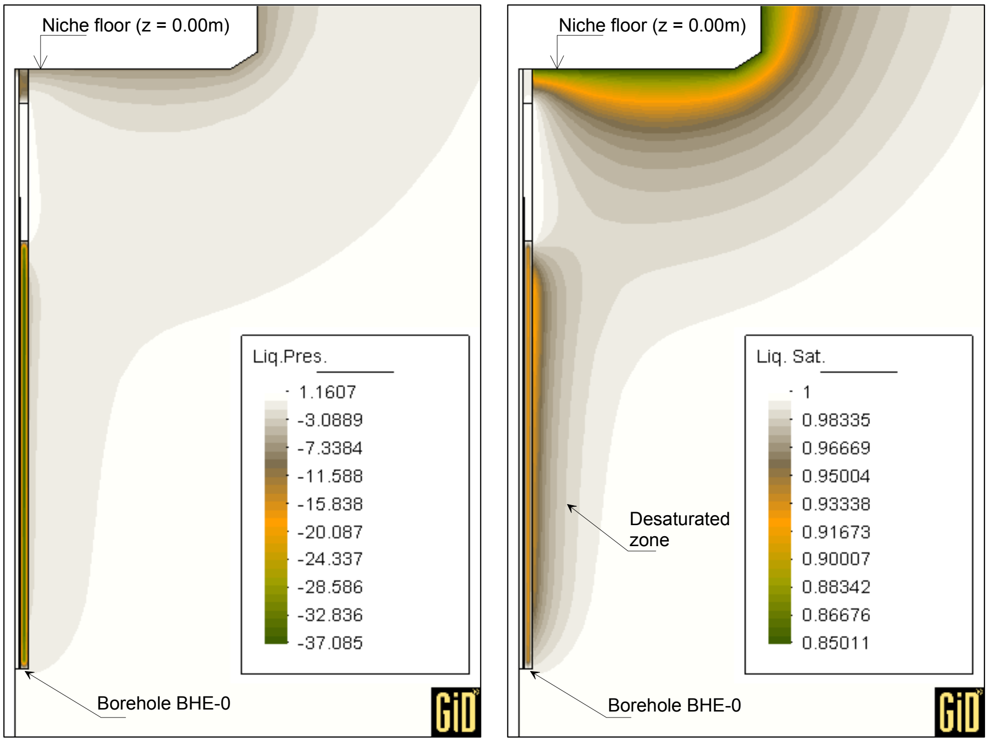

Figure 5.22: (Left): Liquid pressure distribution (MPa) after 45 days of hydration. (Right): Degree of saturation on the surrounding rock after 45 days of hydration.

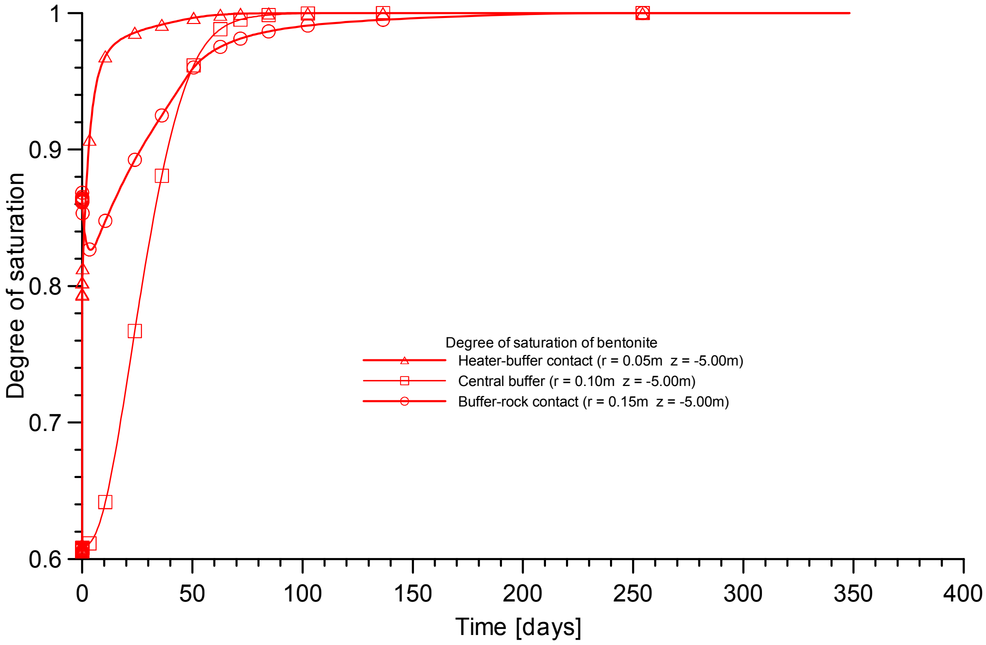

Figure 5.23: Time evolution of the degree of saturation of the bentonite during the hydration phase.

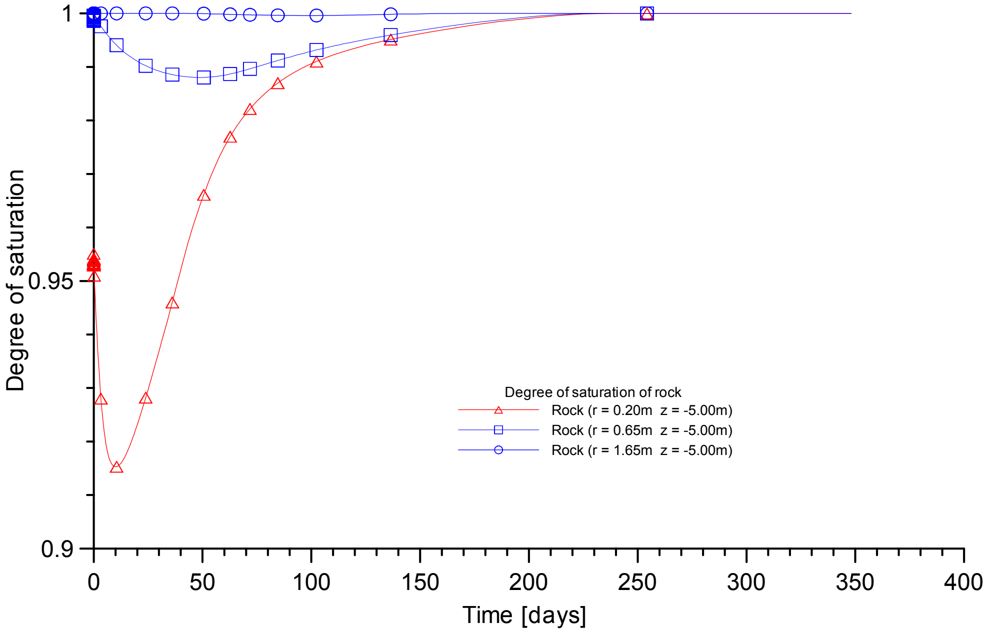

Figure 5.24: Time evolution of the degree of saturation in the surrounding rock during the hydration phase

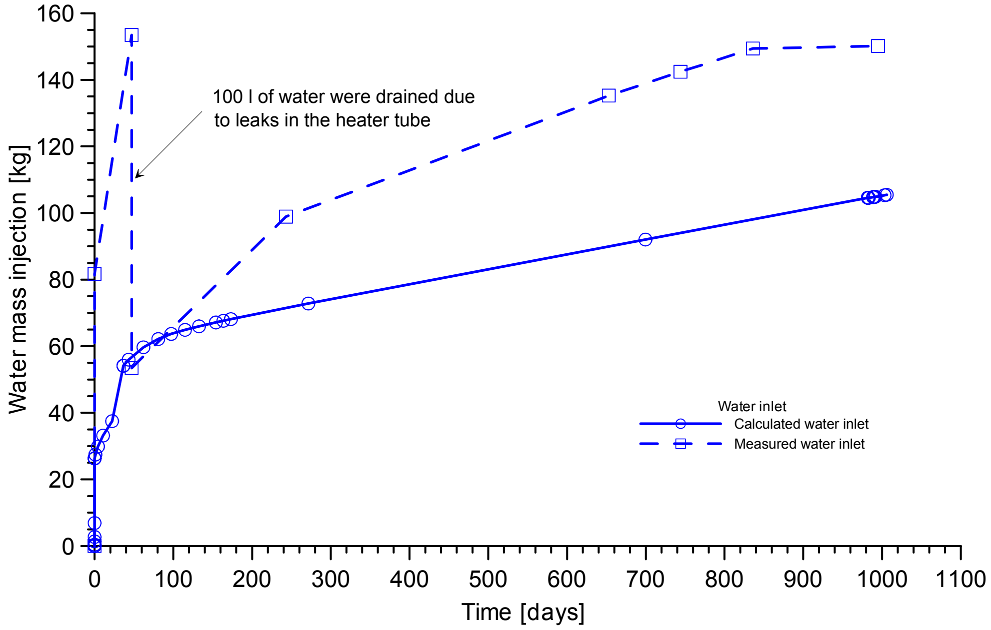

Figure 5.25: Computed and measured water inlet during the hydration phase.

Table 5.7: Measured injected water into the bentonite.

Days	**Water injected**	**Accumulated water injected**
-2	81.74	81.74
47	71.71	153.45
47	-100	53.45**
243	45.47	98.92
653	36.35	135.27
744	7.16	142.43
836	7.00	149.43
995	0.70	150.13

** An estimated amount of 100 *l*. was drained from the borehole BHE-0 due to leaks in the heater tube

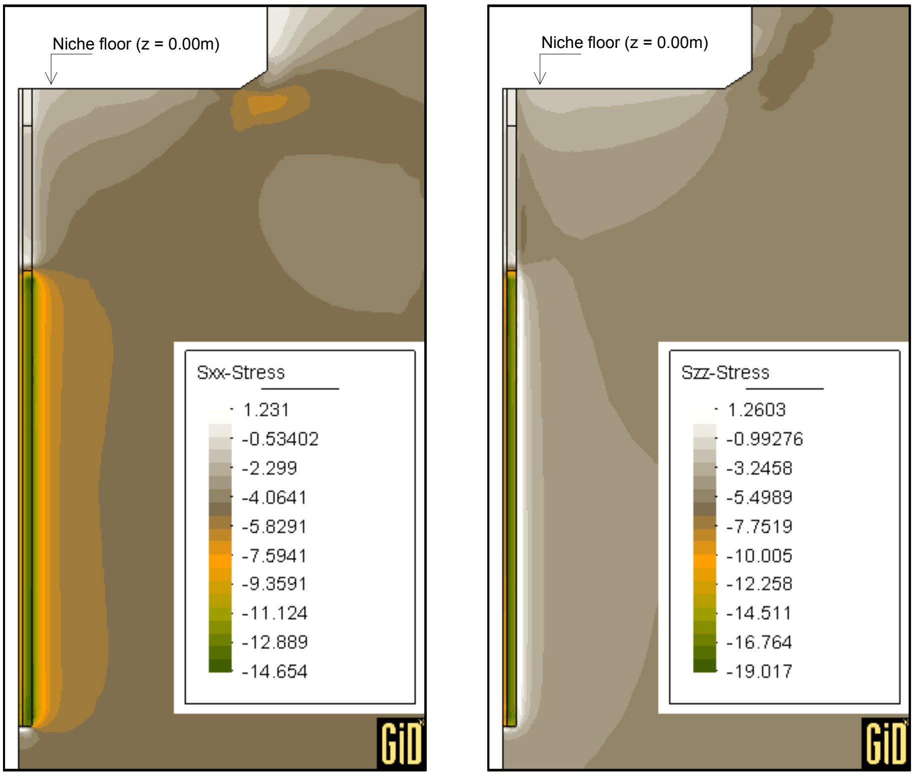

Figure 5.26: (Left): Radial stress (MPa) developed after 980 days of hydrations. (Right): Circumferential stress (MPa) developed after 980 days of hydrations.

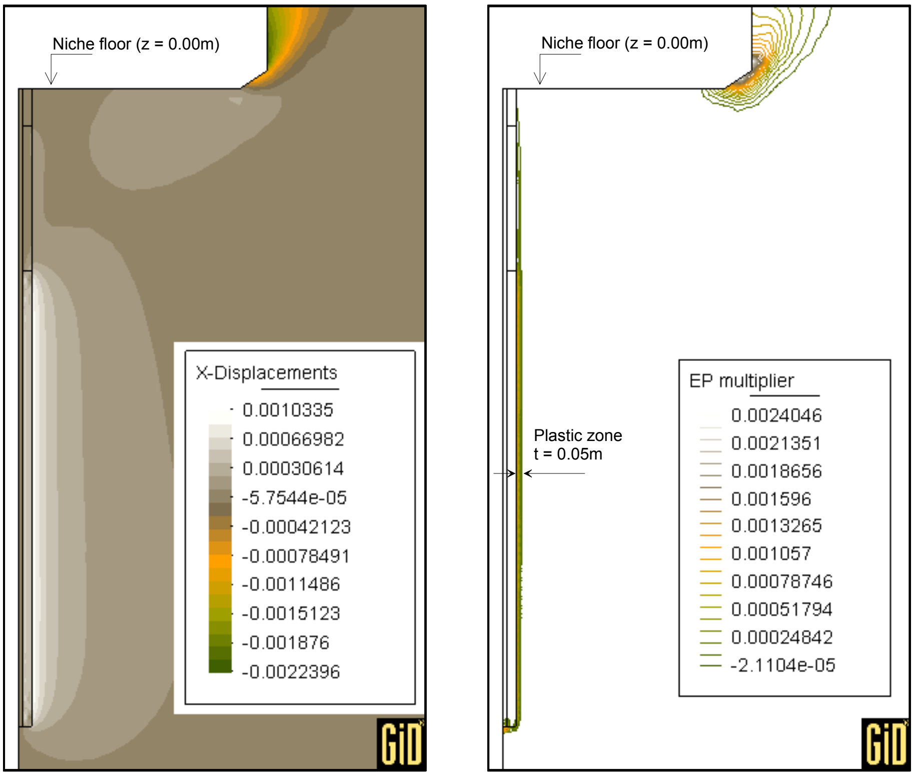

Figure 5.27: (Left): Radial displacements (m) developed by swelling pressure of bentonite during hydration phase. (Right): Plastic zone around of borehole BHE-0

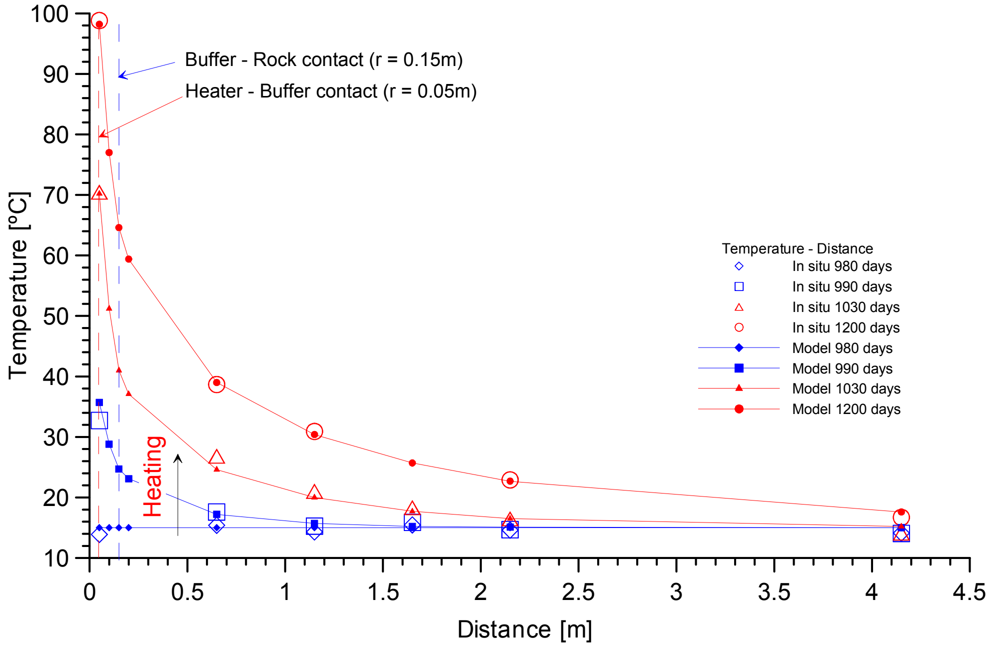

Figure 5.28: Computed and measured distribution of temperature as a function of distance for different times during the heating phase. Points located at 5.0 m depth.

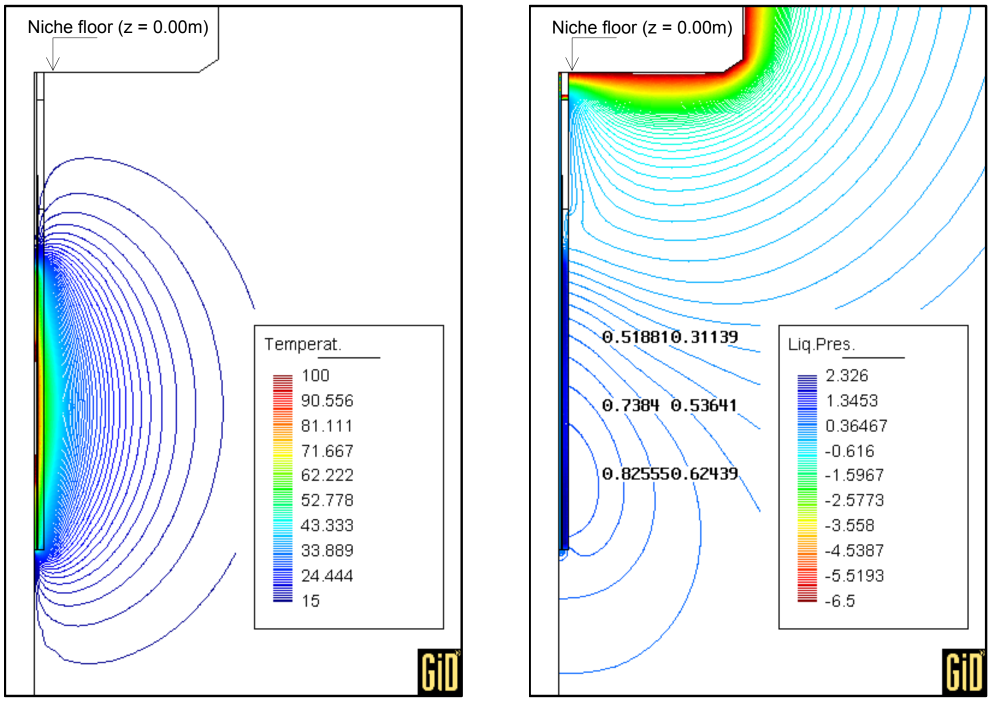

Figure 5.29: (Left): Temperature field (ºC) developed during the heating phase (t =1050 days). (Right): Liquid pressure distribution (MPa) during the heating phase (t = 1050 days).

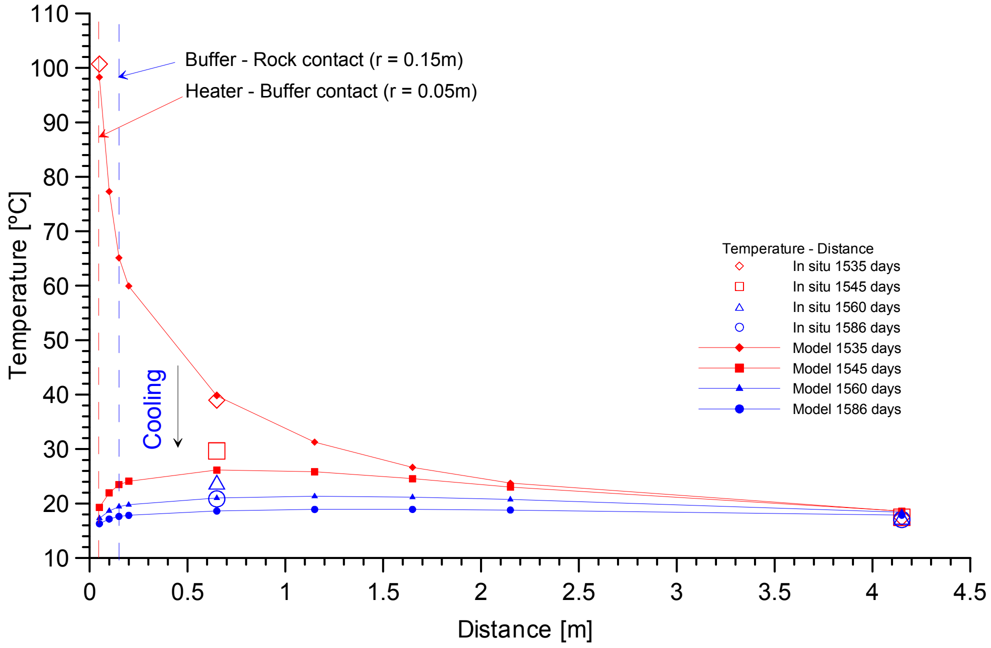

Figure 5.30: Computed and measured distribution of temperature as a function of distance for different times during the cooling phase. Points located at 5.0 m depth.

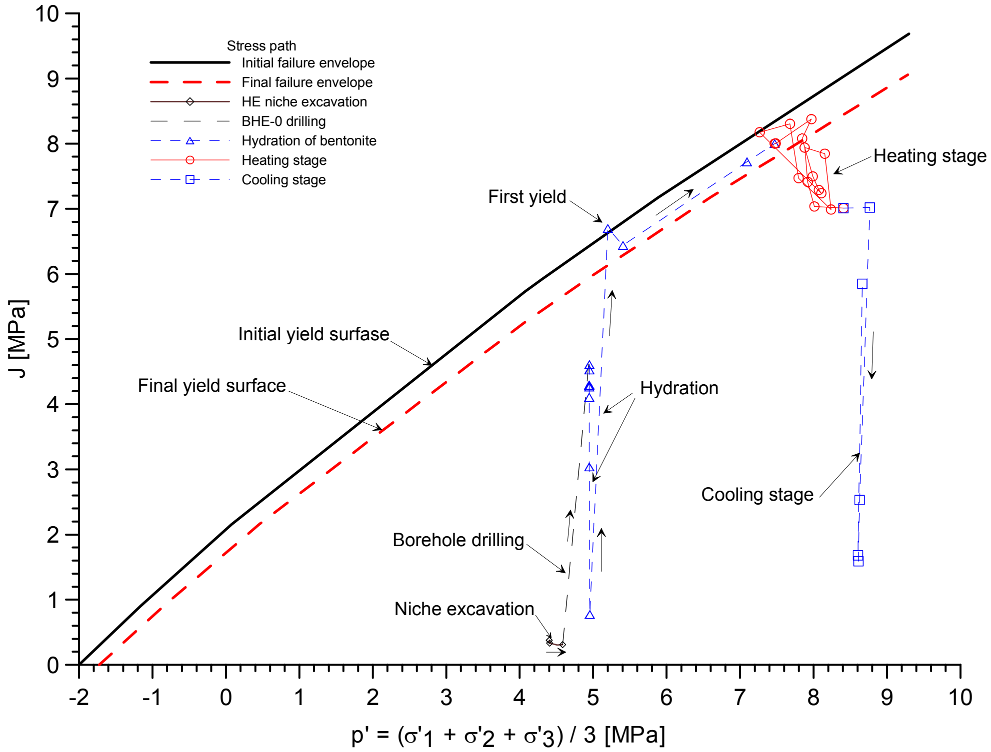

Figure 5.31: Effective stress path followed by a point of the rock close to the interface bentonite-rock (r = 0.18m).

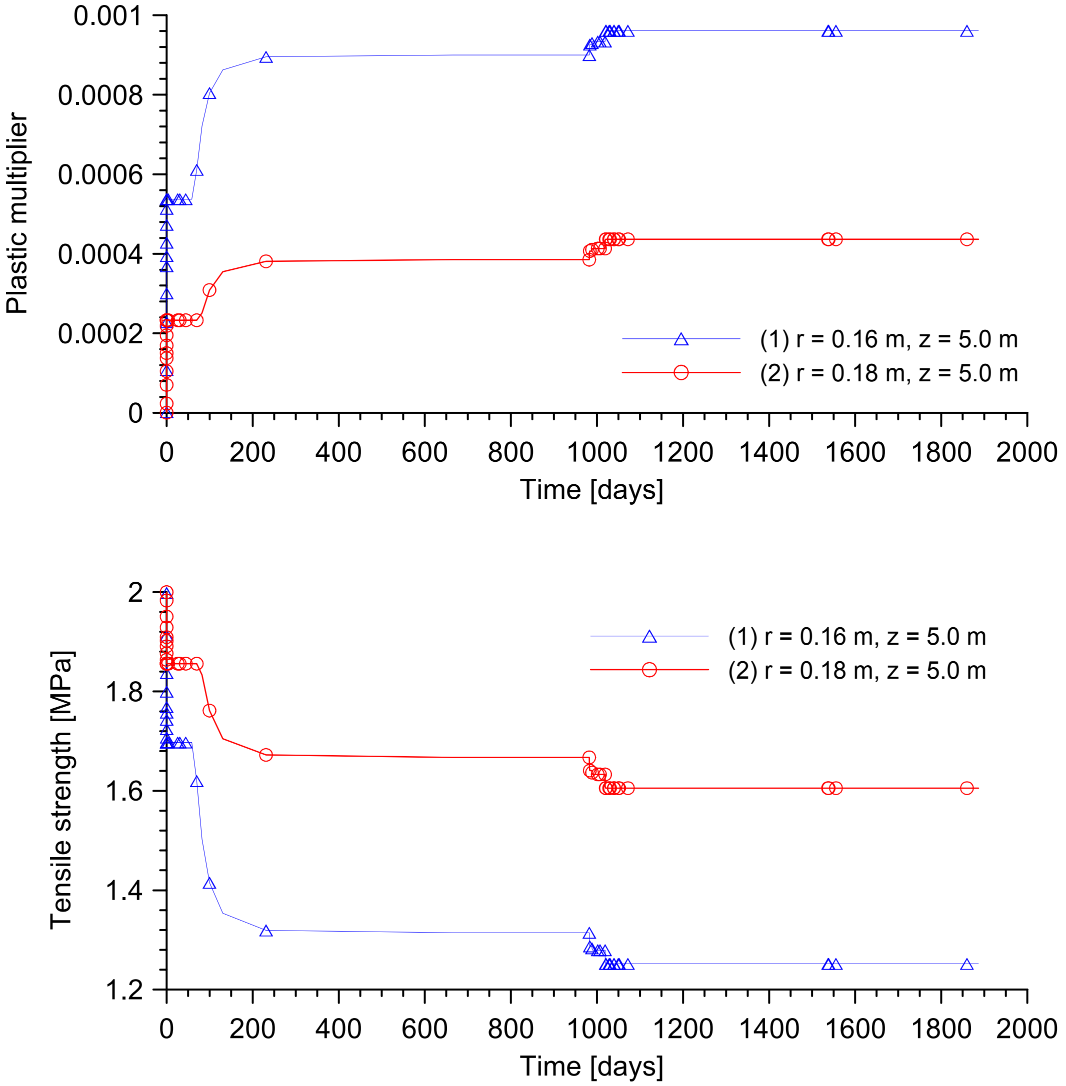

Figure 5.32: (Upper): Time evolution of plastic multiplier computed at radial distances of 0.16m and 0.18m. (Bottom): Time evolution of the tensile strength at radial distance of 0.16m and 0.18m.

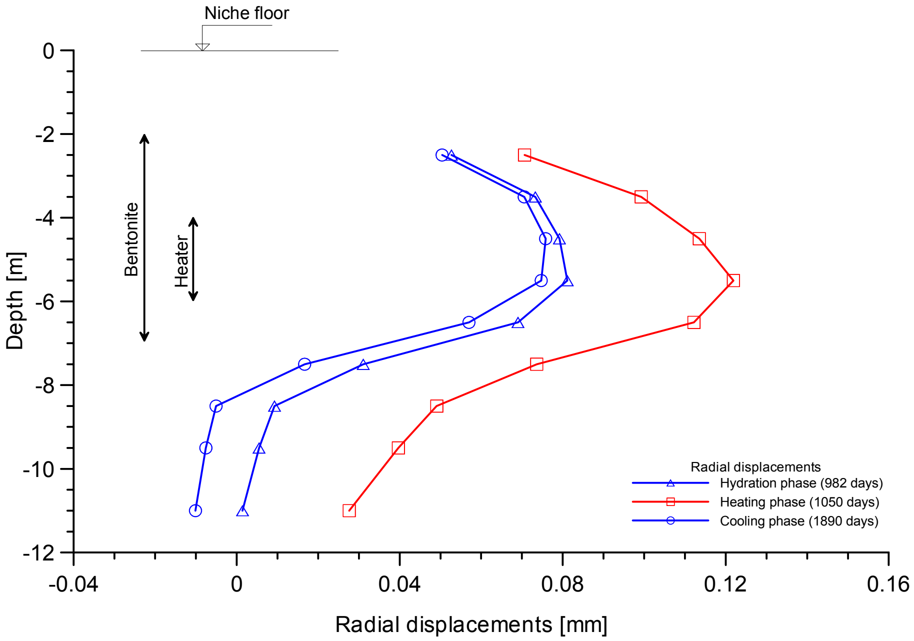

Figure 5.33: Profile of computed radial displacements versus depth.

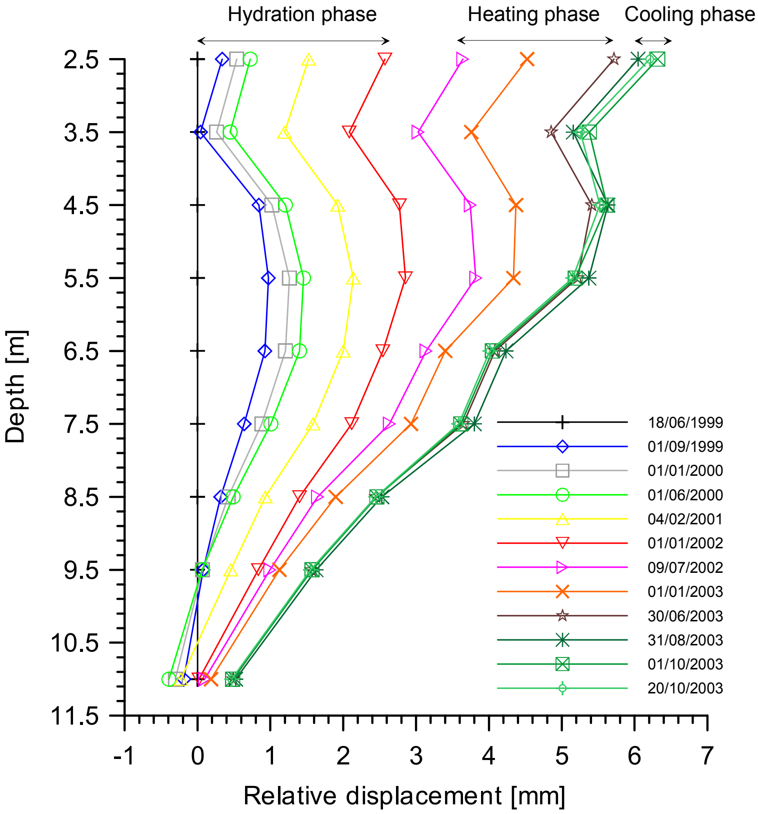

Figure 5.34: Profile of measured radial displacements versus depth.

5.3 Modeling of the laboratory pulse heating test

5.3.1 Geometry of the cell

A T-H-M numerical simulation of the laboratory pulse heating test has been carried out. All phases of the experiment have been simulated. They include the initial hydration and subsequent heating and cooling cycles. An axisymmetric numerical model with respect to the longitudinal axis of the cell has been adopted. Figure 5.35 (Left) shows the geometry of the cell and the different materials considered. A total of five different materials are considered in the simulation: 1- The rock Opalinus clay, 2- The stainless steel (lids and ring), 3- The heater, 4- The porous disc and 5- The epoxi resin. A finite element mesh of 2411 quadrilateral elements and 2567 nodes was developed, as shown in Figure 5.35 (Right). Each node has four degrees of freedom, namely, two displacements (radial and vertical), the liquid pressure and the temperature.

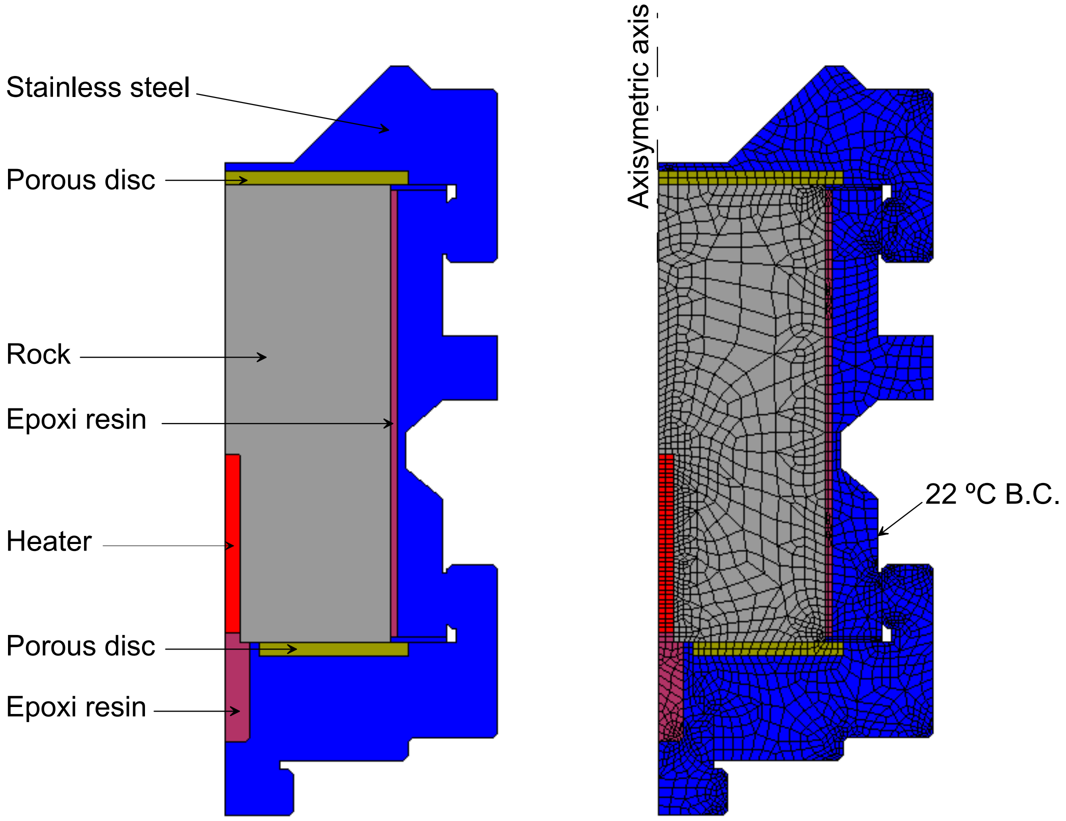

Figure 5.35: (Left): Geometry and materials considered. (Right): Finite Element Mesh of the cell.

5.3.2 Initial and Boundary conditions

The initial conditions of the rock were the following: suction $s = 6.0$ MPa , temperature $T = 22.0$ ºC and an isotropic stress state $\sigma_x = \sigma_y = \sigma_z = -0.15$ MPa . The boundary conditions (B.C.) are variables depending of the phase of the experiment. The boundary conditions are summarized in Table 5.8 and these are shown in Figure 5.36.

Table 5.8: Boundary conditions applied in the cell

	Boundary Conditions
B.C. 1	Null displacements imposed in the base of the cell. All phases of the experiment. Temperature T = 22 ºC was imposed in the base of the cell. All phases of the experiment.
B.C. 2	Temperature T = 22 ºC was imposed in all perimeter of the cell. All phases of the experiment.
B.C. 3	Null displacements in the longitudinal axis of cell. All phases of the experiment. Flux null. All phases of the experiment.
B.C. 4	Water pressure inlet imposed in the bottom porous disc. Variable depending of the phase of experiment, hydration or heating. The history of the water pressure inlet of 0.5 MPa, 0.85 MPa and 1.0 MPa was reproduced in hydration phase, as can be seen in Figure 5.37. Flux null was imposed during heating phase.
B.C. 5	Water pressure outlet imposed in the upper porous disc. Variable depending of the phase of experiment. Water pressure outlet of 0.1 MPa (atmospheric pressure) during hydration phase and heating phase under drained conditions. Flux null during heating phase in undrained conditions.
B.C. 6	Null displacements in the longitudinal axis of heater. Temperature T = 22 ºC during hydration phase. Energy flux (Power) applied on the axis of the heater during heating phase.

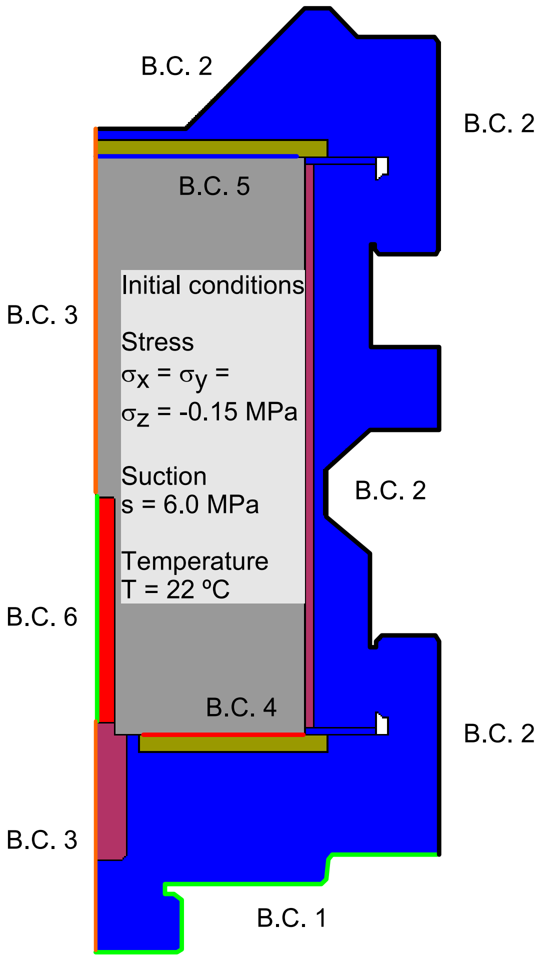

Figure 5.36: Initial and boundary conditions applied to numerical simulations of the pulse heating test.

5.3.3 Material parameters

The damage-elastoplastic model for argillaceous rocks proposed by *Vaunat and Gens (2003)* was used to model the rock. The rock's parameters used to simulate the heating experiment are shown in Table 5.9, Table 5.10 and Table 5.11. The rock parameters used in this simulation are similar to rock parameters used in HE experiment (Section 5.2). The stainless steel was simulated by means of a linear elastic constitutive law with a Young Modulus of E = 0.183E+06 MPa and a Poisson's ratio of $\nu = 0.3$. It was considered as a porous medium with an intrinsic permeability of k = 1.0E-30 m^2 (impermeable) and a porosity n = 0.10E-02. The heater was simulated with the same parameter of the stainless steel. The epoxi resin was simulated by means of a linear elastic law with the same stiffness of the rock. The epoxi resin was also simulated as an impervious material. The metallic porous discs were simulated by means of a linear elastic law with the same mechanical parameters of the stainless steel. The porous discs were simulated with an intrinsic permeability several orders of magnitude higher of the rock (k = 1.0E-16 m^2) and a porosity of n = 0.5.

Table 5.9: Mechanical parameters of Opalinus Clay

Properties	**Value**
E (Young's modulus)	(6000) [MPa]
ν (Poisson's ratio)	(0.27)
UCS (Unconfined Compressive Strength)	(16.0) [MPa]
UTS (Unconfined Tensile Strength)	(2.0) [MPa]
M	(8.0)
χ_0	(2.0)

Table 5.10: Thermal parameters of Opalinus Clay

Properties	**Value**
Thermal conductivity, $\boldsymbol{\lambda_w}$	(2.50) [W m^{-1} K^{-1}]
Linear thermal expansion coefficient, $\boldsymbol{\beta_s}$	($1.35 \cdot 10^{-05}$) [ºC^{-1}]
Specific heat, **Cs**	(874.00) [J kg^{-1} K^{-1}]

Table 5.11: Hydraulic parameters of Opalinus Clay

Properties	**Value**
Intrinsic permeability, **k** (Kozeny model)	$k = k_0 \dfrac{\phi^3}{(1-\phi)^2} \dfrac{(1-\phi_0)^2}{\phi_0^{\,3}}$ ϕ_0: reference porosity (0.185) k_0: intrinsic permeability for matrix (1.0010^{-19}) [m^2]
Water Retention Curve (Modified Van Genuchten model)	$S_e = \dfrac{S_l - S_{rl}}{S_{ls} - S_{rl}} = \left(1 + \left(\dfrac{P_g - P_l}{P}\right)^{\frac{1}{1-\lambda}}\right)^{-\lambda} \left(1 - \dfrac{P_g - P_l}{P_s}\right)^{\lambda_s}$ S_e: Effective saturation ($0 \le S_e \le 1$) P : Material parameter (8.60) [MPa] P_s : Material parameter (700.00) [MPa] λ : Shape function for retention curve (0.32) λ_s : Material parameter (0.66) S_{rl}: Residual saturation (0.00) S_{ls}: Maximum saturation (1.00)

Relative permeability, **k_{rl}** (Van Genuchten model)	$k_{rl} = \sqrt{S_e}\left(1-\left(1-S_e^{1/\lambda}\right)^{\lambda}\right)^2$ S_e: Effective saturation ($0 \le S_e \le 1$) λ : Power (0.35) S_{rl}: Residual saturation (0.00) S_{ls}: Maximum saturation (1.00)
Molecular diffusion of vapour	$D_m^{vapor} = \tau D\left(\frac{(273.15+T)^n}{P_g}\right)$ *D:* diffusion coefficient ($5.45 \cdot 10^{-10}$) [$m^2\ s^{-1}\ K^{-1}\ Pa$] *n:* (2.3) τ: Coefficient of tortuosity (1)
Porosity, *n*	(0.185)

5.3.4 Analysis of numerical simulations

5.3.4.1 Hydration phase

The hydration phase was simulated under isothermal conditions of 22 ºC during a period of 100 days. The history of the water pressures inlet has been reproduced by means of B.C.4. Water pressures at the inlet of 0.5MPa, 0.85MPa and 1.0MPa has been applied. The water pressure at the outlet was applied by means of B.C. 5 (upper porous disc). It remains constant at atmospheric pressure (P_w = 0.1MPa) during all hydrations phase. Figure 5.37 shows the time evolution of the water pressure computed and measured in both sensors (P_w1) and (P_w2). The computed and measured time evolution of water volume inlet during the first 100 days of test is shown in Figure 5.38.

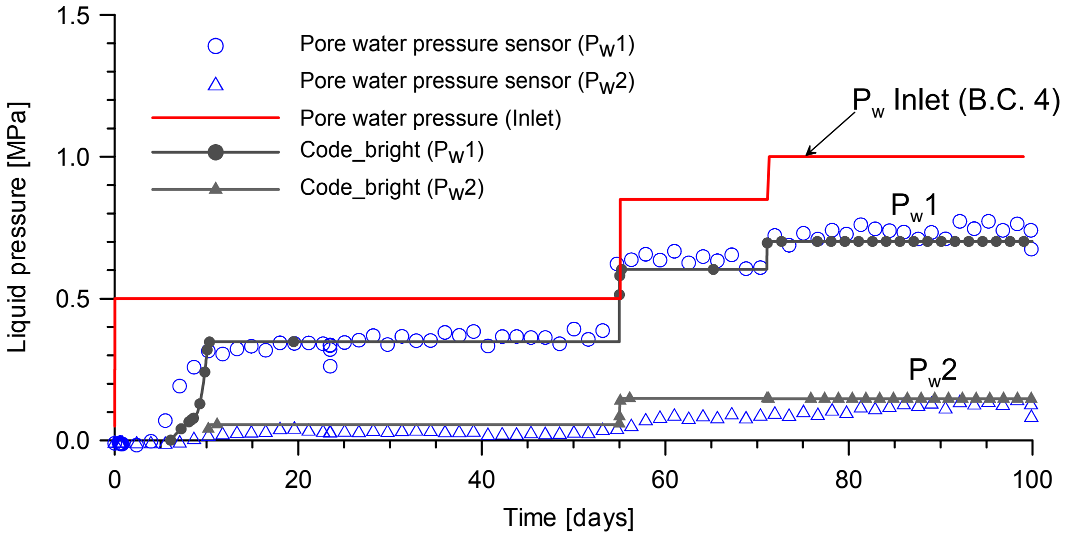

Figure 5.37: Time evolution of water pressure during the hydration phase.

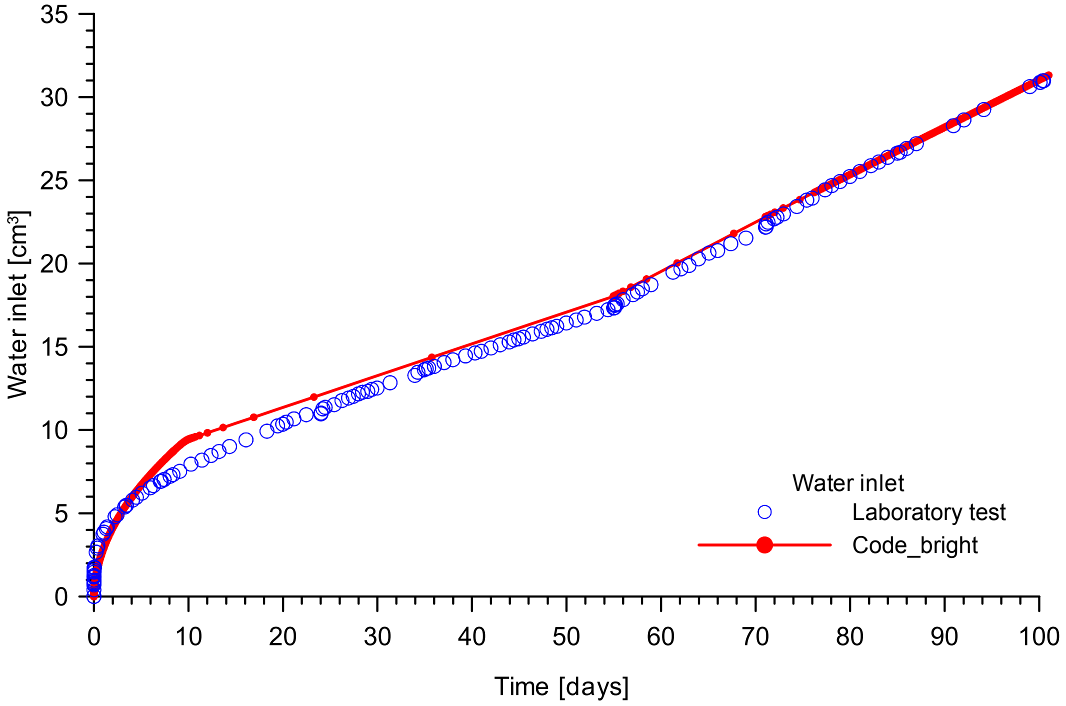

Figure 5.38: Time evolution of water inlet measured and computed (k = 1.00E-19 m^2).

5.3.4.2 Heating phase

The heating tests A, B and C described in Chapter IV have been simulated in order to obtain the hydraulic permeability, thermal conductivity and thermal dilation of skeleton of the Opalinus Clay rock by means of back analysis.

Heating test A

The heating test A was performed under drained conditions with a power input applied of 5.1 W. In this numerical simulation a null flux was considered in the (B.C.4), whereas water outlet remains open to atmosphere (B.C.5). The power was applied by means of energy flux in the longitudinal axis of the heater (B.C.6).

Figure 5.39 shows the results of the numerical simulations of the heating test A. On the upper figure the time evolutions of temperature computed and measured in the sensors (T2) and (T3) are shown. The bottom figure shows the time evolution of pore water pressure computed and measured in the sensor (P_w 1). After 24 hours of cooling (t = 150.55 days) the water inlet was open (B.C.4) at a water pressure of 0.65 MPa. Three different intrinsic permeability values were considered in this simulation,

$k = 1.0E - 20\ \text{m}^2$, $k = 2.5E - 20\ \text{m}^2$ and $k = 5.0E - 20\ \text{m}^2$. The time evolution of temperature and pore water pressure under drained conditions are well captured by the model with an intrinsic permeability of $k = 2.5E - 20\ \text{m}^2$, a thermal conductivity of 2.50 [W m^{-1} K^{-1}] and a linear thermal expansion of the rock of $1.35 \cdot 10^{-05}$ [ºC^{-1}].

Figure 5.40 shows the temperature distribution computed at the beginning of the heating test (t = 148.77 days). The pore water distribution computed at the beginning of the heating test is shown in Figure 5.41. The Figure 5.42, Figure 5.43 and Figure 5.44 show, respectively, the radial stress, vertical stress and circumferential stress distribution computed at the beginning of the heating phase (t = 148.77 days). Figure 5.45 shows the computed damage zone developed around of the heater generated by temperature increment. Figure 5.46 and Figure 5.47 shows the radial strain and vertical strain computed at the beginning of the heating (t = 148.77 days), respectively.

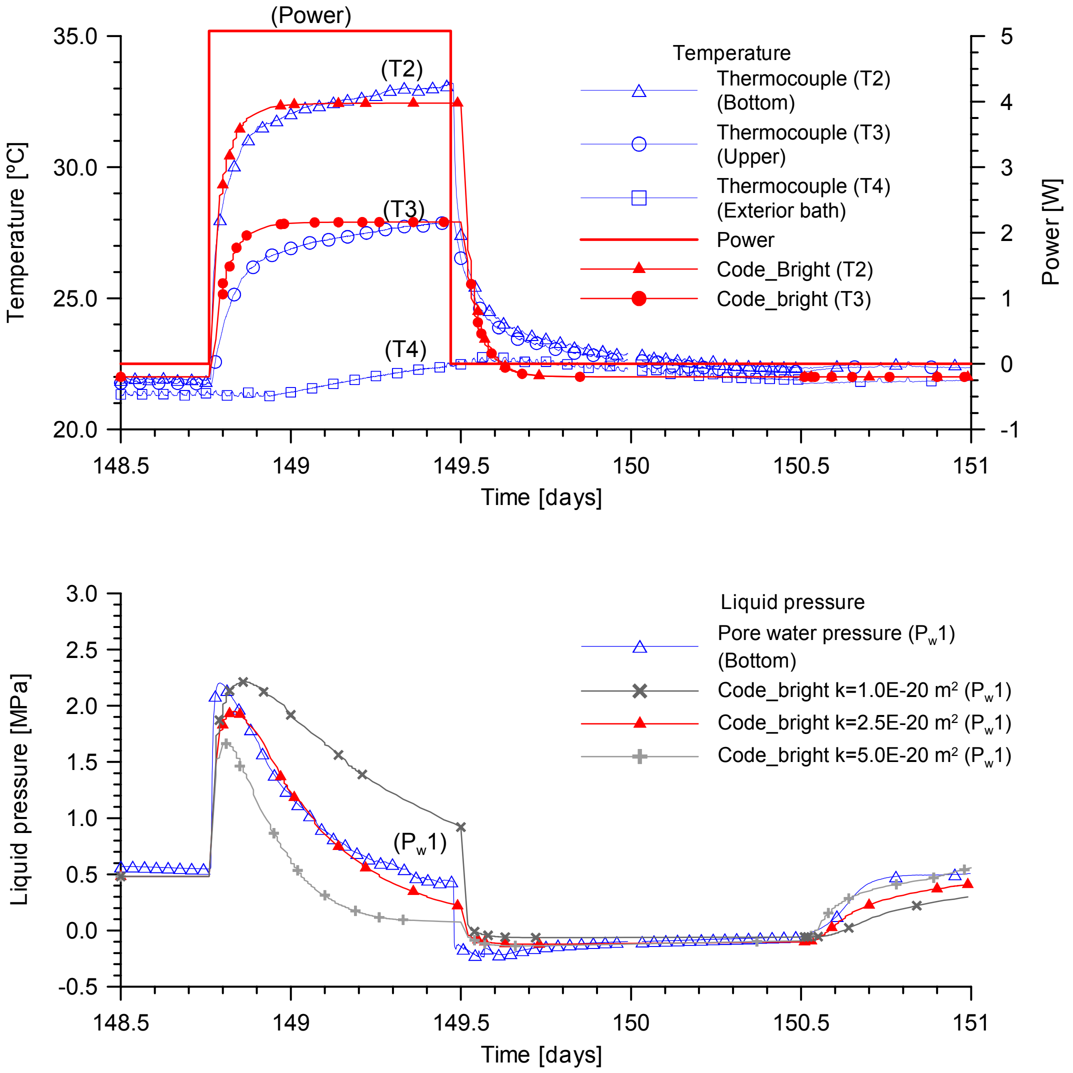

Figure 5.39: Heating test (A) performed under drained conditions. (Upper): Time evolution of temperature computed and measured in thermocouples T2 and T3. (Bottom): Time evolution of pore water pressure computed and measured in water pressure sensor P_w1.

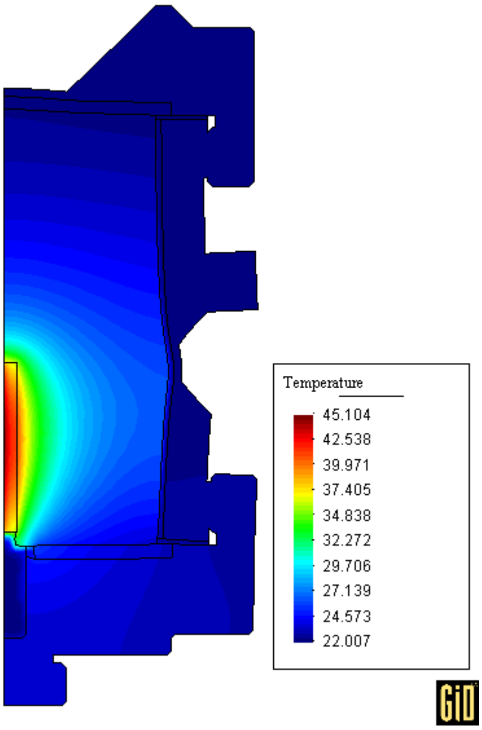

Figure 5.40: Temperature distribution (ºC) at the beginning of heating (t =148.77 days). (Deformation X2000)

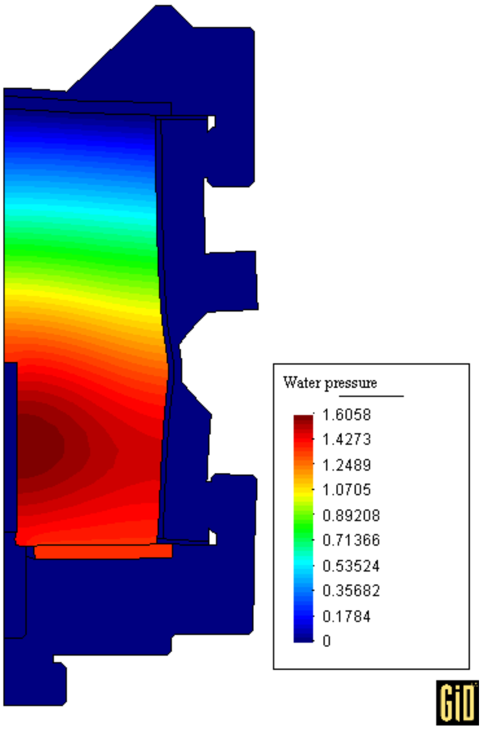

Figure 5.41: Pore water pressure distribution (MPa) at the beginning of the heating (t = 148.77 days). (Deformation X2000)

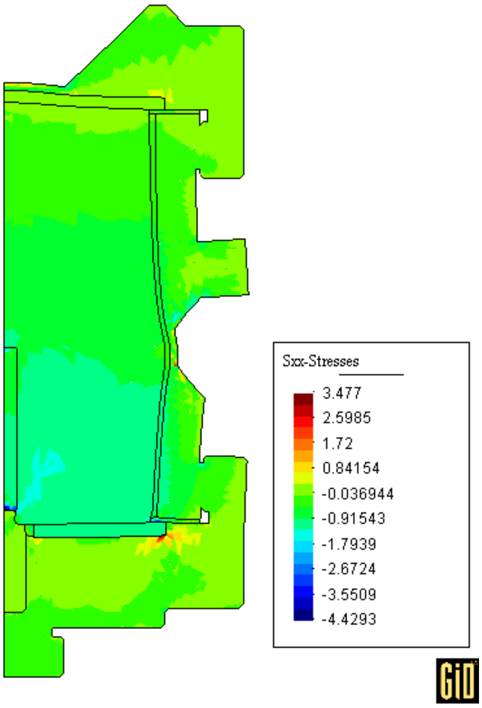

Figure 5.42: Radial stresses distribution (MPa) at the beginning of heating (t = 148.77 days). (Deformation X2000)

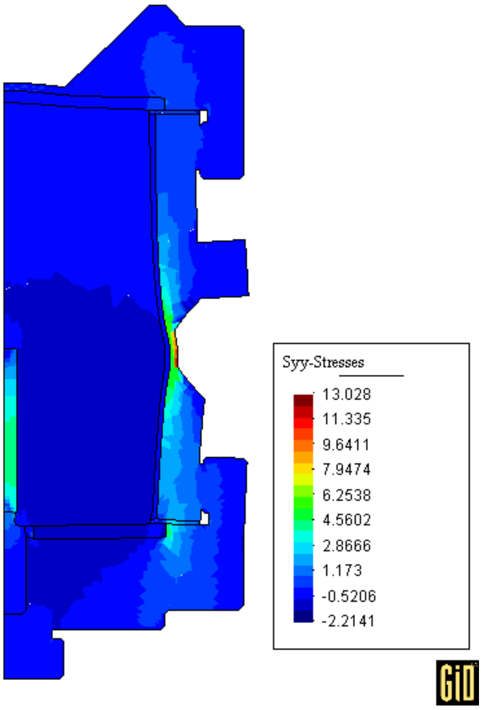

Figure 5.43: Vertical stresses distribution (MPa) at the beginning of the heating (t = 148.77 days). (Deformation X2000)

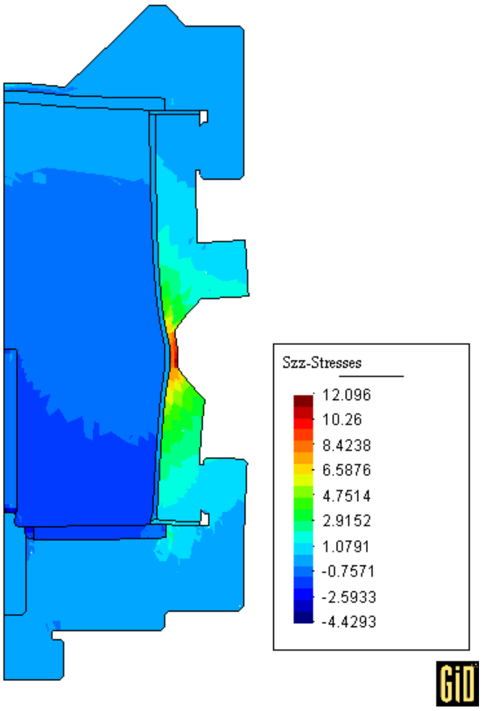

Figure 5.44: Circumferential stress distribution (MPa) at the beginning of heating (t = 148.77 days). (Deformation X2000)

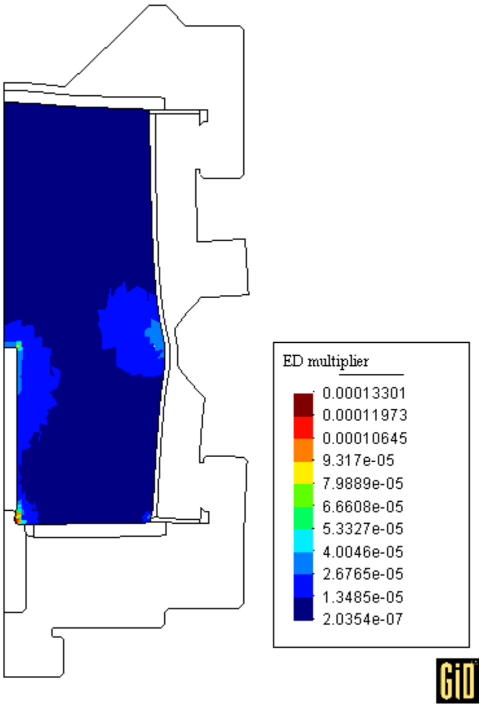

Figure 5.45: Damage multiplier at the beginning of the heating (t = 148.77 days). (Deformation X2000)

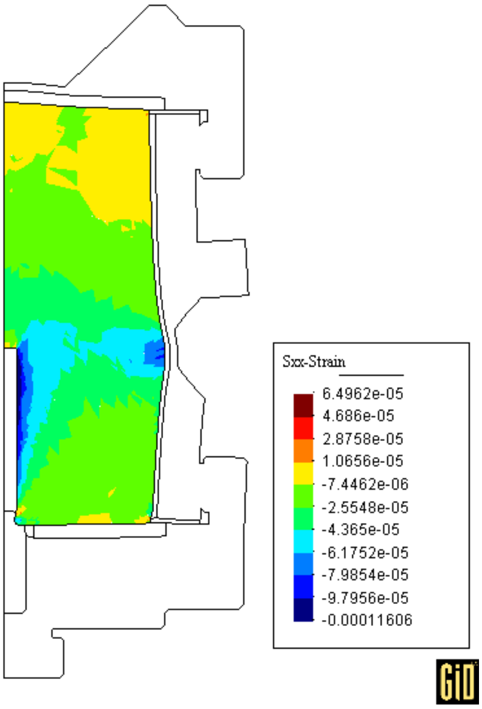

Figure 5.46: Radial strain distribution at the beginning of the heating (t = 148.77 days). (Deformation X2000)

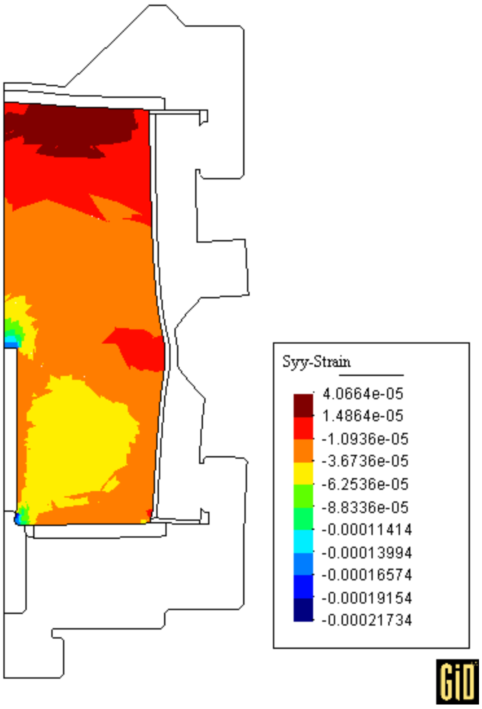

Figure 5.47: Vertical strain distribution at the beginning of the heating (t = 148.77 days). (Deformation X2000)

Heating test B

The heating test B was performed under undrained conditions. A power of 4.9 W was applied during 10.8 hours. After that the power was increased to 8.85 Watt during 3.05 hours. In this numerical simulation a null flux was considered in both boundary conditions (B.C.4) and (B.C.5). The power was applied by means of energy flux in the longitudinal axis of the heater (B.C.6).

Figure 5.48 shows the numerical simulation results of the heating test B. On the upper figure are shown the time evolutions of temperature computed and measured in both sensors (T2) and (T3). Bottom figure show the time evolution of pore water pressures computed and measured in both sensors (P_w 1) and (P_w 2). In this simulations an intrinsic permeability values of $k = 5.0E - 20$ m^2 was considered. The time evolution of pore water pressure computed with an intrinsic permeability of $k = 2.5E - 20$ m^2 is shown in Figure 5.49. Figure 5.50 shows the time evolution of the pore water pressure computed with an intrinsic permeability of $k = 1.0E - 20$ m^2. The time evolution of temperature and pore water pressure under undrained conditions are well captured by the model with a thermal conductivity of 2.50 [W m^{-1} K^{-1}] and a linear thermal expansion of the rock of $1.35 \cdot 10^{-05}$ [ºC^{-1}]. No significant changes in pore water pressure evolution were obtained with different intrinsic permeability values.

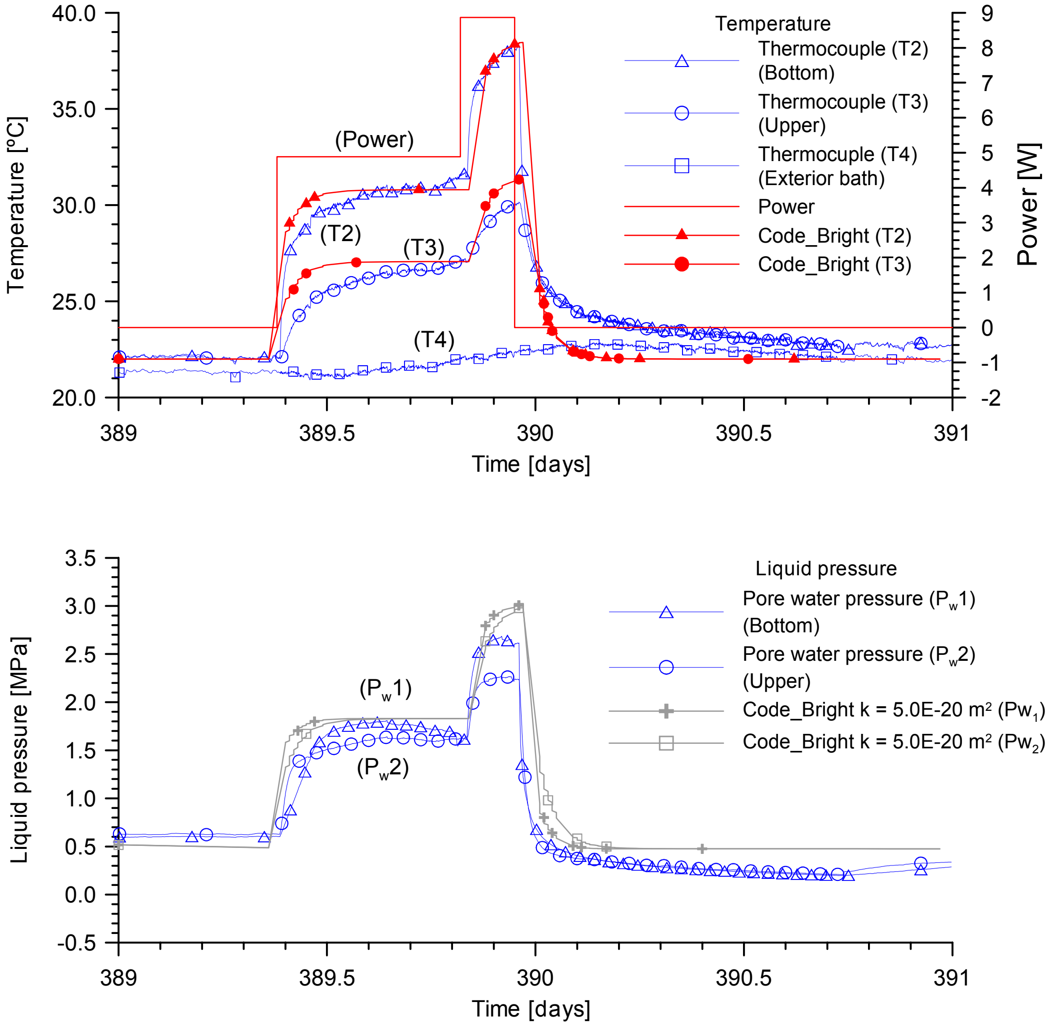

Figure 5.48: Heating test (B) performed under undrained conditions. (Upper): Time evolution of temperature computed and measured in thermocouples T2 and T3. (Bottom): Time evolution pore water pressure computed and measured in both pressure sensors P_w1 and P_w2. Intrinsic permeability of $k=5.0E\text{-}20\ m^2$.

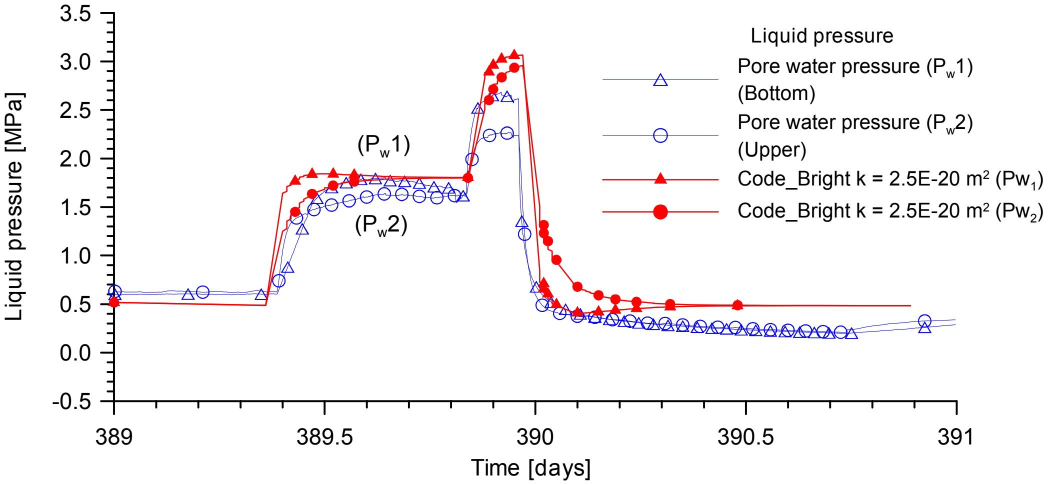

Figure 5.49: Heating test (B) performed under undrained conditions. Time evolution of pore water pressure computed and measured in both pressure sensors P_w1 and P_w2. Intrinsic permeability of $k=2.5E\text{-}20\ m^2$.

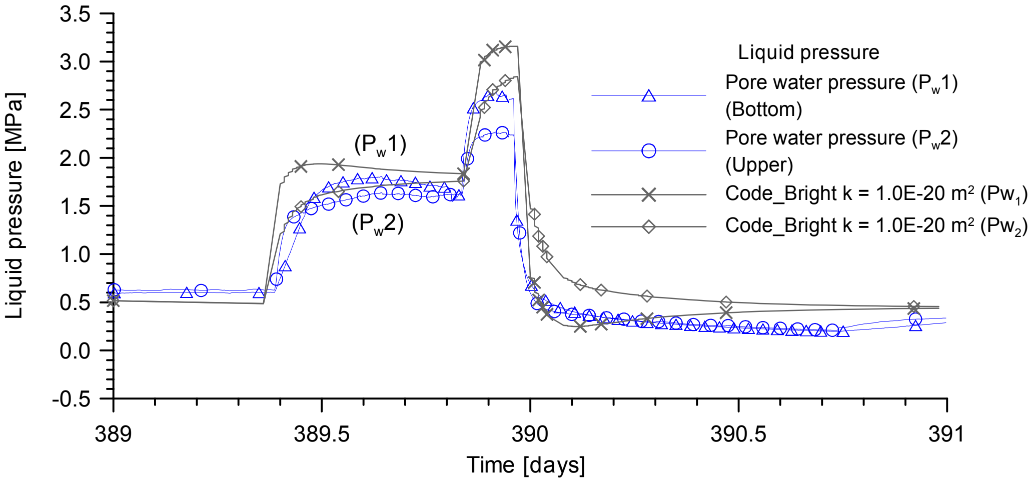

Figure 5.50: Heating test (B) performed under undrained conditions. Time evolution of pore water pressure computed and measured in both pressure sensors P_w1 and P_w2. Intrinsic permeability of $k=1.0E\text{-}20\ m^2$.

Heating test C

The heating test C was performed under drained conditions. A power of 5.15 W was applied during 7.2 hours. After that, the power was increased to 9.36 W during 2.78 hours. In this numerical simulation a null flux was considered in boundary conditions (B.C. 4), whereas atmospheric pressure was applied in the (B.C.5). The power was applied by means of energy flux along the longitudinal axis of the heater (B.C.6).

Figure 5.51 shows the numerical simulation results of the heating test C. On the upper figure the time evolutions of temperature computed and measured in both sensors (T2) and (T3) is shown. The bottom figure shows the time evolution of pore water pressure computed and measured in both sensors (P_w 1) and (P_w 2). The computed values were obtained with an intrinsic permeability values of $k = 5.0E - 20\ \mathrm{m}^2$. The time evolution of pore water pressure computed with an intrinsic permeability of$k = 2.5E - 20\ \mathrm{m}^2$ is shown in Figure 5.52. Figure 5.53 shows the time evolution of the pore water pressure computed with an intrinsic permeability of $k = 1.0E - 20\ \mathrm{m}^2$. The time evolution of temperature and pore water pressure under drained conditions are well captured by the model with an intrinsic permeability of $k = 2.5E - 20\ \mathrm{m}^2$, a thermal conductivity of 2.50 [W m^{-1} K^{-1}] and a linear thermal expansion of the rock of $1.35 \cdot 10^{-05}$ [$^{\circ}\mathrm{C}^{-1}$].

An analysis of sensitivity of rock thermal conductivity (λ) and thermal expansion coefficient of solid (β_s) has been performed in order to quantify its influence in the numerical models. Figure 5.54 shows the analysis of sensitivity of thermal conductivity (λ) performed in test C. Numerical simulations were carried out with rock thermal conductivity values of λ_{sat} =1.25, 2.5 and 5.0 [W m^{-1} K^{-1}], intrinsic permeability of $k = 2.5E - 20\ \mathrm{m}^2$ and thermal expansion coefficient of solid of β_s = 1.0E-05 $^{\circ}\mathrm{C}^{-1}$. On the upper figure the time evolutions of temperature measured and computed at the sensor (T2) is shown. The bottom figure shows the time evolutions of pore water pressure measured and computed at sensor (Pw 1). On the other hand, an analysis of sensitivity of thermal expansion coefficient of solid (βs) performed in test C is shown in Figure 5.55. The upper figure shows the time evolutions of temperature measured and computed at sensor (T2) with a thermal conductivity of $\lambda_{sat} = 2.5\ \mathrm{W\ m^{-1}\ K^{-1}}$. The bottom figure shows the time evolution of pore water pressure measured and computed whit thermal expansion coefficient of solid of β_s = 1.0E-06, 5.0E-06, 1.0E-05 and 2.0E-05 $^{\circ}\mathrm{C}^{-1}$ and intrinsic permeability of $k = 2.5E - 20\ \mathrm{m}^2$.

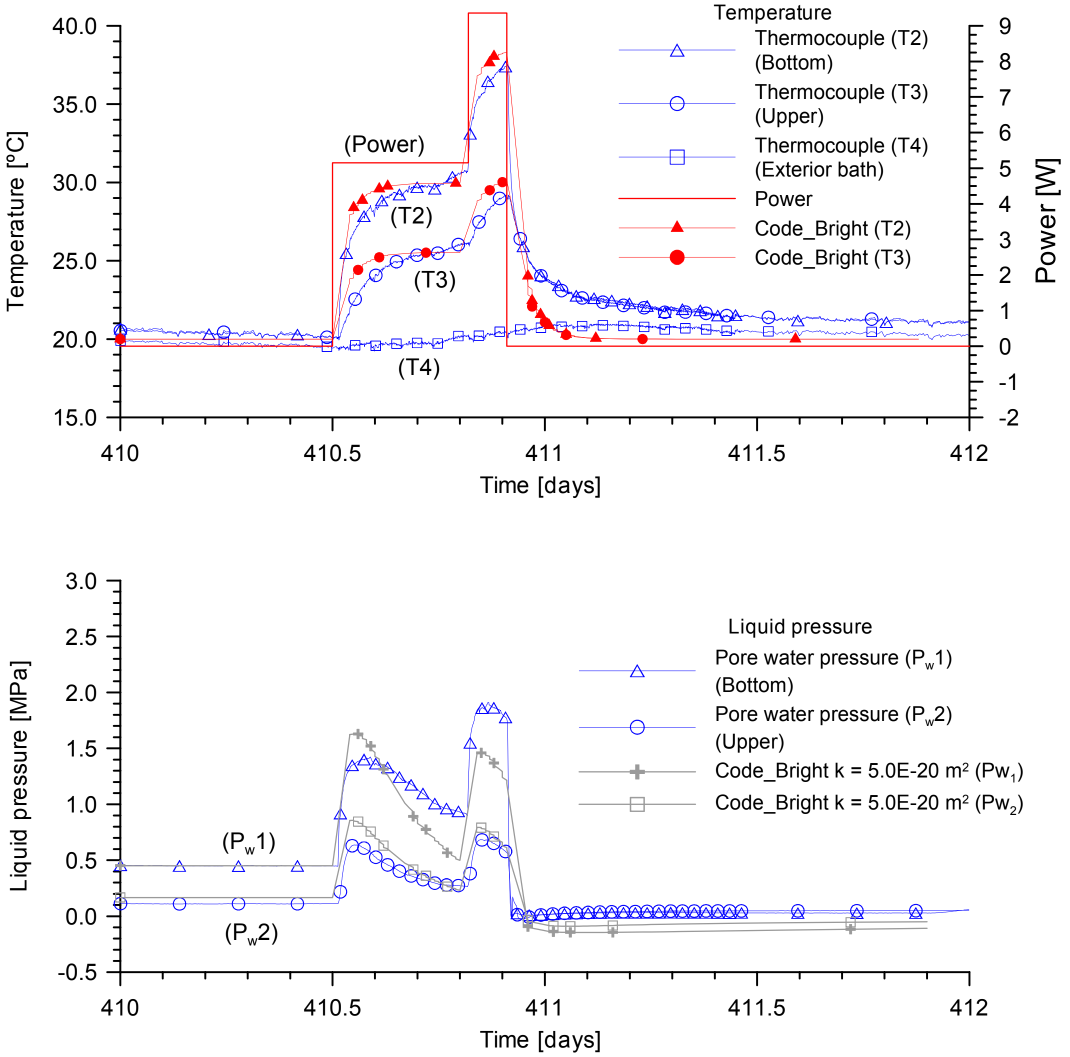

Figure 5.51: Heating test performed under drained conditions. (Upper): Time evolution of temperature computed and measured in thermocouples T2 and T3. (Bottom): Time evolution pore water pressure computed and measured in pressure sensors P_w1 and P_w2. Intrinsic permeability of k=5.0E-20 m^2.

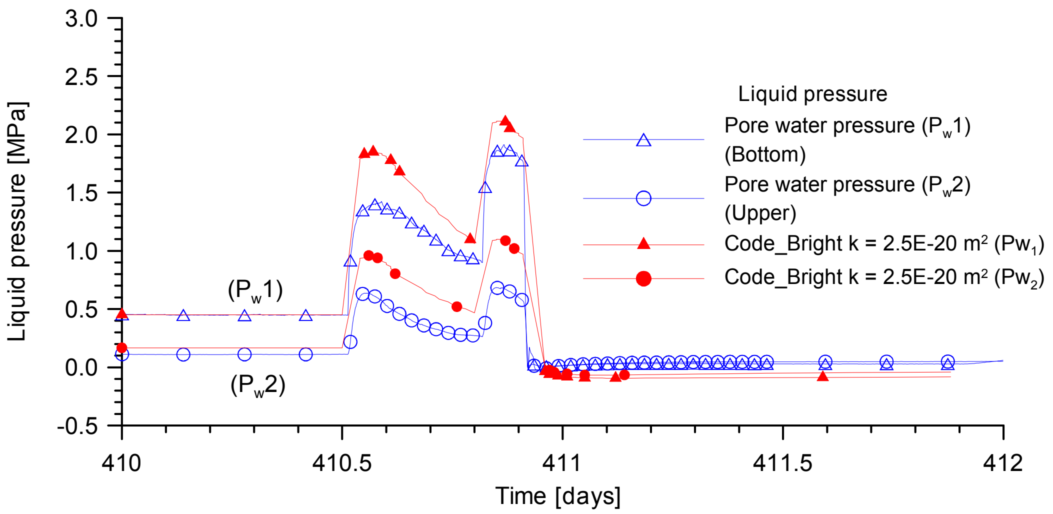

Figure 5.52: Heating test (C) performed under drained conditions. Time evolution of pore water pressure computed and measured in both pressure sensors P_w1 and P_w2. Intrinsic permeability of k = 2.5E-20 m^2.

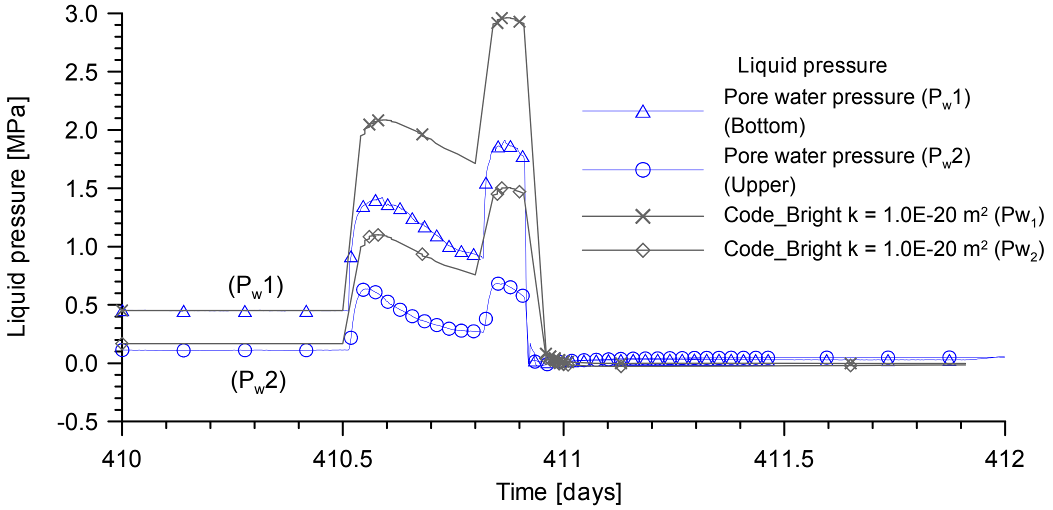

Figure 5.53: Heating test (C) performed under drained conditions. Time evolution of pore water pressure computed and measured in both pressure sensors P_w1 and P_w2. Intrinsic permeability of k = 1.0E-20 m^2.

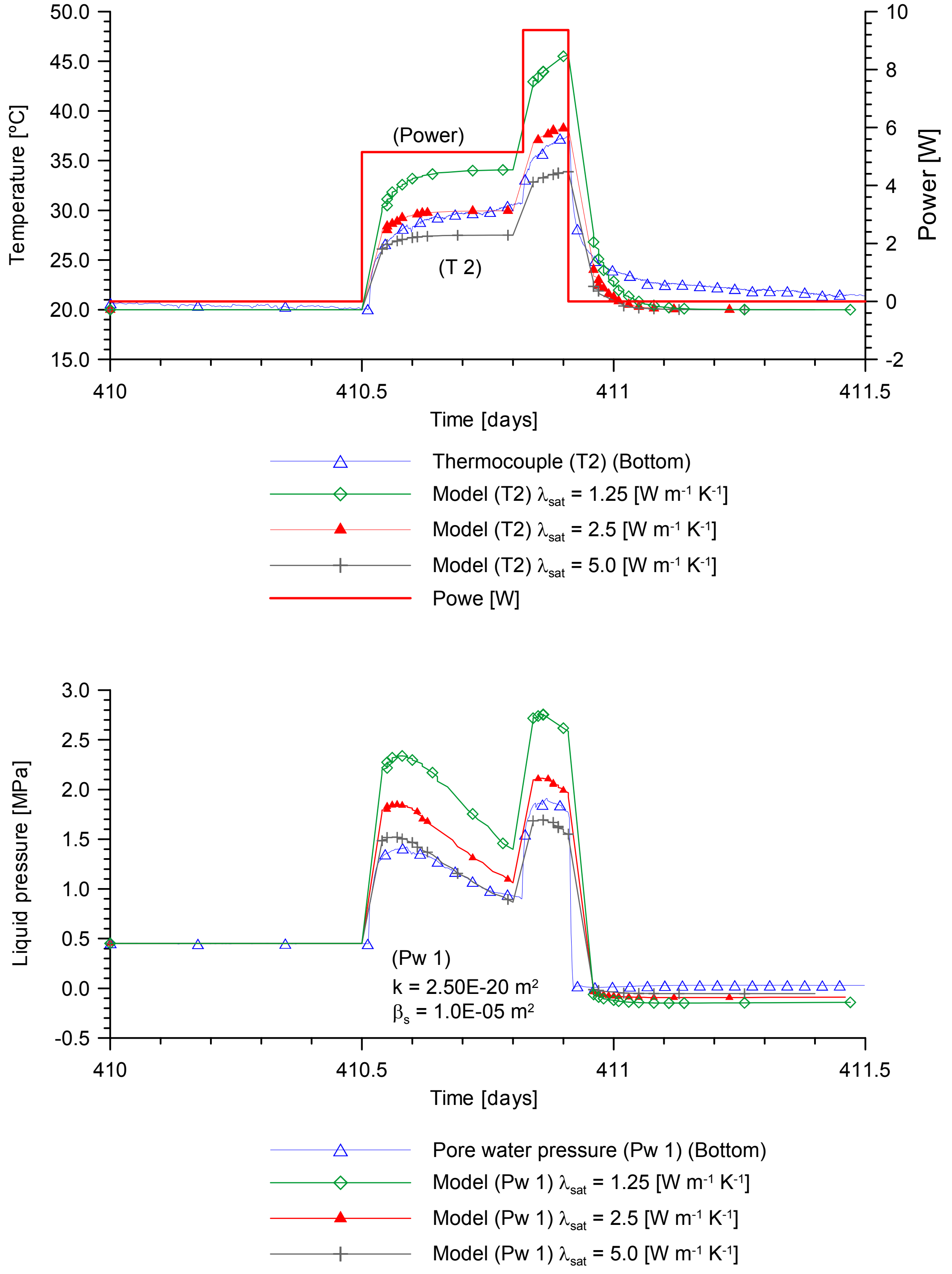

Figure 5.54: Heating test (C) performed under drained conditions. Analysis of sensitivity of rock thermal conductivity. (Upper): Time evolution of temperature measured and computed in temperature sensor (T2) with rock thermal conductivity of λ =1.25, 2.5 and 5.0 [W m^{-1} K^{-1}]. (Bottom): Time evolution of pore water pressure measured and computed in sensor (Pw 1). Intrinsic permeability of k = 2.5E-20 m^2 and linear thermal coefficient expansion βs = 1.0E-05 ºC^{-1}.

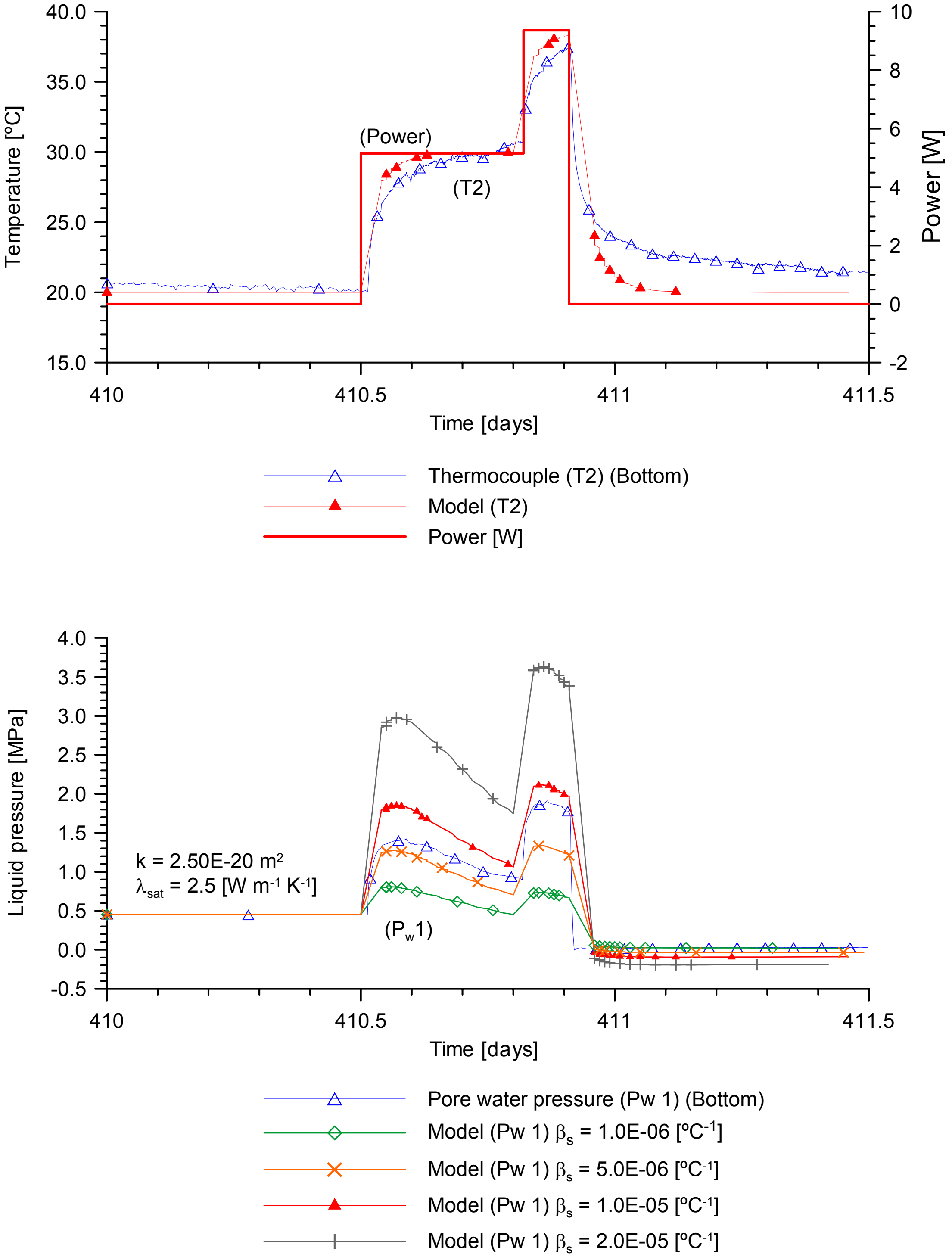

Figure 5.55: Heating test (C) performed under drained conditions. Analysis of sensitivity of rock linear thermal coefficient expansion. (Upper): Time evolution of temperature measured and computed in temperature sensor (T2) with rock thermal conductivity of $\lambda = 2.5$ [W m^{-1} K^{-1}]. (Bottom): Time evolution of pore water pressure measured and computed in sensor (Pw 1) with linear thermal coefficient expansion of β_s = 1.0E-06, 5.0E-06, 1.0E-05 and 2.0E-05 $ºC^{-1}$ and intrinsic permeability of k = 2.5E-20 m^2.

CHAPTER VI

AN ANISOTROPIC CONSTITUTIVE MODEL FOR CLAY SHALES

6.1 Formulation of constitutive model

The shaly nature of the Opalinus Clay rock leads to marked mechanical anisotropic behavior of the rock. A constitutive model able to consider the anisotropic behavior of shaly rock has been developed. The model has been formulated within an elastic-viscoplastic framework *(Perzyna (1966) and Sanchez (1997))* and it has been introduced in CODE_BRIGHT *(Olivella et al. (1996))*. The constitutive model takes into account the anisotropic strength and deformability due to matrix (grain) and discontinuities (joint) *(Wittke (1990))*. A constitutive model for rock with multiple planes of weakness proposed by *Zienkiewicz and Pande (1977-a),* was also considered in the formulation developed.

Figure 6.1 shows the conceptual one dimensional model for a material with elasto-viscoplastic stress-strain behaviour (Perzyna theory). The elastic strain is represented by the spring. This strain is reversible and independent of time. When the applied stress σ is smaller than the failure stress σ_f of the sliding element only elastic strains are produced in the spring. If the applied stress σ is bigger than σ_f the blocks in the sliding elements are displaced relative to one another, and plastic strains are produced. The dashpot situated in parallel with the sliding element only serves to delay the strain. The strain produced is irreversible and it increases linearly with time.

In the constitutive model formulation, the elastic behaviour is characterized by a cross-anisotropic material, where five independent elastic constants are required. The plastic character of the rock is attributed to two components: matrix and a family of discontinuities. The discontinuities introduce the anisotropic plastic behaviour. The failure criterion of the matrix is defined by means of a hyperbolic yield surface in the *p* – *J* space. Matrix degradation is induced by means of an isotropic and kinematic softening controlled by the plastic work. The failure criterion of the family of discontinuities is defined by means of hyperbolic yield surface in terms of shear and effective normal stresses acting on the isotropic planes. The use of hyperbolic yield surface has been proposed by *Zienkiewicz and Pande, (1977-b)* and subsequently used in a formulation of a constitutive model for rock joints *(Gens et al., (1990))*. In a similar way to the matrix formulation, the degradation in the discontinuities is induced by means of an isotropic and kinematic softening law controlled by the plastic work.

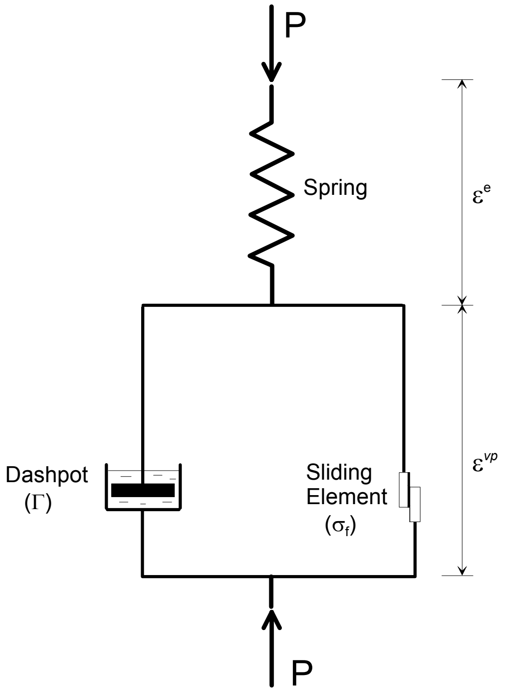

Figure 6.1: Conceptual model of elastoviscoplastic material. Perzyna theory.

6.1.1 Elastic behaviour of transversely isotropic rocks

The stress-strain behaviour in the elastic range for transversely isotropic rock is expressed by means of Hooke law as follow:

$$\sigma' = D' : \varepsilon' \qquad \text{(Eq 6.1)}$$

where σ' is the stress tensor, ε' is the elastic strain tensor and D' is the elastic constitutive tensor.

The (:) symbol define the double contracted tensor product. The apostrophe indicates that the stress and strain are related to the local Cartesian coordinate system (X', Y', Z'). This coordinate system is related to the direction of anisotropy. The Z' axis coincide with the direction of highest deformability, perpendicular to the isotropic plane, whereas the X' and Y' axis are located on the isotropic plane.

The elastic constitutive tensor D' for transversely isotropic solid, expressed in the local coordinate system, is defined in the equation (6.2).

$$D' = \begin{bmatrix} E_1 \frac{1-n\cdot\nu_2^2}{(1+\nu_1)\cdot m} & E_1 \frac{\nu_1+n\cdot\nu_2^2}{(1+\nu_1)\cdot m} & E_1 \frac{\nu_2}{m} & 0 & 0 & 0 \\ E_1 \frac{\nu_1+n\cdot\nu_2^2}{(1+\nu_1)\cdot m} & E_1 \frac{1-n\cdot\nu_2^2}{(1+\nu_1)\cdot m} & E_1 \frac{\nu_2}{m} & 0 & 0 & 0 \\ E_1 \frac{\nu_2}{m} & E_1 \frac{\nu_2}{m} & E_2 \frac{1-\nu_1}{m} & 0 & 0 & 0 \\ 0 & 0 & 0 & \frac{E_1}{2(1+\nu_1)} & 0 & 0 \\ 0 & 0 & 0 & 0 & G_2 & 0 \\ 0 & 0 & 0 & 0 & 0 & G_2 \end{bmatrix} \quad \text{(Eq 6.2)}$$

where:

$$E_1 = \frac{\sigma_{x'}}{\varepsilon_{x'}} = \frac{\sigma_{y'}}{\varepsilon_{y'}},\ E_2 = \frac{\sigma_{z'}}{\varepsilon_{z'}},\ G_2 = \frac{\tau_{z'y'}}{\gamma_{z'y'}} = \frac{\tau_{z'x'}}{\gamma_{z'x'}},\ \nu_1 = -\frac{\varepsilon_{y'}}{\varepsilon_{x'}},\ \nu_2 = -\frac{\varepsilon_{x'}}{\varepsilon_{z'}} = -\frac{\varepsilon_{y'}}{\varepsilon_{z'}},$$

$$n = \frac{E_1}{E_2},\ m = \left(1-\nu_1-2\cdot n\cdot\nu_2^2\right)$$

Five elastic independent constants are required. The Young's moduli E_1 and E_2 are adopted for the directions parallel and perpendicular to the isotropic plane, respectively. G_2 is the shear modulus for shear load in the isotropic plane. ν_1 and ν_2 are the Poisson's ratios. Figure 6.2 shows the definition of the elastic constants for a cross-anisotropic rock in terms of stresses and both normal and shear strain *(Wittke W., 1990).*

The theory of elasticity does not provide an upper limit for the Poisson's ratio in the case of transverse isotropy, (given by the condition $\nu \le 0.5$ in isotropy). Only the following restrictive inequality must be verified.

$$2\cdot\nu_2\cdot\nu_3 < 1-\nu_1 \quad \text{(Eq 6.3)}$$

Experience acquired from laboratory tests on intact rock indicates that ν_1 and ν_2 are always smaller than 0.5 and only ν_3 can take values around or larger than 0.5 in transversely isotropic rock *(Wittke W., 1990)*.

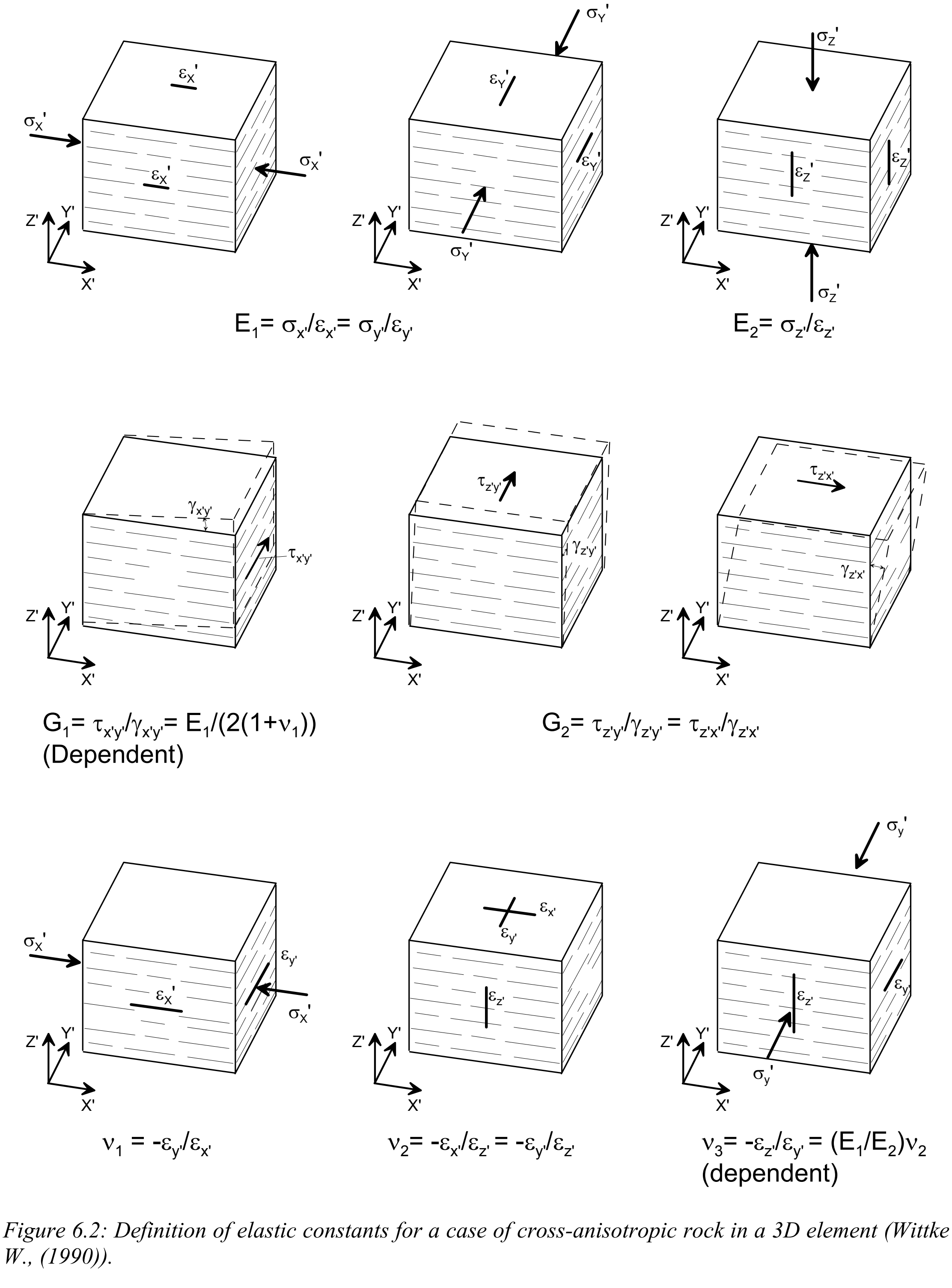

Figure 6.2: Definition of elastic constants for a case of cross-anisotropic rock in a 3D element (Wittke W., (1990)).

The global coordinated system X, Y, Z used to define the engineering structures does not coincide in general with the local coordinate system X’, Y’, Z’ of the anisotropy direction. The link of the global and local coordinate systems is established by means of two angles. These angles describe the direction of a contour, strike (α), and the slope of the line of dip, dip (β), of the isotropic plane in relation to the global coordinate system. Figure 6.3 shows the relationship between the global coordinate system and the orientation of the isotropic plane. Figure 6.4 shows the cross-anisotropic Opalinus clay rock in the wall of the excavation during the dismantling of the HE experiment $\alpha = 60^{\circ}$, $\beta = 32^{\circ}$ *(Nussbaum et al. 2004),* a material which will be characterized by the constitutive model developed.

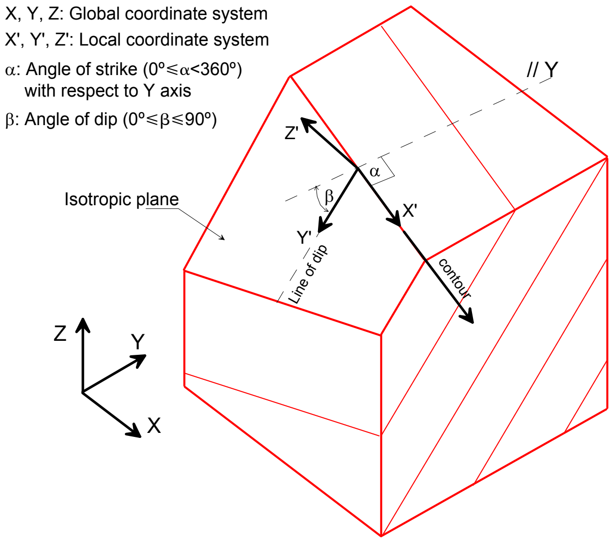

Figure 6.3: Relationship between the global coordinate system and the orientation of the isotropic plane

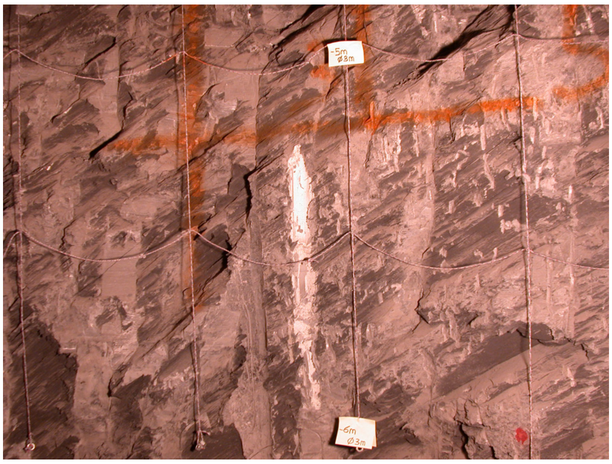

Figure 6.4: Cross-anisotropic Opalinus clay rock in the wall of the excavation, during the dismantling of the HE experiment.

The stress tensors expressed in both local and global coordinate systems are indicated in equations (6.4) and (6.5), respectively.

$$\sigma' = D' : \varepsilon' \qquad \text{(Eq 6.4)}$$

$$\sigma = D : \varepsilon \qquad \text{(Eq 6.5)}$$

The local stress tensor σ' is related to global stress tensor σ by means of coordinate transformation tensor T, equations (6.6) and (6.7). The local strain tensor ε' and global strain tensor ε are related by means of transformation coordinate tensor T^*, equations (6.8) and (6.9).

$$\sigma' = T : \sigma \qquad \text{(Eq 6.6)}$$

$$T = \begin{bmatrix} l_1^2 & m_1^2 & 0 & 2 \cdot l_1 \cdot m_1 & 0 & 0 \\ l_2^2 & m_2^2 & n_2^2 & 2 \cdot l_2 \cdot m_2 & 2 \cdot m_2 \cdot n_2 & 2 \cdot n_2 \cdot l_2 \\ l_3^2 & m_3^2 & n_3^2 & 2 \cdot l_3 \cdot m_3 & 2 \cdot m_3 \cdot n_3 & 2 \cdot n_3 \cdot l_3 \\ l_1 \cdot l_2 & m_1 \cdot m_2 & 0 & l_1 \cdot m_2 + l_2 \cdot m_1 & m_1 \cdot n_2 & n_2 \cdot l_1 \\ l_2 \cdot l_3 & m_2 \cdot m_3 & n_2 \cdot n_3 & l_2 \cdot m_3 + l_3 \cdot m_2 & m_2 \cdot n_3 + m_3 \cdot n_2 & n_2 \cdot l_3 + n_3 \cdot l_2 \\ l_3 \cdot l_1 & m_3 \cdot m_1 & 0 & l_1 \cdot m_3 + l_3 \cdot m_1 & m_1 \cdot n_3 & n_3 \cdot l_1 \end{bmatrix} \qquad \text{(Eq 6.7)}$$

$$\varepsilon' = T^* : \varepsilon \qquad \text{(Eq 6.8)}$$

$$T^* = \begin{bmatrix} l_1^2 & m_1^2 & 0 & l_1 \cdot m_1 & 0 & 0 \\ l_2^2 & m_2^2 & n_2^2 & l_2 \cdot m_2 & m_2 \cdot n_2 & n_2 \cdot l_2 \\ l_3^2 & m_3^2 & n_3^2 & l_3 \cdot m_3 & m_3 \cdot n_3 & n_3 \cdot l_3 \\ 2 \cdot l_1 \cdot l_2 & 2 \cdot m_1 \cdot m_2 & 0 & l_1 \cdot m_2 + l_2 \cdot m_1 & m_1 \cdot n_2 & n_2 \cdot l_1 \\ 2 \cdot l_2 \cdot l_3 & 2 \cdot m_2 \cdot m_3 & 2 \cdot n_2 \cdot n_3 & l_2 \cdot m_3 + l_3 \cdot m_2 & m_2 \cdot n_3 + m_3 \cdot n_2 & n_2 \cdot l_3 + n_3 \cdot l_2 \\ 2 \cdot l_3 \cdot l_1 & 2 \cdot m_3 \cdot m_1 & 0 & l_1 \cdot m_3 + l_3 \cdot m_1 & m_1 \cdot n_3 & n_3 \cdot l_1 \end{bmatrix} \qquad \text{(Eq 6.9)}$$

The transformation tensors T and T^* are function of the angles α and β where:

$l_1 = \sin(\alpha)$, $l_2 = \cos(\beta) \cdot \cos(\alpha)$, $l_3 = -\sin(\beta) \cdot \cos(\alpha)$
$m_1 = \cos(\alpha)$, $m_2 = -\cos(\beta) \cdot \sin(\alpha)$, $m_3 = \sin(\beta) \cdot \sin(\alpha)$
$n_2 = -\sin(\beta)$, $n_3 = -\cos(\beta)$

Replacing equations (6.6) and (6.8) in (6.4) and operating we obtain (6.5), where:

$$D = T^{*T} \, D' T^* \qquad \text{(Eq 6.10)}$$

Equations (6.10) establish the relationship between the stress tensor σ and elastic strain tensor ε in an arbitrary Cartesian coordinates system X,Y,Z; which forms angles α and β with respect to local coordinate system X',Y',Z'.

6.1.2 Viscoplastic flow rule

The total strain rate tensor $\dot{\varepsilon}$ can be divided into an elastic strain rate tensor $\dot{\varepsilon}^e$ and a viscoplastic strain rate tensor $\dot{\varepsilon}^{vp}$. The elastic strain rate is instantaneous and reversible, whereas the viscoplastic strain rate is time dependent and irreversible. The dot indicates the rate of changes in time.

$$\dot{\varepsilon} = \dot{\varepsilon}^e + \dot{\varepsilon}^{vp} \qquad \text{(Eq 6.11)}$$

The elastic strain rate tensor is obtained by the Hooke's law:

$$\dot{\varepsilon}^e = D^{-1} : \dot{\sigma} \qquad \text{(Eq 6.12)}$$

The viscoplastic strain rate includes both viscous and plastic effects and takes into account the contribution of the matrix and the joint. It is given by equation (6.13):

$$\left\{ \dot{\varepsilon}^{vp} \right\} = \Gamma_M \left\langle \phi(F)_M \right\rangle \left\{ \frac{\partial Q_M}{\partial \sigma} \right\} + \Gamma_J \left\langle \phi(F)_J \right\rangle \left\{ \frac{\partial Q_J}{\partial \sigma} \right\} \qquad \text{(Eq 6.13)}$$

where Γ is the viscosity parameter, Q is the plastic potential and F is the yield function. $\phi(F)$ is a monotonically increasing overstress function which define the magnitude of viscoplastic strain rate. It is normalized by initial yield stress F_0. The tensor gradient of the plastic potential $\frac{\partial Q}{\partial \sigma}$ represents the direction of the viscoplastic flow. M and J indicates matrix and joint, respectively. In order to consider the dilatancy effects under shear stress, a non associated flow rule has been adopted $Q \neq F$.

The brackets defined by Macauly $\langle \ \rangle$ control the flow rule in the following way:

$$\left\langle \phi(F) \right\rangle = 0 \qquad \text{if} : F \leq 0 \qquad \text{(Eq 14)}$$

$$\left\langle \phi(F) \right\rangle = \left(\frac{F}{F_0} \right)^{\mathrm{N}} \qquad \text{if} : F > 0 \qquad \text{(Eq 15)}$$

where:

F_0 : initial yield stress

N: Constant

A viscoplastic stress state outside of the yield surface can exist. In this case, there is no condition forcing the stress state to stay inside the yield surface. On the contrary, in the rate independent plastic theory the stress state must always remain inside the yield surface (consistency condition).

6.1.3 Yield function

The failure criterion adopted for the matrix of the Opalinus Clay rock is defined by a rounded hyperbolic yield surface in the meridional plane (p, J, θ = constant), in conjunction with the trigonometric rounding techniques in the octahedral plane (p = constant, J, θ) *(Abbo and Sloan (1993)).* The hyperbolic yield surface adopted is continuous and differentiable for all stress state. The negative branch of the hyperbola has been adopted. The yield function of the matrix depends of three rock parameters, tensile strength (χ_M), cohesion (c_M) and friction angle (ϕ_M). The hyperbolic yield surface of the matrix can be expressed as:

$$F_M = p\cdot\sin\phi + \sqrt{J^2\cdot K^2(\theta) + a^2\cdot\sin^2\phi} - c\cdot\cos\phi = 0 \qquad \text{(Eq 6.16)}$$

where:

$$\begin{aligned} K(\theta) &= \cos(\theta) - \frac{1}{\sqrt{3}}\cdot\sin\phi\cdot\sin\theta \\ a &= c\cdot\cot\phi - \chi \end{aligned} \qquad \text{(Eq 6.17)}$$

The hyperbolic yield surface F_M is expressed in terms of three stress invariants:

$$\begin{aligned} p &= \frac{1}{3}\left(\sigma_x + \sigma_y + \sigma_z\right) \qquad \text{(Mean stress)} \\ J &= \sqrt{\frac{1}{2}\left(s_x^2 + s_y^2 + s_z^2\right) + \tau_{xy}^2 + \tau_{yz}^2 + \tau_{zx}^2} \\ \theta &= \frac{1}{3}\sin^{-1}\left(-\frac{3\sqrt{3}}{2}\frac{J_3}{J^2}\right) \qquad \left(\text{Lode angle: } -30^\circ \le \theta \le 30^\circ\right) \end{aligned} \qquad \text{(Eq 6.18)}$$

where:

$$\begin{aligned} s_x &= \sigma_x - p \\ s_y &= \sigma_y - p \\ s_z &= \sigma_z - p \\ J_3 &= s_x \cdot s_y \cdot s_z + 2 \cdot \tau_{xy} \cdot \tau_{yz} \cdot \tau_{zx} - s_x \tau_{yz}^2 - s_y \tau_{xz}^2 - s_z \tau_{xy}^2 \end{aligned} \qquad \text{(Eq 6.19)}$$

With a suitable choice of $K(\theta)$, the hyperbolic yield surface of the equation (6.16) can be generalized to form a family of useful yield surface which do not possess singular vertices in the octahedral plane. The singular vertices occur at $\theta = \pm 30^\circ$ in the octahedral plane. In the vicinity of the singularities, where $|\theta| > \theta_T$ and θ_T is defined as transition angle, an alternative form of $K(\theta)$, equation (6.17), is defined *(Abbo and Sloan, (1993))*.

$$K(\theta) = \begin{cases} \left(A - B \sin 3\theta\right) & |\theta| > \theta_T \\ \left(\cos\theta - \dfrac{1}{\sqrt{3}} \sin\phi \sin\theta\right) & |\theta| \le \theta_T \end{cases} \qquad \text{(Eq 6.20)}$$

where:

$$\begin{aligned} A &= \frac{1}{3}\cos\theta_T \left(3 + \tan\theta_T \tan 3\theta_T + \frac{1}{\sqrt{3}} sign(\theta)\left(\tan 3\theta_T - 3\tan\theta_T\right)\sin\phi\right) \\ B &= \frac{1}{3\cos 3\theta_T}\left(sign(\theta)\sin\theta_T + \frac{1}{\sqrt{3}}\sin\phi\cos\theta_T\right) \\ sign(\theta) &= \begin{cases} +1 \text{ for } \theta \ge 0^\circ \\ -1 \text{ for } \theta < 0^\circ \end{cases} \end{aligned} \qquad \text{(Eq 6.21)}$$

The value of the transition angle is between $0 \le \theta_T \le 30^\circ$. In practice a typical value adopted is $\theta_T = 25^\circ$. A hyperbolic yield function rounded in both the meridional plane (p, J) and the octahedral plane (J, θ) can be defined using the equation (6.16) with $K(\theta)$ given by (6.20), where the yield surface is continuous and differentiable for all stress states. Figure 6.5 and Figure 6.6 shows the hyperbolic yield surface in both meridional and octahedral plane, respectively.

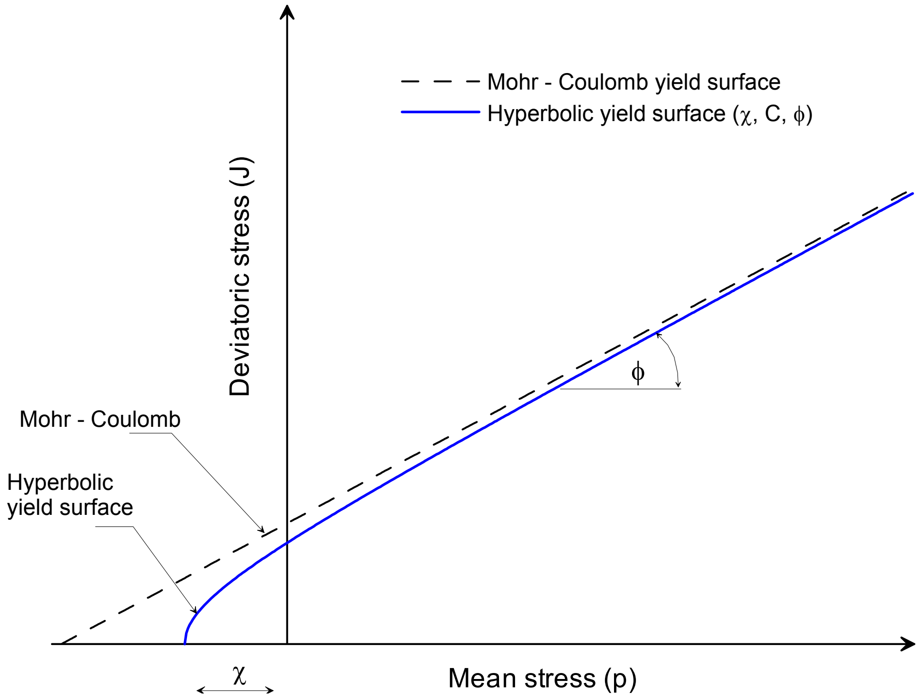

Figure 6.5: Hyperbolic yield function rounded in the meridional plane.

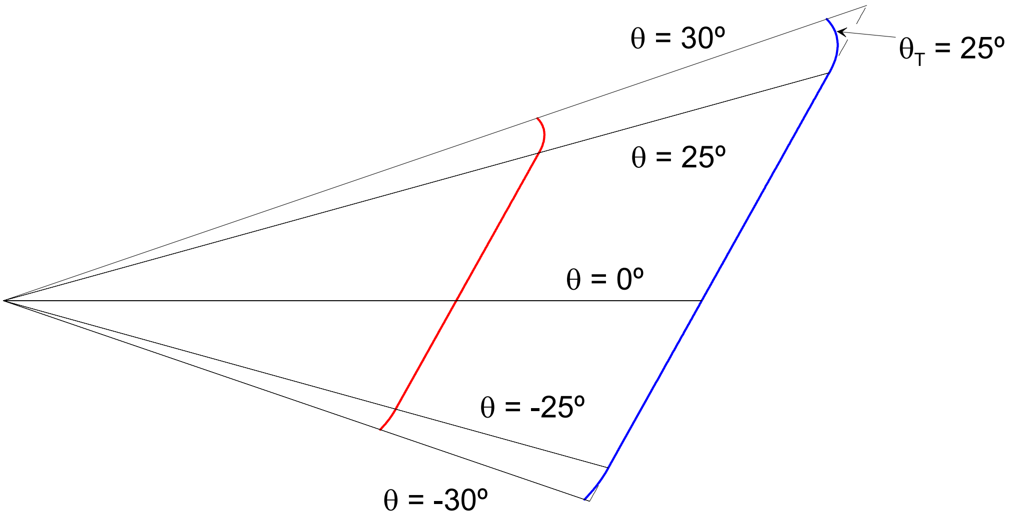

Figure 6.6: Hyperbolic yield function rounded in the octahedral plane.

The failure criterion applied to the joints (isotropy plane) of the argillaceous rock is defined by a hyperbolic yield function. It is a function of three parameter of the joint: tensile strength (χ_J), cohesion (c_J) and friction angle (ϕ_J). It is expressed in terms of effective normal stresses $(\sigma_{z'})$ and shear stress (τ_J) acting on the isotropic planes *(Carol & Prat (1990) in Lopez (1999))*. The hyperbolic yield surface adopted is continuous and differentiable for all stress state. The negative branch of the hyperbola has been adopted. The hyperbolic yield surface for the joint can be expressed as:

$$F_J = {\tau_J}^2 - (c_J - \sigma_N \tan\phi_J)^2 + (c_J - \chi_J \tan\phi_J)^2 = 0 \qquad \text{(Eq 6.22)}$$

where:

$$\begin{aligned} \tau_J &= \sqrt{{\tau_{y'z'}}^2 + {\tau_{z'x'}}^2} && \text{shear stress acting in the isotropic plane} \\ \sigma_N &= \sigma_{z'} && \text{effective normal stress acting in the isotropic plane} \end{aligned} \qquad \text{(Eq 6.23)}$$

6.1.4 Softening law

The quasi brittle behaviour of the argillaceous rocks is simulated by means of a translation and contraction of the hyperbolic yield function (kinematic and isotropic softening). The softening behaviour is given by decreasing the parameters $(\chi, c \text{ and } \phi)$. The decreasing law of the parameters $(\chi, c \text{ and } \phi)$ is controlled by a scale function $S(\xi)$ *(Carol & Prat, 1990 in Lopez C.M. 1999)* defined as:

$$S(\xi) = \frac{e^{-\alpha} \cdot \xi}{1 + (e^{-\alpha} - 1) \cdot \xi} \qquad \text{(Eq 6.24)}$$

Figure 6.7 shows the evolution of parameters of yield surfaces as a function of the scale function $S(\xi)$. In this case, the scale function depends of the plastic work $W^p = \sigma^T \varepsilon^{vp}$. The scale function can be different for each parameter $S_\chi(\xi)$, $S_c(\xi)$ and $S_\phi(\xi)$, depending of the parameters α adopted. The evolution law of the parameters is defined by the following relationships *(Lopez C.M., 1999)*:

$$\chi = \chi_0 (1 - S_\chi(\xi)) \qquad \text{(Eq 6.25)}$$

$$c = c_0 \left[1 - S_c(\xi) - \frac{\chi_0}{c_0} \tan\phi_0 \left(S_\chi(\xi) - S_c(\xi) \right) \right] \qquad \text{(Eq 6.26)}$$

$$\tan\phi = \tan\phi_0 - (\tan\phi_0 - \tan\phi_{res}) \cdot S_\phi(\xi) \qquad \text{(Eq 6.27)}$$

Equation (6.25) gives the evolution of the tensile strength from $\chi = \chi_0$ for $S_\chi(\xi) = 0$ to $\chi = 0$ for $S_\chi(\xi) = 1$. Equation (6.26) gives the evolution of cohesion from $c = c_0$ for $S_c(\xi) = 0$ to $c = 0$ for $S_c(\xi) = 1$. The evolution of c is linked with the evolution of χ in order to ensure the correct evolution in the tensile-shear zone. Equation (6.26) produces a translation and contraction of the hyperbola, representing a kinematic and isotropic softening. The curvature radius of the hyperbola decrease from a initial hyperbolic surface, $(r/r_0) = 1$, until, it reaches the final straight line $(r/r_0) = 0$. Equation (6.27) gives the evolution of the friction angle from $\phi = \phi_0$ for $S_\phi(\xi) = 0$ to $\phi = \phi_{residual}$ for $S_\phi(\xi) = 1$.

Figure 6.8 and Figure 6.9 show the evolution of hyperbolic yield surfaces adopted for the matrix in both the meridional plane $(p, J)\big|_{\theta=-30^\circ}$ and octahedral plane $(J, \theta)\big|_{p=5.0\text{ MPa}}$, respectively. In this case, the evolution of the parameters $(\chi, c \text{ and } \phi)$ was performed with $\alpha = 0$. The line with triangles represents the initial yield surface, where $\xi = 0$, $\chi = \chi_0 = 2.0MPa$, $c = c_0 = 4.0MPa$ and $\phi = \phi_0 = 35^\circ$. The transition angle of $\theta_T = 25^\circ$ was adopted. The line with circles in the Figure 6.8 and Figure 6.9 represents the yield surface with the degradation already initiated. The parameter values are $\xi = 0.5$, $\chi = 1.0\text{ MPa}$, $c = 2.0\text{ MPa}$ and $\phi = 25.8^\circ$. The total degradation of rock is shown in Figure 6.8 and Figure 6.9 with the final yield surface represented by a line with squares. The parameter values are $\xi = 1$, $\chi = 0\text{ MPa}$, $c = 0\text{ MPa}$ and $\phi = \phi_{res} = 15^\circ$. In similar way, the evolution of the yield surface for the rock joint is shown in Figure 6.10.

The plastic potential Q is similar to hyperbolic yield function F, but it depends of the tensile strength (χ), cohesion (c) and dilatancy angle (ψ). The dilatancy angle (ψ) is, in general, smaller than friction angle (ϕ). The evolution of the viscoplastic potential function Q is given by the decreasing of the parameters $(\chi, c \text{ and } \psi)$. The evolution law of the dilatancy angle (ψ) is performed in similar way to the friction angle (ϕ) (equation, 6.27).

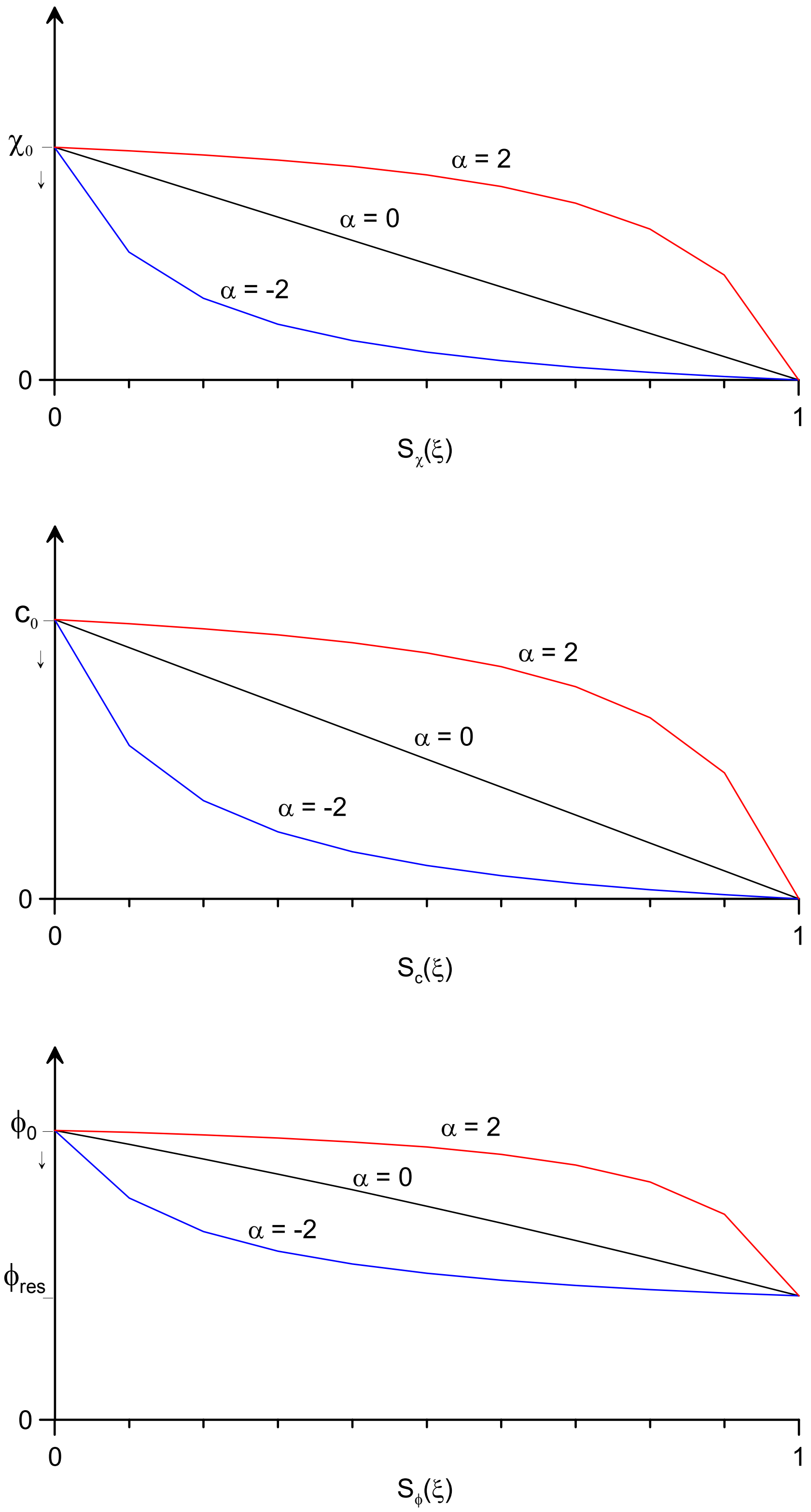

Figure 6.7: Evolution of the parameters of the yield surfaces as a function of the scale function $S(\xi)$ *for different values of* α*.*

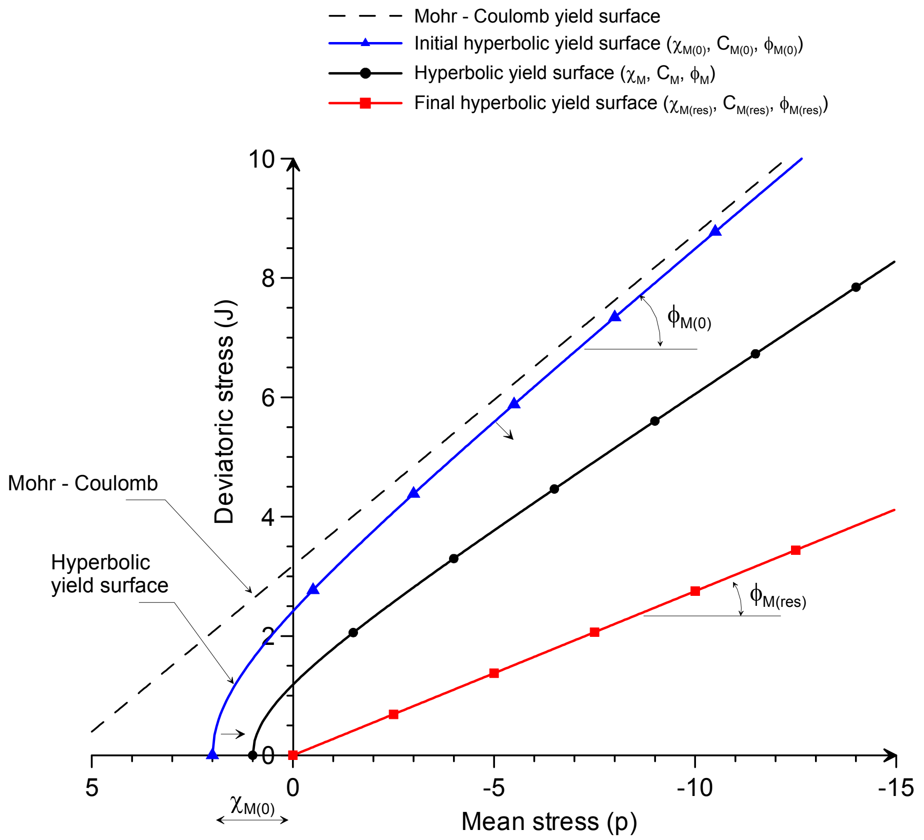

Figure 6.8: Evolution of hyperbolic yield surface adopted for rock matrix in a meridional plane. (Lode angle $\theta = -30^o$).

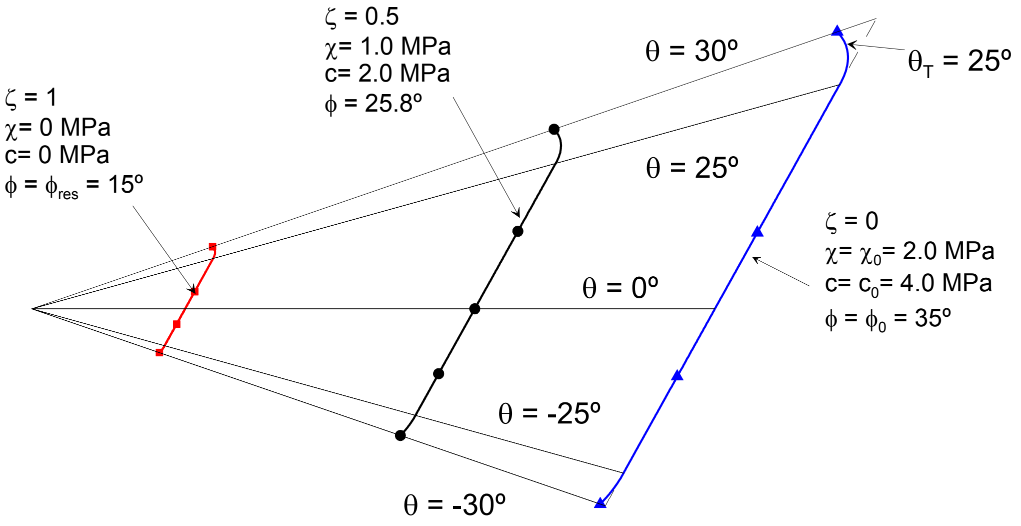

Figure 6.9: Evolution of hyperbolic yield surface adopted for rock matrix in the octahedral plane (mean stress p = 5.0 MPa).

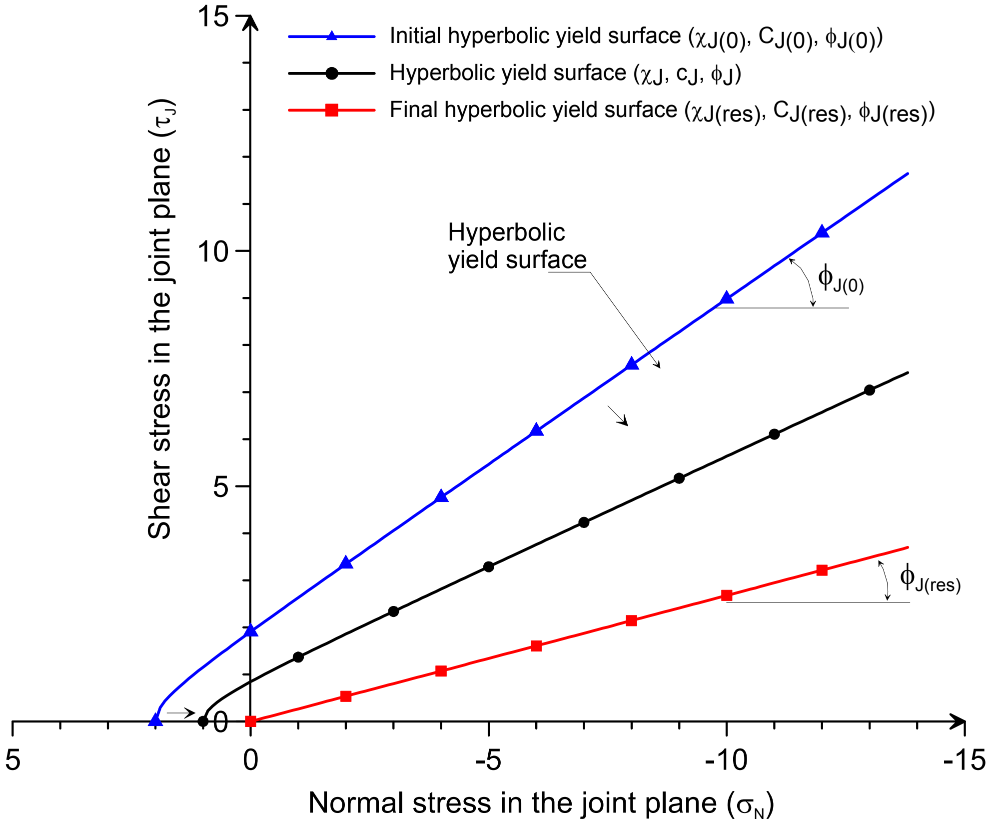

Figure 6.10: Evolution of the hyperbolic yield surface adopted for the joints of rock.

6.2 Programming in CODE_BRIGTH

The programming of the constitutive model into the finite elements code CODE_BRIGHT follows the formulation of viscoplasticity proposed by *(Zienkiewicz and Taylor, 1994).*

To start, from the additive decompositions of strain (Eq 6.11) and the elastic strain (Eq 6.12) the equilibrium conditions are defined as:

$$\int_v B^T \sigma dv - f = 0 \qquad \text{(Eq 6.28)}$$

Equation (6.28) is satisfied for all times if the initial conditions are known. Equations (6.11), (6.12) and (6.28) constitute a system of differential equations of first order with non linear coefficients, whose solutions is obtained by means of iterative methods.

Considering a time t_n, at the beginning, where the displacements u_n, stress σ_n and loads f_n are known, a non linear algebraic equations system which relates the initial conditions with the final conditions in a time $t_{n+1} = \Delta t + t_n$ can be written. Therefore, a set of non linear equilibrium equations is solved as follow:

$$\Psi_{n+1} \equiv \int_v B^T \sigma_{n+1} dv - f_{n+1} = 0 \tag{Eq 6.29}$$

where Ψ is the residual in the loads equilibrium.

The stress increment in the time t_n can be written from equations (6.11) and (6.12) as follows:

$$\Delta\sigma_n = D\left(\Delta\varepsilon - \Delta\varepsilon^{vp}\right) \tag{Eq 6.30}$$

The viscoplastic strain increment $\Delta\varepsilon^{vp}$ is obtained as a function of viscoplastic strain rate evaluated in an intermediate point θ as follows:

$$\Delta\varepsilon^{vp} = \Delta t\, \dot{\varepsilon}^{vp}_{n+\theta} \tag{Eq 6.31}$$

where:

$$\frac{d\varepsilon^{vp}_{n+\theta}}{dt} = \dot{\varepsilon}^{vp}_{n+\theta} = \left(1-\theta\right)\dot{\varepsilon}^{vp}_{n} + \theta\,\dot{\varepsilon}^{vp}_{n+1} \tag{Eq 6.32}$$

Replacing the equation (6.31) in equation (6.30) the non linear equation is obtained as:

$$R_{n+1} \equiv \Delta\sigma_n - DB\Delta u_n + D\Delta t\,\dot{\varepsilon}^{vp}_{n+\theta} = 0 \tag{Eq 6.33}$$

The equations system (6.29) to (6.33) can be solved by mean of an iterative method. The Newton-Raphson method has been adopted where, removing the indices n and n+1, the iterative/incremental process can be written as follow:

$$\Psi^{i+1} = 0 = \Psi^i + \int_v B^T \delta\sigma^i dv \tag{Eq 6.34}$$

The non linear equilibrium equation (6.33) can be written in a similar form using equations (6.31) and (6.32) and assuming that $\dot{\varepsilon}^{vp}$ is only a function of stress σ. It is written as:

$$R^{i+1} = 0 = R^i + \delta\sigma^i - DB\delta u^i + D\Delta t \left(\frac{\partial\dot{\varepsilon}^{vp}}{\partial\sigma}\right)_{n+\theta} \delta\sigma^i = 0 \tag{Eq 6.35}$$

where:

$$\left(\frac{\partial\dot{\varepsilon}^{vp}}{\partial\sigma}\right)_{n+\theta} = \theta\frac{\partial\dot{\varepsilon}^{vp}_{n+1}}{\partial\sigma} = \theta G \tag{Eq 6.36}$$

where G is the tensor gradient of viscoplastic strain rate.

The non linear equations system obtained in the equation (6.35) can be expressed in a compacted form as follows:

$$\delta\sigma^i = \left(I + D\cdot\Delta t\cdot\theta\cdot G\right)^{-1}\left(D\cdot B\cdot\delta u^i - R^i\right) \tag{Eq 6.37}$$

$$\begin{gathered} D^* = \left(I + D\cdot\Delta t\cdot\theta\cdot G\right)^{-1} \\ D^{**} = D^*\cdot D \end{gathered} \tag{Eq 6.38}$$

where D^{**} represents the tangent tensor.

Replacing equation (6.37) in to equation (6.34) we obtain the non linear equilibrium equations system:

$$\left(\int_v B^T\cdot D^{**}\cdot B\cdot dv\right)\delta u^i = -\Psi^i + \int_v B^T\cdot D^*\cdot R^i\cdot dv \tag{Eq 6.39}$$

The viscoplastic strain rate gradient tensor G is used to compute the tensor D^* and to update the stress (Eq 6.37). It is computed as:

$$\begin{gathered} G = \frac{\partial \dot{\varepsilon}^{vp}}{\partial\sigma} = \frac{\partial}{\partial\sigma}\left(\Gamma\cdot\phi(F)\cdot\frac{\partial Q}{\partial\sigma}\right) \\ G = \Gamma\left\{\left(\frac{\partial\phi(F)}{\partial\sigma}\left(\frac{\partial Q}{\partial\sigma}\right)^T\right)^T + \phi(F)\frac{\partial^2 Q}{\partial\sigma^2}\right\} \end{gathered} \tag{Eq 6.40}$$

6.3 Calibration of the constitutive model

The laboratory triaxial tests of Opalinus Clay reported by *Schnier (2004)* have been reproduced in order to calibrate the mechanical constitutive model. A 3D numerical model of the tested samples has been performed. The samples were 100 mm in diameter and 250 mm height, with a bulk density $\rho = 2.4$ g/cm^3 and water content $w = 0.07$. The samples were discretized in a 3D finite element mesh having 2541 nodes and 2160 linear quadrilateral prism elements, with 8 integration points. Figure 6.11 shows the finite element mesh of the samples tested. Numerical simulations of samples with angles of dip of 0º, 15º, 30º, 45º, 60º, 75º and 90º have been performed. Table 6.1 shows the mechanical parameters of the rock used in the model. Some mechanical parameters has been taken from *Bock, (2001)* and the others has been adopted to fit the laboratory tests.

The boundary conditions applied in the numerical model were the following:

a- Confining pressure of $\sigma_3 = 1.0\ MPa$ was applied to the sample.

b- The vertical displacements of the nodes located on the upper side of the sample were fixed.

c- Vertical displacements were imposed in the nodes located on the lower side of the sample. A vertical strain rate of $\dot{\varepsilon} = 0.00001\ {}^1\!/_s$ was imposed.

Figure 6.12 to Figure 6.18 show the stress-strain behaviour and the stress path for the numerical simulations of samples with angle of dip of 0º, 15º, 30º, 45º, 60º, 75º and 90º, respectively. The numerical simulations of samples with angles of dip of 0º, 45º and 90º have been compared with the triaxial laboratory tests. The summary of stress-strain behavior of all samples is shown in Figure 6.19. Figure 6.20 plots the variation of the strength with the angle of dip. Figure 6.21 shows the shear strain produced in the samples with different angles of dip.

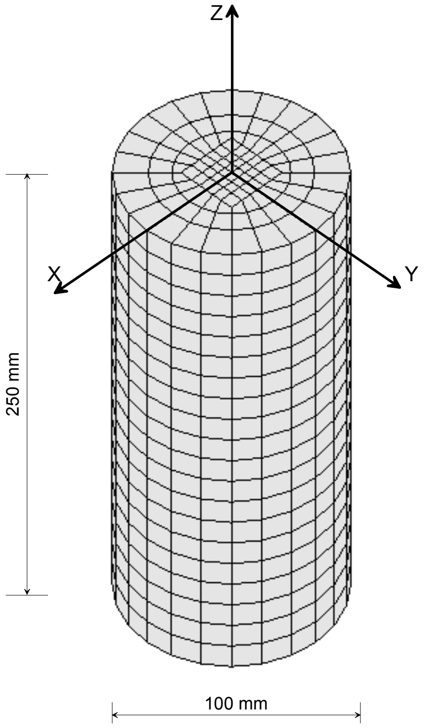

Figure 6.11: Finite element mesh of the samples tested. (ϕ = 100 mm, h = 250mm)

Table 6.1: Mechanical parameters of Opalinus Clay

Deformation parameters of transverse rock			
Tangent modulus $E_{X'-X'} = E_{Y'-Y'}$ (// bedding planes)	***(Bock (2001))***	[MPa]	3000
Tangent modulus $E_{Z'-Z'}$ ($\perp$ bedding planes)	***(Bock (2001))***	[MPa]	1500
Poisson's ratio. ν_{XY}	***(Bock (2001))***	-	0.33
Poisson's ratio. $\nu_{ZX} = \nu_{ZY}$	***(Bock (2001))***	-	0.24
Shear modulus $G_{ZX} = G_{ZY}$		[MPa]	650
α = angle of strike ($0^o < \alpha < 180^o$), with respect to Y axis		[º]	90.0
Dip angle ($0^o < \beta < 90^o$)		[º]	0, 15, 30, 45, 60, 75 and 90
Viscous parameters			
$\Gamma_M = \Gamma_J$		[1/sec]	1.00E-08
$N_M = N_J$		-	2 - 5
F_{0M}		[MPa]	12.0
F_{0J}		[MPa]	1.0
Strength parameters of matrix			
Uniaxial compressive strength UCS$\perp$ - UCS$_{//}$	***(Bock (2001))***	[MPa]	12.0
Uniaxial tensile strength UTS$\perp$ - UTS$_{//}$ (χ)		[MPa]	5.0
Cohesion (c)		[MPa]	6.0
Friction angle (ϕ)	***(Bock (2001))***	[º]	30.0
Residual friction angle (ϕ_R)		[º]	15.0
Dilatancy angle (ψ)		[º]	25.0
Strength parameters of the joint			
Tensile strength (χ_{joint})		[MPa]	2.0
Cohesion (c_{joint})		[MPa]	2.0
Friction angle (ϕ_{joint})	***(Bock (2001))***	[º]	23.0
Residual friction angle (ϕ_R)		[º]	15.0
Dilatancy angle (ψ)		[º]	20.0

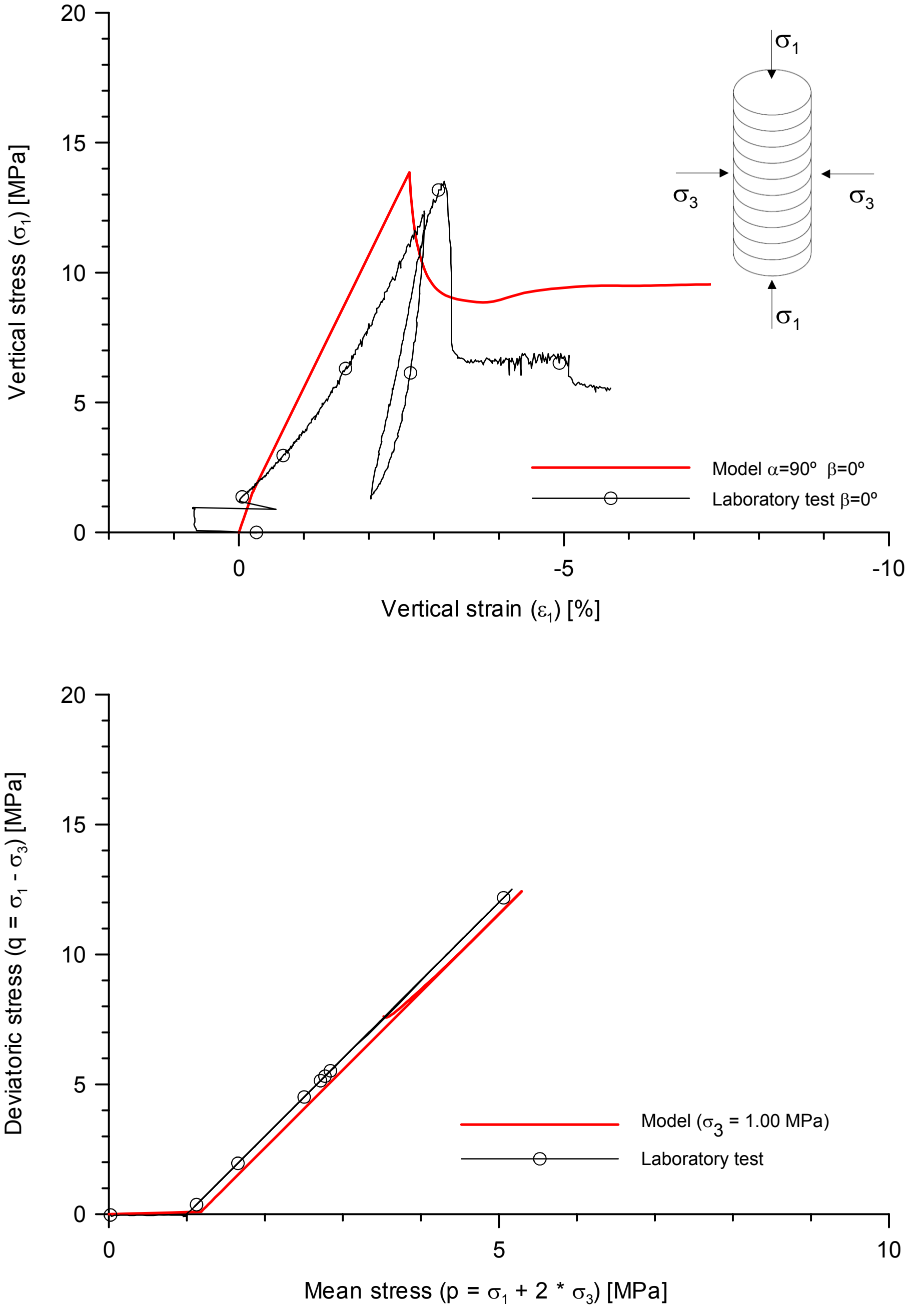

Figure 6.12: Comparison between numerical simulations and triaxial laboratory test for a sample with angle of dip of 0°. (Upper): Stress-strain behaviour, (Bottom): Stress path. Number of iterations: 2650

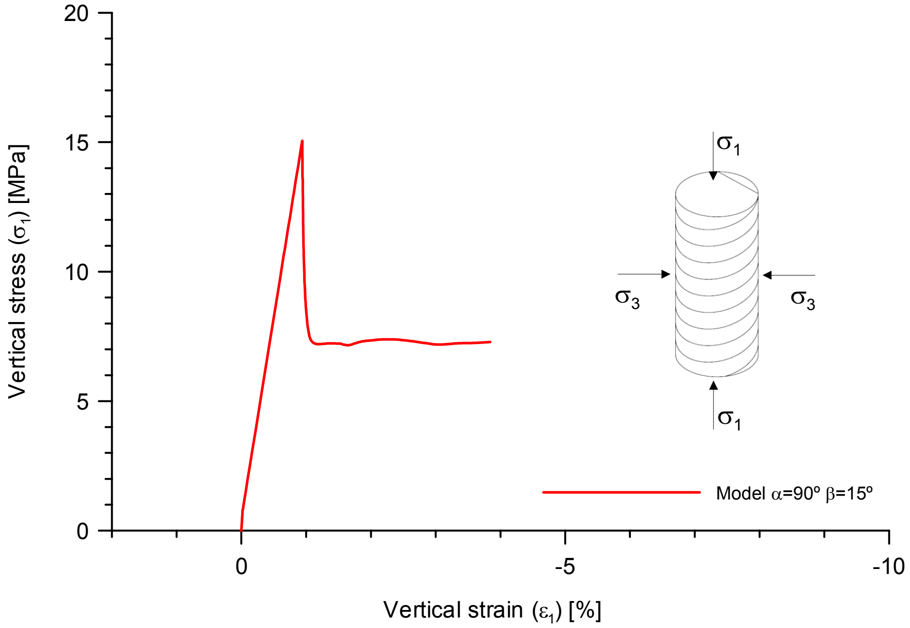

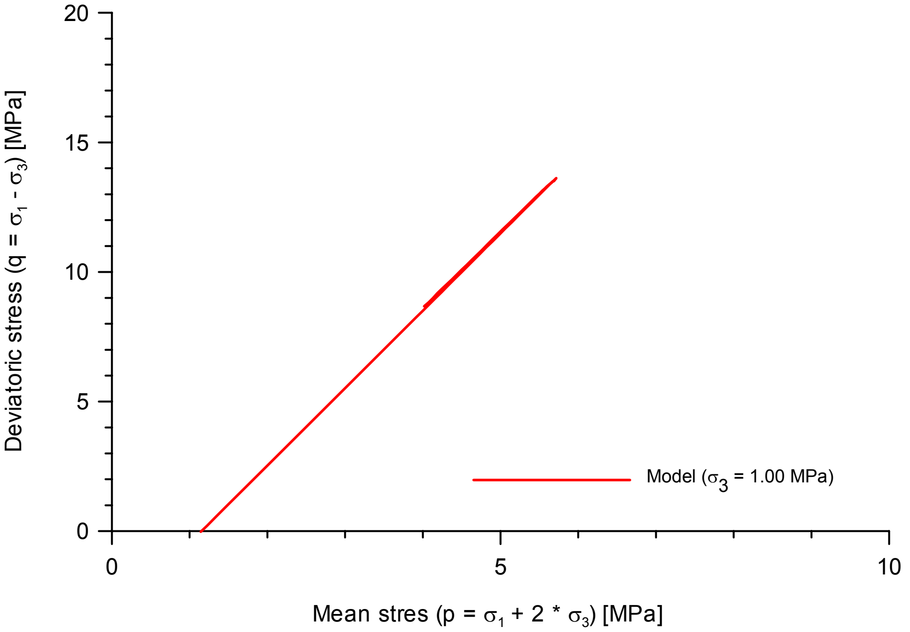

Figure 6.13: Numerical simulations for a sample with angle of dip of 15°. (Upper): Stress-strain behaviour. (Bottom): Stress path. Number of iterations: 305

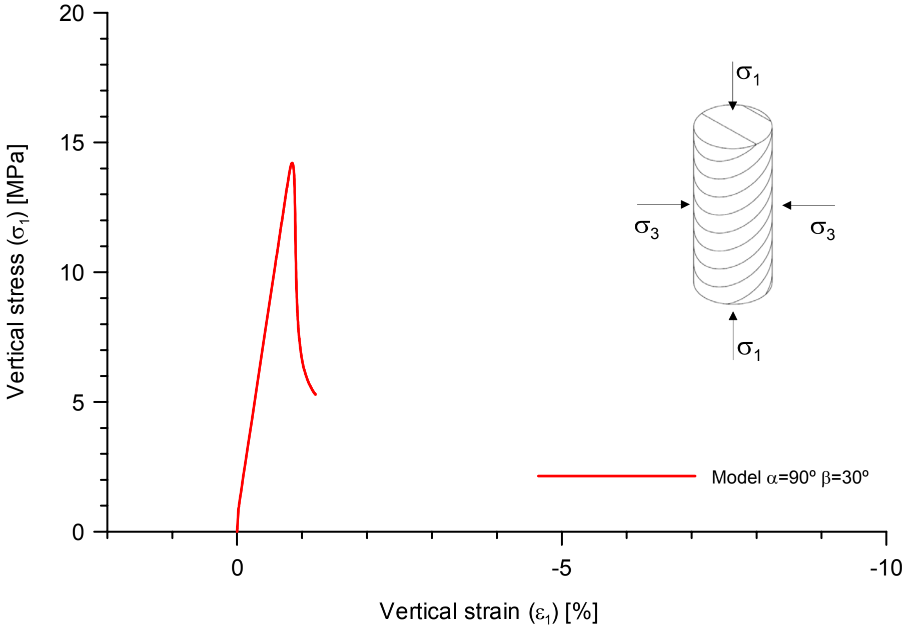

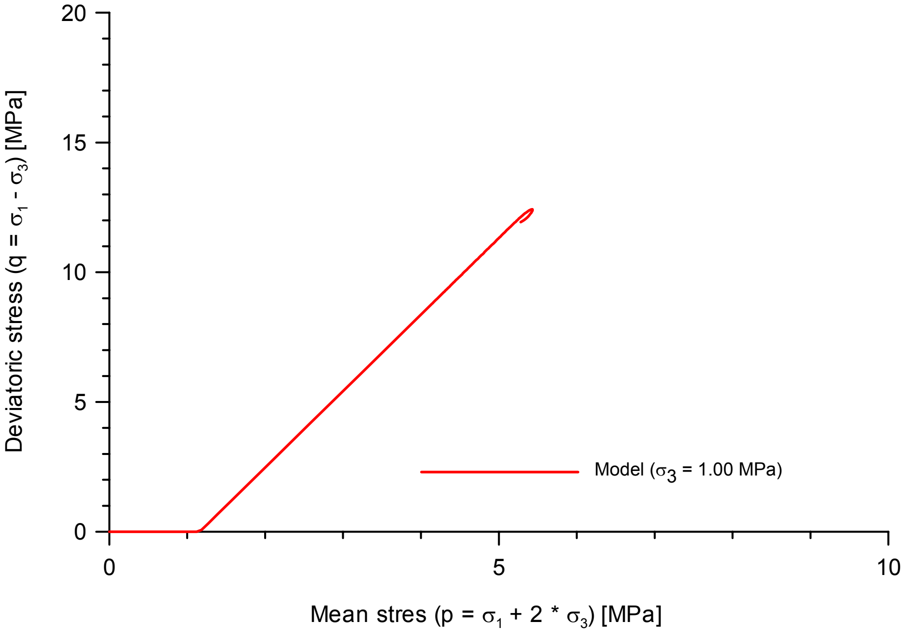

Figure 6.14: Numerical simulations for a sample with angle of dip of 30º. (Upper): Stress-strain behaviour. (Bottom): Stress path. Number of iterations: 520

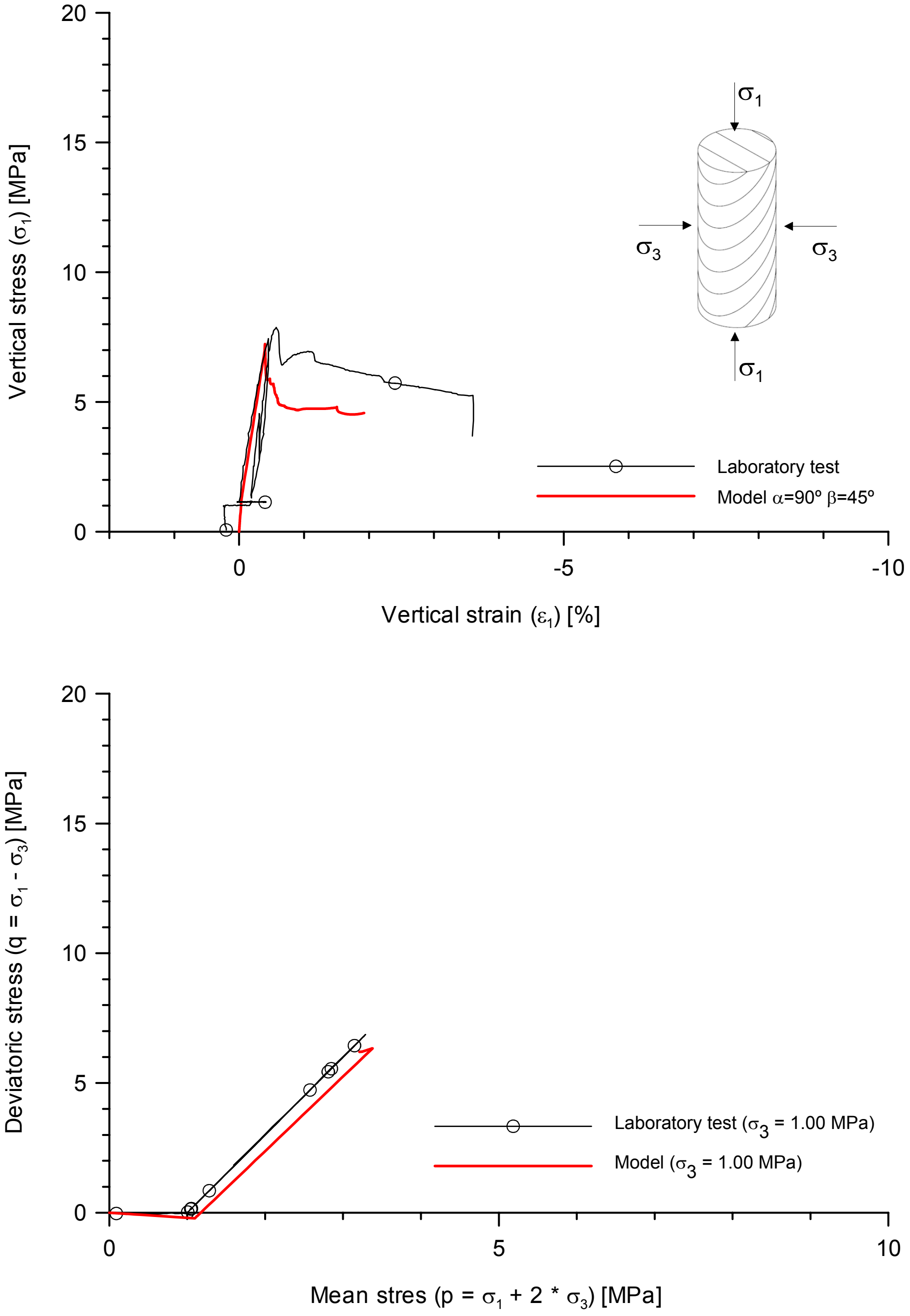

Figure 6.15: Comparison between numerical simulations and triaxial laboratory test for a sample with angle of dip of 45º. (Upper): Stress-strain behaviour. (Bottom): Stress path. Number of iterations: 1490

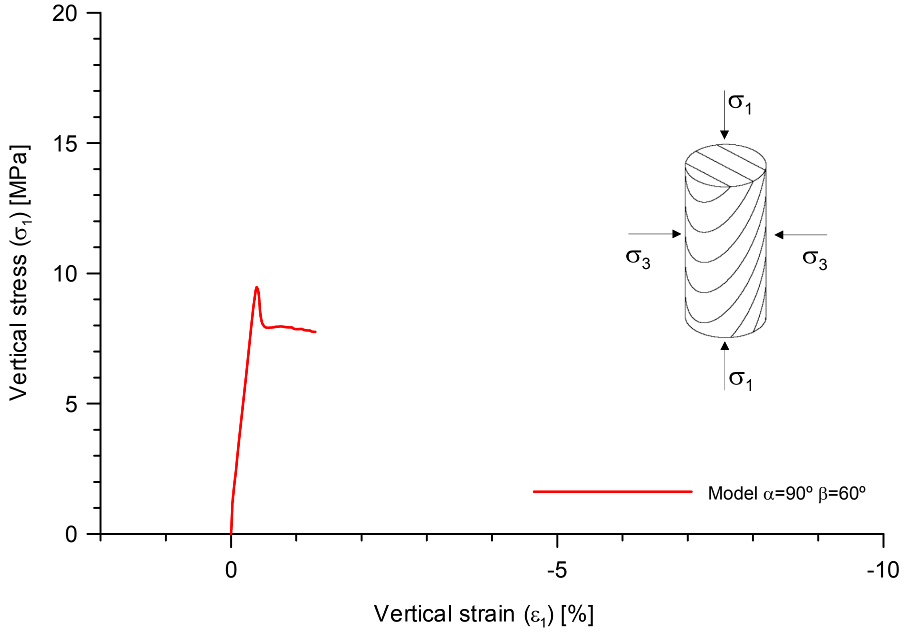

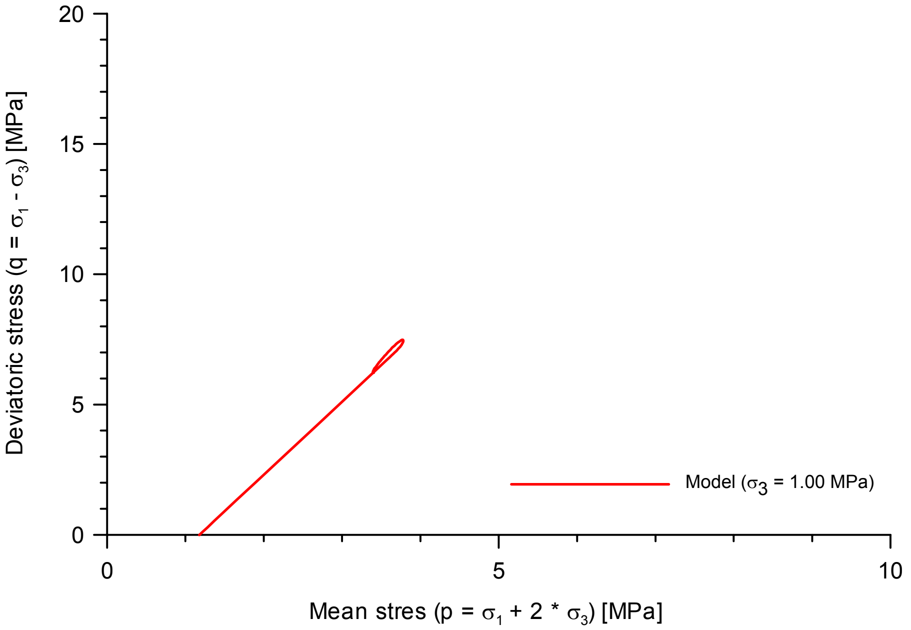

Figure 6.16: Numerical simulations for a sample with angle of dip of 60°. (Upper): Stress-strain behaviour. (Bottom): Stress path. Number of iterations: 215

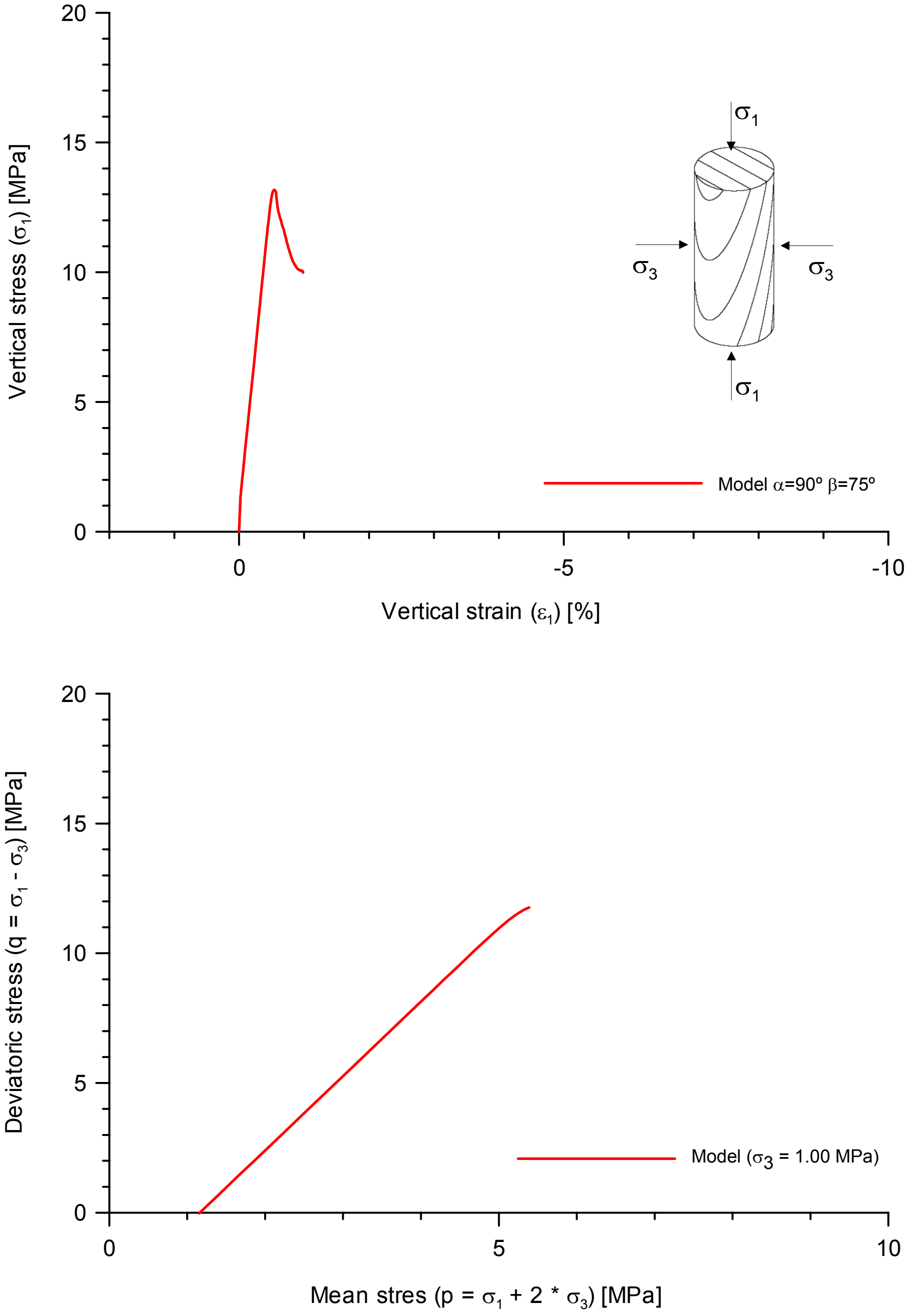

Figure 6.17: Numerical simulations for a sample with angle of dip of 75º. (Upper): Stress-strain behaviour. (Bottom): Stress path. Number of iterations: 310

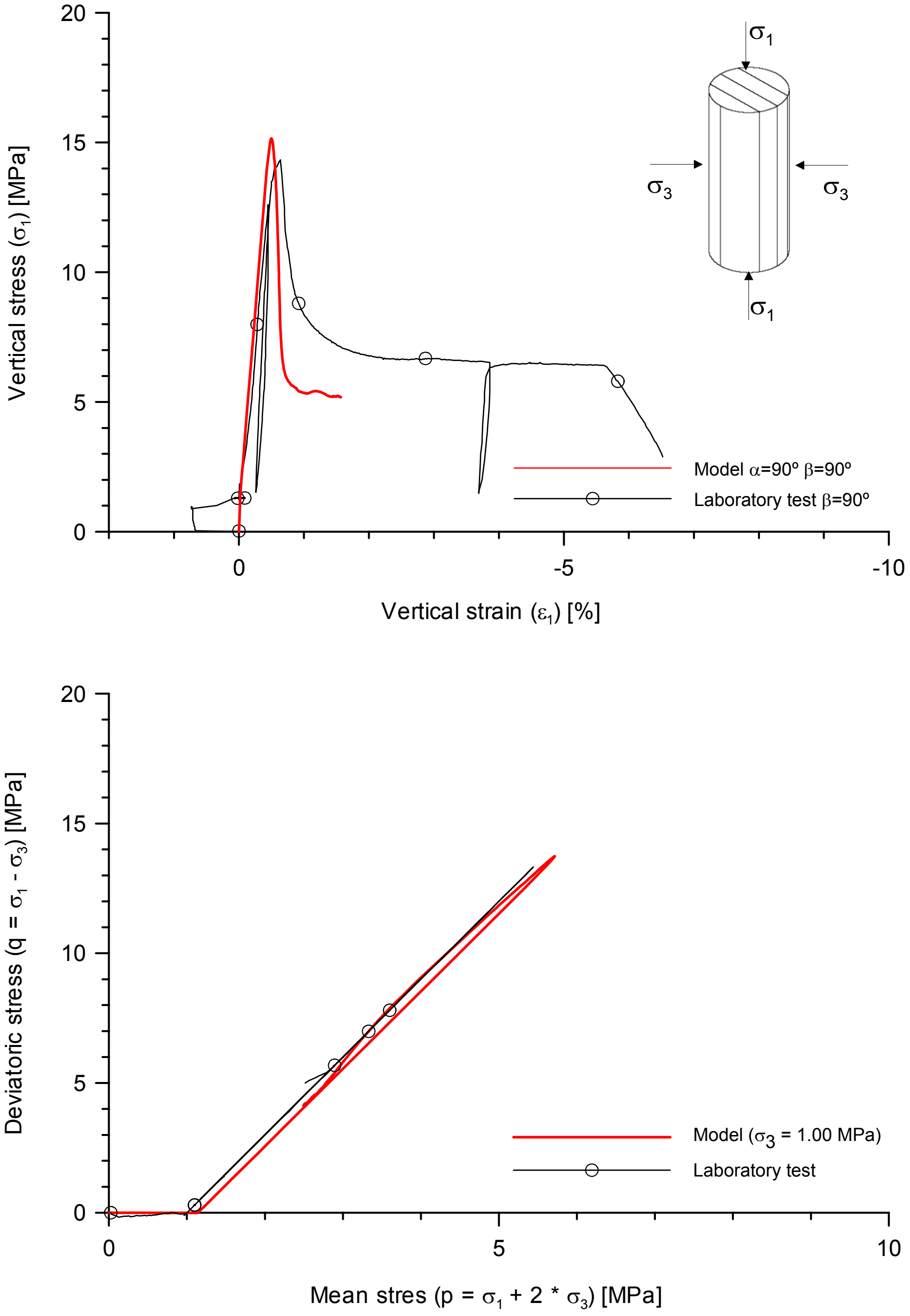

Figure 6.18: Comparison between numerical simulations and triaxial laboratory test for a sample with angle of dip of 90º. (Upper): Stress-strain behaviour. (Bottom): Stress path. Number of iterations: 295

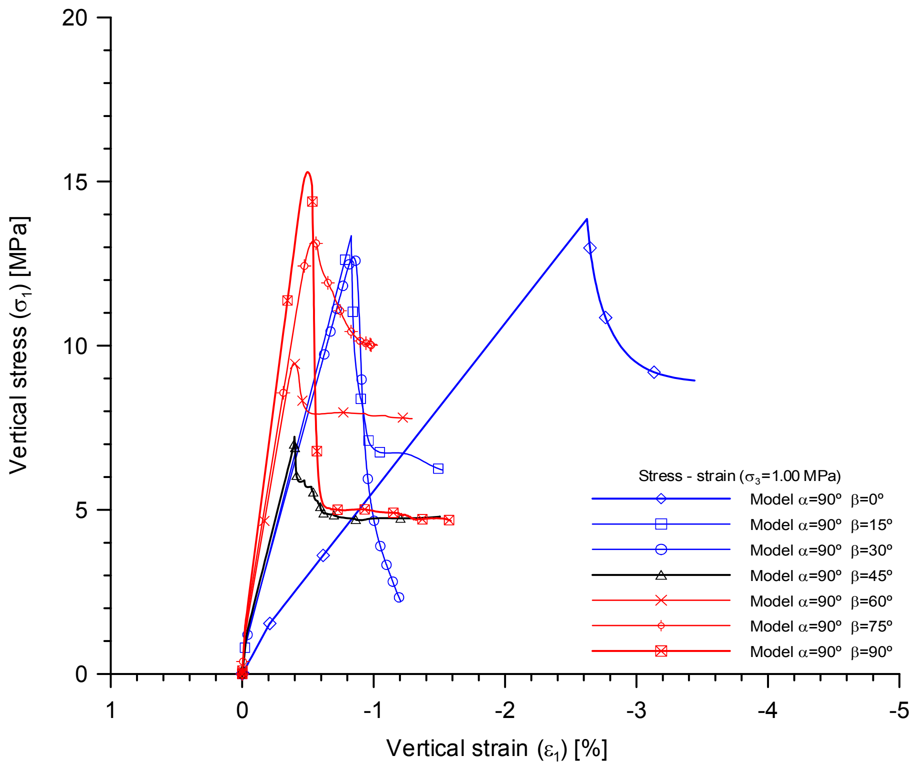

Figure 6.19: Stress-strain behaviour of the samples with different angles of dip.

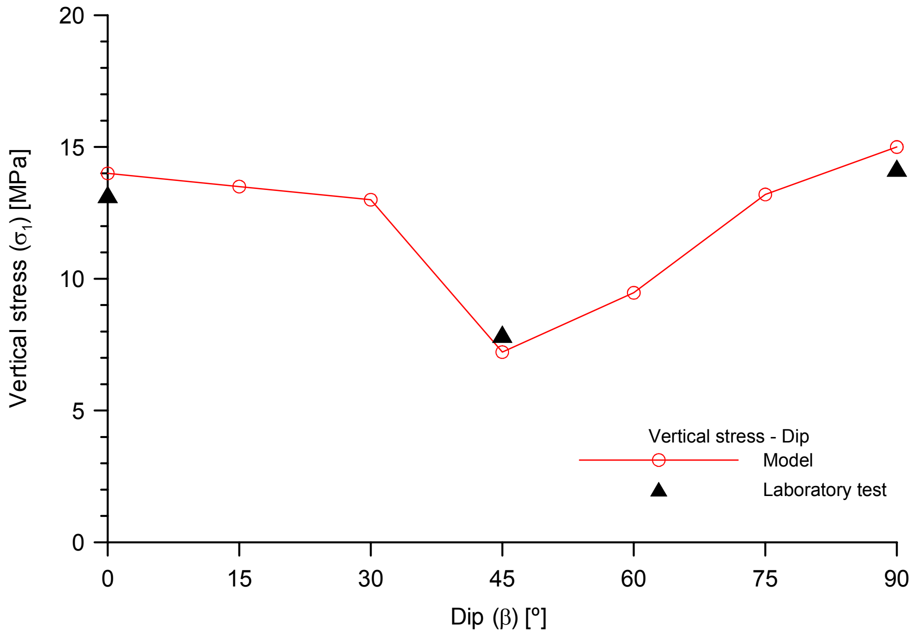

Figure 6.20: Variation of strength with the angle of dip.

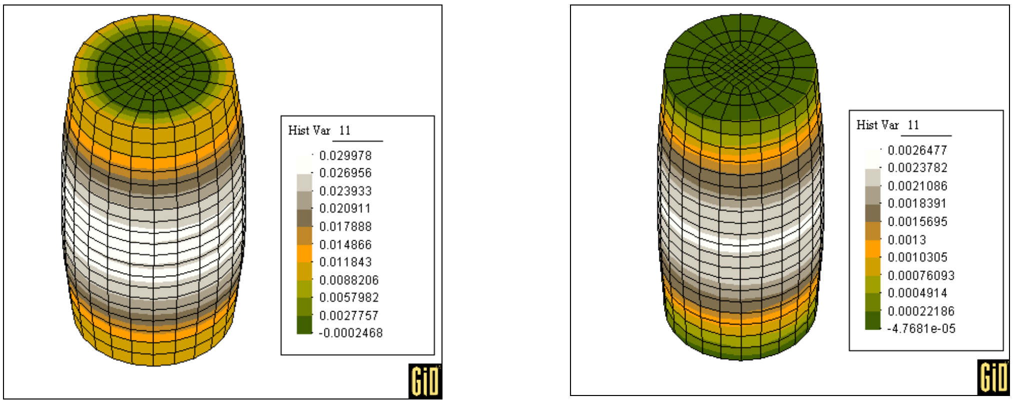

a) Shear strain (β = 0°) *b) Shear strain (β = 15°)*

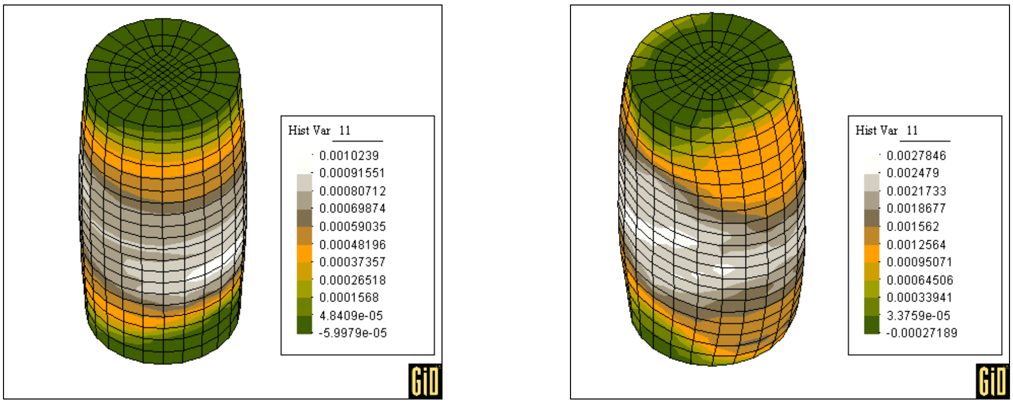

c) Shear strain (β = 30°) *d) Shear strain (β = 45°)*

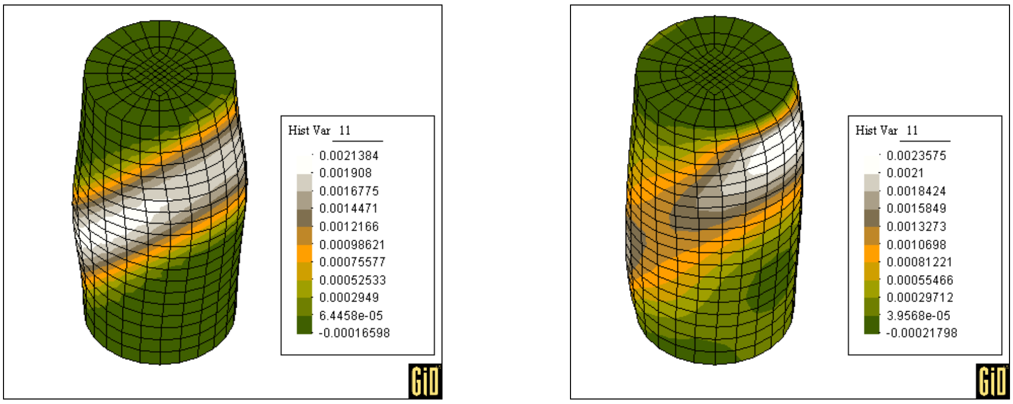

e) Shear strain (β = 60°) *f) Shear strain (β = 75°)*

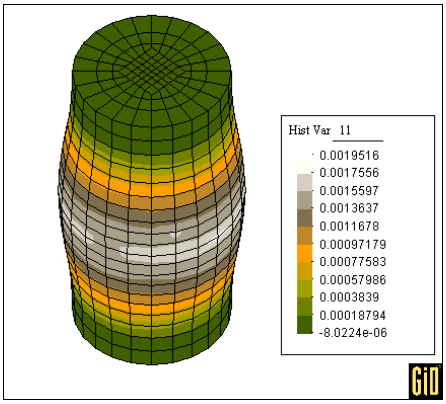

g) Shear strain (β = 90°)

Figure 6.21: Shear strain for samples with different angles of dip.

CHAPTER VII

3D T-H-M MODELLING OF HE AND VE EXPERIMENTS INCLUDING ROCK ANISOTROPY

7.1 Introduction

In this chapter the 3D numerical simulations of the “in situ” heating experiment (HE) and drying effects in the “in situ” ventilation experiment (VE) performed at the Mont Terri underground rock laboratory will be analyzed. The anisotropic constitutive model developed in chapter VI will be applied.

7.2 3D modelling of HE experiment

The HE experiment was discretized by means fo a 3D finite element mesh of 12491 nodes and 11088 linear quadrilateral prism elements, having 8 integration points. Each node has five degrees of freedom, namely, three displacements (X, Y and Z directions), the liquid pressure and the temperature. The domain is 20.30 m length in both horizontal directions (X and Y), and 20.00 m height (vertical direction Z). The borehole BHE-0 is 300 mm in diameter and 7.00 m depth. The coordinate system has its origin at the intersection between the floor of the HE niche and the longitudinal axis of borehole BHE-0. Figure 7.1 shows isometric view of the finite element mesh developed to simulate the HE experiment. Figure 7.2 shows the plan view of the finite element mesh and both global and local coordinate system. Figure 7.3 shows the front view of the borehole BHE-0.

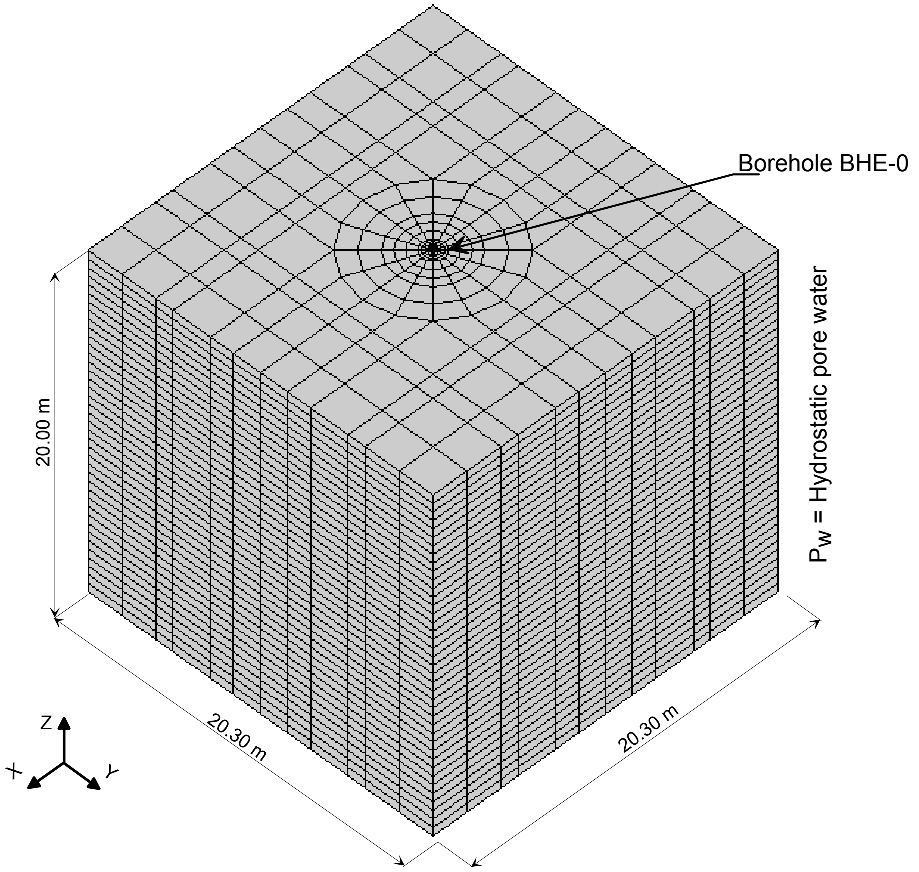

Figure 7.1: 3D finite element mesh used in the model.

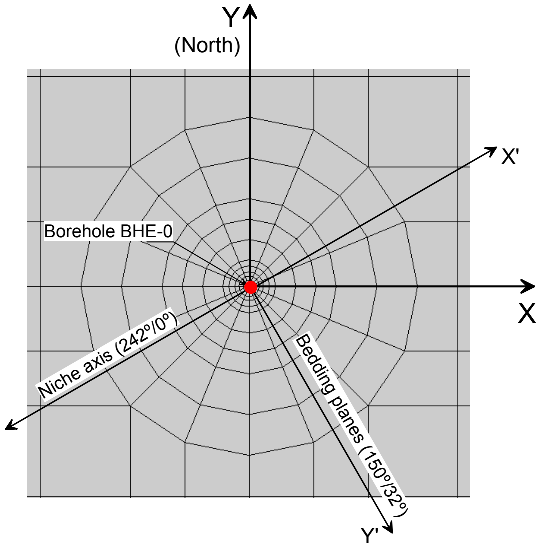

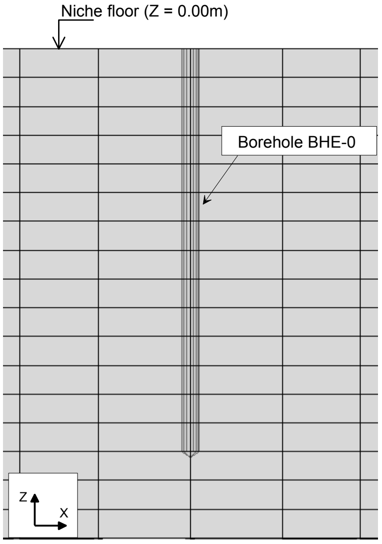

Figure 7.2: Upper view of the finite element mesh.

Figure 7.3: Vertical view of the borehole BHE-0 in 3D finite element mesh.

7.2.1 Initial and boundary conditions

The initial vertical stress in the host rock was $\sigma_z = -6.0 \text{ MPa}$ and the two horizontal stresses were equal to $\sigma_x = \sigma_y = -4.0 \text{ MPa}$. A hydrostatic absolute pore water pressure distribution was applied, where $P_w = 0.10 \text{ MPa}$ correspond to the HE niche floor (depth = 0.00 m). The initial temperature at the host rock was 15 ºC.

Before simulating the different phases of the experiment, a stage of equilibrium of stress and pores water pressures was performed. In this phase, the radial displacements of the nodes located on the borehole wall were impeded.

The 3D numerical model of the HE experiment covers the following steps:

Step 1: Excavation of the borehole BHE-0. The borehole excavation was simulated permitting the free displacements of the nodes located on the borehole wall. A boundary condition of suction $s = 6.8 \text{ MPa}$ was applied on the borehole wall. During the borehole excavation the suction was increased from $s = 6.8 \text{ MPa}$ to $s = 11.5 \text{ MPa}$. The excavation phase was performed under isothermal conditions at a temperature of 15 ºC. The excavations phase lasted 10 days.

Step 2: Hydration of bentonite phase. The bentonite swelling pressure was simulated by means of radial pressure of $\sigma_r = 15.0 \text{ MPa}$ applied on the borehole wall, from -2.0 m to -7.0 m depth. The radial stresses were increased from 0 MPa to 15 MPa during the first 200 days of hydration phase. Then, the radial stresses remained constant until the end of the experiment. The hydration phase was performed under isothermal conditions at a temperature of 15º C. The hydration phase lasted 33 months.

Step 3: Heating phase. A temperature boundary condition of $T = 65 \text{ ºC}$ was applied on the borehole wall, from -4.0 m to -6.0 m depth. The temperature applied corresponds to the maximum temperature reached by the rock at the bentonite-rock contact (r = 0.15 m), as it was shown in the 2D model (chapter V). The heating phase lasted 18 months.

Step 4: Cooling phase. The boundary condition of temperature on the borehole wall was removed permitting the temperature to recover the initial conditions. The cooling phase lasted 9 months.

7.2.2 Opalinus Clay parameters

The mechanical, hydraulic and thermal parameters of the Opalinus Clay rock used in the 3D model have been taken from *(Hohner & Bossart (1998); Bock (2001); Muñoz et al., (2001); Muñoz et al., (2003); Nussbaum et al. (2004))*. They are summarized in *Table 7.1*, *Table 7.2* and *Table 7.3*.

Table 7.1: Mechanical parameters of Opalinus Clay

Deformation parameters of transverse rock		
Tangent modulus $E_{X'-X'} = E_{Y'-Y'}$ (// bedding planes)	[MPa]	3000
Tangent modulus $E_{Z'-Z'}$ ($\perp$ bedding planes)	[MPa]	1500
Poisson's ratio. ν_{XY}	-	0.33
Poisson's ratio. $\nu_{ZX} = \nu_{ZY}$	-	0.24
Shear modulus $G_{ZX} = G_{ZY}$	[MPa]	650
$\alpha =$ angle of strike ($0^{\circ} < \alpha < 180^{\circ}$), with respect to Y axis	[°]	60.0
Dip angle ($0^{\circ} < \beta < 90^{\circ}$)	[°]	35.0
Viscous parameters		
$\Gamma_M = \Gamma_J$	[1/sec]	1.00E-05
$N_M = N_J$	-	3
F_{0M}	[MPa]	12.0
F_{0J}	[MPa]	1.0
Strength parameters of matrix		
Uniaxial compressive strength $UCS\perp - UCS_{//}$	[MPa]	12.0
Uniaxial tensile strength $UTS\perp - UTS_{//}$ (χ)	[MPa]	5.0
Cohesion (c)	[MPa]	6.0
Friction angle (ϕ)	[°]	30.0
Residual friction angle (ϕ_R)	[°]	15.0
Dilatancy angle (ψ)	[°]	25.0
Strength parameters of the joint		
Tensile strength (χ_{joint})	[MPa]	2.0
Cohesion (c_{joint})	[MPa]	2.0
Friction angle (ϕ_{joint})	[°]	23.0
Residual friction angle (ϕ_R)	[°]	15.0
Dilatancy angle (ψ)	[°]	20.0

Table 7.2: Hydraulic parameters of Opalinus Clay

Properties	***Value***
Intrinsic permeability, **k** (Kozeny model)	$k = k_0 \frac{\phi^3}{(1-\phi)^2}\frac{(1-\phi_0)^2}{\phi_0^3}$ ϕ_0: reference porosity (0.137) k_0: intrinsic permeability for matrix ($3.50 \cdot 10^{-19}$) [m^2]
Water Retention Curve (Modified Van Genuchten model)	$S_e = \frac{S_l - S_{rl}}{S_{ls} - S_{rl}} = \left(1 + \left(\frac{P_g - P_l}{P}\right)^{\frac{1}{1-\lambda}}\right)^{-\lambda} \left(1 - \frac{P_g - P_l}{P_s}\right)^{\lambda_s}$ S_e: Effective saturation ($0 \leq S_e \leq 1$) P : Material parameter (3.90) [MPa] P_s : Material parameter (700.00) [MPa] λ : Shape function for retention curve (0.128) λ_s : Material parameter (2.73) S_{rl}: Residual saturation (0.00) S_{ls}: Maximum saturation (1.00)
Relative permeability, $\mathbf{k_{rl}}$ (Van Genuchten model)	$k_{rl} = \sqrt{S_e}\left(1 - \left(1 - S_e^{1/\lambda}\right)^{\lambda}\right)^2$ S_e: Effective saturation ($0 \leq S_e \leq 1$) λ : Power (0.29) S_{rl}: Residual saturation (0.00) S_{ls}: Maximum saturation (1.00)
Porosity, **n**	(0.137)

Table 7.3: Thermal parameters of Opalinus Clay

Properties		***Value***
Thermal conductivity	[$W\ m^{-1}\ K^{-1}$]	2.10
Linear thermal expansion coefficient, $\mathbf{b_s}$	[$°C^{-1}$]	$1.00 \cdot 10^{-05}$
Specific heat, **Cs**	[$J\ kg^{-1}\ K^{-1}$]	874.0

7.2.3 Analysis of results

The results of the 3D numerical model are presented and compared with in situ data, following the main phases of the experiment. The experimental data were taken from *(García-Siñeriz and Rey, 1999 – 2004*). In all phases of the experiment the temperature field, the pore water pressure distribution, stress state and displacement around of the borehole BHE-0 were analyzed. The isotropic and anisotropic 3D numerical model have been analyzed and compared. Figure 7.4 shows the upper view of the HE experiment and the points where the different variables are analyzed. Points (1), (2), (3) were located in the X direction at 5.0 m depth and at radial distance of 0.65 m, 1.65 m and

4.15 m, respectively. Points (4), (5), (6) were located in the Y direction at 5.0 m depth and at radial distance of 0.65 m, 1.65 m and 4.15 m, respectively. Points (7) and (8) are located at radial distance of 1.65 m in the direction of the bedding plane.

The temperature sensors TB05_05.00, TB06_05.00 and TB01_05.00 were chosen in order to plot the time evolution of the measured temperatures. The position of the temperature sensors is indicated in Figure 7.4 as points (1), (2) and (3). Figure 7.5 shows the measured and calculated evolution of temperature. The distribution of temperature field around the borehole is shown in Figure 7.6. During the excavation and hydration phases the temperature remains constant at 15 ºC. A temperature of 39.50 ºC has been reached in point (1), whereas in point (2) a temperature of 25.70 ºC was reached. A temperature of 18.10 ºC was reached in point (3). At the beginning of the cooling phase a sudden drop in temperature is produced when the power is removed. After 45 days of cooling phase, the calculated temperature is below 20 ºC. The distribution of the temperatures is well captured by the model.

The pore water pressure sensors QB 19/2 and QB 20/2 were chosen to plot the measured pore water pressure evolution. They are located in points (1) and (2) in Figure 7.4, respectively. Figure 7.7 shows the measured and calculated pore water pressure evolution. The distribution of the pore water pressure around the borehole is shown in Figure 7.8. The suction applied during the excavation phase produce a transitory state of the pore water pressure in the rock around the borehole. The pore water pressure decreases from 0.15 MPa to -0.15 MPa (Sr = 0.99) in the point (1). In the point (2), the pore water pressure descends from 0.15 MPa to 0.06 MPa. The pore water pressures reach a stable value after 450 days of hydration in both points (1) and (2). At the beginning of the heating phase, the calculated liquid pressure increases suddenly from 0.15 MPa to 0.90 MPa in point (1). The maximum calculated pore water pressure in point (2) is 0.79 MPa. At the beginning of the cooling phase a sudden drop of the pore water pressure was produced, and then, the liquid pressure increases slowly until a stable condition was reached.

The stress state evolution is analyzed in points located at 5.0 m depth and 0.10 m depth from the borehole wall $\left(r_X = r_Y = 0.25 \text{ m}; z = -5.0 \text{ m}\right)$. The stress state evolution is shown in Figure 7.9, for all phases of the experiment. During the excavation phase the radial stress decreases from $\sigma_r = -4.00\text{MPa}$ to $\sigma_r = -1.90\text{MPa}$. The radial stress represents the boundary condition applied on the borehole wall during the hydration, heating and cooling phases. During the first 200 days of hydration phase, the radial stress increases from $\sigma_r = -1.90\text{MPa}$ to $\sigma_r = -9.60\text{MPa}$ and then it remains constant until the end of the experiment. The circumferential stress increases from $\sigma_c = -4.00\text{MPa}$ to $\sigma_c = -6.20\text{MPa}$ during the excavation phase. Due to radial stress increment (swelling pressure simulation) during the hydration phases, the circumferential stress decreases until it reaches a tensile stress of $\sigma_c = 1.63\text{MPa}$. The vertical stress on the X direction remains essentially constant $(\sigma_Z = -6.0 \text{ MPa})$, during excavation and hydration phases, whereas in the Y direction it increases to $\sigma_Z = -6.6 \text{ MPa}$ during the hydration phase. A transitory increment of vertical stress was calculated during the heating phase.

Radial displacements have been calculated on the borehole wall in both X and Y directions $(r_X = r_Y = 0.15 \text{ m}; z = -5.0 \text{ m})$, as shown in Figure 7.10. During the excavation phase the radial displacements indicate a motion towards the borehole. Radial displacements in both X and Y directions have been calculated in points (2) and (5), respectively, see Figure 7.11. The profile of radial displacements versus depth at time 1535 days (end of heating phase) was calculated on the bedding plan direction, points (7) and (8), as shown in Figure 7.12. Figure 7.13 and Figure 7.14 show the deformed borehole in the isotropic and anisotropic model at end of excavations phase, respectively. The deformations of the borehole at end of hydration phase in the isotropic and anisotropic model are shown in Figure 7.15 and Figure 7.16, respectively.

The bentonite swelling pressure produces a plastic zone in the surrounding rock of 0.08 m in thickness. Figure 7.17 and Figure 7.18 show the plastic zone developed in a horizontal section at 5.0 m depth, for the isotropic and anisotropic model, respectively.

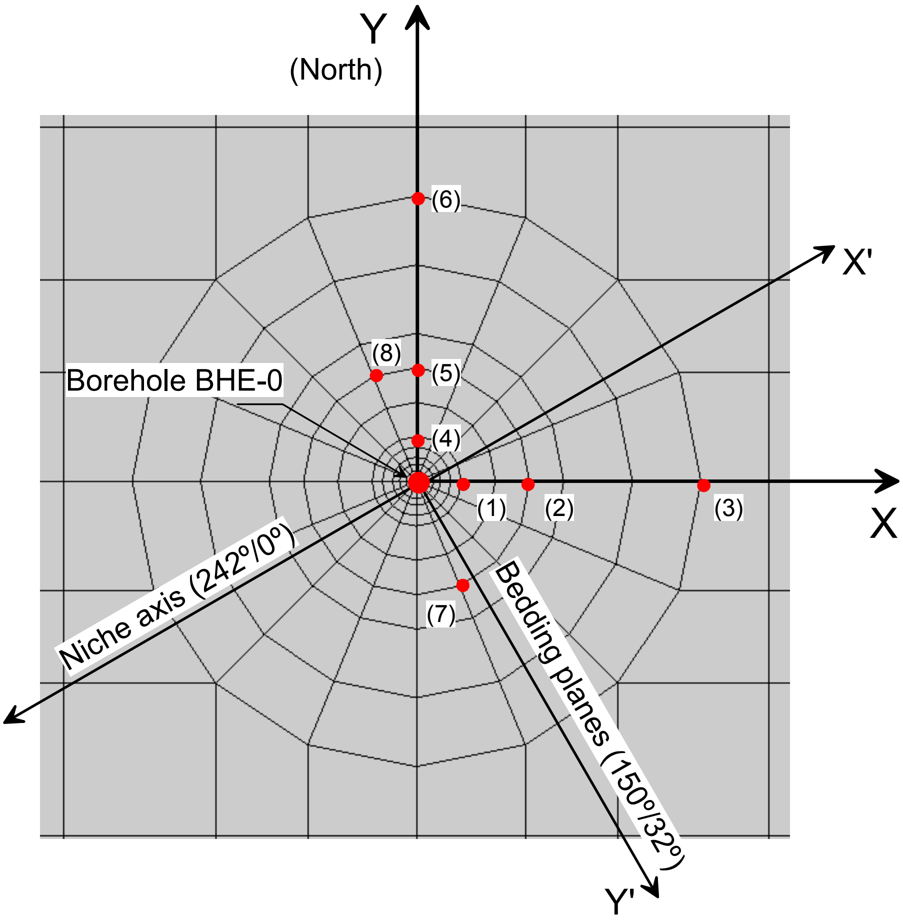

Figure 7.4: Upper view of the finite element mesh of the HE experiment.

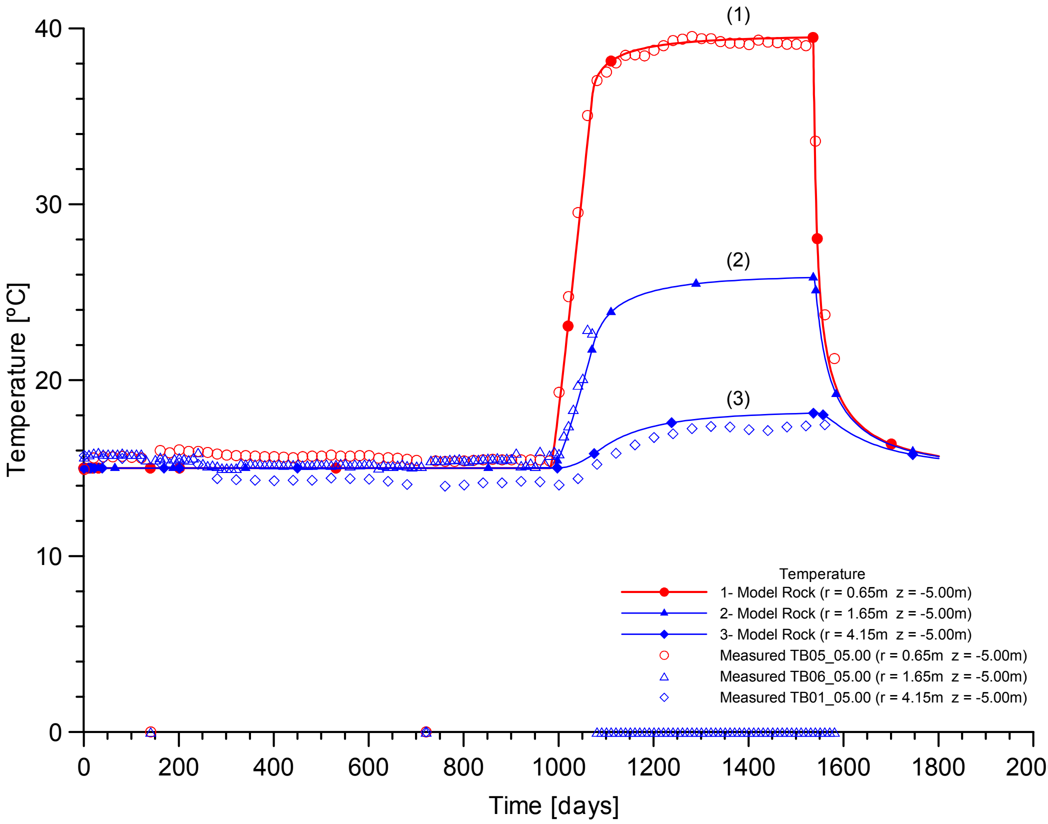

Figure 7.5: Evolution of temperatures with time in points located in the rock during the excavation, hydration, heating and cooling phases.

Figure 7.6: Distribution of temperature field around of the borehole at time 1070 days.

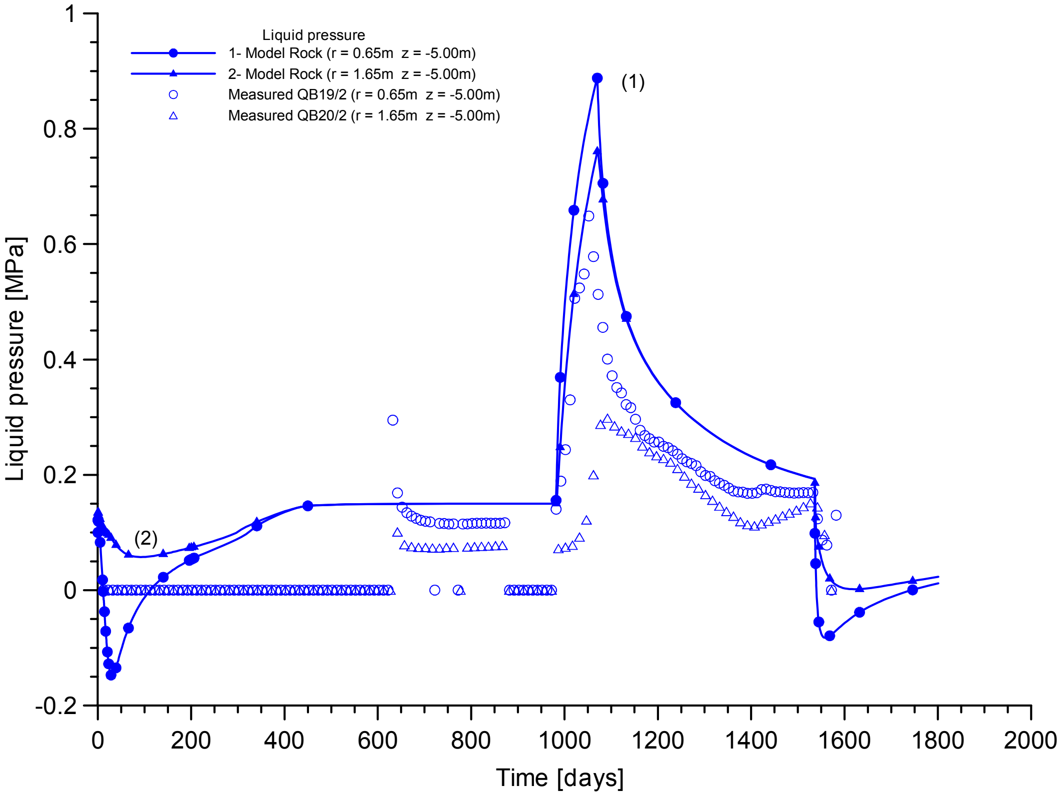

Figure 7.7: Evolution of liquid pressure with time in points located in rock during the excavation, hydration, heating and cooling phase.

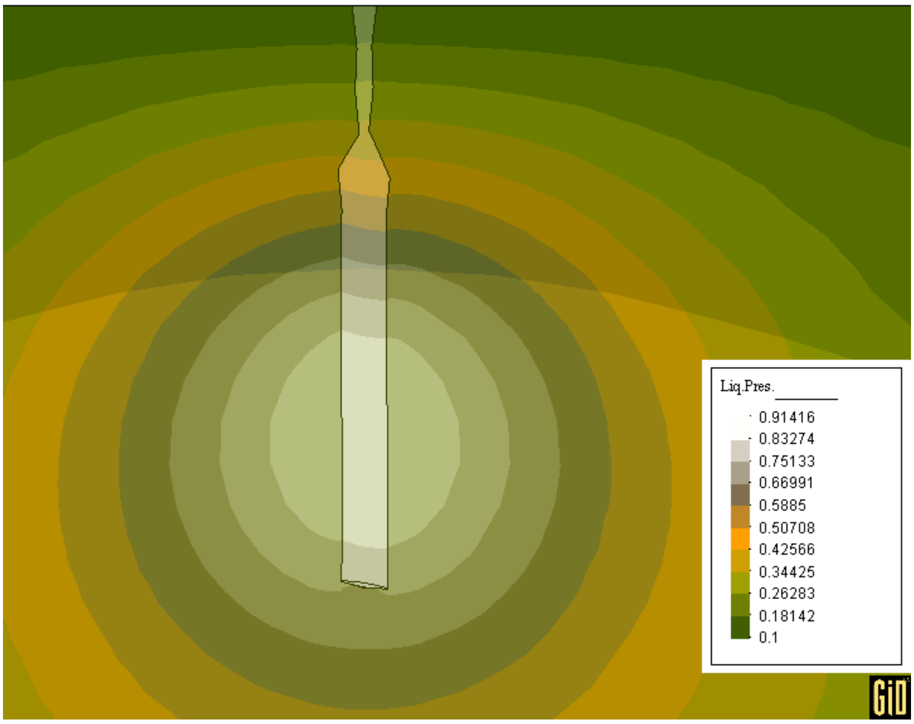

Figure 7.8: Distribution of the liquid pressure around of the borehole at time 1070 days.

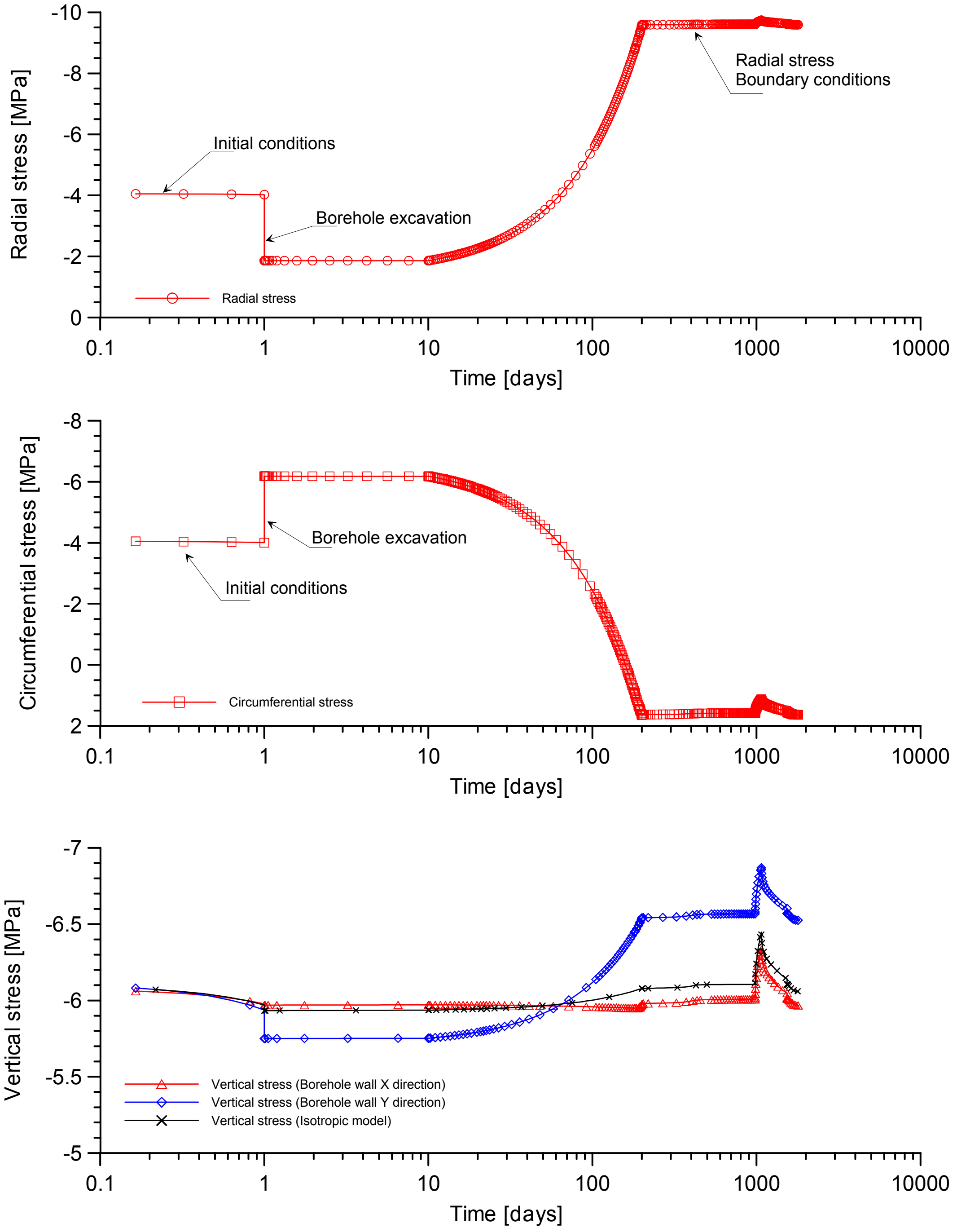

Figure 7.9: Evolution of the stress state on borehole wall. (Upper): Radial stress. (Middle): Circumferential stress. (Bottom): Vertical stress.

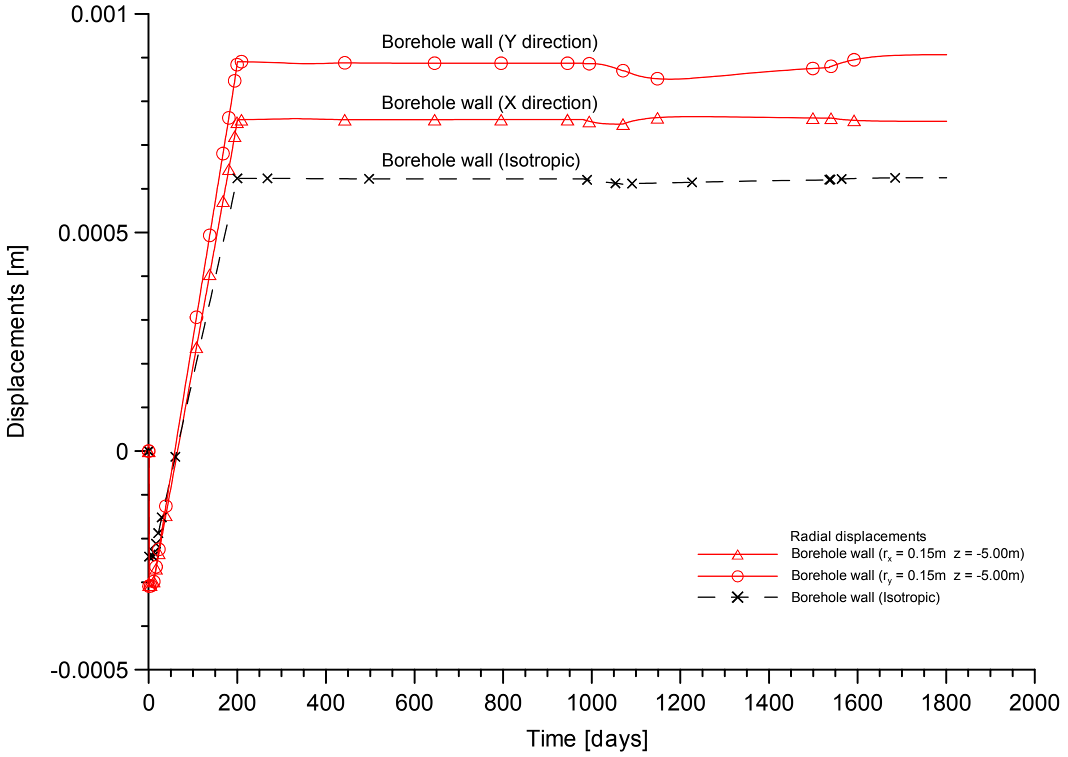

Figure 7.10: Evolution of the calculated radial displacement on the borehole wall during the excavation, hydration, heating and cooling phases.

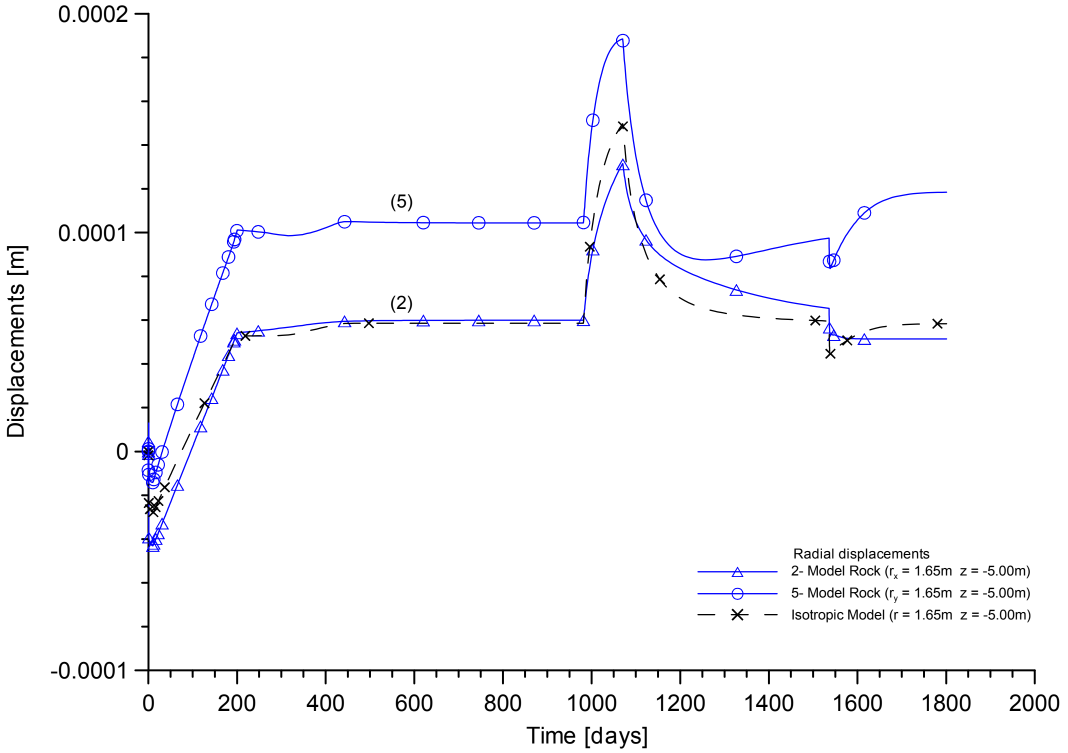

Figure 7.11: Evolution of the calculated radial displacement in points (2) and (5) during the excavation, hydration, heating and cooling phases.

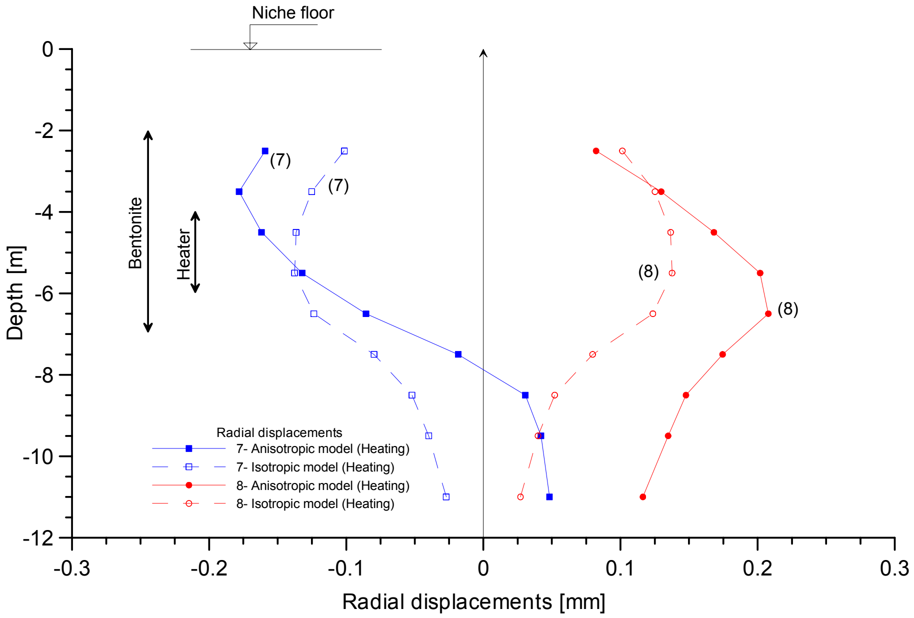

Figure 7.12: Profile of calculated radial displacements versus depth at the end of heating phase (1535 days) in points (7) and (8).

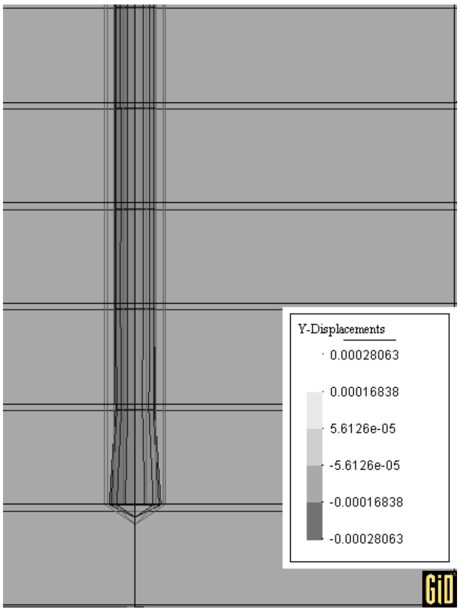

Figure 7.13: Deformation of the borehole at the end of excavation. Isotropic model.

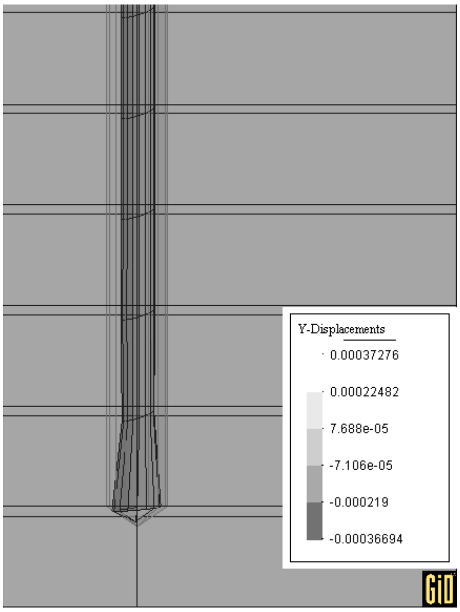

Figure 7.14: Deformation of the borehole at the end of excavation. Anisotropic model.

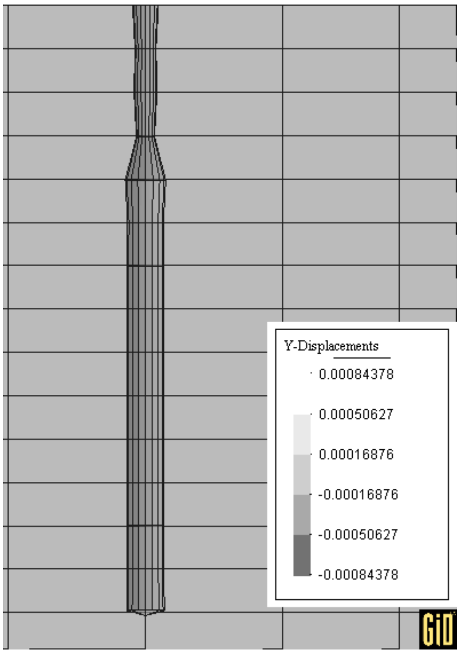

Figure 7.15: Deformation of the borehole after 982 days of hydrations. Isotropic model.

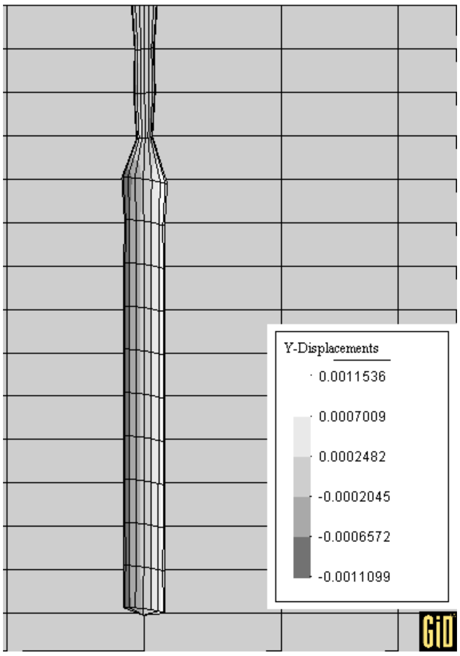

Figure 7.16: Deformation of the borehole after 982 days of hydrations. Anisotropic model.

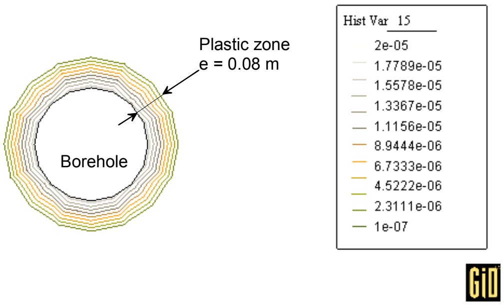

Figure 7.17: Plastic zone developed in a horizontal section at 5.0 m depth. Isotropic model.

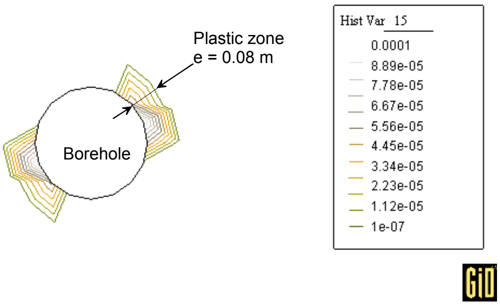

Figure 7.18: Plastic zone developed in a horizontal section at 5.0 m depth. Anisotropic model.

7.3 3D Modelling of VE experiment

The VE project is a ventilation experiment that is being performed at the Mont Terri underground laboratory in an unlined RB micro tunnel, excavated in 1999 in the shaly Opalinus clay formation. The objective of the "VE project" is to evaluate "in situ" the consequences of desaturation in a consolidated clay formation. The design of a radioactive waste repository, in terms of drifts spacing and repository size, depends on the thermal load that the rock and the engineered clay barrier may accept. It depends directly on their degree of saturation. It is, therefore, vitally important from the point of view of repository design optimization, that the desaturation-resaturation times of the rock be assessed, along with their impact on the future resaturation times of the engineered clay barrier. Furthermore, desaturation may give rise to cracking by drying, which would increase the disturbed area by excavation of the drifts (EDZ), resulting in a substantial increase in its hydraulic conductivity.

7.3.1 Drying and wetting influence in hydraulic permeability

A hydraulic model that can explain the drying-wetting effects observed in Opalinus clay rock is presented in this section. Drying and wetting of argillaceous rocks have a strong influence in the mechanical and hydraulic properties. The argillaceous rocks have the propensity of softening when the moisture is available. Also, the moisture of the air can lead to significant changes of properties immediately adjacent zone to underground openings in the argillaceous rock *(Martin & Lanyon (2003)).* Changes in the intrinsic permeability of 2 to 4 order of magnitude in Opalinus clay rock, has been measured with pneumatic test in the immediately adjacent zone of the tunnel wall *(Bossart et al. (2002))*. In these pneumatic tests profiles of permeability along (small diameter) radial boreholes drilled into the EDZ were obtained. This zone extends to a maximum distance of about 1.0 m from the tunnel wall.

Experimental evidences of the changes in the intrinsic permeability with the degree of saturation have been measured by means of gas permeability tests in Opalinus clay rock (Chapter IV). Two simultaneous processes occur during the rock hydration. On the one hand, the reduction of the thickness of fissures occurs when they are hydrated, due to rock's swelling. On the other hand, under saturated conditions a great part of the flow passes through the more permeable planes of discontinuity, whereas under unsaturated conditions these fissures may be dry and the flow fundamentally takes place through the rock matrix.

The cubic law is used to compute the intrinsic permeability, where the joint thickness is computed by means of an exponential function of the degree of saturations. A similar model has been proposed by *Olivella and Gens (2000),* where the intrinsic permeability depends of the macro porosity. The macro porosity is computed by means of an exponential function of the degree of saturation. After that, the intrinsic permeability is computed as a function of the macro porosity by means of Kozeny relationship.

The hydraulic model for argillaceous rocks developed here is presented as follow:

a- The intrinsic permeability is computed by means of cubic law (Eq 7.1):

$$k = \frac{b^3}{12a} \qquad \text{(Eq 7.1)}$$

where b is the joint thickness and a is the gap between joints.

b- The joint thickness b is affected by an exponential function $F_J\left(S_l\right)$ that depends of the degree of saturation (Eq 7.2):

$$b = b_0 \cdot F_J\left(S_l\right) \qquad \text{(Eq 7.2)}$$

where b_0 is the initial joint thickness and $F_J\left(S_l\right)$ is the exponential function that is expressed as follows:

$$F_J = e^{\left(\beta\left(1-S_l\right)\right)} \qquad \text{(Eq 7.3)}$$

where β is a parameter of the model and S_l is the degree of saturation.

7.3.2 Geometry of the VE experiment

The VE experiment was discretized with a 3D finite element mesh of 17472 nodes and 16000 linear quadrilateral prism elements. The domain is 40.00 m in long in X and Z directions, horizontal and vertical respectively. The tunnel has a diameter of 1.30 m and the length of discretization along the Y direction is 10.0 m. The coordinate system has its origin at the center of the tunnel. Figure 7.19 shows an isometric view of the 3D finite element mesh carried out to simulate the VE experiment. Figure 7.20 shows the frontal view of the finite element mesh.

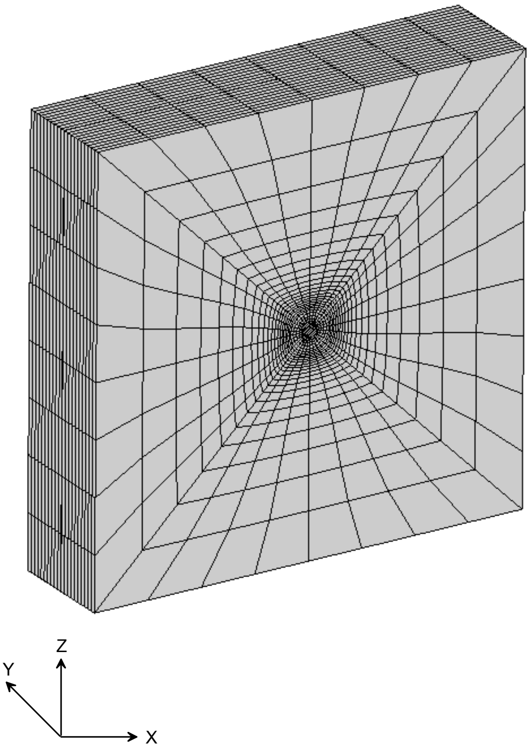

Figure 7.19: 3D mesh carried out for simulate the VE experiment.

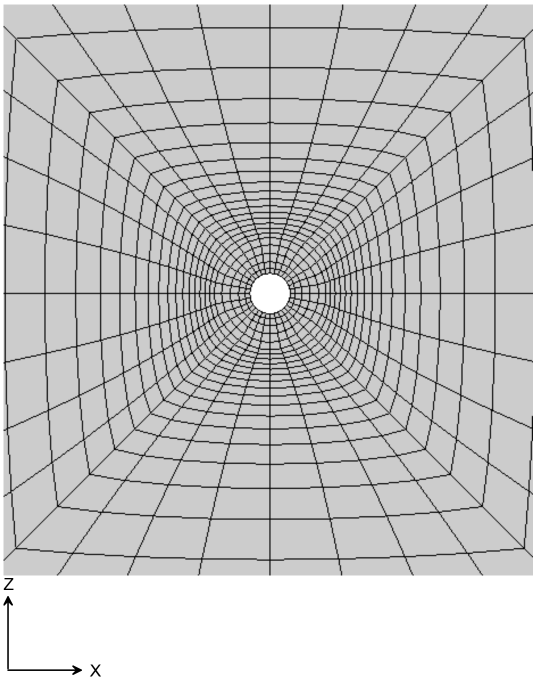

Figure 7.20: Frontal view of the VE numerical simulation.

7.3.3 Initial and boundary conditions

The initial stresses state at the tunnel depth was applied according to in situ stress measurement *(Martin & Lanyon (2003))* as follows: a- vertical stress $\sigma_z = -7.0\ \text{MPa}$, b- horizontal stress in X direction $\sigma_x = -2.0\ \text{MPa}$ and horizontal stress in Y direction $\sigma_y = -4.0\ \text{MPa}$. A hydrostatic pore water pressure distribution was applied, where $P_w = 2.0\ \text{MPa}$ corresponds to the VE tunnel depth. A constant temperature of 15 ºC was considered. The mechanical parameters of the Opalinus clay rock are indicated in Table 7.1 with an angle of strike α = 90 º and dip angle β = 30º *(Nussbaum et al. (2002))*.

The numerical model of the VE experiment covers the following steps *(Mayor et al. (2005))*:

Step 1: A period before forced ventilation of 1470 days was simulated. A boundary condition of RH = 93 %, equivalent to a suction $s = 9.8$ MPa was applied on the wall of the tunnel.

Step 2: The forced ventilation period is divided as follows:

a- 62 days with RH= 96 %, equivalent to a suction $s = 5.5$ MPa. In this period sensors of pore water pressures and displacements were installed.

b- 10 days with RH = 90 %, equivalent to a suction $s = 14.0$ MPa

c- 21 days with RH = 84 %, equivalent to a suction $s = 23.5$ MPa

d- 63 days with RH = 47 %, equivalent to a suction $s = 102.0$ MPa

e- 150 days with RH = 15 %, equivalent to a suction $s = 255.0$ MPa

7.3.4 Analysis of results

Two calculations were carried out with different values of the parameter β in order to consider the influence of the degree of saturation on the hydraulic permeability. The first calculation was performed with β = 0, which means that the joint's thickness is not affected by the degree of saturation. The second run was performed with β = 4; in this case joint's thickness is affected by the degree of saturation.

The pore water pressure distribution at time t = 1775 days of test is shown in Figure 7.21. It corresponds to 245 days of forced ventilation phase, where a suction of 255 MPa was applied in the perimeter of the tunnel. Figure 7.22 shows the distribution of degree of saturation at end of the drying phase. The plastic strain work computed at the end of the drying phase is shown in Figure 7.23. The time evolution of the degree of saturation computed in points located at 315º from the roof of the tunnel (anticlockwise) and at a radial distance of R = 0.65 m (wall of tunnel), R = 1.30 m and R = 1.80 m is shown in Figure 7.24. The time evolution of the intrinsic permeability is shown in Figure 7.24 (Bottom). Figure 7.25 shows the time evolution of the pore water pressure computed in points located at 1.15 m, 2.05 m and 2.60 m depth. A sudden reduction in pore water pressure is computed due to drying effects in the wall of the tunnel when a value of β = 4 is adopted. The locations of the pore water pressure sensors installed in sections SA1, SA2, SA3 and SA4 can be seen in Figure 7.26.

Figure 7.27 shows the comparisons between the pore water pressure measured at 2.10 m depth from the wall of the tunnel and the computed values obtained with $\beta = 0$ and $\beta = 4$. The fall in pore water pressure produced by the forced ventilation phase can not be reproduced with $\beta = 0$, whereas the sudden reduction of pore water pressure is well captured with $\beta = 4$.

The comparison of the profiles of degree of saturation-depth at time 1775 days, computed with $\beta = 0$ and $\beta = 4$ are shown in Figure 7.28 (Upper), whereas the profiles of intrinsic permeability-depth are shown in Figure 7.28 (Bottom). As can be seen in the profiles computed with $\beta = 4$, an unsaturated zone having a thickness of 1.30 m around the tunnel is computed and consequently the intrinsic permeability in the wall of the tunnel increases six order of magnitude.

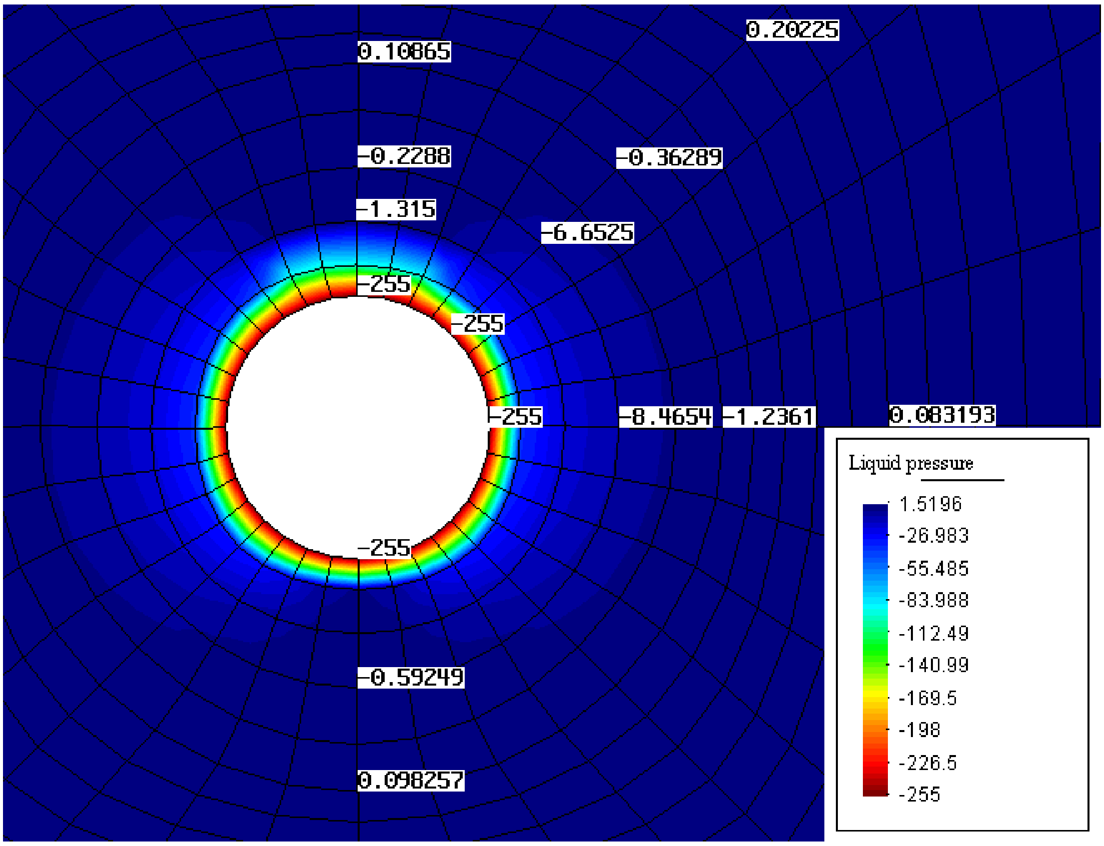

Figure 7.21: Pore water pressure distribution at end of forced ventilation phase, time t = 1775 days.

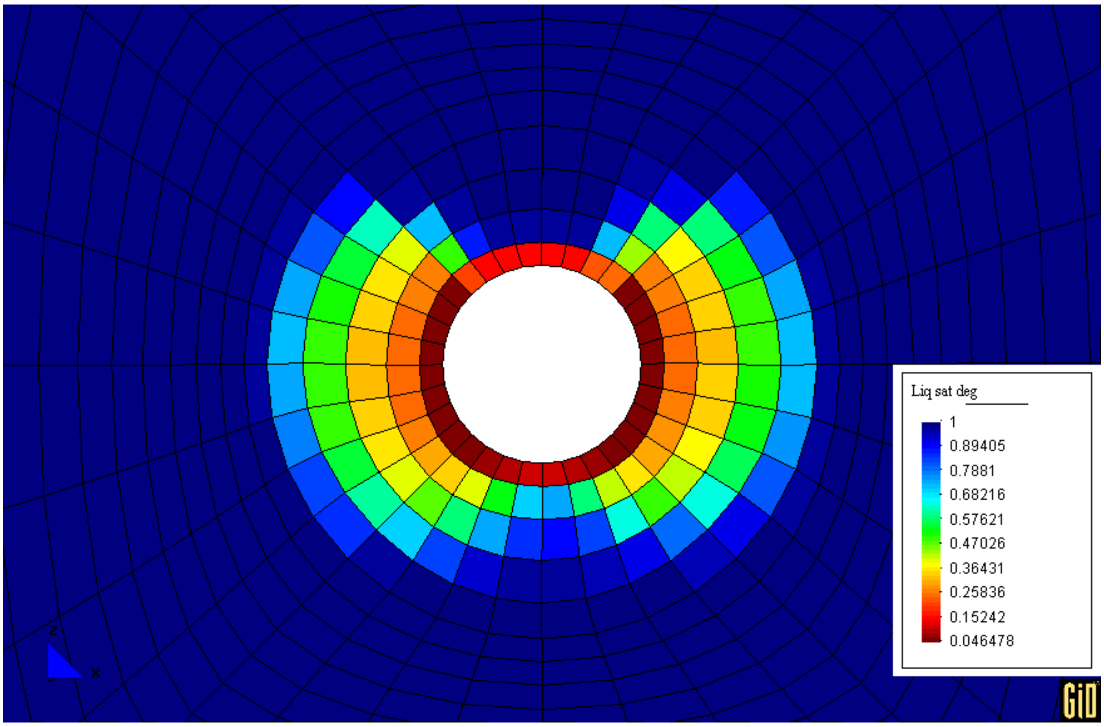

Figure 7.22: Distribution of the degree of saturations at end of the forced ventilation phase, time t = 1775 days.

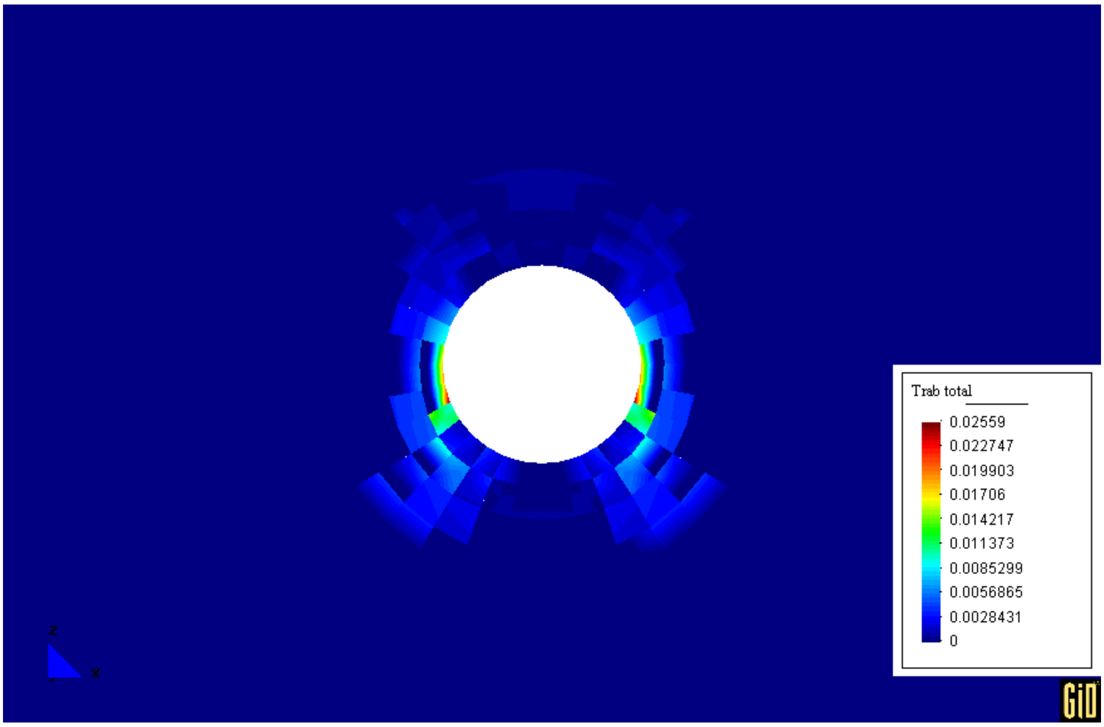

Figure 7.23: Distribution of strain work computed end of forced ventilation phase, time t = 1775 days.

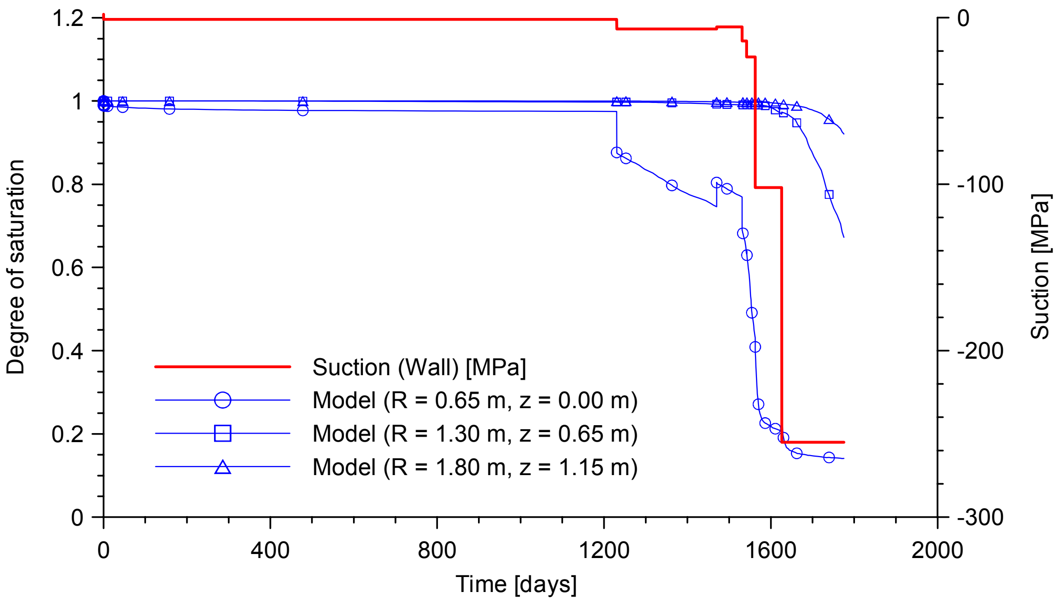

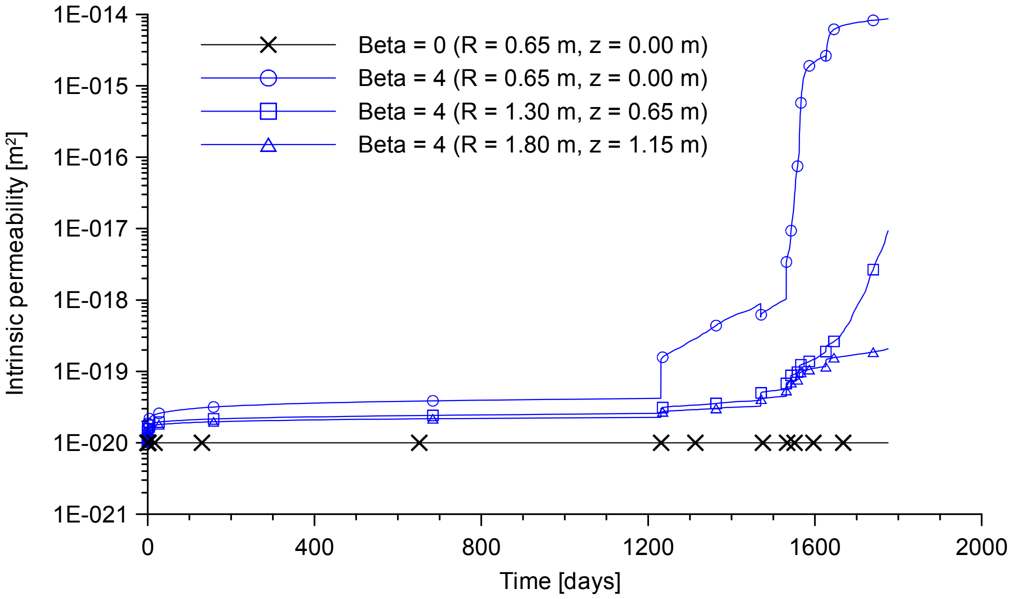

Figure 7.24: (Upper): Time evolution of degree of saturation computed with $\beta = 4$ during all phases of the experiment at radial distances of $R = 0.65$ m (wall of the tunnel), $R = 1.30$ m and $R = 1.80$ m. (Bottom): Time evolution of intrinsic permeability computed with $\beta = 0$ and $\beta = 4$.

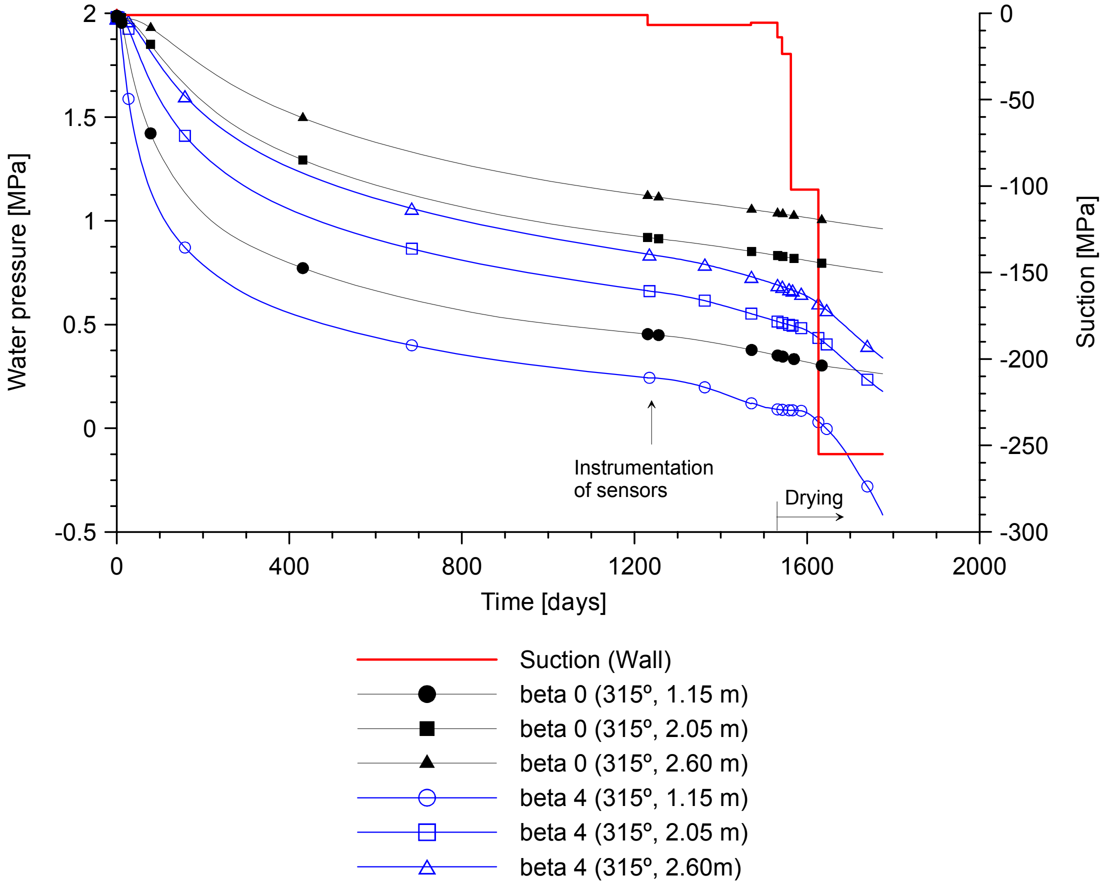

Figure 7.25: Time evolution of pore water pressure computed during all phases of the experiment at 1.15 m, 2.05 m and 2.60 m depth. Computed values with $\beta = 0$ and $\beta = 4$.

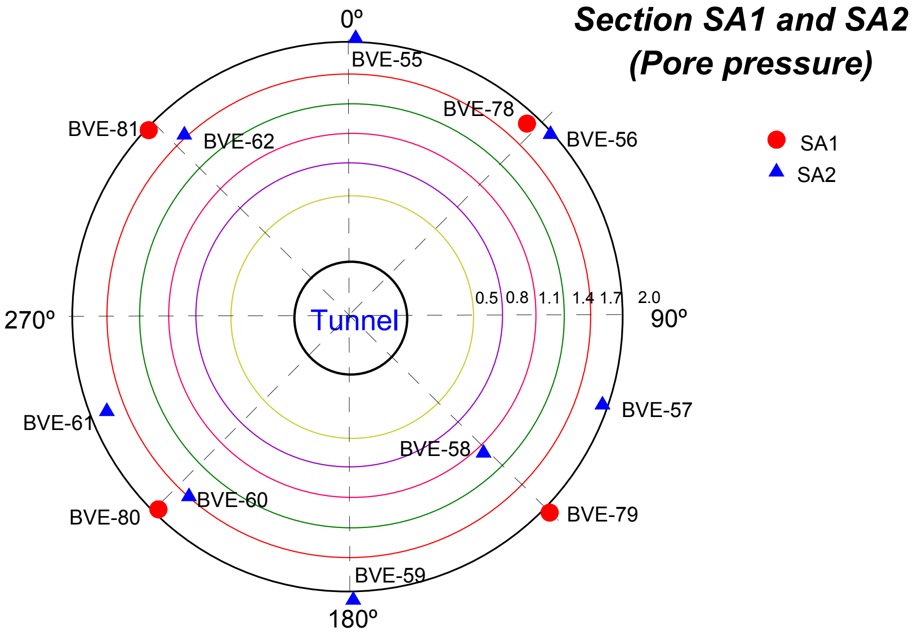

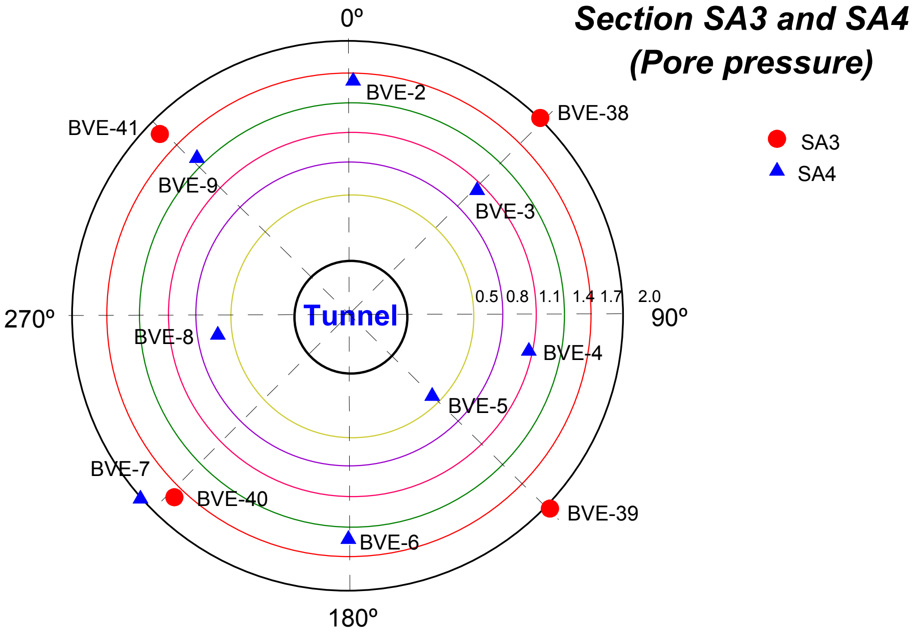

Figure 7.26: Pore water pressure sensors locations in the sections SA1, SA2, SA3 and SA4.

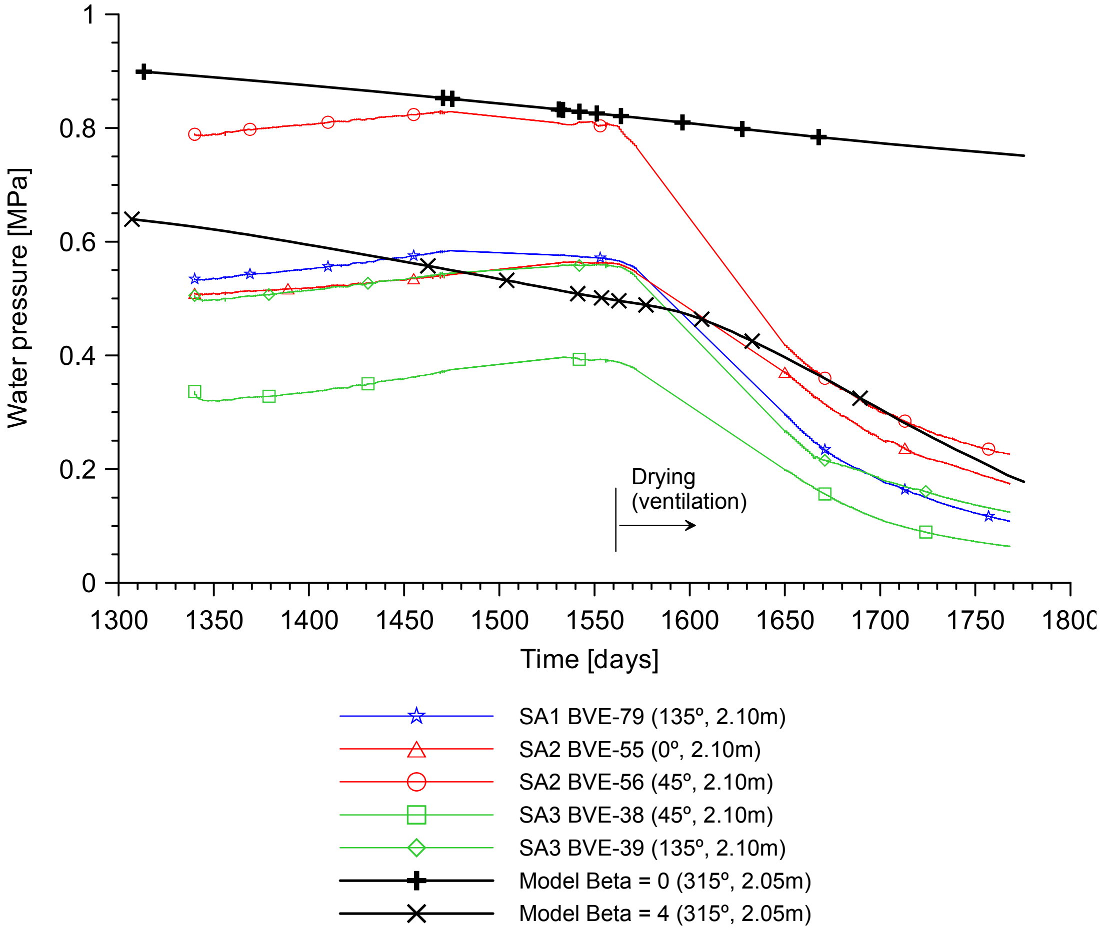

Figure 7.27: Time evolution of pore water pressure measured at 2.10 m depth during the drying phase. Computed values with $\beta = 0$ and $\beta = 4$.

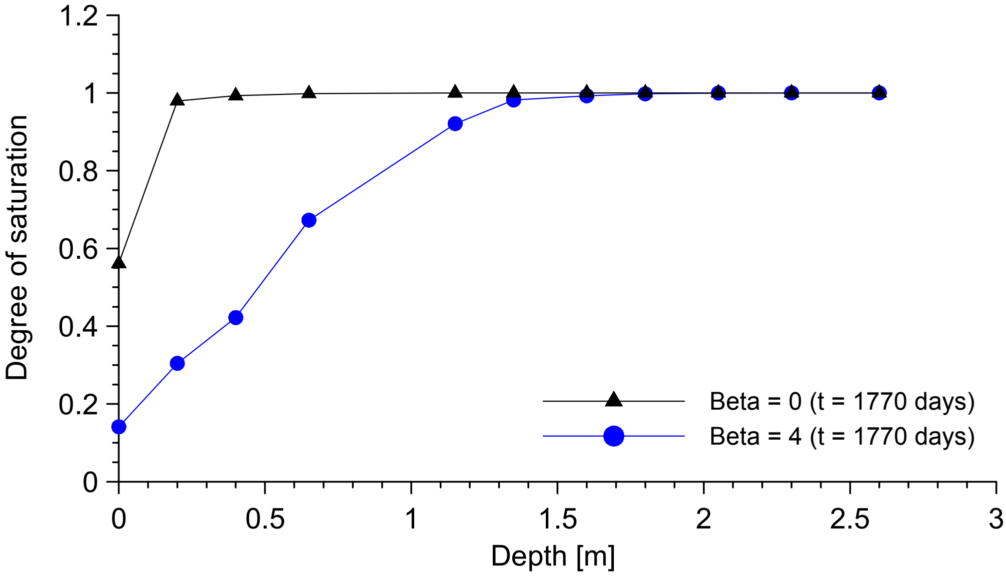

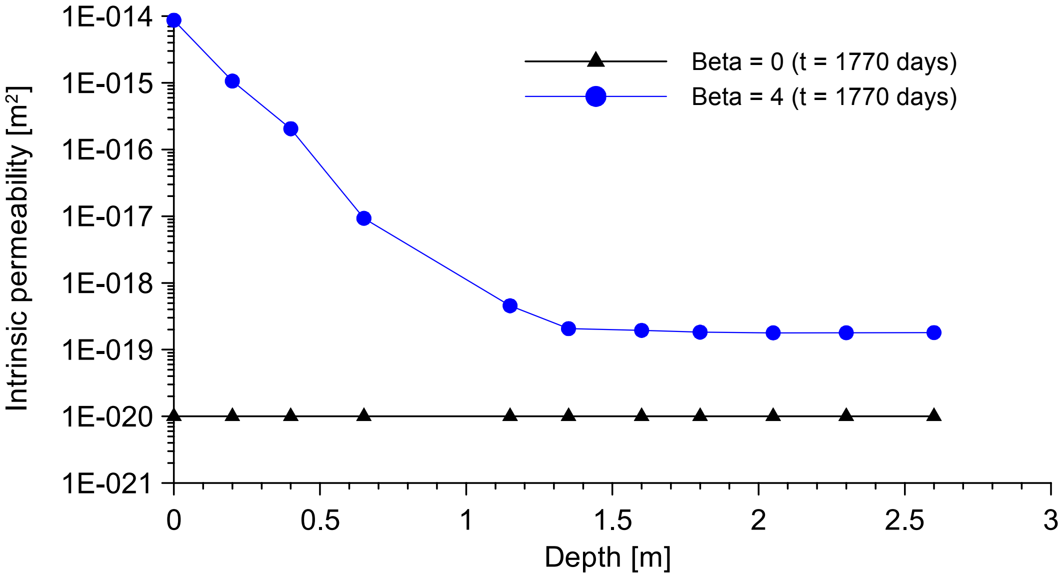

Figure 7.28: (Upper): Profile of degree of saturation- depth computed in drying phase with $\beta = 0$ and $\beta = 4$. (Bottom): profile of intrinsic permeability-depth computed in drying phase.

CHAPTER VIII

SUMMARY, CONCLUSIONS AND FUTURE RESEARCH WORKS

8.1 Summary and Conclusions

As a summary of the work performed, concerning rock characterization, experimental results and numerical results, the following conclusions are advanced:

8.1.1 Rock laboratory characterization

Opalinus clay rock has been extensively characterized by means of laboratory tests at both micro-structural and macro-structural scale. From the macro-structural point of view, the water retention properties, the hydraulic conductivity and the behaviour under uniaxial compression conditions have been carried out.

The water retention curve allowing volume change of specimens, was determined by means of vapor equilibrium technique following drying and wetting paths. The volumetric strain due to suction was measured in the specimens. The water retention curve under isochoric conditions was determined following the drying paths. This test was carried out applying the axis translation technique for a range of suctions ranging from 0 to 3 MPa and vapor equilibrium technique for suction values between 3 and 83 MPa. The saturated hydraulic conductivity was determined by means of direct measurements in infiltration test. The infiltration tests were carried out in a permeameter specially designed for this test. The unsaturated permeability of the rock was determined indirectly by back-analysis of the infiltration tests and of a drying test. Back-analysis was performed by means of a 1D numerical model using the computer program CODE_BRIGHT. A relevant aspect in the hydraulic permeability is the presence of micro-fissures in the rock. The aperture of the micro-fissures is strongly dependent of the degree of saturations. Under unsaturated conditions a great part of the flow passes through the more permeable planes of discontinuity. On the other hand, near saturated conditions these fissures may be closed due to rock swelling and the flow fundamentally takes place through the rock matrix. The micro-structural analysis focused in X-ray diffraction, mercury intrusion porosimeter (MIP) and scanning electron microscopy (SEM) technique. A qualitative characterization of the mineralogical composition of Opalinus Clay rock has been performed by means of X-ray diffraction using a powdered sample. Clay minerals, such as kaolinite, illite and chlorite, presented an intermediate intensity. A mono-modal pore size distribution (PSD) of rock was determined by means of MIP. From the (PSD) the water retention curve, the saturated hydraulic permeability and relative permeability were computed. These computed values are consistent with the direct measurements. Direct observations of the rock fabric were carried out by means of SEM. The pore size observed in the photomicrographs varies between 5 and 15 μm, which corresponds to the macro-porosity determined in MIP. The size of the clay aggregates observed is about 32 μm.

8.1.2 Coupled THM behaviour

The coupled THM behaviour of the rock has been widely analyzed in both in-situ and laboratory tests. Concerning the in situ test, the analysis was directed to the interaction between the bentonite buffer and host rock in the near field. The numerical simulation of the in-situ experiment, using CODE_BRIGHT has been an important tool for the interpretation of the experiment. All phases of the experiment were simulated using the constitutive model of *Vaunat and Gens, (2003)*. The excavation phases, (HE niche excavation and drilling the borehole BHE-0) were carried out in order to obtain a suitable stress state, pore water pressures and temperatures values in the near field of the experiment. Once this is established, the numerical simulation covers the bentonite buffer emplacement, bentonite buffer hydration phase, heating phase and cooling phase. The high initial suction of bentonite (136 MPa) produces a transitory process of desaturation in a rock annulus of 0.7 m thickness approximately. A subsequent resaturation in the surrounding rock follows this stage. The rock reaches the full saturation after 250 days of hydration approximately. The high swelling pressures of bentonite produce changes in the stress state of the surrounding rock during the hydration phase. The significant change of the stress state extends to a maximum distance of 1.0 m. Plastic strains were computed in a narrow annulus of rock of 0.05 m thickness. The time evolution of temperature and the distribution of temperature as a function of distance for different times during the heating phase were computed and compared with in-situ data. Temperature increments generate significant positive water pressures. The computed and measured values of temperature and pore water pressure increments are well captured by the model. Pore water pressure dissipation occurs and they tend towards the initial condition when the rate of heating tend to 0. Plastic strains induced by temperature increments were computed in the rock. The temperature decreases quickly when the power was removed. After 25 days of cooling the temperature drops to lees than 25º C in the whole area of influence of the test. The pore water pressure decreases suddenly with the drop of temperature. The computed transitory stress changes lead to a radial displacement towards the heater (unloading effect). Long term, steady state stresses do not seem to be affected by the heating and cooling phases except for a narrow zone immediate to the bentonite buffer.

Regarding laboratory tests, the coupled THM behaviour of the rock has been measured by means of a pulse heating test. An isochoric thermo-hydraulic cell was specially designed and developed to measure the time evolution of temperature and pores water pressure developed during the heating of the rock. In this cell gas permeability tests in both unsaturated and saturated conditions, saturated hydraulic permeability test and pulse heating tests in undrained and drained conditions were carried out. Gas permeability values of k_g = 8.07E-14 m^2 and k_g = 2.62E-17 m^2 were measured in both unsaturated (S_l = 0.85) and saturated conditions, respectively. The large difference between unsaturated and saturated gas permeability of the rock may be due to a change in macro porosity induced by drying. Two simultaneous processes occur during the rock hydration. The first process is the reduction of the thickness of fissures that occurs when the rock is hydrated, due to rock's swelling. On the other hand, under saturated conditions a great part of the flow passes through the more permeable planes of discontinuity, whereas under unsaturated conditions these fissures may be dry and the flow fundamentally takes place through the rock matrix. Although the rock's matrix is more impermeable, it has a greater capacity of water retention. Only when the rock is practically saturated, the water occupies the discontinuities and the permeability increase abruptly. The intrinsic permeability of the rock depends of the fractures thickness, which is dependent of the degree of saturation and the confinement conditions. Saturated hydraulic permeability (K_{sat} = 1.04E-12 m/s) was determined by direct measurement of water inflow. A swelling pressure of 2.0 MPa was measured suddenly at the beginning of the rock hydration. After that, the swelling pressure increases continuously with time up to a value of 3.0 MPa. An irreversible process in pore water pressure evolution was observed at the heating tests in drained conditions. A sudden pore water pressure increment was measured (Heating test A, C and D). A subsequent dissipation occurs when the rate of heating is lower than 0.05 ºC/min. A sudden decrease of pore water pressure and negative values were measured after cooling. Knowing the rock volumetric strain ε_v measured in drained heating test, a volumetric thermal expansion of the rock of $\alpha_{rock} = 1.17E\text{-}05\ ºC^{-1}$ was determined using the total volume of drained pore water. On the other hand, a reversible process in pore water pressure evolution was observed under undrained conditions. Pore water pressure dissipation was not recorded. A rapid pore water pressure reduction occurs and positive values were recorded at the cooling phase. The coupled THM behaviour observed in laboratory drained heating test is consistent with the in situ measurements.

The hydration phase, and the drained and undrained pulse heating tests have been simulated by means of CODE_BRIGHT. Analyses of sensitivity of three different parameters namely, intrinsic permeability (k_w), saturated thermal conductivity (λ_{sat}) and thermal coefficient expansion (β_s) have been carried out in order to reproduce all processes. All process are well captured by the numerical simulations with the following set of parameters $k_w = 2.5E\text{-}20\ m^2$, $\lambda_{sat} = 2.5\ W\ m^{-1}K^{-1}$, and $\beta_s = 1.0E\text{-}05\ ºC^{-1}$.

The pore water pressure increments are induced by the thermal expansion of the water, because the coefficient of thermal expansion of water is higher than the thermal expansion coefficient of the solid skeleton. The magnitude of the increments of pore water pressures is mainly controlled by the rate of temperature increase, the rock permeability, thermal conductivity, thermal expansion coefficient, rock porosity, the rock stiffness and geometry and boundary conditions of the experiment. The increment in pore water pressure due to heating may induce the rock fracture. On the other hand, a rapid cooling may induce a transient increase of suction. The permeability of porous media of extremely low hydraulic conductivity (1.0E-12 to 1.0E-14), as argillaceous formations, can be determined by means of pulse heating test.

Rock degradation has been measured in the laboratory by means of a thermal expansion test of rock (non-isochoric conditions) where non-linear and irreversible strains were measured in successive heating-cooling cycles. Rock degradation can be interpreted as an increment of the rock permeability. As a consequence of rock degradation a decrease in pore water pressure increments was measured in successive cycles of heating-cooling carried out with the same power input as in isochoric conditions.

8.1.3 Anisotropic constitutive modelling

A constitutive model to consider the anisotropic and quasi brittle behaviour of the argillaceous rocks has been developed. The model has been formulated within a viscoplastic framework and it takes into account the anisotropic strength and deformability of both matrix and joints. A non associated flow rule was adopted. Model integration was written in a Fortran subroutine and introduced in CODE_BRIGHT. The failure criterion of both matrix and joints are defined by means of hyperbolic yield surfaces in p-J and τ-σ spaces, respectively. The yield surfaces of the matrix and joint depends of three parameters: tensile strength (χ), cohesion (c) and friction angle (ϕ). The yield surfaces are rounded in both meridional and octahedral planes, being these continuous and differentiable for all stress state. The quasi brittle behaviour of argillaceous rock is simulated by means of isotropic and kinematic softening controlled by plastic work.

The constitutive model was calibrated by means of a 3D numerical simulation of a set of laboratory triaxial tests performed in Opalinus Clay specimens having different angles of dip. The quasi brittle failure and variation of strength with different angle of dip are well captured by the model. The anisotropic constitutive model has been applied in a 3D numerical simulation of the HE experiment. The time evolution of temperatures and pore water pressure are well captured by the model. A comparison between isotropic and anisotropic modeling was carried out in order to analyze the stress and displacements in the near field. Regarding the evolution of stress, displacements and plastic zones developed in the near field, large differences were found between the isotropic and the anisotropic model.

8.1.4 Drying and wetting effects in argillaceous rock

A hydraulic model has been developed to reproduce the significant changes of hydraulic permeability in the rock immediately adjacent to an underground opening in argillaceous rock. Changes in intrinsic permeability of 2 to 4 order of magnitude in Opalinus clay have been measured in the "in-situ" test in the adjacent zone of the tunnel wall subjected to drying effects (atmospheric conditions). Changes of 3 orders of magnitude in gas permeability, when the degree of saturation changes from $S_l = 0.85$ to $S_l = 1$ were also measured in laboratory test. The intrinsic permeability is computed by means of a cubic law, where the joint thickness of the rock is controlled by an exponential function of the degree of saturation. The ventilation experiment (VE) carried out in an unlined micro tunnel was simulated under 3D conditions. A drop in pore water pressure was measured at 2.10 m depth during the forced ventilation phase. The fall of pore water pressure is well captured by the model. An unsaturated zone, 1.30 m deep, around the tunnel was computed. A change of intrinsic permeability about six orders of magnitude was computed on the wall of the tunnel.

8.2 Futures research

The following aspects would improve the current state of the art in THM modelling of argillaceous rocks such as clay shales:

- Evaluation of the hydraulic conductivity considering different families of discontinuities.

- Investigation of macro structure changes of the rock induced by saturation. This could be evaluated by means of ESEM having control of relative humidity and by means of mercury intrusion porosimetry (MIP).

- In order to consider the changes of water permeability due to changes of saturation and confining stresses, it could be possible to consider the rock as a double structure material (discontinuities and matrix). A first step is the determination of the water retention curve of the two structural levels. The second step is the analysis of changes of the water retention curves of both joints and matrix induced by changes in stresses.

- An alternative procedure to measure the effects of the saturation and confinement stresses on rock permeability is to determine the gas permeability for different degrees of saturation. Samples subjected to a given confinement stress in a triaxial cell (say 1.0 to 3.0 MPa) under controlled degree of saturation for example (Sr = 40%, 60%, 80% and 95%) by means of the vapour equilibrium technique could be used to measure the gas permeability of the rock.

- The next improvement of the developed anisotropic model is to couple it with the effect of suction.

- A more sophisticated model to be developed would integrate an anisotropic mechanical constitutive model of double structure and a hydraulic model that would take into account changes in joint thickness with suction changes.

CHAPTER IX

REFERENCES

Abbo A.J, Sloan S.W., 1993. “A smooth hyperbolic approximation to the Mohr-Coulomb yield criterion” University of Newcastle.

Airo C., Umilta G., Valore C., 2000. “Foundation settlements of two embankments dams founded on scaly cáliz” Proc. 2nd Int. Symp. The geotechnics of hard soils – soft rocks, Evangelista & Picarelli (Eds.), Balkema, Rotterdam, pp. 1607-1612

Alonso E.E., Gens A., Josa A., 1990. “A constitutive model for partially saturated soils” Geotechnique 40, Nº 3, pp. 405 - 430

Alonso E.E., Gens A., Lloret A., 1991. “Double structure model for the prediction of long-term movements in expansive materials” Computer Methods and Advances in Geomechanics, Beer, Booker, Carter, (Eds.), Balkema, pp. 541-548

Alonso E.E., Gens A., Vaunat, J., 1998. “Yield and irreversible behaviour in expansive soil” Proceedings of the 5th International Workshop on Key issues in Waste Isolation Research, 2-4 December, Barcelona, Spain.

Alonso E.E., Alcoverro J., 1999. “CATSIUS CLAY Project: Calculations and testing of behaviour of unsaturated clay as barrier in radioactive waste repositories. Stage 2: Validation exercises at laboratory scale” Technical publication Nº 11/99 ENRESA, Spain.

Alonso E.E., Vaunat J., Gens A., 1999. “Modelling the mechanical behaviour of expansive clays” Engineering Geology, Vol. 54, Nº 1-2, pp. 173-183.

Alonso, E.E., 2000. “General report: cutting and natural slopes” The geotechnics of hard soils – soft rock, Evangelista & Picarelli (Eds.), Balkema, Rotterdam, pp 1557-1587

Alonso E.E., Vaunat J., 2001. "An appraisal of structure level interactions in expansive soils" Fernandes et al. (Eds.), Applications of Computational Mechanics in Geotechnical Engineering, Balkema, pp. 17-30

Alonso E.E., Alcoverro J., 2004. "Swelling and Degradation of Argillaceous Rocks" Keynote lecture, Proc. 3rd Int. Unsaturated soils. Recife, Brazil. Balkema, pp 951-969.

Alonso E.E., Alcoverro J., 2005. "The FEBEX Test as a benchmark case for THM modelling. Historical perspective and lessons learned" Proceedings of the international symposium on large scale field tests in granite. Sitges, Barcelona, Spain, 12 – 14th November 2003. Alonso & Ledesma (Eds.), Balkema, Leiden, The Netherlands. pp 3-19

Astudillo Pastor J., 2001. "El almacenamiento geológico profundo de los residuos radiactivos de alta actividad. Principios básicos y tecnología". ENRESA

Baldi G., Hueckel T., Peano A., Pellegrini R., 1991. "Developments in modelling of thermo-hydro-geomechanical behaviour of Boom clay and clay-based buffer materials" Nuclear science and technology, Vol. 1 & 2

Bear J., 1979. "Dynamic of fluid in porous media" American Elsevier.

Bear J., Bensabat J., Nir A., 1991. "Heat and mass transfer in unsaturated porous media at a hot boundary: I. One –dimensional analytical model" Transport in Porous Media, Vol. 6, pp. 281-298

Bock K., 2001. "Rock Mechanics Analyses and Synthesis: RA Experiment. Rock Mechanics Analyses and Synthesis: Data Report on Rock Mechanics" Mont Terri Technical Report 2000-02. Q+S Consult

Booker J.R., Savvidou C., 1985. "Consolidation around a point heat source" Int. Journal for Numerical and Analytical Methods in Geomechanics, Vol. 9, pp 173-184

Bossart P., Meier P., Moeri A., Trick T., Mayor J., 2002. "Geological and hydraulic characterization of the excavation disturbed zone in the Opalinus Clay of the Mont Terri Rock Laboratory" Engineering Geology, Vol. 66, pp. 19-38

Burland J.B., 1990. "On the compressibility and shear strength of natural clays" Geotechnique 40, Nº 3, pp. 329-378

Carol I., Pratt P., 1990. "A statically constrained microplane model for the smeared analysis of concrete cracking" Bicanic N. and Mang H., (Eds.), Pineridge Press

Computer aided analysis and design of concrete structures, 2, Zell-am-See, Austria, pp. 919-930.

Carol I., Rizzi E. & Willam K. 2001. "On the formulation of anisotropic elastic degradation. 1. Theory based on a pseudo-logarithmic damage tensor rate" Int. Journal Solids Structures, 38: 491-518.

CODE_BRIGHT user's guide, 2004. Departamento de Ingeniería del Terreno. E.T.S. Ingenieros de Caminos, Canales y Puertos de Barcelona. Universidad Politécnica de Cataluña.

Croisé, J., Klubertanz G., 2002. "Conceptual model" VE Experiment Project, Deliverable D1b, COLENCO.

Delage, P., Howat, M.D., Cui, Y.J., 1998. "The relationship between suction and swelling properties in a heavily compacted unsaturated clay" Engineering Geology, 50, pp. 31-48

Delage, P., Sultan, N., Cui, Y.J., 2000. "On the thermal consolidations of Boom clay" Canadian Geotechnical Journal, 37, pp. 343-354

Del Olmo C., Fioravante V., Gera F., Hueckel T., Mayor J.C., Pellegrini R., 1996. "Thermo - mechanical properties of Deep Argillaceous Formations" Engineering Geology, 41, pp. 87-102

Dimos A., 1991. "Measurement of soil suction using transistor psychrometer" Internal Report IR/91-3, Special Research Section, Materials Technology Department, Vic Roads

FEBEX Project, (2000). "Full-scale engineered barriers experiment for a deep geological repository for high level radioactive waste in crystalline host rock". Final project report. EUR 19612 EN, European Commission, Brussels.

Floría E., Sanz F. J. and García-Siñeriz J. L., 2002. "Drying test: evaporation rate from core samples of "Opalinus Clay" under controlled environmental conditions" Ventilation experiment VE, Project Deliverable 6, AITEMIN, January of 2002.

Forlati F., Lancellota R., Scavia C., Simeoni L., 1998. "Swelling processes in sliding marly layers in the Langhe region, Italy" Proc. 2nd Int. Symp. The geotechnics of hard soils – soft rocks, Evangelista & Picarelli (Eds.), Balkema, Rotterdam, pp. 1089-1099

Fuentes-Castillana J.L., García-Siñeriz J.L., Tuñón S., 2001. "Mont Terri – Heating Experiment (HE): As- built" Mont Terri Technical Report, Aitemin.

Fuentes-Cantillana J.L., 2005. "The FEBEX In situ test: lessons learned on the engineering aspects of horizontal buffer construction and canister emplacement" Proceedings of the international symposium on large scale field tests in granite. Sitges, Barcelona, Spain, 12 – 14th November 2003. Alonso & Ledesma (Eds.), Balkema, Leiden, The Netherlands. pp 61-70

García-Siñeriz J.L., Rey M., 1999-2004. "Sensor Data Reports Nº 1 through Nº D2/5: Heating Experiment (HE)" Mont Terri Technical Report, Aitemin.

Gatmiri B., Delage P., 1997. "A Formulation of Fully Coupled Thermal-Hydraulic-Mechanical Behaviour of Saturated Porous Media - Numerical Approach" Int. Journal for Numerical and Analytical Methods in Geomechanics, Vol. 21, pp. 199-225

Gens A.; Carol I.; Alonso E.E., 1990. "Constitutive model for rock joints formulation and numerical implementation" Computers and Geotechnics, Vol. 9, Nº 1-2, pp. 3-20

Gens A., Alonso E.E., 1992. "A framework for the behaviour of unsaturated expansive clays" Canadian Geotechnical Journal, Vol. 29, pp. 1013-1032

Gens A., Alonso E.E., Lloret A., Batlle F., 1993. "Prediction of long term swelling of expansive soft rock: a double-structure approach" Proceeding Int. Symposium Geotechnical engineering of hard soils – soft rocks, Anagnostopoulos et al. (Eds.), Balkema, Rotterdam, pp. 495-500

Gens A., 1995. "Constitutive laws" In Gens A., Jouanna P. & Schrefler B. (Eds): Modern issues in non-saturated soils, Springer-Verlag.

Gens A., García-Molina A.J., Olivella S., Alonso E.E., Huertas F., 1998. "Analysis of a full scale in situ test simulating repository conditions" Int. Journal of Numerical and Analytical Methods in Geomechanics, Vol. 22, pp. 515-548

Gens A., Alonso E.E., Vaunat J., 1999. "Double structure model for expansive clays" Proceedings of the 7th International Symposium on Plasticity and its Current Applications, Khan, A.S., (Eds.), Neat Press, Cancún, México, 5-13 January 1999, pp. 565-568

Gens A., Nova R., 1993. "Conceptual bases for a constitutive model for bonded soils and weak rocks" Proc. Int. Symp. Geotechnical engineering of hard soils – soft rocks, Anagnostopoulos et al. (Eds.), Balkema, Rotterdam, pp. 485-494

Gens A., Olivella S., 2001. "THM phenomena in saturated and unsaturated porous media, Fundamentals and formulation" Revue française de genie civil, Environmental Geomechanics, Charlier R., and Gens A., (Eds.), Hermès Science Publications, Vol. 5 – nº 6/2001, pp. 693-717

Hohner M., Bossart P., 1998. "Geological, mineralogical, geochemical, geomechanical and hydraulic parameters of Opalinus Clay derived by in-situ and laboratory experiments" Mont Terri Technical Note 98-49, Uni Barcelona & Geotechnical Institute Ltd.

Horseman S.T., McEwen T.J., 1996. "Thermal constraints on disposal of heat-emitting wate in argillaceous rocks" Engineering geology, 41, pp. 5-16

Hueckel T., Pellegrini R., Del Olmo C., 1998. "Constitutive study of thermo-elasto-plasticity of deep carbonatic clays" Int. Journal of Numerical Analytical Methods in Geomechanics, Vol. 22, pp. 549-574

Hueckel T., Loret B., Gajo A., 2001. "Swelling clays as reactive deformable two phase materials: basic concepts and options" Workshop on Clay behaviour: Chemo-mechanical coupling, Maratea.

Huertas F., Fuentes-Cantillana J.L., Julien F., Rivas P., Linares J., Fariña P., Ghoreychi M., Jockwer N., Kickmaier W., Martinez M.A., Samper J., Alonso E. and Elorza F.J., 2000. "Full-scale engineered barriers experiment for a deep geological repository for high-level radioactive waste in crystalline host rock (FEBEX project)" European Commission EUR 19147. Luxembourg.

Janssen L.G.J., Prij J., Kevenaar J.W.A.M., Jong C.J.T., Klok J., Beemsterboer C., 1984. "The thermo-mechanical behaviour of a salt dome with a heat-generating waste repository" Final report, Nuclear science and technology.

Kavvadas M.J., 2000. "General report: Modelling de soil behaviour – selection of soil parameters" Proc. 2nd Int. Symp. The geotechnics of hard soils – soft rocks, Evangelista & Picarelli (Eds.), Balkema, Rotterdam, pp. 1441-1481

Keusen H.R., Gauguin J., Schuler P., Buletti M., 1989. "Grimsel Test Site" Geology, Technical Report 87-14E, Nagra

Leroueil S., Vaughan P.R., 1990. "The general and congruent effects of structure in natural soils and weak rocks" Geotechnique 40, Nº 3, pp. 467-488

Lloret A., Villar M.V., Pintado X., 2002. "Ensayos THM: Informe de síntesis, FEBEX project". Informe 70-UPC-M-0-04. CIEMAT/DIAE/54520/1/02

López C.M., 1999. "Análisis microestructural de la fractura del hormigón utilizando elementos finitos tipo junta. Aplicación a diferentes hormigones" Tesis Doctoral. Universidad Politécnica de Cataluña.

Ma C., Hueckel T., 1993. "Thermomechanical effects on adsorbed water in clays around a heat source" Int. Journal for Numerical and Analytical Methods in Geomechanics, Vol. 17, pp. 175-196

Martin C.D. & Lanyon G.W., 2003. "Measurement of in-situ stress of weak rocks at Mont Terri Rock Laboratory, Switzerland" Int. Journal of Rock Mechanics & Mining Science, Vol. 40, pp. 1077-1088

Mayor J.C., Velasco M., García-Siñeriz J.L., 2005. "Ventilation Experiment in the Mont Terri Underground Laboratory" Proc. Clay In Natural Engineered Barriers for Radioactive Waste Confinement, Tours, France, 14 – 18 March.

Mitchell J.K., 1993. "Fundamentals of soil behaviour" University of California, Berkeley, Second edition.

Muñoz J.J., Lloret A., Alonso E., 2001. "HE experiment: Phase 5. Rock laboratory tests" Technical Report C.I.M.N.E.-UPC

Muñoz J.J., Lloret A., Alonso E., 2003. "VE Experiment. Laboratory Report: Characterization of hydraulic rock properties under saturated and non saturated conditions" Technical Report, Project Deliverable D4

Musso G., Romero E., 2005. "Chemo-Mechanical Behaviour of high-density bentonites. Imbibition and diffusion test" Proceedings of the Int. symposium on large scale field tests in granite. Sitges, Barcelona, Spain, 12–14th November 2003. Alonso & Ledesma (Eds.), Balkema, Leiden, The Netherlands. pp. 283-291

Nussbaum Ch., Graf A., Bossart P., 2004. "Geological and structural mapping of the HE-B shaft" Mont Terri Technical Report, Geotechnical Institute Ltd., St-Ursanne, Trainee Geotechnical Institute

Nussbaum Ch., Kennedy K., Steiger H. and Bossart P., 2002. "VE tunnel section geologic map & photodocumentation" Mont Terri Technical Report, Geotechnical Institute AG and NAGRA

Olivella S., Carrera J., Gens A., Alonso E.E., 1994. "Non-isothermal Multiphase Flow of Brine and Gas Though Saline Media" Transport in porous media, Vol. 15, pp. 271-293.

Olivella S., 1995. "Non-isothermal Multiphase Flow of Brine and Gas Though Saline

Media" PhD Thesis, Geotechnical Engineering Department, Technical University of Catalunya, Barcelona, Spain.

Olivella S., Gens A., Carrera J., Alonso E.E., 1996. "Numerical Formulation for a Simulator (CODE_BRIGHT) for the Coupled Analysis of Saline Media" Int. Journal Engineering Computations, Vol. 13 (7), pp. 87 - 112.

Olivella S. & Gens A., 2000. "Vapour Transport in Low Permeability Unsaturated Soils with Capillary Effects" Transport in Porous Media, Vol. 40, pp. 219 - 241.

Pearson F., 1998. "Artificial waters for use in laboratory and field experiments with Opalinus Clay" Paul Scherrer Institut. TM 44-98-08

Perry, 1992. "Manual del Ingeniero Químico" Sexta edición, Tomo 1.

Perzyna P., 1966. "Fundamental problems in Viscoplasticity" Advances in Applied Mechanics, Academic Press, New York, Vol. 9, pp. 243-377

Picarelli L., Olivares L., Di Maio C., Urcioli G., 2000. "Properties and behaviour of tectonized clay shales in Italy" Proc. 2nd Int. Symposium The geotechnics of hard soils – soft rocks, Evangelista & Picarelli (Eds.), Balkema, Rotterdam, pp. 1211-1241

Pintado X., 2002. "Caracterización del comportamiento termo-hidro-mecánico de arcillas expansivas" Tesis Doctoral, Universidad Politécnica de Catalunya, Barcelona, España.

Pusch R., 1986. "Permanent crystal lattice contraction – a primary mechanism in thermally induced alteration of Na-bentonite" Int. Journal Scientific Basis for Nuclear Waste Management. Material Research Symposium, Seefeld K.B. (Eds.), Boston, Vol. 84, pp. 791-802

Romero E., Gens A., Lloret A., 1999. "Water permeability, water retention and microstructure of unsaturated compacted Boom clay" Engineering Geology, Vol. 54, pp. 117-127

Romero E., 1999. "Thermo-hydro-mechanical behaviour of unsaturated Boom clay: an experimental study" PhD Thesis, Technical University of Catalonia, Barcelona, Spain

Romero E., 2001. "Controlled suction technique" 4º Simposio Bresilerio de Solos Nao Saturados, Gehling W.Y.Y. & Schnaid F. (Eds.). Porto Alegre, Brasil, pp. 535-542

Sánchez M.J., 1997. "Implementación de Modelos Viscoelásticos-Viscoplasticos, para suelos, en elementos finitos y simulación de movimientos diferidos en taludes" Tesina de Master, Universidad Politécnica de Cataluña, Barcelona, España

Sánchez M.J., 2004. "Thermo-Hydro-Mechanical coupled analysis in low permeability media" PhD Thesis, Technical University of Catalunya, Barcelona, Spain.

Sánchez M. & Gens A. (2005). Final Report on THM modelling. FEBEX II. UPC-Geomechanical Group. ENRESA Report: 70-UPC-L-5-015

Schnier H., 2004. "Documentation of laboratory triaxial strength test" Deliverable 6/2b, WP3/ Task 31 Predismantling laboratory test, Technical Report Heating Experiment (HE), BGR-Federal Institute for Geosciences and Natural Resources

Steiner W., 1993. "Swelling rock in tunnels: rock characterization, effect of horizontal stresses and construction procedures" Int. Journal Rock Mechanics Mining Science & Geomechanics, Vol. 30 (4), pp. 361-380

Thury M., Bossart P., 1999. "The Mont Terri rock laboratory, a new international research project in a Mesozoic shale formation, in Switzerland" Engineering Geology, Vol. 52, pp. 347-359

Vaughan P.R., 1997. "Engineering behaviour of weak rocks: some answers and some questions" Proc. Int. Symposium Geotechnical engineering of hard soils – soft rocks, Anagnostopoulos et al. (Eds.), Balkema, Rotterdam, pp. 1741-1765

Vaunat J., Gens A., Ledesma A., Alonso E.E., 1999. "Validation of double-scale plastic model for expansive soils" Proceedings of the 7th International Symposium on Plasticity and its Current Applications, Khan, A.S., (Eds.), Neat Press, Cancún, México, 5-13 January 1999, pp. 605-608.

Vaunat, J. and Gens, A., 2003. "Bond degradation and irreversible strains in soft argillaceous rock" Proceedings of 12th Panamerican Conference on Soil Mechanics and Geotechnical Engineering, 23th – 25th June 2003, Boston, United States. Cullighan P.J., Einstein H.H. and Whittle A. (Eds.) Pub. VGE, ISBN 3-7739-5985-0, vol. 1, pp. 479-484.

Velasco M., Pedraza L., 2002. "Modelling concepts and recommended values of the Opalinus clay parameters" VE Experiment Project, Deliverable 1a, DM Iberia

Villar M.V., 2002. "Thermo-hydro-mechanical characterization of a bentonite from Cabo de Gata" PhD thesis, Universidad Complutense, ENRESA Technical Report 04/2002, Madrid

Villar M.V., Romero E., Lloret A., 2005. "Thermo-mechanical and geochemical effects on the permeability of high-density clays" Proceedings of the international symposium on large scale field tests in granite, Sitges, Barcelona, Spain, 12 – 14th November 2003. Alonso & Ledesma (Eds.), Balkema, Leiden, The Netherlands. pp. 177-191

Wittke W., 1990. “Rock Mechanics: Theory and Applications with Case Histories” Ed. Springer-Verlag

Yoshimi Y., Osterberg J.O., 1963. “Compression of partially saturated cohesive soils” Journal Soil Mechanics and Foundations Division, ASCE 89, SM4: 1-24

Zienkiewicz O., Pande G., 1977-a. “Time-dependent multi-laminate model of rocks - A numerical study of deformation and failure of rock masses” Int. Journal Numerical and Analytical Methods in Geomechanics, Vol. 1, pp 219-247

Zienkiewicz O., Pande G., 1977-b. “Some useful forms of isotropic yield surfaces for soil and rock mechanics” Finite Elements in Geomechanics, Gudehus G. (Ed.), John Wiley & Sons, Nueva York, EEUU, pp 179-190

Zienkeiwicz O.C., Taylor R.L., 1994. “El Método de Elementos Finitos”, Vol. 2, Mac Graw Hill, CIMNE.

APPENDIX

A.1 Appendix A

Table A.1: Initial state of specimens

Specimen	Suction [MPa]	W	Sr
1	89.7	0.0418	0.4902
2	89.7	0.0406	0.4765
3	89.7	0.0395	0.4637
4	89.7	0.0408	0.4789
5	89.7	0.0412	0.4831
6	89.7	0.0407	0.4775
7	89.7	0.0404	0.4741
8	89.7	0.0409	0.4807
9	89.7	0.0415	0.4870
10	89.7	0.0402	0.4719
11	89.7	0.0396	0.4652
12	89.7	0.0394	0.4620
13	89.7	0.0417	0.4901
14	89.7	0.0404	0.4739
15	89.7	0.0404	0.4744
16	89.7	0.0407	0.4782
17	89.7	0.0389	0.4561
18	89.7	0.0402	0.4714
19	89.7	0.0407	0.4782
20	89.7	0.0401	0.4706
21	89.7	0.0410	0.4810
22	89.7	0.0396	0.4654
23	89.7	0.0401	0.4706
24	89.7	0.0413	0.4852

Table A.2: Initial Wetting

Specimen	Suction [MPa]	W	Sr
1	3.8	0.0807	0.9474
2	3.8	0.0795	0.9332
3	3.8	0.0786	0.9224
4	3.8	0.0799	0.9380
5	3.8	0.0806	0.9462
6	3.8	0.0790	0.9276
7	3.8	0.0777	0.9126
8	3.8	0.0785	0.9212
9	3.8	0.0788	0.9245
10	3.8	0.0783	0.9193
11	3.8	0.0776	0.9105
12	3.8	0.0770	0.9035

Table A.3: Drying path

Specimen	Suction [MPa]	W	Sr
1	3.8	0.0810	0.9507
2	6.3	0.0758	0.8897
3	8.42	0.0714	0.8386
4	12.83	0.0669	0.7851
5	24.53	0.0613	0.7190
6	34	0.0545	0.6403
7	56.52	0.0438	0.5148
8	83.82	0.0366	0.4292
9	111.67	0.0290	0.3407
10	150.8	0.0226	0.2650
11	309.5	0.0106	0.1239
12	344.5	0.0089	0.1050

Table A.4: Initial Drying

Specimen	*Suction [MPa]*	*W*	*Sr*
13	*344.5*	*0.0103*	*0.1204*
14	*344.5*	*0.0096*	*0.1125*
15	*344.5*	*0.0105*	*0.1234*
16	*344.5*	*0.0112*	*0.1311*
17	*344.5*	*0.0089*	*0.1045*
18	*344.5*	*0.0095*	*0.1115*
19	*344.5*	*0.0104*	*0.1226*
20	*344.5*	*0.0095*	*0.1120*
21	*344.5*	*0.0099*	*0.1168*
22	*344.5*	*0.0094*	*0.1098*
23	*344.5*	*0.0094*	*0.1107*
24	*344.5*	*0.0098*	*0.1146*

Table A.5: Wetting path

Specimen	*Suction [Mpa]*	*W*	*Sr*
13	*3.8*	*0.0806*	*0.9458*
14	*6.3*	*0.0738*	*0.8665*
15	*8.42*	*0.0684*	*0.8028*
16	*12.83*	*0.0581*	*0.6824*
17	*24.53*	*0.0472*	*0.5537*
18	*34*	*0.0420*	*0.4932*
19	*56.52*	*0.0343*	*0.4024*
20	*83.82*	*0.0275*	*0.3225*
21	*111.67*	*0.0229*	*0.2688*
22	*150.8*	*0.0199*	*0.2337*
23	*309.5*	*0.0107*	*0.1251*
24	*344.5*	*0.0095*	*0.1113*

Table A.6: Results of tests to determine the water retention curve along the drying path.

Suction	Sample 1		Sample 2	
[MPa]	Water content (*w*)	Degree of saturation (S_r)	Water content (*w*)	Degree of saturation (S_r)
15 (init. state)	0.065	0.71	0.062	0.71
0	0.092	1.0	0.087	1.00
0.1	0.09	0.98	0.086	0.99
0.5	0.089	0.97	0.085	0.98
1	0.087	0.95	0.084	0.96
2	0.085	0.93	0.083	0.95
3	0.084	0.92	0.082	0.94
6.3	0.076	0.83	0.072	0.83
25	0.065	0.71	0.062	0.71
34	0.061	0.67	0.059	0.68
83	0.035	0.38	0.033	0.38

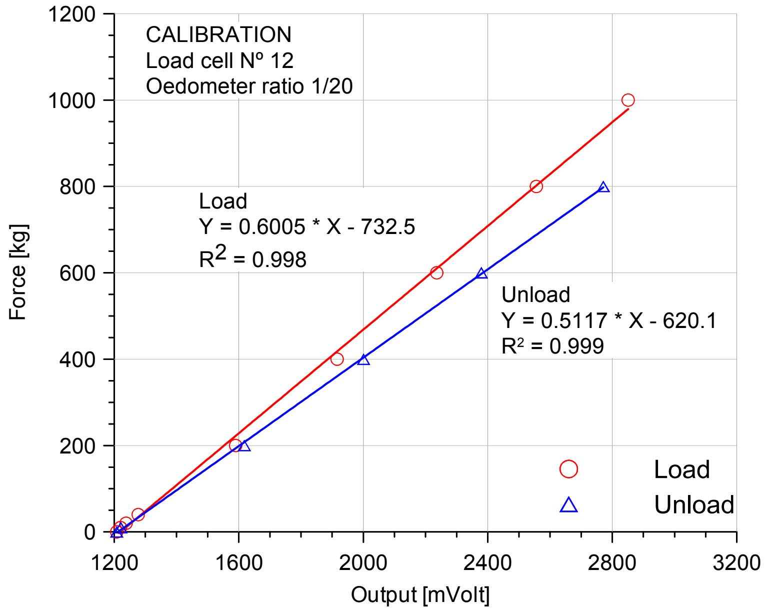

Figure A.1: Calibration curve of load cell Nº 12 used in isochoric cell.

A.2 Appendix B

Calibrations curves of sensors

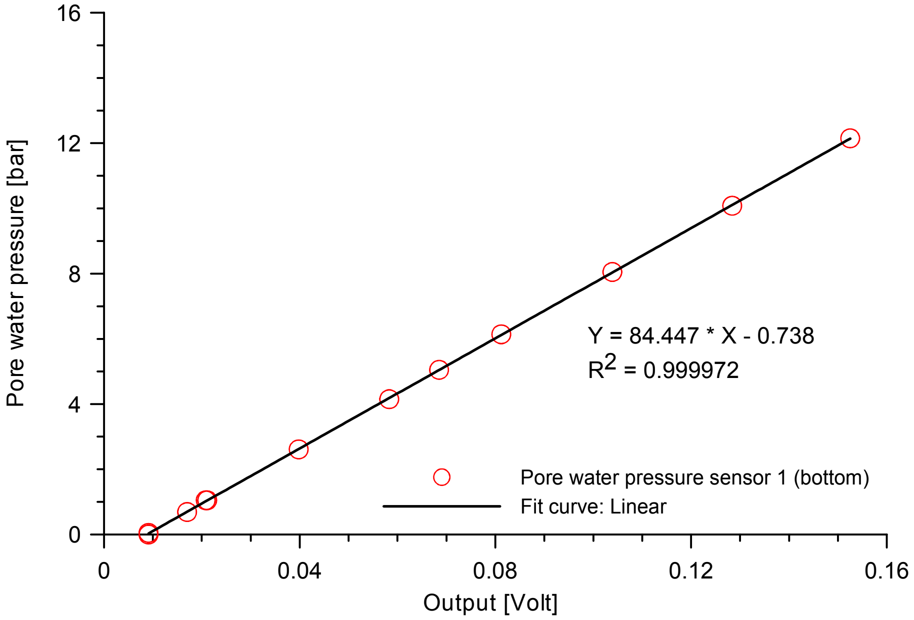

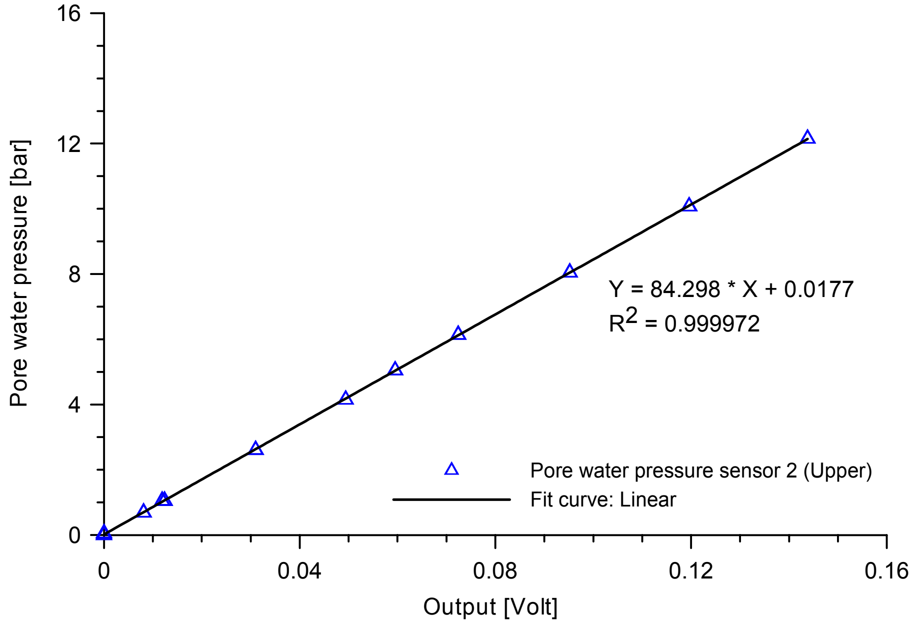

Figure B.2: Calibrations curves of the pore water pressures sensors installed into the heater cell.

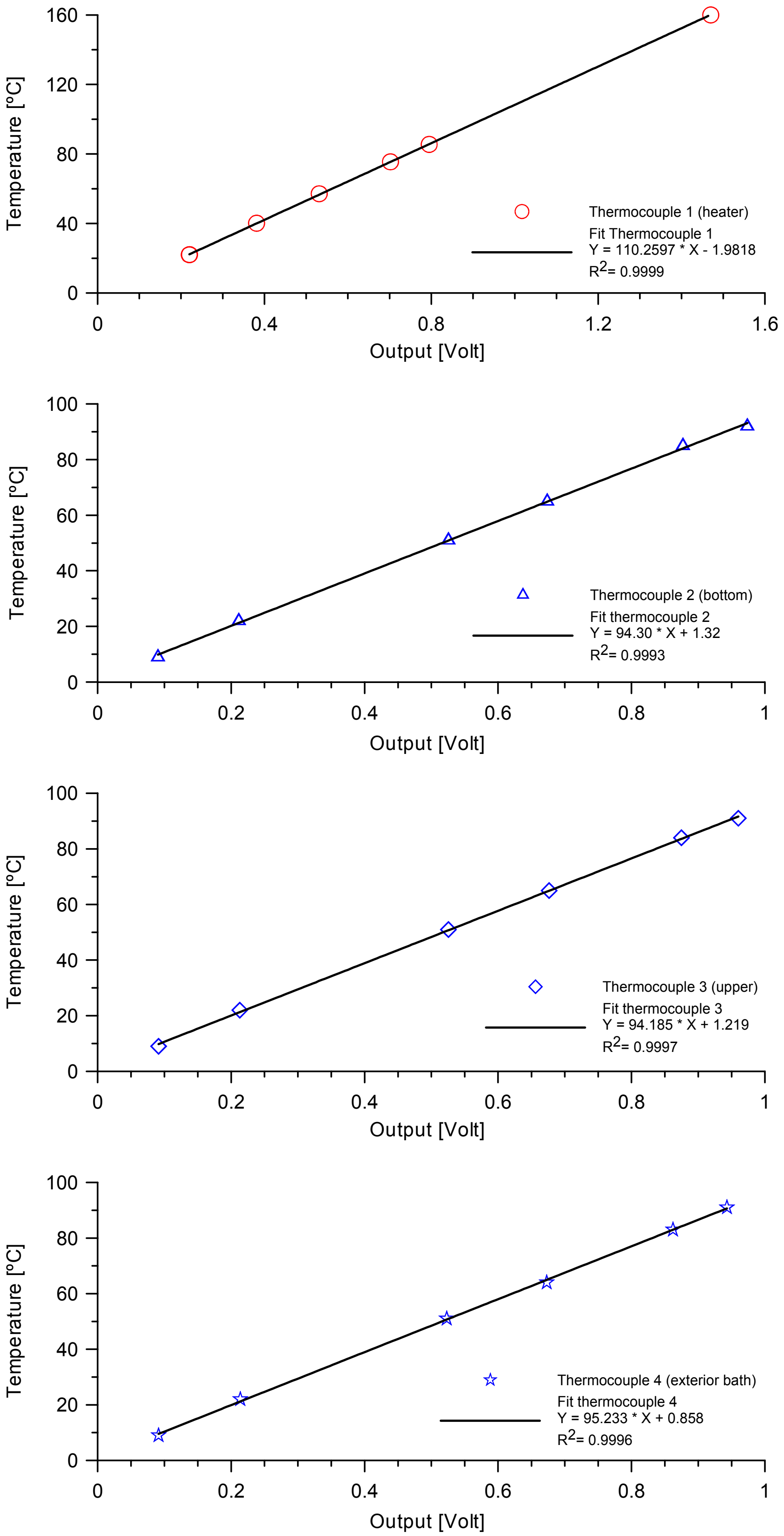

Figure B.3: Calibrations curves of the thermocouples installed in the heater cell.

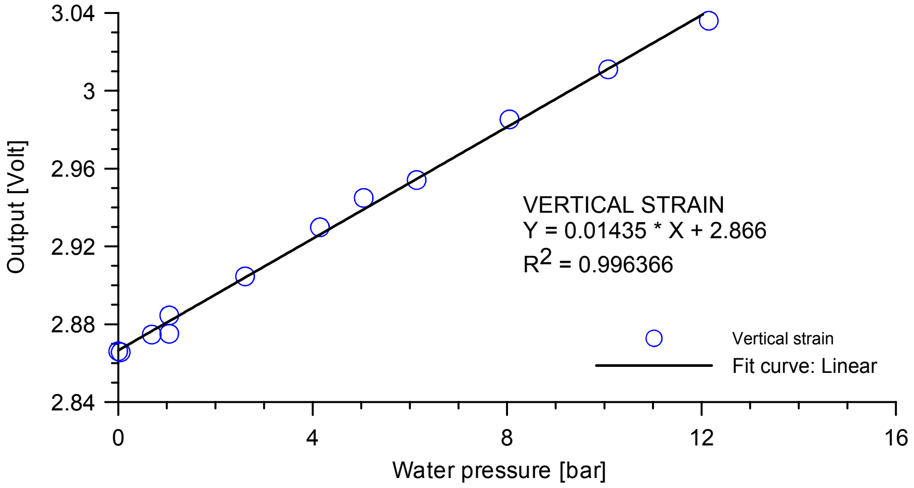

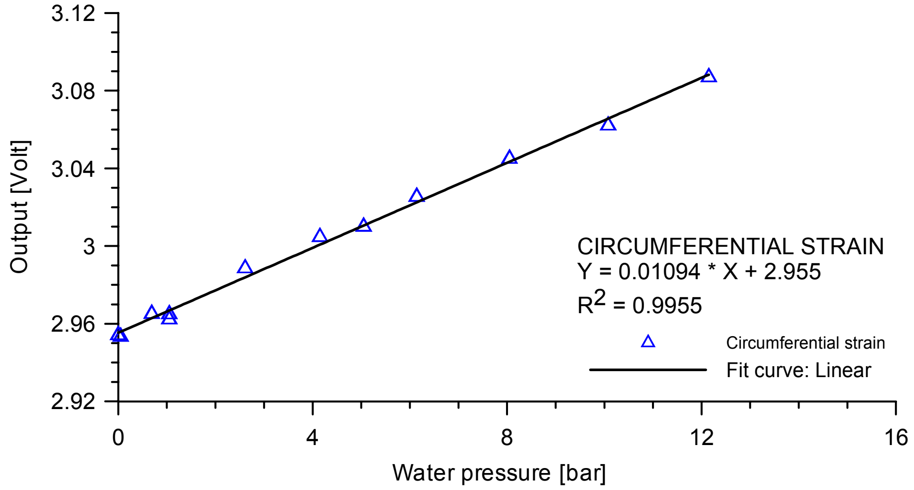

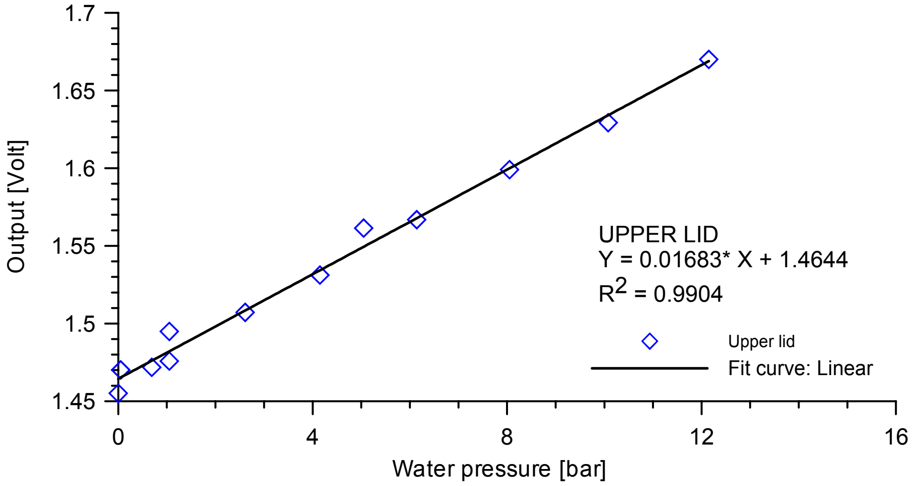

Figure B.4: Calibrations curves of the strain gages installed in the heater cell.

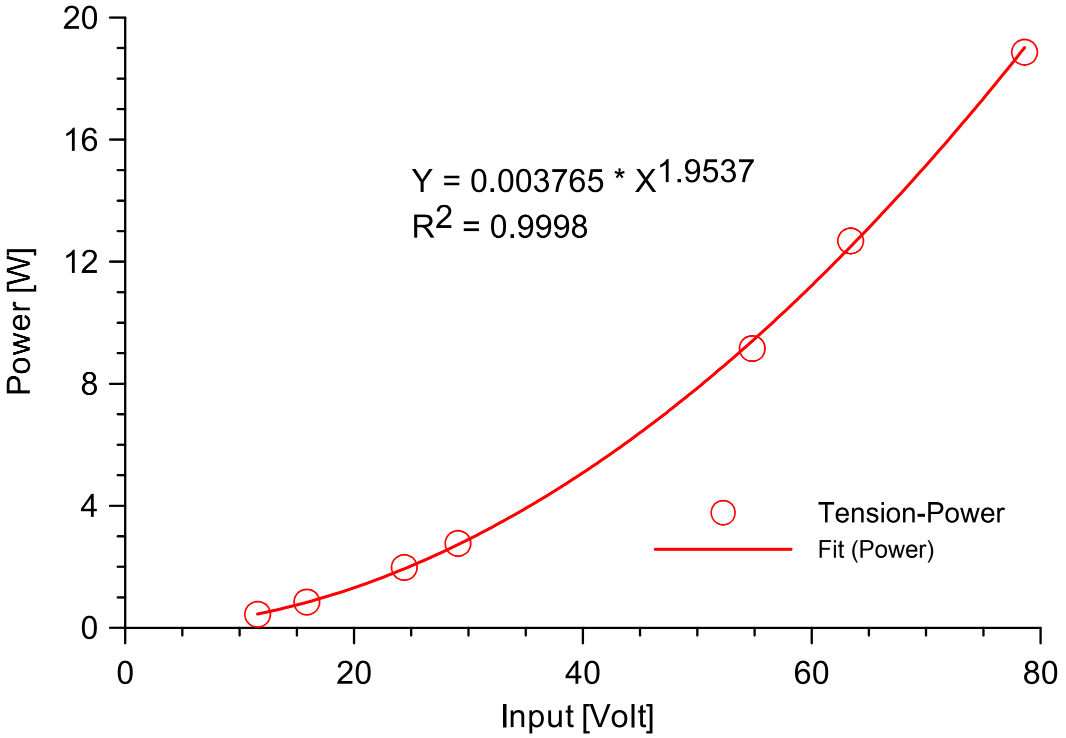

Figure B.5: Calibrations curves of the heater installed into the heater cell.